Circumventing the Tradeoff between Optical Absorption and Exciton Diffusion in Organic Photovoltaics

by

Matthew E. Sykes

A dissertation submitted in partial fulfillment
of the requirements for the degree of
Doctor of Philosophy
(Materials Science and Engineering)
in the University of Michigan
2015

Doctoral Committee:

Associate Professor Max Shtein, Chair
Professor Peter F. Green
Associate Professor Jinsang Kim
Associate Professor Pei-Cheng Ku

Acknowledgements

I would first like to thank my advisor, Prof. Max Shtein for his patience, insight, and encouragement over the past several years. His passion and enthusiasm for discovery was infectious from the moment I first applied to join his group and has been a constant source of inspiration throughout my work. Additionally his high standards, rigor, and the latitude he provides have honed me as a researcher. I would also like to thank my committee members, Profs. Peter Green, Jinsang Kim, and Pei-Cheng Ku, along with Prof. Jennifer Ogilvie for their guidance and support over the course of our many collaborations.

I have had the sincere pleasure of working with a great number of talented, helpful, and friendly coworkers and collaborators including Kanika Agrawal, Jojo Amonoo, Kwang Hyup An, Adam Barito, David Bilby, Shaurjo Biswas, Ban Dong, Bradley Frieberg, Sandro Gvakharia, Mark Hendryx, Bingyuan Huang, Yansha Jin, Gwan Ho Jung, Anton Li, Steven Morris, Sam Nola, Olga Shalev, Daniel Wilcox, and Yiying Zhao. Without you none of this work would have been possible. In addition I would like to give thanks to Brian Lassiter and Anurag Panda for their helpful discussions and assistance with equipment. The past 6 years in Ann Arbor were some of the most memorable of my life, and friends such as Ben Buer, Heather and Kevin Grossklaus, Lisa Jordan, Denis Nothern, John Thomas, and my labmates all helped make this place a home.

Finally I would like to thank my family – in particular my mother Helen, stepfather Bruce, father Mark, and stepmother Marilyn. You have always been a source of strength and

encouragement, even in my darkest moments, and never lost faith in my ability to succeed. Your constant love and support has made me appreciate the journey instead of the destination and realize that success is achieved only through doing what you love. Above all else I must thank my wife Diana, who has supported, pushed, carried, and grown alongside me throughout this long process. Without her love and companionship, this journey would have been an empty one.

Table of Contents

List of Tables

List of Figures

Abstract

Organic photovoltaic (OPV) cells have recently emerged in the last decade as a viable alternative to contemporary solar cells for power generation due to their low cost, compatibility with low-temperature and high-throughput processing methods, compatibility with flexible and stretchable substrates, low toxicity, and elemental abundance. Unlike inorganic materials, organic molecules exhibit narrow absorption bands, and photocurrent generation in OPVs generally is limited by poor optical absorption across the solar spectrum. This is further compounded by the short exciton diffusion length (L_D) in most organics compounds (~10 nm) which is an order of magnitude lower than the absorption depth (~100 nm). As a result, planar OPV active layer thicknesses must be approximately equal to L_D to ensure efficient diffusion of photogenerated excitons to a heterojunction, where dissociation into free charges occurs. In this dissertation, we examine multiple techniques to circumvent the fundamental tradeoff between absorption and diffusion in OPVs by modifying the structure of the active layers and by enhancing optical coupling.

We first develop a rigorous and predictive device model to probe the steps of the photoconversion process and provide a framework for evaluating the processes of absorption, diffusion, and dissociation in OPVs. We next demonstrate the relationship between active layer morphology and exciton diffusion/dissociation efficiencies in a planar-mixed heterojunction OPVs employing a thin mixed layer. We demonstrate a simple model to account for two-dimensional exciton diffusion in planar-mixed heterojunction OPVs and evaluate the domain

size-dependent kinetics of the dissociation process. We also show how diffusion efficiency can be controlled through interface engineering. By inserting a transparent exciton dissociation layer (EDL) to form a second heterojunction at the anode, we demonstrate a 66% enhancement in diffusion efficiency in the neighboring interlayer without affecting light absorption. We extend this concept to establish design rules enabling nearly 100% efficient exciton diffusion and a 40% increase in power generation. Finally we investigate the enhancement of light absorption in thin-film OPVs using plasmonic coupling within a metallic nanocavity. We show a 9-fold improvement in absorption efficiency and a 4-fold enhancement of photocurrent output at resonance, without modification to the active layers or diffusion efficiency.

Chapter 1

Introduction to organic photovoltaics

1.1 Motivation

1.1.1 Demand for solar energy

Since the beginning of the industrial revolution, the world has witnessed a rampant development of fossil fuel sources for global energy production, a concomitant increase in greenhouse gas (e.g. CO_2, methane, etc.) emissions, and a global average temperature rise of ~0.8 °C. Compounding the effect of increased output from human activity, greenhouse gas depletion from the atmosphere has been shown to occur at a relatively slow rate. The lifetime of atmospheric CO_2 alone is roughly 300 years, and thus atmospheric CO_2 levels are continually increasing. Consequently, the IPCC has recently projected a global average surface temperature rise of 1.1 to 6.4 °C and an average sea level rise of 18 to 59 cm over the course of the 21st century.[1] The full impact of these environmental changes is difficult if not impossible to predict, however major loss of land along coastal regions (including the inundation of countless major cities worldwide), food and water supply shortages, ocean acidification, increased severe weather events, and ecological disruption and the loss of biodiversity are all assured. A recent worldwide taxonomic study[2] has found that human activity since the industrial revolution has increased global

extinction rates over 114 times the background level, indicating we are abruptly entering (and causing) the 6th mass extinction event in the Earth's geologic history.

Apart from global conservation efforts such as improved natural resource management, efforts to mitigate climate change must focus on reducing fossil fuel dependence and the large-scale deployment of low-carbon output renewable energy sources. As of 2013, fossil fuels represented 83% of global energy consumption, with only 11% derived from renewables (**Figure 1.1**).[3] Global energy demands are constantly increasing, projected by the IEA to increase by 37% by 2040 due to economic and population growth.[3] This presents a moving target for renewable energy sources to meet, and a rapid deployment will be necessary to keep pace with worldwide demand. Otherwise, at its current rate, the annual CO_2 output of 1000 gigatonnes (necessary to limit the global temperature rise to 2 °C) is projected to be reached by 2040.[1]

The United States alone represents 2.4 TW of the world's energy demand, and 16.2% of its carbon emissions (as of 2010). Recent roadmaps for the US have shown it is entirely possible with current technologies to not only reach the IPCC's recommendation of a 50% reduction in carbon output by 2050, but to be 100% reliant on clean energy (including energy needs for transportation) by that time.[4] This shift is projected to not only increase economic output (a net increase of 2 million jobs in the energy/construction sectors), but also reduce annual air-pollution related mortalities by 40,000 - 60,000 in the US and save ~3.6% of the US gross-domestic product annually from climate and pollution-derived costs. Thus the development and deployment of clean energy technologies poses little technological, economic, and environmental downside, and is limited only by social and political hurdles.

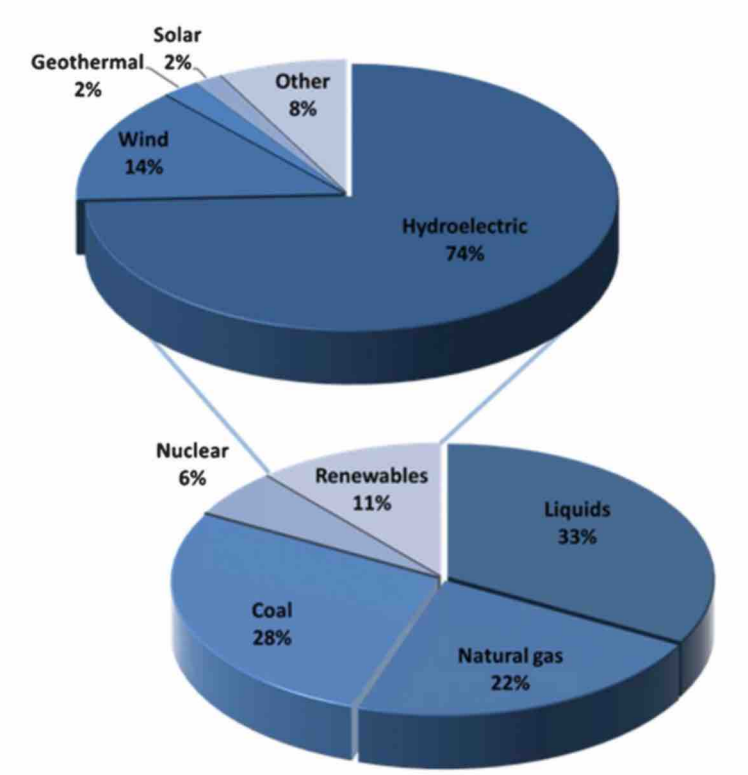

Figure 1.1 Breakdown of global energy consumption as of 2013 derived from the IEA reference case. [5]

1.1.2 Advantages of organic photovoltaics

For 100% clean energy production in the US by 2050, it is projected a 0.052% land area coverage by roof-installed photovoltaics (PVs) and 0.31% coverage of grid-scale PV power plants will be necessary, providing 45.2% of the projected US energy needs (**Figure 1.2**).[4] Thus, PV technologies represent a large fraction of the estimated power production, matched only by wind energy sources (50%). To reach this goal, PV deployment including rooftop installations, concentrated solar power (CSP), and conventional PV solar farms will all be necessary. However, with improvements in PV efficiency and the advent of disruptive technologies such as window and building-integrated PV systems, the footprint requirements of PV plants can be further reduced.

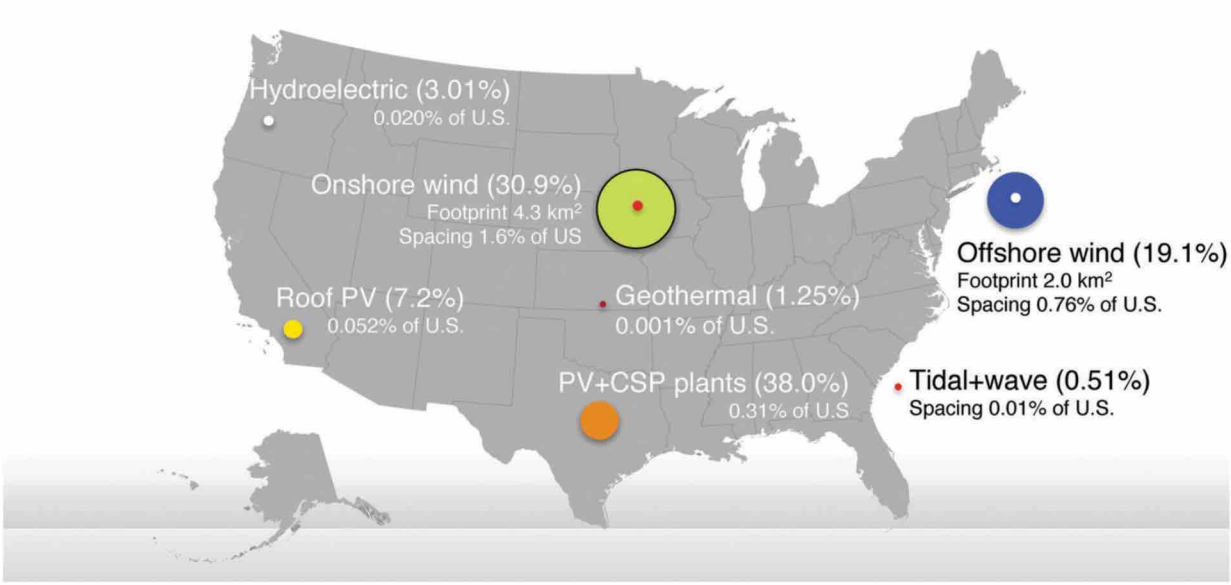

Figure 1.2 Spacing and footprint areas required for individual clean energy sources (beyond existing 2013 sources) to power 100% of US by 2050. Positions of dots do not indicate actual positions of energy farms. [4]

A number of PV technologies are existing or emerging as commercially viable, and no single technology is capable of fulfilling the requirements for all PV applications. Instead, a diversification will be necessary for PV deployment at the terawatt scale.[6] Traditional PV technologies use inorganic materials such as silicon (Si) or gallium arsenide (GaAs) which must be grown at high temperatures on expensive crystalline or glass substrates capable of handling their processing conditions. Module costs for these technologies have dropped nearly 3-fold since 2009, with nearly all mature inorganic PVs on the market sold below \$1/W and module costs per area of \$120/m^2 - \$160/m^2 (**Figure 1.3**).[6] However installed costs are often substantially higher (around \$3 - \$3.50 per installed watt) in part due to module weight, requiring bulky support structures for stability. Such "soft costs" have, to date, limited the adoption of roof-installed PV systems in particular as they prohibitively increase the initial investment required. Additionally, crystalline PV fabrication is inherently an energy-intensive batch process, limiting large-scale production and requiring an average 2 – 4 years just to return the energy

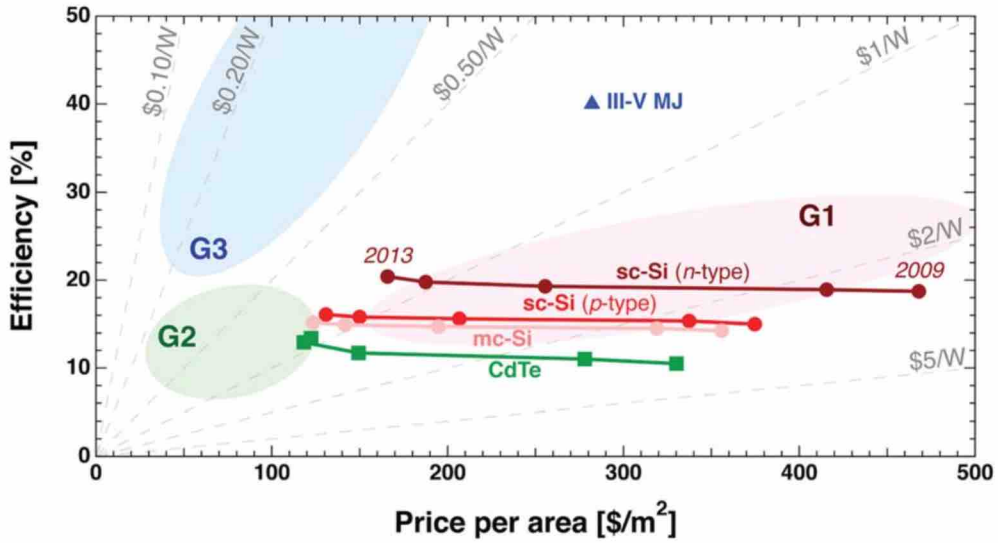

Figure 1.3 Average module efficiencies and price per area shown for several commercial inorganic PV technologies from 2009 to 2013. The three shaded regions (G1-G3) represent target zones for first, second, and third "generation" technology development. [6]

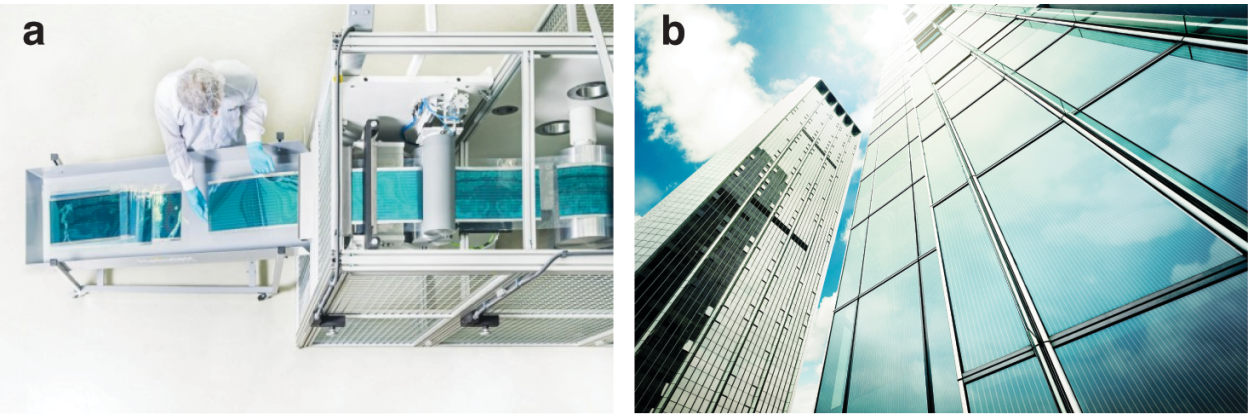

Figure 1.4 (a) Continuous processing through reel-to-reel production of flexible OPV modules on thin, plastic substrates. (b) Building-integrated OPV modules decorating windows and façades on a high-rise. Images courtesy of Heliatek GmbH.

invested in its fabrication (energy payback time).[5]

While PV cells such as those based on crystalline silicon have so far dominated the global market, thin-film PV technologies such as organic photovoltaic (OPV) cells are currently under development as alternative energy sources. OPV devices have a number of unique potential advantages over inorganic solar cells due to their compatibility with low-temperature and high-throughput processing methods, short energy payback time (less than 6 months), elemental abundance, and compatibility with flexible and stretchable substrates (**Figure 1.4**).[5-9] This allows them to be deployed in applications where lightweight and flexible form factors are desirable, such as roof-installed and building-integrated PV systems, without expensive installation costs. When combined with continuous fabrication methods such as roll-to-roll processing, OPVs have the potential for large-scale production beyond what is possible with inorganic PV.

1.1.3 Current state of the art photovoltaics

PV performance is most commonly assessed through power conversion efficiency (PCE), or the ratio of the electrical power output to the optical power incident on the device (e.g. from the Sun). As a reference standard, PVs are tested under conditions approximating the solar spectrum at a zenith angle of ~48° and an illumination intensity of 1000 W/m^2, also known as the global air-mass 1.5 (AM 1.5G).[10] This method represents the yearly average of solar irradiance at mid-latitudes on the Earth's surface, accounting for atmospheric absorption and diffuse scattering. The current record efficiencies for PV cells are shown in **Figure 1.5** as certified by the National Renewable Energy Laboratory (NREL).

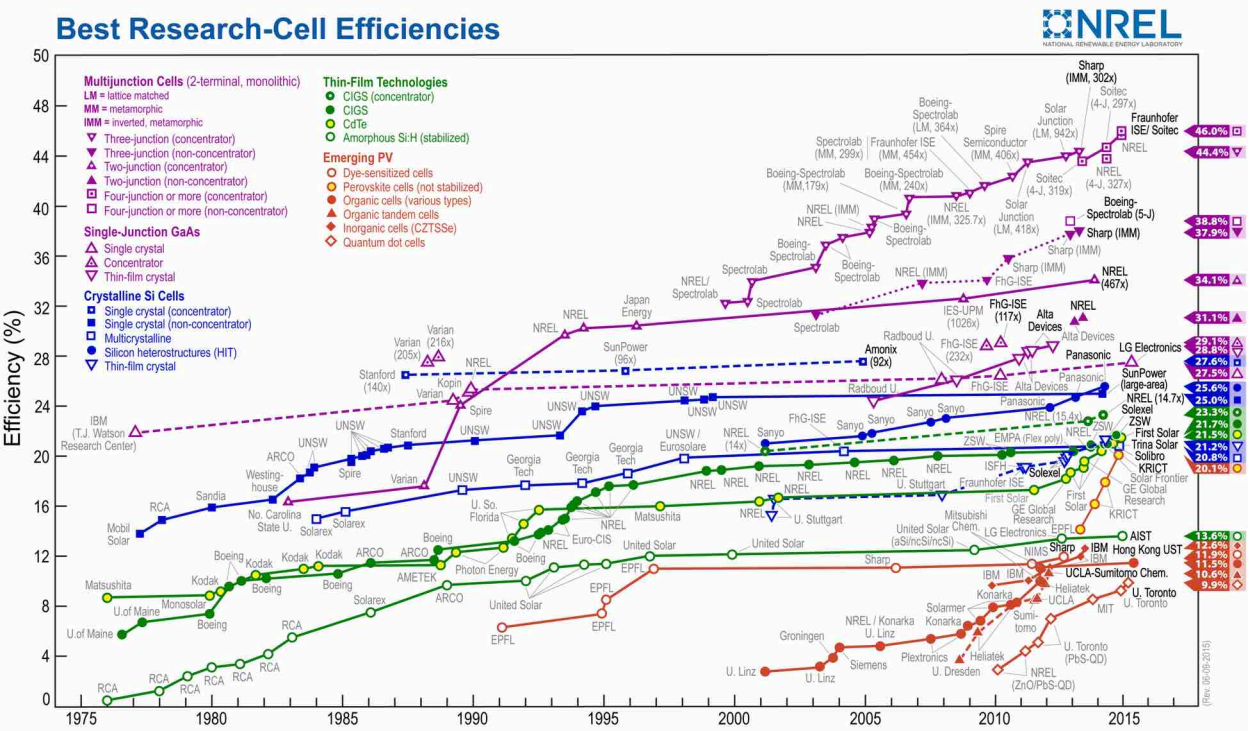

Figure 1.5 Progress in record certified efficiencies for various solar cell technologies. Courtesy of NREL.

OPV efficiencies have exhibited an exponential growth in performance with time and have recently surpassed 11%. The performance of OPV cells continues to improve rapidly, and recent work has predicted an ultimate thermodynamic PCE limit of 22 – 27% for single-junction OPV devices.[11] This estimate is founded on several assumptions of OPV operation, including perfect light absorption above the organic semiconductor band gap. However, this is practically difficult to achieve in OPVs, and this thesis will explore various means of improving absorption to drive performance closer to the thermodynamic limit.

1.1.4 This work

The thesis is organized as follows: the remainder of Chapter 1 will introduce the physics of organic semiconductors and devices and provide the necessary background for understanding

OPV operation, fabrication, characterization, simulation, and the factors limiting light absorption. The next two chapters focus on improving the internal efficiency of OPVs after light is absorbed through the control of exciton diffusion. Chapter 2 will explore the physics of exciton diffusion in devices and its relation to active layer morphology. In Chapter 3 techniques for improving exciton diffusion efficiency by interface modification and the introduction of exciton dissociation layers are presented. In Chapter 4 a method to improve light absorption in devices through surface plasmon polariton coupling is explored. Finally in Chapter 5 the work is summarized and future directions are outlined for improving light absorption and exciton diffusion in OPVs.

1.2 Properties of organic semiconductors

Organic semiconductors are carbon-based materials that fall into two broad categories: polymers and small molecules (**Figure 1.6**). Typically, covalently-bonded macrocycles composed of carbon, nitrogen, oxygen, and sulfur groups are decorated and functionalized with various ligands to produce a monomer unit or small molecule. In polymers, these units are repeated in a linear chain thousands of times to create a large backbone. One of the unique advantages (or disadvantages) of such materials is the nearly infinite number of possible compounds that can be synthesized. The electrical, optical, and thermal properties can all be systematically tailored through chemical structure, making organics promising for PV applications in particular. In this thesis we will focus on the physics of small molecular semiconductors in OPVs, however most of the concepts are directly applicable to polymer-based OPVs.

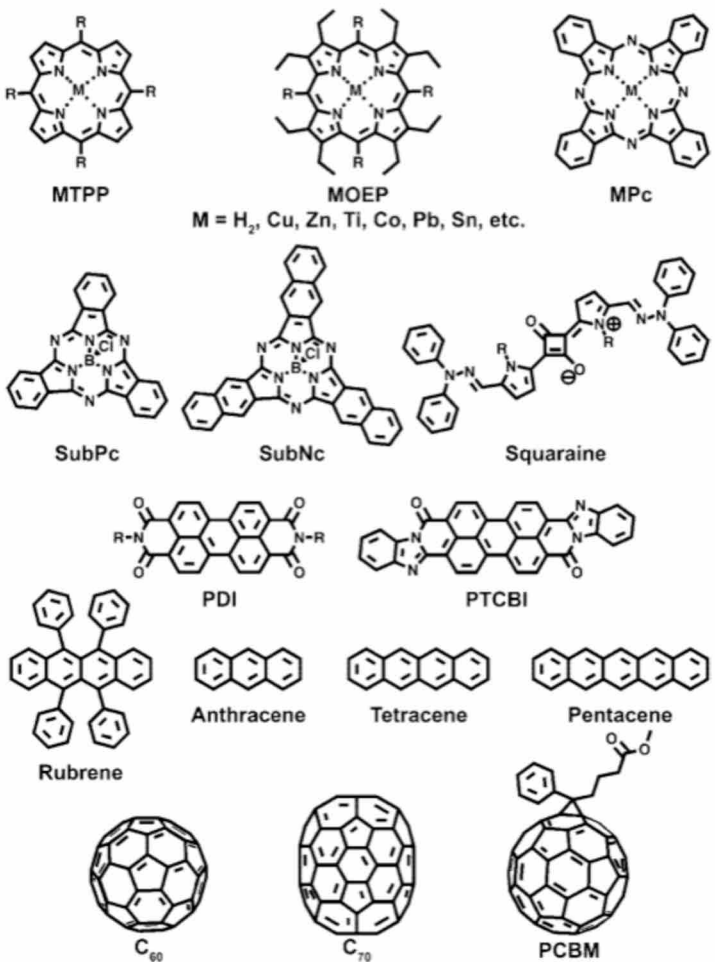

Figure 1.6 Archetypal small molecule organic compounds used in organic photovoltaics. [12]

1.2.1 Bonding and crystal structure

While the *intra*molecular bonds between atoms in organics are covalent, in the solid-state organics generally exhibit *inter*molecular van der Waals bonding between molecules. The low bonding strength characteristic of van der Waals bonds makes organic materials inherently "soft", exhibiting low sublimation temperatures and low Young's moduli. The latter lends to the mechanical flexibility and elasticity inherent to organics. Without the need for lattice matching or epitaxial growth as in crystalline inorganic semiconductors (e.g. Si, GaAs), small molecules can be deposited on virtually any substrate surface.

In the majority of OPVs, molecules are deposited as thin films through a variety of processing strategies. In most cases films are amorphous, however polycrystalline morphologies can also arise. A common molecular arrangement at room temperature is the herringbone motif (triclinic crystal structure) as seen in acenes such as pentacene and planar phthalocyanines (**Figure 1.7**). Other organics with non-planar macrocycles can exhibit a wide variety of crystal structures and symmetries, such as the face centered cubic packing of fullerene C_{60} molecules or the orthorhombic packing of bowl-shaped subphthalocyanines.[13, 14] In most cases, multiple polymorphs exist at various temperatures in the bulk phase, and substrate interactions can also impact molecular ordering within the first several monolayers.

Molecular ordering is thin films is independent of the substrate's crystallographic orientation due to the large size mismatch between molecule and substrate atomic arrangements and the low bonding strength of the van der Waals attractive forces. Thus organic thin films exhibit no preferential orientation for their crystallographic axes in-plane. However, due to the interaction with the substrate surface, polycrystalline and amorphous films generally exhibit birefringence with uniaxial symmetry. Preferential orientation is observed relative to the plane of the substrate, with no preferential ordering direction in-plane. For this reason, in both polycrystalline and amorphous compounds, optical and electrical transport properties of organic semiconductors can vary substantially in-plane versus out-of-plane and are often reported separately.

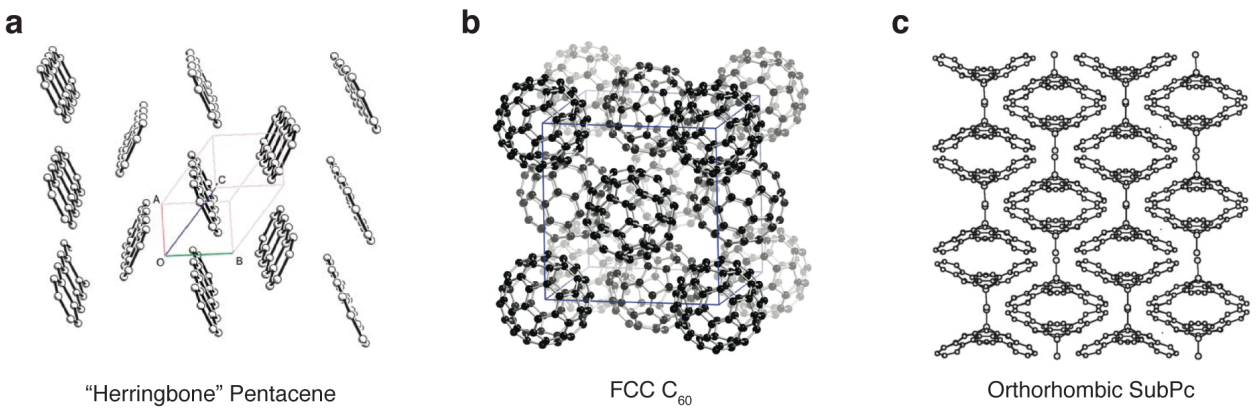

Figure 1.7 Examples of crystal structures commonly observed in small molecule solids at room temperature including (a) pentacene, (b) fullerene C_{60}, and (c) boron subphthalocyanine chloride (SubPc). [13, 14]

1.2.2 Molecular energy levels

Just as individual atoms have quantized orbital levels that electrons occupy, organic molecules possess delocalized electronic orbitals shared amongst their constituent atoms (**Figure 1.8**). The delocalization of the aromatic pi-bonds and molecular breathing modes broaden the molecular orbital levels, yielding a distribution of orbital energies that remain occupied by electrons in the ground state. The highest such orbital energy is termed the highest occupied molecular orbital (HOMO), while the lowest unoccupied molecular orbital (LUMO) represents the lowest energy unoccupied orbital in the molecular ground state.

The difference between the HOMO and LUMO levels is the optical energy gap or bandgap (E_g) of the molecule, representing the minimum energy required to promote an electron from an occupied to unoccupied energy level. Since orbitals at or below the HOMO level energy are all occupied, electron transport through molecules must occur through the LUMO level. Conversely, holes (the positive charge resulting from an absent electron) are transported through the HOMO level of the molecule. As will be seen later in this chapter, the HOMO and LUMO

levels of a molecule determine not only its optical properties (e.g. absorption spectrum) but also its function in electronic devices.

1.2.3 Charge transport

In inorganic semiconductors, strong interatomic bonds and a periodic lattice structure give rise to conduction and valence bands that transport charge. While in some cases, organics grown as single crystals exhibit band-like transport, the vast majority of applications such as OPVs employ thin films with a significant degree of molecular disorder. In such films, wavefunction overlap between the molecular orbitals is poor, and charges are confined to individual molecules instead of being delocalized over a lattice. Instead of the ballistic motion characteristic of band transport, charges in organics transport through hopping from one molecule to another *via* the direct exchange of the electron or hole wavefunction. This thermally activated hopping process is mediated by the overlap between the orbitals of neighboring molecules and is thus sensitive to their relative orientations.[15]

Defects in organics significantly modify the hopping rate of charges between molecules. There are two broad categories of defects: *extrinsic* defects arising from impurities incorporated during deposition or generated *via* photo- or chemical-induced decomposition and *intrinsic* defects arising from molecular disorder and the local reorganization of molecules when a charge is present.[16] Extrinsic defects usually result in deep-level traps, situated deep within the bandgap of the material. Intrinsic defects are generally shallow with respect to the HOMO/LUMO levels and are often described by either a Gaussian or exponential distribution (**Figure 1.9**a).

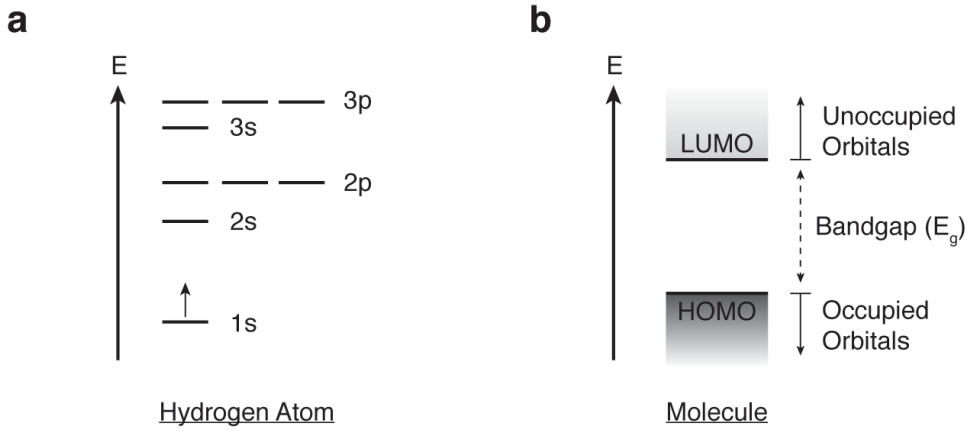

Figure 1.8 Energy level diagrams of (a) the low-energy quantized orbitals in a hydrogen atom, with the arrow indicating the single valence electron in the 1s ground state, and (b) the broadened orbital levels of a molecule. The spacing between HOMO and LUMO levels is indicated by E_g, representing the forbidden energy range that electrons may not occupy in the molecule. Occupancy is allowed below the HOMO and above the LUMO, as indicated.

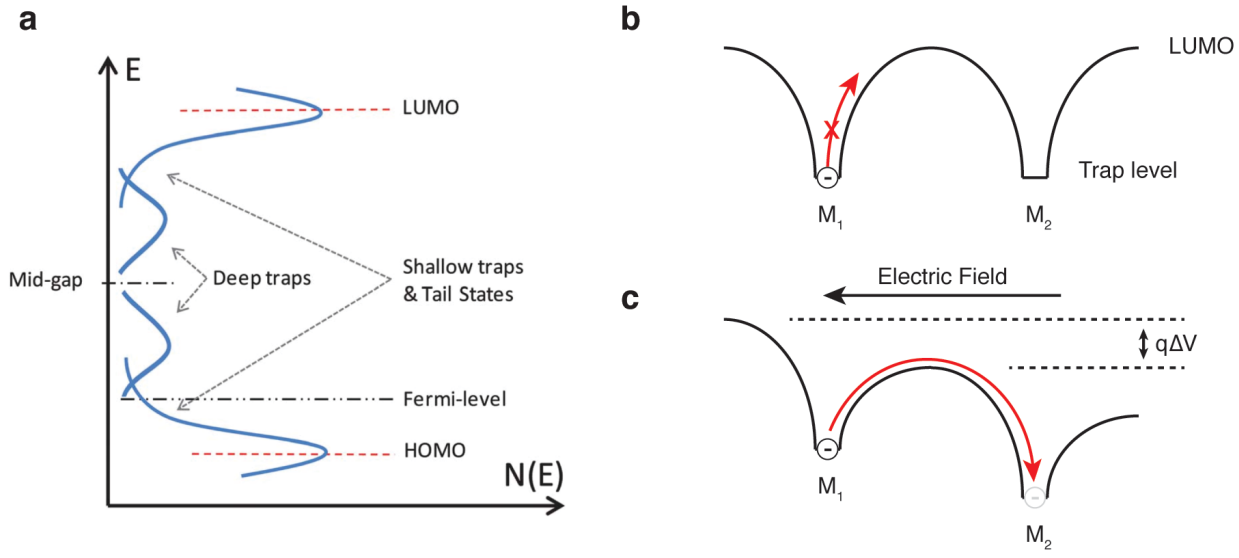

Figure 1.9 (a) Conceptual diagram of the trap density of states (N) distribution as a function of energy in a disordered organic film. (b) Schematic of electron (polaron) hopping between two molecules M_1 and M_2 (vertical axis is energy) and (c) the field-assisted lowering of the activation barrier for hopping in the direction of the applied field. [16]

When a molecule is in a charged state, a physical reorganization in the molecule's structure occurs as the intramolecular bonds become strained. Due to the low dielectric constant of most organic materials ($\varepsilon_r \sim 3$), weak polarizations are induced in the neighboring molecules to screen the charged molecule, accompanied by molecular reorganization. Thus the movement of charge in organics is coupled to the local displacement of molecules (also known as phonons). For this reason, charges in organic semiconductors are often referred to as positively or negatively charged "polarons".[15]

Although intermolecular polaron hopping is thermally activated, it can be assisted by the application of an electric field (**Figure 1.9**b,c). Field-induced lowering of the activation barrier increases the probability of hopping in the direction of the applied field. The field- and temperature-dependent mobility (μ) of polarons in organics is most commonly described by the Poole-Frenkel relation:

$$\mu = \mu_0 \exp\left(-\frac{\Delta}{kT}\right)\exp\left(\gamma E^{1/2}\right) \tag{1.1}$$

where μ_0 is the zero-field mobility at absolute zero, Δ is the activation energy (average trap depth), kT is the thermal energy, γ is the field activation parameter, and E is the applied electric field.[17] As can be seen in Equation (1.1), mobility *increases* with temperature in organics as opposed to *decreasing* with temperature in systems exhibiting band transport (due to increased phonon scattering of charges).

1.2.4 Excitons

When an electron and hole are electrostatically bound in a material, it is termed an "exciton". There are three fundamental types of excitons: Frenkel excitons, where both electron and hole reside on the same molecule, charge transfer (CT) excitons, where the electron and hole reside

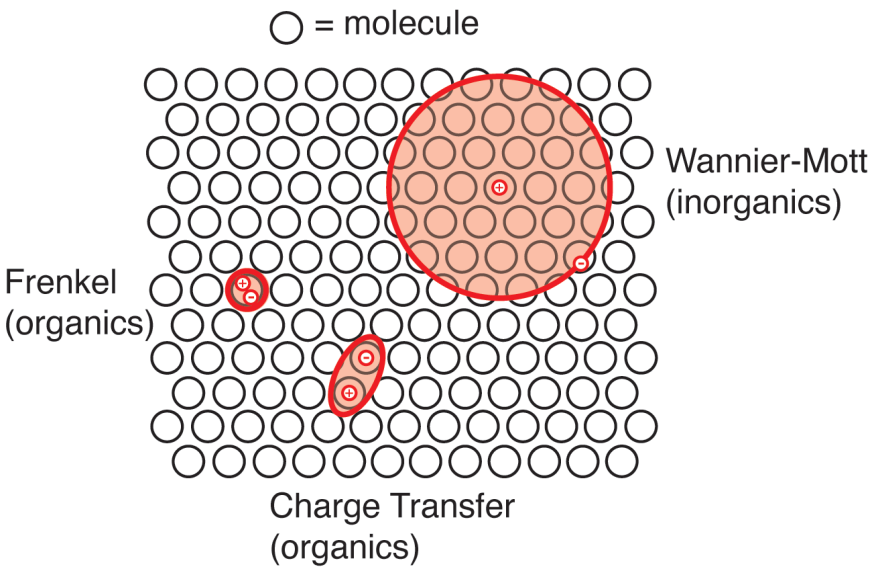

Figure 1.10 Schematic representation of the three possible exciton types: Frenkel, charge transfer, and Wannier-Mott.

on neighboring molecules, and Wannier-Mott excitons, where the electron and hole are separated by many times the intermolecular spacing (**Figure 1.10**). All three exciton types exhibit significantly different Coulombic binding energies (E_B):

$$E_B = \frac{q^2}{4\pi\varepsilon_r\varepsilon_0 r} \tag{1.2}$$

where q is the elementary charge, ε_0 is the permittivity of free space, and r is the electron-hole separation distance. For Wannier-Mott excitons, E_B is typically on the order of 5-10 meV, while Frenkel and CT excitons exhibit binding energies of 0.1 – 1 eV. Due to the low dielectric constant ($\varepsilon_r \sim 3$) of organic semiconductors, charges are poorly screened from one another by the surrounding medium, yielding only Frenkel and CT excitons. This is in stark contrast to inorganic semiconductors such as Si ($\varepsilon_r \sim 12$), whose dielectric constants are generally much higher and charges are delocalized along the crystal lattice. The high permittivity effectively masks the attractive forces of the electron-hole pair, yielding Wannier-Mott excitons (at low temperatures). At room temperature, these are thermodynamically unstable as their binding

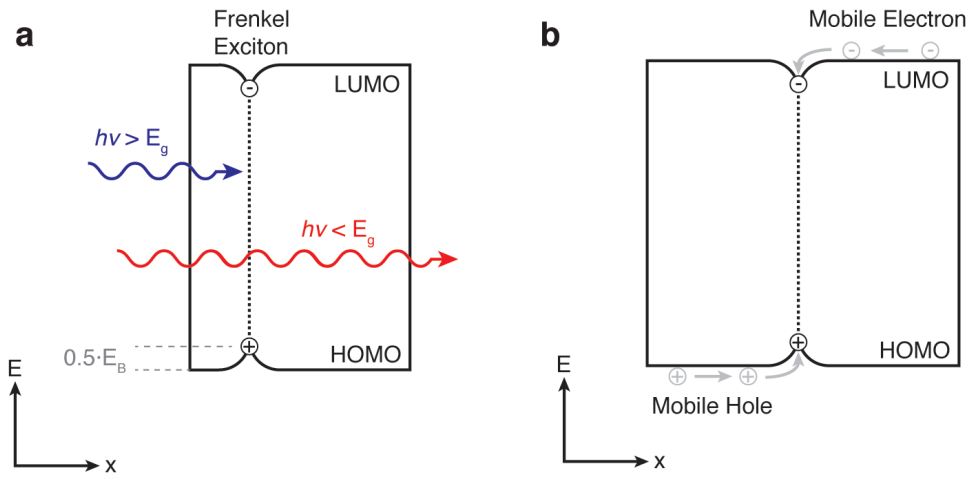

Figure 1.11 Energy level diagrams detailing the process of (a) optical and (b) electrical generation of excitons in an organic semiconductor. Exciton formation is followed by a near-instantaneous relaxation of the bound electron and hole towards the middle of the bandgap due to their Coulombic attraction.

energy is lower than kT (= 26 meV).

Excitons can be formed either through the absorption of a photon whose energy is greater than the bandgap (optical generation) or through the electrostatic capture of a mobile hole or electron by its opposite charge (electrical generation), as illustrated in **Figure 1.11**. Immediately upon formation, the strong Coulombic attraction between the electron and hole causes excitons to energetically relax, with this energy lost to heat. Thus we draw excitons as trapped within the bandgap of the molecule, as their equilibrium energy is lower than their energy of formation (HOMO-LUMO difference) by E_B. While the electrical generation process does occur at high injection current densities, the operating conditions of OPVs are generally far from this regime. Thus, the remainder of this thesis solely focuses on the optical generation of excitons through the process of light absorption.

Excitons are considered quasiparticles with a net-neutral charge, causing their motion to be unaffected by applied fields (unlike polarons). Consequently, exciton migration occurs

through diffusive energy transfer processes. There are two dominant energy transfer mechanisms responsible for exciton diffusion in organic semiconductors: Förster resonant energy transfer (FRET) and Dexter transfer.[18] FRET is a non-radiative process involving the exchange of energy between two molecules through resonant electromagnetic coupling. As an exciton may be considered a point dipole with a characteristic frequency, the resonant transfer of an exciton from one molecule to another may occur by inducing the transition dipole in a nearby molecule through Coulombic interactions. Physically this can be thought of as the emission of a "virtual" photon by one molecule and its reabsorption by another. However, the FRET process only occurs at separation distances much shorter than the wavelength of light, thus no actual photon emission (radiation) occurs. In the simplest case of two molecules separated by a distance d, the rate of Förster transfer (k_F) can be described by:

$$k_F(d) = \frac{1}{\tau}\left(\frac{R_0}{d}\right)^6 \tag{1.3}$$

where τ is the exciton lifetime and R_0 is the Förster radius, describing the distance at which the rate of transfer between two dipoles is equivalent to the inverse of the intrinsic exciton lifetime. The Förster radius is then calculated by:

$$R_0^6 = \frac{9\eta_{PL}\kappa^2}{128\pi^5 n^4}\int \lambda^4 F(\lambda)\sigma(\lambda)d\lambda \tag{1.4}$$

Here n is the real component of the refractive index, η_{PL} is the photoluminescence (PL) quantum yield, κ is the orientation factor, λ is the wavelength of light, F is the normalized fluorescence spectrum of the emitting molecule, and σ is the absorption cross section of the acceptor molecule. FRET can occur between molecules of the same type if there is sufficient overlap between their absorption and emission spectra (low Stokes' shift) as well as between dissimilar molecules. Typical R_0 values are in the range of 1 – 10 nm, while intermolecular spacing

distances are generally on the order of 1 nm or less.[18] Thus FRET represents a long-range energy transfer process with respect to the intermolecular distance. Furthermore, it is important to note that FRET requires the exciton being transferred to have a finite quantum yield:

$$\eta_{PL} = \frac{k_r}{k_r + k_{nr}} = k_r \tau \tag{1.5}$$

where k_r and k_{nr} are the radiative and non-radiative rates of exciton recombination. For excitons where radiative recombination to the ground state is spin-forbidden (such as triplets), the FRET process does not occur.

In contrast to FRET, the Dexter process describes exciton energy transfer between nearest-neighbor molecules through direct electron exchange. When there is sufficient overlap between the wavefunctions of the excited molecule and the ground state of a neighboring molecule, direct electron transfer may occur. The rate of Dexter transfer (k_D) can be described by:

$$k_D(d) = KJ \exp\left(-\frac{2d}{L}\right) \tag{1.6}$$

where K is the related to the orbital interaction, J is a spectral overlap integral, and L is the van der Waals radius. The exponential decay of the Dexter transfer rate with distance constricts the transfer to nearest-neighbors. However, this process, unlike FRET, is independent of the exciton PL quantum yield. Thus it is assumed to occur in all organics, regardless of exciton character. For fluorescent molecules in general, it can be safely assumed that both processes are occurring simultaneously during the exciton diffusion process.

Under normal conditions of OPV operation, exciton densities in the active organic layers are sufficiently low such that higher order processes (e.g. exciton-exciton annihilation) are

negligible. In the case that exciton diffusion occurs through an isotropic random walk, the exciton diffusivity (D) can be directly calculated to first-order:

$$D = Ad^2 k_{ET} \tag{1.7}$$

where A is a prefactor accounting for intermolecular disorder (~1), d is the average intermolecular spacing, and k_{ET} is the dominant rate of energy transfer (either Dexter or FRET).[19] The assumption of random motion is valid in most organics, in particular those with limited long-range order or amorphous character, and as a result exciton migration follows Fick's laws. Combined with the characteristic exciton lifetime of the organic semiconductor, the exciton diffusion length (L_D) is described by:

$$L_D = N\sqrt{D\tau} \tag{1.8}$$

where N = $\sqrt{1}$, $\sqrt{2}$, or $\sqrt{3}$ for isotropic diffusion occurring in 1, 2, or 3 dimensions, respectively. It is important to note here that an additional prefactor of $\sqrt{2}$, accounting for diffusion in the positive or negative direction during each successive diffusion step, is incorporated into the diffusivity term in the above formalism.

When comparing D and L_D terms, the diffusivity describes an intrinsic average hopping rate of excitons between molecules, while the L_D represents the root-mean-squared (RMS) displacement of excitons over the course of their lifetime. In other words, L_D describes a characteristic distance over which an exciton can migrate during its lifetime prior to decay. However, in actuality the probability distribution (P) for excitons reaching a distance R from their point of generation follows the complementary error function according to Fick's second law, $P(R) = \mathrm{erfc}(-R/L_D)$, and a range of distances are accessed during the diffusion process. However, as is standard practice, L_D is used as an average parameter to describe the displacement of excitons in the system.

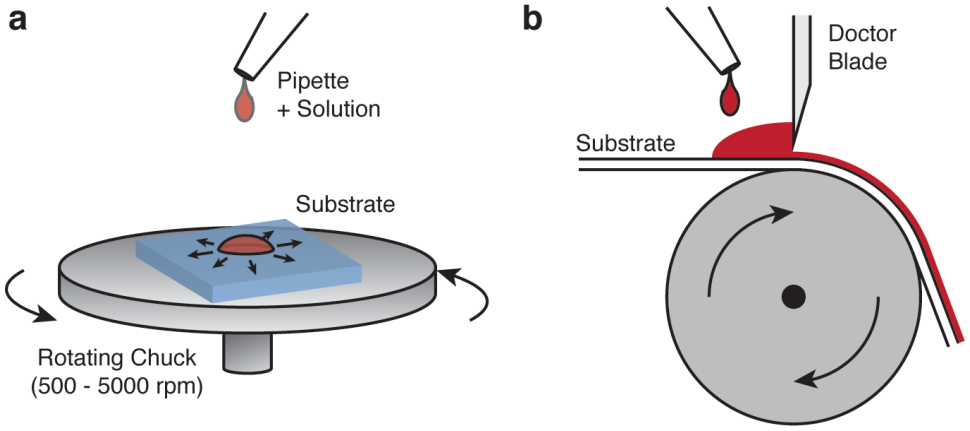

Figure 1.12 Diagrams of the (a) spin-coating and (b) doctor blade coating process for solution deposition of organics.

1.3 Processing organic thin films

The fabrication of organic semiconductor thin films is inherently determined by the molecular weight (MW) of the compound used, its solubility, and its thermal stability. For polymers, oligomers, high MW small molecules, and compounds whose decomposition temperature is at or below the sublimation temperature, solution-processing techniques are employed. However, in the case of low MW small molecules (typically in the range of 200 – 1000 g/mol) with sublimation temperatures below their decomposition temperature, vacuum-based methods are commonly used to deposit thin films from the vapor phase.[20] While various deposition methods exist, we will restrict our discussion to those compatible with high-throughput, large scale, and large area production.[8, 21]

1.3.1 Solution-based deposition methods

The most ubiquitous solution processing technique (at the lab scale) involves spin-coating polymers or small molecules on the desired substrate (**Figure 1.12**a). The substrate is affixed to a rotating chuck by a low vacuum seal and rotates at frequencies in the range of 500 – 5,000 rpm.

A solution of the desired organic compound (or compounds) is first applied to cover the substrate surface. Upon rotation, excess solution spreads and detaches from the substrate edges, creating a uniform liquid film on the surface whose solvent rapidly evaporates. The organic semiconductor is left behind as a precipitate during the evaporation process, conformally coating the substrate surface.[22] The rotation rate, ramp rate, and dwell time of the spin-coating process are all used as process parameters to control the final film thickness.

An alternative solution processing method is the doctor blading technique (**Figure 1.12**b), where a flat blade (as opposed to mechanical rotation) is used to remove the excess liquid from the surface of the substrate during substrate translation.[21] The final film thickness is primarily controlled through the blade-substrate separation distance as the process parameter. A particular advantage of doctor blading is its compatibility with high throughput, reel-to-reel production methods, while spin-coating is inherently a batch process.

Regardless of processing strategy, the concentration and formulation of the solution is critical to the resultant film quality, thickness, and morphology upon drying. The choice of solvent determines not only the solubility limit of the organic compound, but also the solvent evaporation rate during drying. These two factors have been shown to be essential in the film formation process, as they determine the rate of solute precipitation and the kinetics of molecular ordering in the film.[22]

The use of high volumes of toxic organic solvents, intermixing with underlying layers, and the need of an additional drying step all limit the adoption of solution-based deposition techniques at commercial scales. However, for many materials there is no alternative processing strategy available. Indeed in this thesis we will use spin-coating for the application of select polymers as interfacial layers in OPVs.[23]

1.3.2 Vacuum-based deposition methods

By far the most common technique for small molecule deposition is vacuum thermal evaporation (VTE). Alternative deposition strategies have recently been developed such as organic vapor phase deposition (OVPD) which circumvent many of the drawbacks of VTE and will be discussed shortly.[8] In all cases, pure organic source materials in crystalline powder form are evaporated from a source and condensed from the vapor phase onto a substrate. The VTE process (**Figure 1.13**) is carried out under high vacuum (~10^{-7} Torr) and employs resistively heated boats to sublimate the source materials. By controlling the power delivered to the sources, the rate of deposition (proportional to the sublimation rate) can be precisely controlled. Under high vacuum conditions, the mean free path of molecules is on the order of 100 m. Thus the molecular vapor is ballistically transported across the VTE chamber (~ 1 m) and impinges on the substrate through direct line-of-sight. The deposition profile for point sources follows a cosine-squared dependence with deposition angle, yielding a thickness variation over the substrate of roughly 5% in most systems. Improved uniformity can be achieved by incorporating of multiple sources or by increasing the dimensions of the VTE chamber, however material utilization efficiency (~3%) will suffer as a result. Finally, the temperature of the substrate can be used to control the rate of molecule adsorption and the resultant crystallinity of the deposited film, but it is commonly maintained at room temperature.

One of the advantages of the VTE technique is its compatibility with a wide variety of source materials including metals, transition metal oxides, and organics. However the requirement of high vacuum, the low materials utilization efficiency, and the decrease in thickness uniformity on textured or large area substrates increases costs for large-scale production. In the OVPD process (**Figure 1.14**), a source material is evaporated into a carrier gas

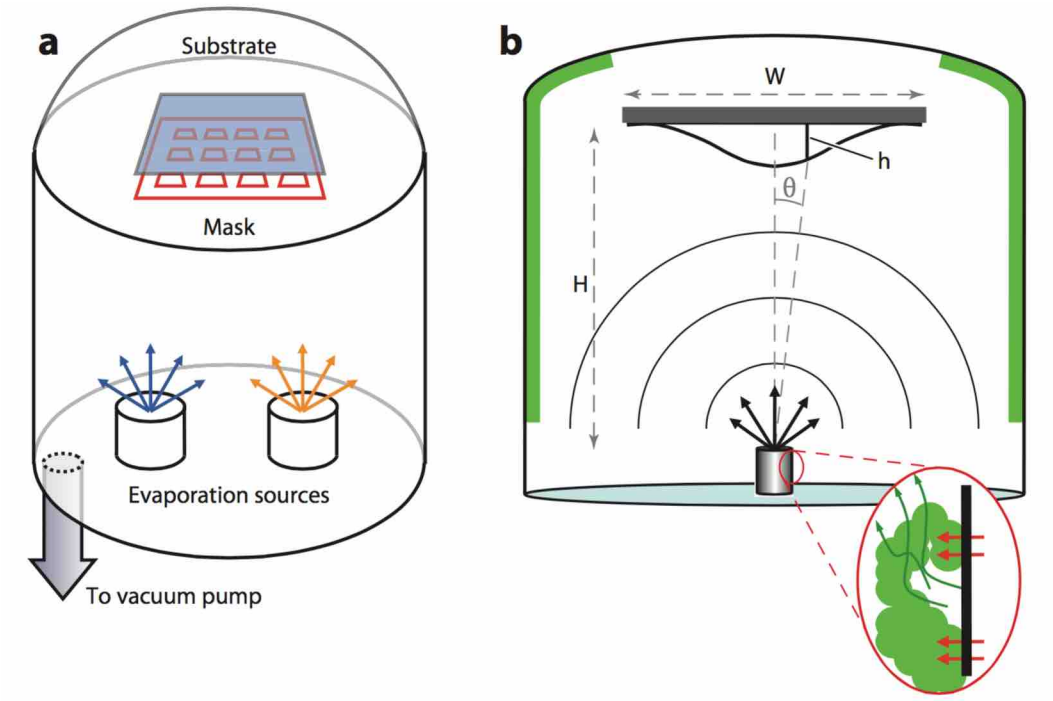

Figure 1.13 (a) A simplified schematic of a vacuum thermal evaporation (VTE) chamber, shown with two sources and a shadow mask. (b) An illustration of film nonuniformity inherent in point-source deposition, as well as unevenness of heating inside the evaporation source due to the poor thermal conductivity of crystalline organic powders. [8]

that transports it to a cooled substrate where it condenses. The use of a carrier gas to direct the molecular flux allows this process to be conducted under low vacuum, and the walls of the chamber are heated to minimize surface condensation of the molecular vapor and reduce material losses. As a consequence, materials utilization efficiencies exceeding 40% can be achieved. As the mean free path of the molecules in the carrier gas is significantly lowered, deposition on the substrate is a diffuse as opposed to ballistic process. As a result, a uniform coating can be applied over large area and rough substrates. Precise control of the film morphology is also possible by tuning the source temperature, flow rate, chamber pressure, and substrate temperature.[24] Furthermore in both OVPD and VTE the codeposition of multiple organics is made possible in by the introduction of multiple sources.

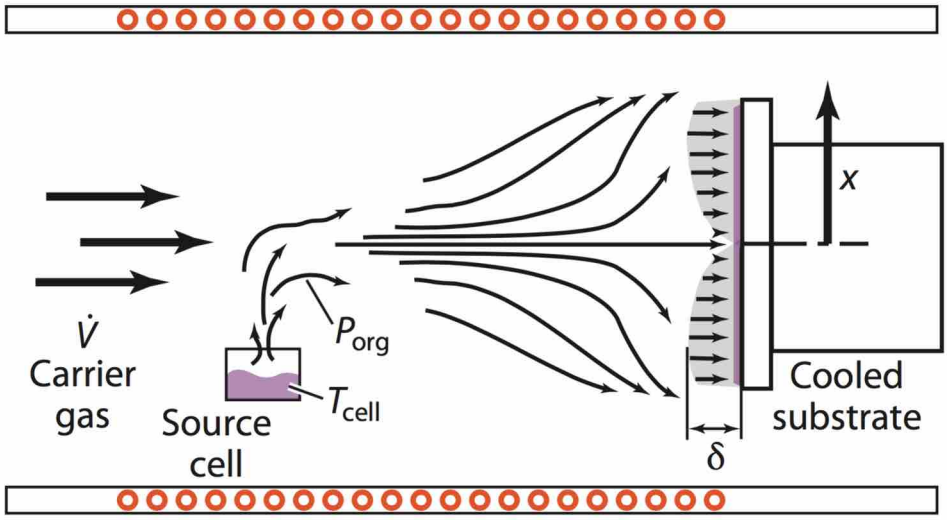

Figure 1.14 An illustration of organic vapor phase deposition (OVPD), where organic source material is evaporated into a stream of hot carrier gas. The vapor and carrier gas flow toward a cooled substrate, where selective condensation of organic material occurs. Flow and boundary-layer uniformity contribute to growth of films of uniform thickness across the substrate; δ denotes the boundary-layer thickness. [24]

Practical device fabrication often requires extensive patterning of the active layers and electrodes. With VTE and OVPD, a shadow mask is used (**Figure 1.13**), while other direct methods of patterning have also been developed, such as organic vapor jet printing (OVJP).[8] The work discussed in this thesis employs VTE as the sole deposition method for the organic, oxide, and metal layers in all OPV devices, unless otherwise stated.

1.4 Device physics

The low dielectric constant of organics makes OPV operation fundamentally different from traditional inorganic PVs. Light absorption generates strongly bound excitons, which require a significant driving force to separate into useable photocurrent, as opposed to the direct generation of free carriers in inorganic devices. Another consequence is the lack of charge screening throughout the device, causing a built-in electric field to be established by the

difference in work function of the electrodes. In contrast, inorganic PVs such as Si require extrinsic doping of the crystal lattice to establish an internal field for current generation.

In its most basic form, an OPV consists of a planar layer (or layers) of active organic material sandwiched between a conducting anode and cathode. Electrical current is injected/extracted by the electrodes, with the anode providing a hole-selective contact and the cathode an electron-selective contact. Light absorption in the active layers generates excitons, which are subsequently dissociated into free carriers and collected at the electrodes as photocurrent with the assistance of the built-in field. In traditional OPV devices, one of the electrodes is semi-transparent, composed of either a transparent conducting oxide (such as ITO), a thin metal layer, or conducting polymer, while the other is a thick reflective metal. The presence of a metallic back-reflector causes the optical field of photons incident on the device to constructively or destructively interfere with itself, creating regions of high field intensity and improving light absorption. A detailed discussion of this effect and the optics of thin film OPV devices will be presented later in Section 1.5.

1.4.1 Donor-Acceptor heterojunction

Since its introduction by C.W. Tang in 1986, nearly all OPVs employ a donor-acceptor heterojunction as the primary means of dissociating photogenerated excitons into free charges (**Figure 1.15**).[25] The heterojunction is formed at the interface between two organic materials, an electron donor and an electron acceptor, by an energetic offset in HOMO and LUMO levels. Excitons reaching this interface separate into a charge transfer (CT) state shared across the heterojunction, as it is energetically favorable to transfer a hole (electron) from the donor to acceptor (acceptor to donor).[26] Without the presence of such an interface, the dissociation of

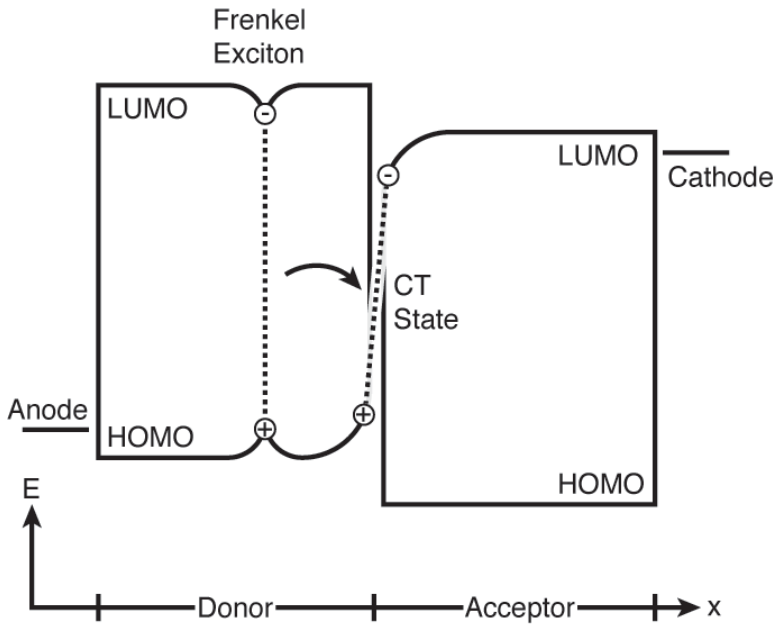

Figure 1.15 Schematic energy level diagram showing a basic donor-acceptor heterojunction and the transfer of a Frenkel exciton to the CT state upon reaching the interface.

excitons can only occur through field-assisted bulk dissociation. While this process, also known as autoionization, does occur in OPVs under normal operating conditions (~10^6 V/cm), it has an inherently low efficiency due to the high E_B (< 10% probability).[27] Thus bulk dissociation alone is impractical for photocurrent generation in OPVs.

1.4.2 Working principle

Photocurrent generation in an OPV occurs through a stepwise process involving (1) optical generation of an exciton through light absorption, (2) exciton diffusion to the heterojunction where it charge transfers to form the CT state, (3) dissociation of the CT state into free carriers, and (4) collection of the carriers by the electrodes in the form of current (**Figure 1.16**). Each step can be characterized by an individual efficiency: absorption (η_A), diffusion (η_D), CT dissociation (η_{CT}), and charge collection (η_{CC}), with the product of these efficiencies being the external quantum efficiency (EQE):

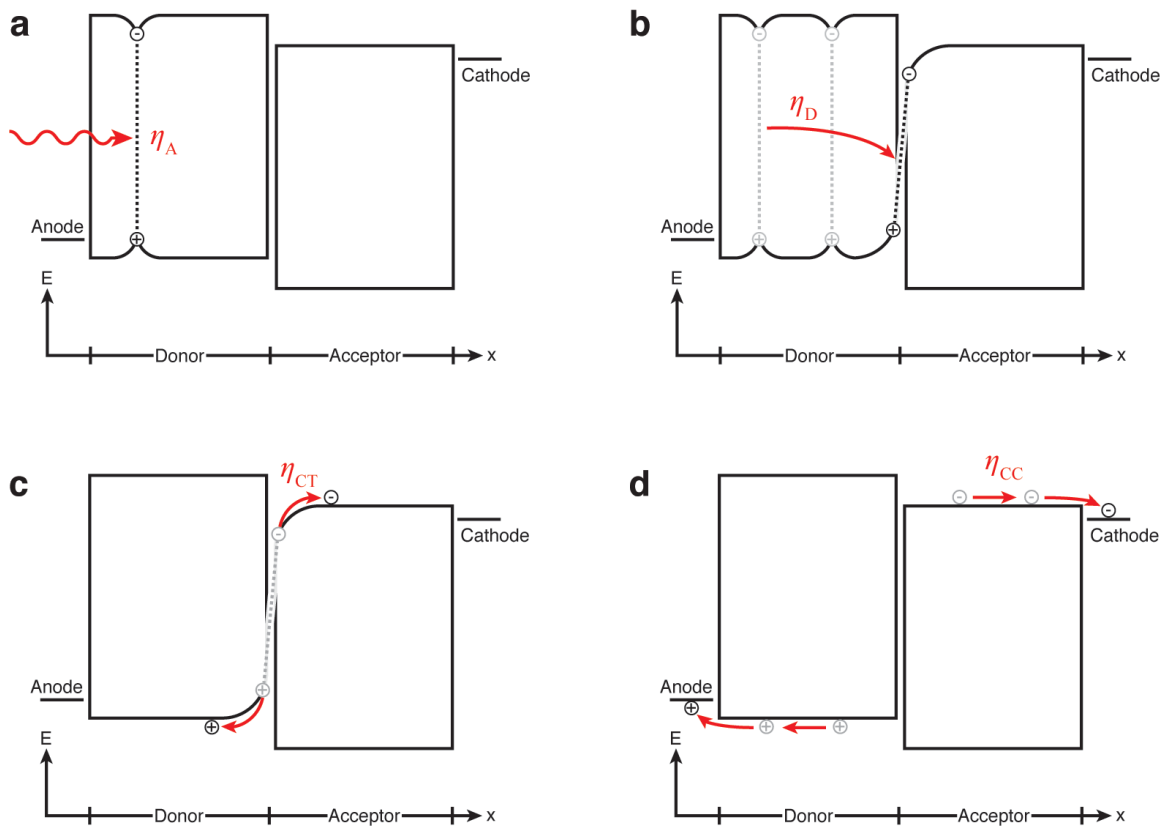

Figure 1.16 Energy level diagrams detailing the stepwise process of photocurrent generation through (a) exciton generation, (b) exciton diffusion to the heterojunction, (c) CT state dissociation to free carriers, and (d) carrier collection at the electrodes, along with their corresponding efficiencies.

$$EQE(\lambda,V) = \eta_A(\lambda)\cdot\eta_D(\lambda)\cdot\eta_{CT}(V)\cdot\eta_{CC}(V) \tag{1.9}$$

The total photocurrent output from a solar cell represents a convolution of the incident spectral irradiance and the cell's EQE, which is wavelength and bias dependent. From Equation (1.9), the absorption and diffusion steps are wavelength-dependent, while the CT dissociation and charge collection steps are considered to be solely a function of applied bias (to first order). Additionally η_A can be calculated using the transfer matrix method (Section 1.5.2) and factored out to yield the internal quantum efficiency (IQE):

$$IQE(\lambda,V) = \eta_D(\lambda)\cdot\eta_{CT}(V)\cdot\eta_{CC}(V) \tag{1.10}$$

which describes the exciton and charge dynamics internal to the device, independent of changes in absorption.

We note the efficiency of CT formation from the Frenkel state is assumed to be unity in this treatment.[26] In the case of planar devices with discrete active layers, dissociated charges encounter a barrier-free path to the electrodes upon dissociation, and η_{CC} can be assumed 100% efficient. Finally we note the process of CT dissociation remains a highly debated subject, however this simplistic treatment captures the overall probability of dissociation without regard to the underlying mechanics.

1.4.3 Charge-transfer state

Multiple competing theories have been proposed to describe the CT dissociation process at the heterojunction.[28-33] The earliest approach developed in 1984 is formally known as the Onsager-Braun (OB) model, in which the CT state is treated as a Coulombically-bound polaron pair.[29] In this case, η_{CT} can be calculated by:

$$\eta_{CT}(V) = \frac{k_d(V)}{k_d(V) + k_r} \tag{1.11}$$

where k_r is the Langevin recombination rate:

$$k_r = \frac{q \cdot \mu}{\varepsilon_r \varepsilon_0} \tag{1.12}$$

and k_d is the field-dependent dissociation rate of the bound polaron pair:

$$k_d(V) = \frac{3q}{4\pi\varepsilon_r\varepsilon_0 a_0^3} \exp\left(\frac{-E_B}{kT}\right) \cdot \frac{J\left[2\sqrt{2}(-b)^{1/2}\right]}{\sqrt{2}(-b)^{1/2}} \tag{1.13}$$

$$b = \frac{q^3\left(V - V_{bi}\right)}{8\pi d\varepsilon_r\varepsilon_0 k^2 T^2} \tag{1.14}$$

with V_{bi}, d, and a_0 being the built-in potential from the electrodes, the field depletion width (generally assumed to be the active layer thickness), and the capture radius of the polaron pair, respectively. The binding energy in Equation (1.13) is the standard Coulombic binding energy (Equation (1.2)) assuming a separation distance of a_0, and J is the Bessel function of first order. While the OB model has been shown to accurately reproduce many aspects of OPV behavior,[34] later theoretical studies have shown that it underestimates CT dissociation efficiency (**Figure 1.17**).[31]

Recently, a number of ultrafast spectroscopy measurements have called into question the assumption of such a localized, bound state at the heterojunction during the dissociation process.[28, 30, 35] In many donor-acceptor systems, in particular those employing fullerene acceptors, a rapid separation (~100 fs) of polarons at the heterojunction is observed at timescales competitive with the thermalization rate (**Figure 1.18**). This type of "hot" dissociation mechanism has been explained by Gelinas *et al.* to occur through the entropy-driven coherent delocalization of the electron (or hole) wavefunction over nanocrystalline aggregates at the donor-acceptor interface at short timescales.[30] In materials systems with a high degree of molecular ordering, nanocrystalline aggregates provide delocalized band-like states through which charges can rapidly separate. This process does not preclude the formation of Coulombically-bound CT states, but rather produces an energetic distribution of accessible CT states of which a fraction exhibit localization (OB character) and the remainder directly dissociate to free carriers (without the assistance of an applied field). Such a field-insensitive η_{CT} has been shown in a number of OPV materials systems to date.[36] Additionally, Barker *et al.* and Monahan *et al.* have both directly demonstrated the production of these two distinct CT

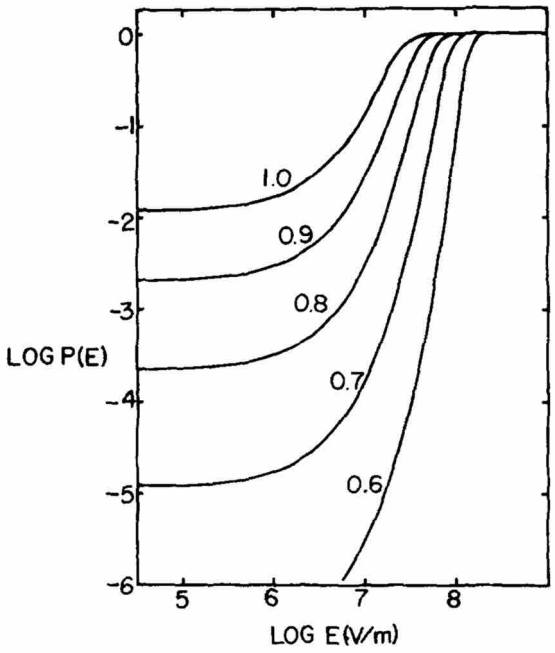

Figure 1.17 Dissociation probability (P) for a Coulombically-bound polaron pair at the heterojunction as a function of the applied electric field (E) for various a_0 values (0.6 – 1.0 nm). [29]

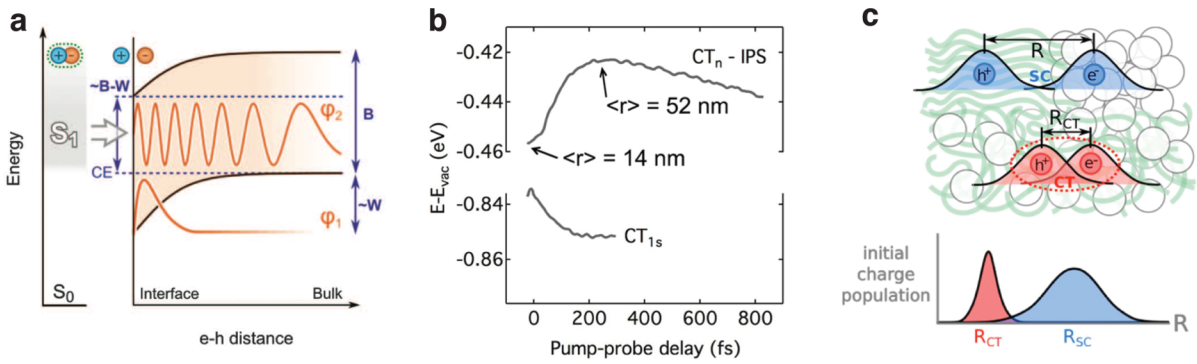

Figure 1.18 (a) Energy diagram of the CT process for a singlet exciton (S_1) transferring into a localized (φ_1) or delocalized (φ_2) state. Orange lines indicate the spatial distribution of the wavefunctions, and B and W indicate the energy distributions of band-like (B) states and those trapped in the local potential well (W). (b) Ultrafast spectroscopy data of a bound (CT_{1s}) and delocalized (CT_n) state at an organic interface. The CT_{1s} state relaxes in energy upon formation due to electrostatic binding, while the CT_n *increases* in energy and separation distance due to entropy-driven delocalization. (c) The resultant picture of the CT states in a blended heterojunction, where two distinct populations of delocalized (SC) and localized (CT) states form. [28, 30, 35]

populations – the spatially delocalized and localized (bound) CT states at the heterojunction.[28, 35]

As the delocalized fraction of CT states is inherently dependent on the intermolecular coupling strength of both donor and acceptor molecules and the degree of molecular disorder near the heterojunction,[28] the question arises of how to simplify the treatment of such a complex system. It is important to note that what has been described up to this point is the "geminate" dissociation of CT states, i.e. the dissociation of an electron and hole both generated through the same photoexcitation event. In actuality, many such events are occurring simultaneously at any given time, and it is furthermore likely that previously dissociated (or electrically-injected) carriers capture one another to form a CT state. Such cases are termed "bimolecular" processes, as the constituent charges originate from two molecules as opposed to one (geminate). In contrast to the hot CT states formed through geminate processes, bimolecular CT states are formed under equilibrium conditions (the originating charges are in thermal equilibrium). Thus, bimolecular charge capture can be assumed to form *only* localized, bound states as treatable by the OB model.

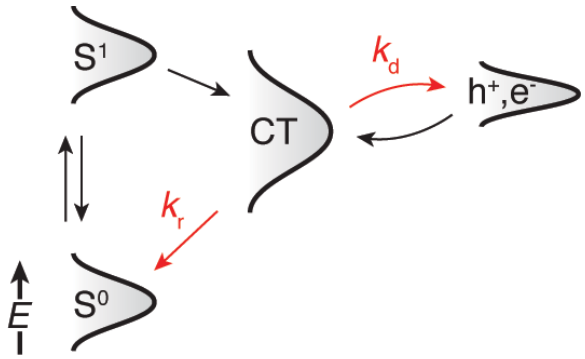

Figure 1.19 Jablonski diagram of the exchange processes between excitons (S^1), the CT state, free charges (h^+ and e^-), and the molecular ground state (S^0). The CT state itself is intermediate in the production of photocurrent, and can be characterized by the balance of the CT state dissociation rate (k_d) and recombination rate to S_0 (k_r).

As the CT state represents the intermediate state through which nearly all excitons dissociate and charges recombine within an OPV, its treatment is critical to understanding device operation. Due to the bimolecular recombination of injected charges, the formalism adopted by Giebink *et al.* is valid under dark conditions. However under illumination, geminate and bimolecular recombination processes both contribute to the overall η_{CT} of photogenerated excitons, and the application of the OB model is inappropriate in most cases. To avoid this issue, we adopt the approach of Verreet *et al.*[37] and treat η_{CT} as a kinetic balance of the net field-dependent rates of dissociation and recombination (**Figure 1.19**):

$$\frac{k_d(V)}{k_r} = \frac{k_d(V)}{k_{d0}} \cdot \frac{k_{d0}}{k_r} \tag{1.15}$$

where k_{d0} is the average zero-field dissociation rate of the CT states and the normalized rate of dissociation k_d/k_{d0} is the first-order Bessel function. When combined with Equation (1.11), this phenomenological approach describes the net dissociation efficiency without assuming a Coulombic binding radius for all involved CT states. Using this model, the only fitting parameters are the relative rate of dissociation to recombination k_{d0}/k_r, V_{bi}, and d. Unfortunately this approach (and all others to date) is incapable of predicting device performance based on intrinsic active material properties. However, it provides a necessary means for quantifying the relative rates of charge separation and recombination in OPV systems.

1.4.4 Current-voltage behavior

Since the donor and acceptor materials in an OPV are designed to be hole and electron-conducting, respectively, the device acts as a basic p-n junction and operates as a photodiode. Under forward applied bias ($V > 0$), a positive voltage is applied to the anode with respect to the cathode. Under this condition, holes injected from the anode into the HOMO of the donor and

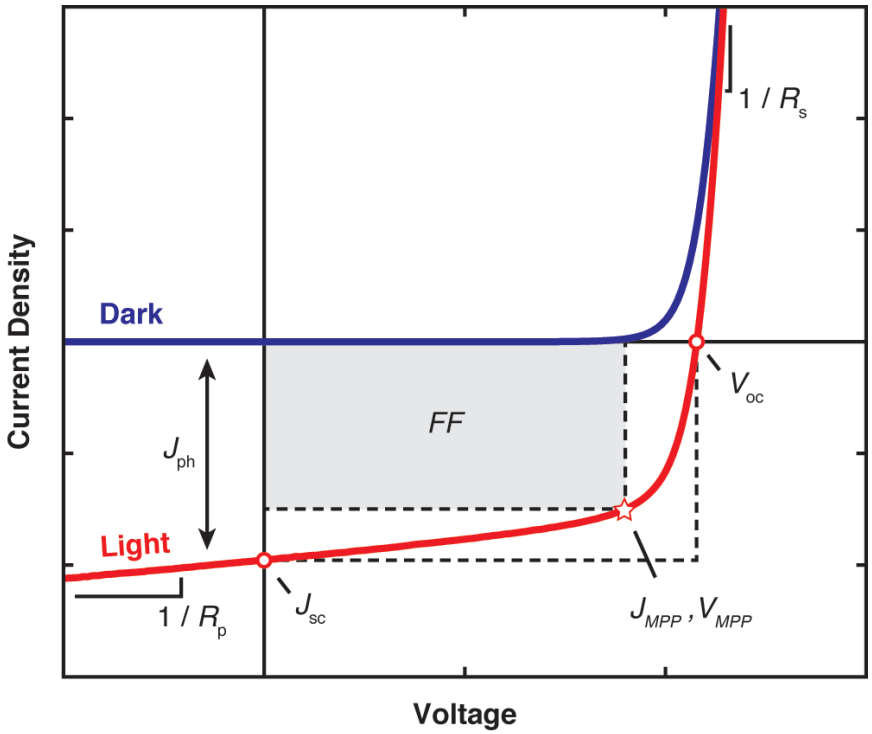

Figure 1.20 An annotated *J-V* curve typical of OPVs displaying the key parameters that determine electrical performance.

electrons from the cathode in the LUMO of the acceptor recombine through Coulombically-bound CT states at the heterojunction. In reverse bias ($V < 0$) conditions however, a large injection barrier exists for electron injection from the anode and hole injection from the cathode, and thus the injected current flowing through the device is negligible. This asymmetry in the forward and reverse bias operation of the OPV is what defines the diode behavior of the solar cell.

A characteristic plot of the current density-voltage (*J-V*) behavior of a solar cell is shown in **Figure 1.20** under both dark and light (illumination) conditions. Current density is commonly reported for devices as it is normalized to the device area and is independent of sample size. As can be seen, under forward bias the current exhibits exponential behavior past a threshold voltage, while it remains relatively flat under low positive-bias and reverse-bias conditions. The

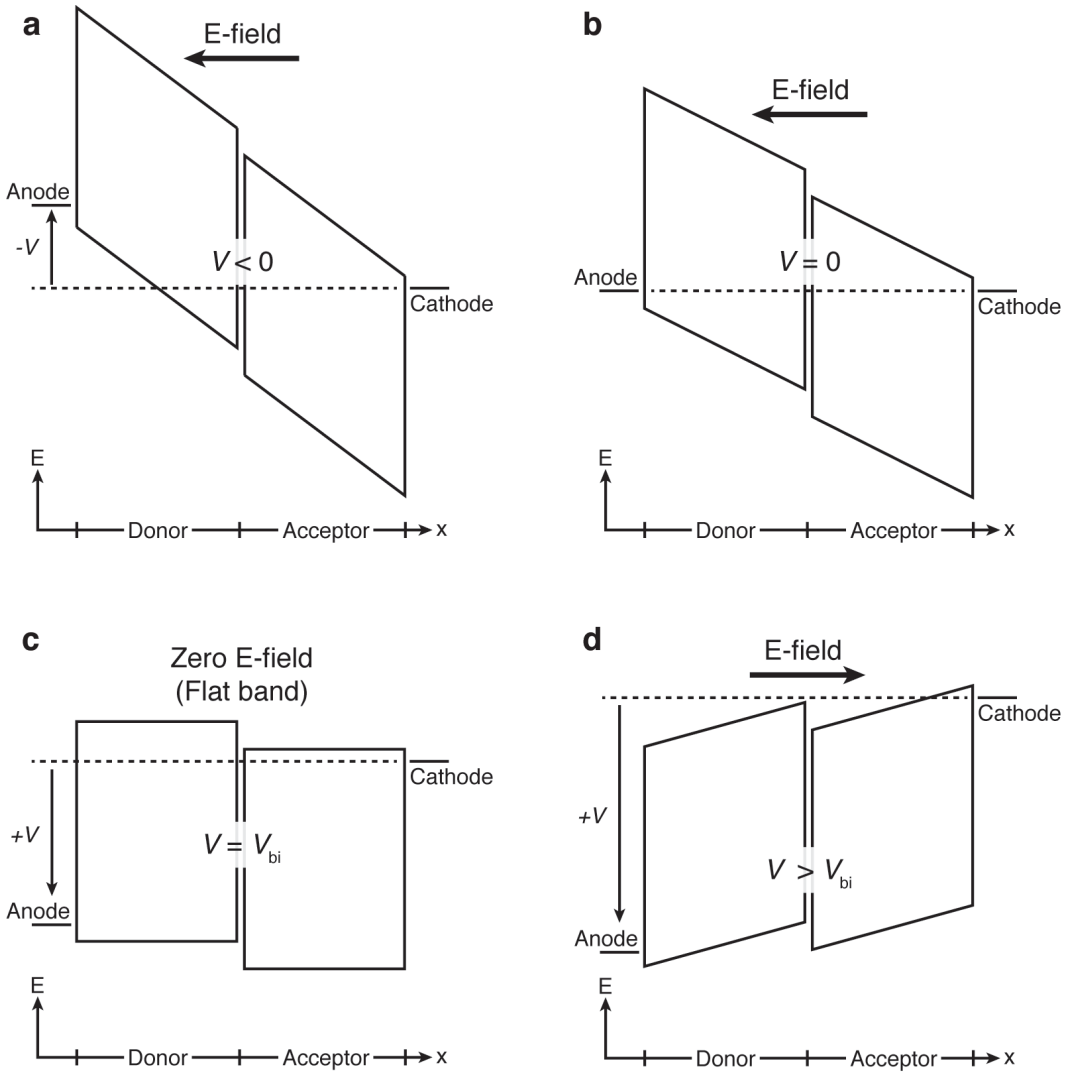

Figure 1.21 Schematic energy level diagrams of the internal electric field within a planar OPV under (a) reverse, (b) zero, and (c,d) forward-bias conditions. Ohmic contacts and negligible space charge effects are assumed in this illustration.

delayed turn-on of the forward-bias current arises from the voltage required to compensate the built-in field provided by the contacts (**Figure 1.21**). At zero applied bias, a negative electric field is established between anode and cathode, which provides the necessary driving force for charge separation at the heterojunction and collection by the contacts. The built-in field itself arises from the alignment of the Fermi levels in the organics and contacts under equilibrium conditions. Assuming Ohmic contacts, the built-in field is directly compensated when $V = V_{bi}$,

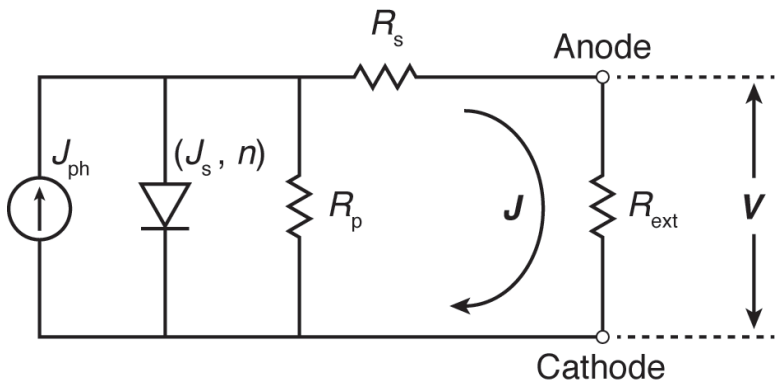

Figure 1.22 Circuit diagram of an ideal photodiode under illumination. The photocurrent source, diode, and shunt resistance elements are all in parallel and in series with the cell's series resistance. Upon application of an external load (R_{ext}), current flow connects the anode to cathode.

yielding flat-band conditions within the active layers (**Figure 1.21**c). We note that energy level diagrams of OPVs are generally drawn under such flat-band conditions for simplicity. Past V_{bi} the internal electric field no longer opposes the injection current, and it increases exponentially with bias. Often the V_{bi} is approximated by the difference in the bare electrode workfunctions ($V_{bi} \approx \phi_C - \phi_A$), however molecular dipoles at the organic-electrode interfaces[38] or Fermi level pinning[39, 40] generally render this assumption invalid.

Under illumination, photocurrent flows in the direction of the built-in field and is thus negative in value (current flows from cathode to anode). Thus the light *J-V* curve shifts downward relative to the dark condition (**Figure 1.20**). When a passive external load is applied to the device under illumination (**Figure 1.22**), the device operates in the 4th quadrant (positive bias, negative current). At an external load of zero (V = 0), this constitutes "short-circuit" conditions, and the output of the cell is the short-circuit current (J_{sc}), equivalent to the photocurrent output of the cell at zero bias. Conversely an infinite external load forces the current flowing through the circuit to zero, which occurs under "open-circuit" conditions and is termed the open-circuit voltage (V_{oc}). At an intermediate load, a maximum output power is reach, which we term the maximum power point (MPP) of the device. The PCE is then defined by:

$$PCE = \frac{J_{MPP} \cdot V_{MPP}}{P_{in}} = \frac{FF \cdot J_{sc} \cdot V_{oc}}{P_{in}} \tag{1.16}$$

where P_{in} is the incident optical power on the cell and the fill factor (*FF*) is a measure of the square-ness of the curve at the MPP.

Recent work by Giebink *et al.*[34] has demonstrated a generalized equation to describe the *J-V* performance of OPVs in the dark:

$$J(V) = J_{sD}\left\{\exp\left(\frac{q\left(V - J(V)\cdot R_s\right)}{n_D kT}\right) - 1\right\} + J_{sA}\left\{\exp\left(\frac{q\left(V - J(V)\cdot R_s\right)}{n_A kT}\right) - 1\right\} + \frac{V - J(V)\cdot R_s}{R_p} \tag{1.17}$$

where J_s, n, R_s, and R_p are the reverse saturation current, ideality factor, series resistance, and parallel (or shunt) resistance of the device and the subscripts D and A denote recombination in the donor or acceptor layer. This approach treats the recombination process of the injected charges with the OB model, assuming a Coulombic binding between polaron pairs at the heterojunction. Two populations of recombining charges are considered separately – mobile electrons recombining with trapped holes in the donor (J_{sD}, n_D) and mobile holes recombining with trapped electrons in the acceptor (J_{sA}, n_A). This treatment arises from a mismatch in mobilities between most donor/acceptor materials and dissimilar trap densities and depths in the two layers. At cryogenic temperatures, both recombination regimes are often observable in the *J-V* response, however at room temperature a large mismatch in J_s values between donor and acceptor causes recombination in one layer to be dominant. In this case, Equation (1.17) can be simplified to the ideal diode equation:

$$J(V) = J_s\left\{\exp\left(\frac{q\left(V - J(V)\cdot R_s\right)}{nkT}\right) - 1\right\} + \frac{V - J(V)\cdot R_s}{R_p} \tag{1.18}$$

Under illumination, a photocurrent term (J_{ph}) is added:

$$J(V) = J_s \left\{ \exp\left(\frac{q\left(V - J(V)\cdot R_s\right)}{nkT} \right) - 1 \right\} + \frac{V - J(V)\cdot R_s}{R_p} - J_{ph}(V) \tag{1.19}$$

where $J_{ph}(0) = J_{sc}$. The voltage dependence of the photocurrent directly arises from the CT dissociation efficiency (Equations (1.11) and (1.15)) if η_{CC} is unity, as will be discussed shortly.

The series and shunt resistances (**Figure 1.22**) account for current leakage through the organic layers and the overall cell resistance at high current densities, respectively. While R_s remains constant, R_p often drops by 1-2 orders of magnitude from dark to light conditions (**Figure 1.20**). The origin of the reduced shunt resistance is still debated, however it is commonly attributed to photoconductivity processes within the active layers. The two leading theories are autoionization (i.e. bulk dissociation) of excitons[41-43] and the increase of charge mobility in the active layers from exciton-charge annihilation.[44] In this thesis we adopt the former treatment, and consider the current generated through photoconductivity as an additive term to photocurrent arising from CT dissociation at the heterojunction.

Finally we consider the V_{oc} of an OPV, which at its theoretical maximum is the difference in donor HOMO and acceptor LUMO at the heterojunction (ΔE_{HL}). In the OB treatment of the heterojunction however, this is further reduced by the polaron pair binding energy yielding $V_{oc,max} = \Delta E_{HL} - E_B$. In actuality, due to the presence of both bound and delocalized CT state populations (Section 1.4.3), the maximum V_{oc} falls between these two values.[45] From Equation (1.19) we can calculate V_{oc} by setting $J(V_{oc}) = 0$. This yields the implicit solution:

$$V_{oc} = \frac{nkT}{q} \ln\left(\frac{J_{ph}(V_{oc})}{J_s} - \frac{V_{oc}}{J_s R_p} + 1 \right) \tag{1.20}$$

which in the limit of $J_{ph} >> J_s - V_{oc}/R_p$ yields:

$$V_{oc} = \frac{nkT}{q} \ln\left(\frac{J_{ph}(V_{oc})}{J_s}\right) \tag{1.21}$$

Thus open-circuit voltage increases logarithmically with higher photocurrent (illumination intensity) and lower reverse saturation current.

1.4.5 Spectral response

As mentioned previously, photocurrent output represents a convolution of the wavelength-dependent EQE and the spectral irradiance incident on the device (**Figure 1.23**). The J_{ph} can thus be directly calculated through:

$$J_{ph}(V) = \int \frac{q\lambda}{hc} EQE(\lambda, V) S(\lambda) d\lambda \tag{1.22}$$

for any given light source. Here q is the elementary charge, λ is the wavelength of light, h is Planck's constant, c is the speed of light in vacuum, and S is the spectral irradiance (in units W/m^2-nm). Since η_{CT} and η_{CC} are often close to unity at zero applied bias in optimized OPVs,[26] Equation (1.22) has been shown to accurately predict J_{sc} when intrinsic materials properties such as the refractive index and L_D are known for all relevant device layers.[46] Although no such model exists for predicting the full current-voltage behavior of devices *ab-initio*, a well-defined framework has been developed for predicting the J_{sc} output of devices and is widely used for device architecture optimization. In the following section, we will introduce the basic physics necessary for modeling photocurrent in OPVs, which we will use as a powerful analytical tool for characterizing device performance.

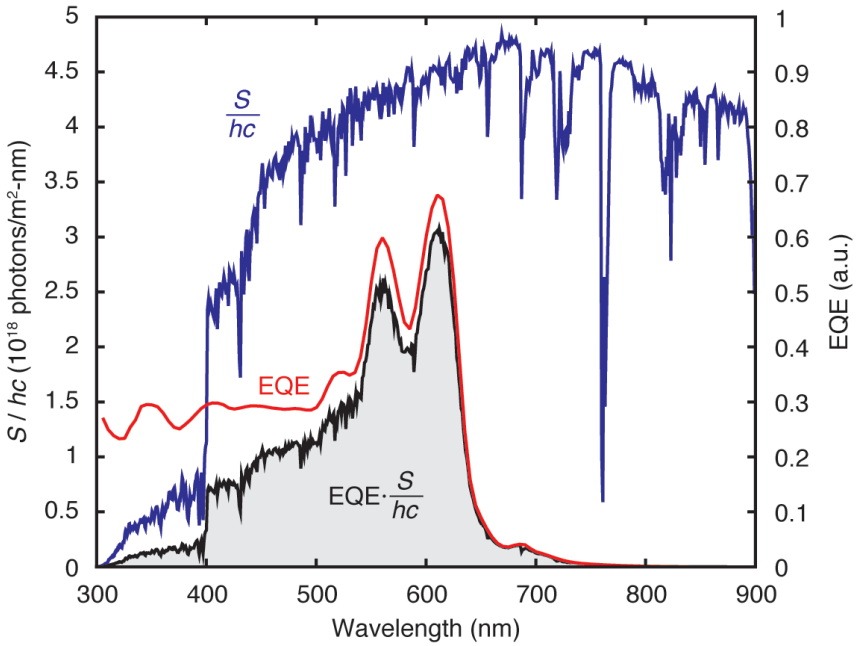

Figure 1.23 The solar spectral photon flux (irradiance normalized to photon energy) for AM 1.5 global conditions, the EQE, and their product as a function of wavelength for a simulated DBP:C_{60} device. The J_{sc} of an OPV is represented by the integral under the curve, as shown shaded in gray.

1.5 Modeling photocurrent generation

The process of photocurrent generation in OPVs differs substantially from most inorganic PV systems. Unlike bulk absorbers such as silicon, OPVs employ multilayered thin-films whose thicknesses in the organic active layers and electrodes are typically on the order of, or less than, the visible wavelengths of light. Due to their wave nature, interference occurs between the incident and reflected waves of photons throughout the device structure. These interactions of the forward and backwards-propagating waves give rise to regions of constructive and destructive interference in the optical field intensity throughout the OPV layers. Here we present the optical methods used for calculating the wave propagation, optical field strength, and resultant absorption rate in an arbitrary OPV structure. Since the absorption rate is directly proportional to the optical generation rate of excitons in the active layers, we can solve the steady-state diffusion

equations to calculate the spatial exciton profile, flux reaching the heterojunction, and EQE as a function of wavelength. Hereafter we consider the EQE only at short-circuit conditions (V = 0 V), and use the intrinsic materials properties L_D and the complex refractive index ($\tilde{n}$) in simulations. These values can be reliably and independently measured by techniques such as photoluminescence (PL) quenching[47-49] and spectroscopic ellipsometry,[50] respectively, to high precision.

1.5.1 Optical coherence and scattering

The refraction (bending) of plane-waves of light at the interface of two dielectric materials is described by Snell's law:

$$n_1 \sin(\theta_1) = n_2 \sin(\theta_2) \tag{1.23}$$

where (n_1,θ_1) and (n_2,θ_2) correspond to the refractive index and angle of propagation in layers 1 and 2, respectively (**Figure 1.24**). This defines an allowed range of angles through which light can freely couple between mediums, as limited by their refractive indices. When coupling light from a low-to-high index medium, e.g. from air into glass, propagation at angles above $\theta_2 = \sin^{-1}\left(\frac{n_1}{n_2}\right)$ (where $n_2 > n_1$ and $\theta_1 = 90°$) in the glass becomes inaccessible due to refraction. Similarly, when coupling light from a high-to-low index medium, e.g. from glass to air, light incident from the glass side above this angle (also known as the critical angle, θ_c) experiences total internal reflection from the interface and is trapped in the glass medium. Fundamentally, the angles accessible to light propagation in each layer constitute a continuum of "modes", and modes beyond the critical angle in the higher-index medium are forbidden in the lower index

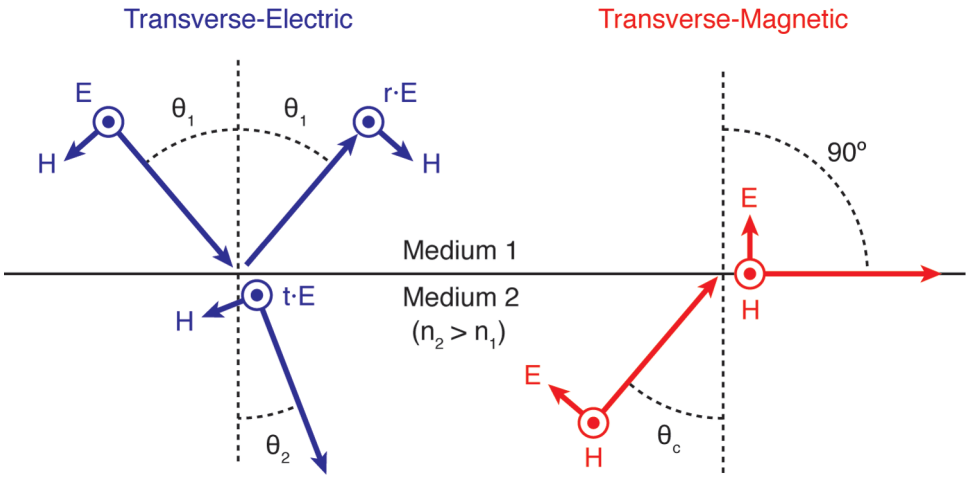

Figure 1.24 Diagram of plane-wave propagation across the interface between two dielectrics for a TE wave (blue) and a TM wave (red). Two conditions are shown: refraction below the critical angle (left), and total internal reflection at the critical angle (right). Vectors indicating the orientation of the electric (E) and magnetic (H) fields are also indicated.

medium. Modes trapped in a high-index medium are known as "waveguided modes," while those accessible to free space are generally termed "leaky" modes, as they can transit from one layer to the next. As the volume of the layer shrinks and becomes finite, the continuum of accessible modes is reduced to a discrete set defined by the waveguide geometry, dimensions, and refractive index.

As shown in **Figure 1.24**, for angles below θ_c, a fraction of light is either transmitted or reflected by the interface. To compute the reflectivity or transmissivity across an interface, we first must consider the polarization of light (i.e. the orientation of its magnetic and electric fields). Light with its electric field parallel to the interface is known as transverse-electric (TE) polarized, while light with an interface-parallel magnetic field is denoted transverse-magnetic (TM). Due to the continuity of Maxwell's equations, the in-plane components of the electric and magnetic fields must be continuous across the interface. From this boundary condition and Snell's law (which imposes phase matching across the interface), the reflection coefficients (r) can be calculated by:

$$r_{TE} = \frac{n_1 \cos\theta_1 - n_2 \cos\theta_2}{n_1 \cos\theta_1 + n_2 \cos\theta_2} \tag{1.24}$$

$$r_{TM} = \frac{n_2 \cos\theta_1 - n_1 \cos\theta_2}{n_2 \cos\theta_1 + n_1 \cos\theta_2} \tag{1.25}$$

and the transmission coefficients (t) by:

$$t_{TE} = \frac{2n_1 \cos\theta_1}{n_1 \cos\theta_1 + n_2 \cos\theta_2} \tag{1.26}$$

$$t_{TM} = \frac{2n_1 \cos\theta_1}{n_2 \cos\theta_1 + n_1 \cos\theta_2} \tag{1.27}$$

for light propagating from layer 1 into layer 2. The total fraction of light transmitted or reflected, known as the transmissivity (T) and reflectivity (R), are then defined by:

$$T = |t|^2 \tag{1.28}$$

$$R = |r|^2 \tag{1.29}$$

for any polarization. As is the case in most OPV operating conditions, at normal incidence $\theta_1 = \theta_2 = 0$, and the reflectivity and transmissivity for both TE and TM polarizations are identical.

Having introduced the coupling of light across an interface, we now consider its propagation and dissipation. When a layer is considered semi-infinite, light propagation is attenuated by the intrinsic polarizability of the medium, which is defined by its extinction coefficient, or the imaginary component of the refractive index (k). In such a case, the intensity of light drops exponentially with propagation distance according to the Beer-Lambert law:

$$I(x) = I_0 \exp(-\alpha x) \tag{1.30}$$

where I is the optical field intensity, x is the propagation distance in the medium, and α is the attenuation coefficient, defined by:

$$\alpha = \frac{4\pi k}{\lambda} \tag{1.31}$$

Thus the attenuation coefficient is often used as a metric to describe the necessary thickness for efficient absorption in a material. The above assumption of a semi-infinite medium, however, can only be applied to bulk layers much greater than the thickness of light, and whose optical fields exhibit no coherent interactions. Unfortunately, this is not the case in thin-film multilayered structures such as OPVs.

The coherence length of light measures the propagation distance over which the average phase of light is maintained. When layer thicknesses are reduced to the coherence length, coherent interference renders Equation (1.30) invalid. In the case of thermal sources such as the sun or a lamp, phase matching between emitted photons is exceedingly low, and the coherence length is on the order of the wavelength of light itself. In optically coherent layers, interference effects must then be accounted for using the transfer matrix method,[51] as will be discussed in the following section.

Apart from the light source, the spatial coherence of a plane wave in a multilayer structure is affected by the roughness of its interfaces.[52] A finite roughness breaks the phase matching of light along the interface, as light propagates varying distances in the initial medium. This can lead to conditions of partial coherence that are exceedingly difficult to model.[53] The resultant phase offset is directly proportional to the roughness and the refractive index mismatch at the interface, thus an organic/organic interface with large roughness but similar refractive indices may have little effect on coherence, while an organic/metal interface with even a small degree of roughness can substantially disrupt coherence in the structure. For this reason, care must be taken when applying optical models to OPV structures, as certain organic semiconductors such as acenes are often highly crystalline and do not form planar films. In such

cases partial coherence can make not only modeling a complex task, but the determination of refractive indices equally dubious. Our model assumes ideal (flat) interfaces, which in the materials systems we employ (R_{rms} ~ 5 nm or less) is a valid approximation. It is indeed possible to account for sources of error from roughness,[52, 54] however this is outside the scope of our studies, where it is considered a small effect.

1.5.2 Transfer matrix method

To model the EQE, we must first calculate the spatial absorption profile within the device. As OPVs are comprised of layers of thin films on the order of 10 – 100 nm, an insulating substrate is required to provide structural support and a deposition surface. Typical device architectures, which we will term "substrate-illuminated", employ a semitransparent electrode on the substrate surface subsequently capped by any buffer layers, active device layers, and finally a thick metallic back-reflector.[26] In this geometry, devices are illuminated through the substrate (hence the moniker), which is thick enough to be treated as optically incoherent, as shown in **Figure 1.25**. An alternative, less common architecture uses a thick back-reflector deposited directly on the substrate with the subsequent active layers, buffer layers, and finally a semitransparent electrode deposited on top. In this "top-illuminated" geometry, light is coupled directly from free space into the coherent layers of the device.[55-57] While both geometries require the same transfer matrix calculations for the coherent portion of the device structure, an additional step is required for substrate-illuminated devices to account for optically-incoherent reflections from the air-substrate and substrate-coherent multilayer interfaces. All of the devices presented in this

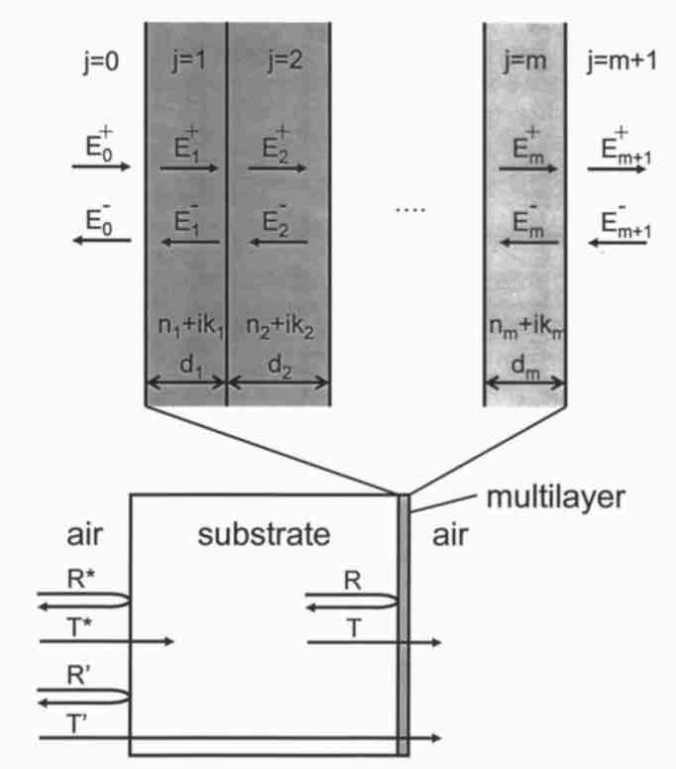

Figure 1.25 Geometry of a substrate-illuminated OPV, with the coherent multilayer stack indicated to the right of the incoherent substrate. Wave propagation within the multilayer is shown, and light intensity is corrected for substrate reflections. Note the diagram is not to-scale. [26]

thesis use the substrate-illuminated geometry, hence we present the formalism to include incoherent reflections. However, in the case of top-illuminated structures, a direct calculation of the coherent transfer matrix should suffice, provided no light leaks into the substrate.

While a variety of transfer matrix formalisms exist for coherent multilayers, we focus on the scattering matrix formalism as demonstrated by Petterrson *et al*. for OPVs.[51] As mentioned previously, this approach assumes planar layers and treats light propagation as effectively one-dimensional (out-of-plane relative to the substrate). In the scattering matrix approach, the forward (E^+) and backward-propagating (E^-) electric fields of light across an interface or structure (**Figure 1.25**) can be related as a set of vectors:

$$\begin{bmatrix} E_i^+ \\ E_i^- \end{bmatrix} = S \begin{bmatrix} E_f^+ \\ E_f^- \end{bmatrix} \tag{1.32}$$

where the subscripts i and f indicate the initial and final layers in the structure being evaluated, and S is a 2x2 scattering matrix. S is a mathematical construct to account for the recursive transmission and reflection events in the structure as light propagates between layers i and f, and is composed by the product of two distinct types of matrices - the interface matrix (I_{jk}):

$$I_{jk} = \frac{1}{t_{jk}} \begin{bmatrix} 1 & r_{jk} \\ r_{jk} & 1 \end{bmatrix} \tag{1.33}$$

between two layers, j and k, describing the reflection and transmission at the interface (**Figure 1.24**), and the propagation matrix (L_j):

$$L_j = \begin{bmatrix} e^{-i\xi_j d_j} & 0 \\ 0 & e^{-i\xi_j d_j} \end{bmatrix} \tag{1.34}$$

describing field attenuation through interference and propagation. The variables r_{jk} and t_{jk} represent the Fresnel reflection and transmission coefficients for the j-k interface (Equations (1.24)-(1.27)), d_j is the thickness of layer j, and ξ_j is defined by:

$$\xi_j = \frac{2\pi\tilde{n}_j}{\lambda}\cos\theta_j \tag{1.35}$$

the complex phase in layer j. The total scattering matrix relating layers $(i - 1)$ and $(m + 1)$ can then by constructed by:

$$S = \begin{bmatrix} S_{11} & S_{12} \\ S_{21} & S_{22} \end{bmatrix} = \left(\prod_{i=1}^{m} I_{(i-1)} L_i \right) \cdot I_{m(m+1)} \tag{1.36}$$

To calculate the total field scattering from the coherent layers of the device, we can calculate S between the substrate ($i = 0$) and top air surface ($f = N + 1$), where N is the number of layers in the device:

$$\begin{bmatrix} E_0^+ \\ E_0^- \end{bmatrix} = S \begin{bmatrix} E_{N+1}^+ \\ 0 \end{bmatrix} \tag{1.37}$$

assuming there is no illumination from the top air interface. This assumption is especially valid in the case of thick back-reflector, as it exhibits a negligible transmissivity. The transmission and reflection coefficients from the total device stack are then defined by:

$$t = \frac{E_{N+1}^+}{E_0^+} = \frac{1}{S_{11}} \tag{1.38}$$

$$r = \frac{E_0^-}{E_0^+} = \frac{S_{21}}{S_{11}} \tag{1.39}$$

where S is the total scattering matrix between layers 0 and $N + 1$.

While the total reflectivity of the device proves especially useful in confirming layer thicknesses and the validity of the optical model (total R and T can be directly measured), EQE calculations require we model the field profile within the device structure to calculate absorption in the active layers alone, neglecting parasitic absorption in the contacts and substrate. This can be accomplished by separating the system into two half-spaces about a given layer j within the structure:

$$S = S_j^+ L_j S_j^- \tag{1.40}$$

and calculating scattering into the layer from the left and right interfaces independently:

$$S_j^+ = \left(\prod_{m=1}^{j-1} I_{(m-1)m} L_m \right) \cdot I_{(j-1)j} \tag{1.41}$$

$$S_j^- = \left(\prod_{m=j+1}^{N} I_{(m-1)m} L_m \right) \cdot I_{N(N+1)} \tag{1.42}$$

with N here denoting the total number of coherent layers in the stack. With the scattering matrices for forward and backward-propagating waves entering layer j, we can then calculate the normalized propagating electric fields in both directions:

$$\frac{E_j^+}{E_0^+} = t_j^+ = \frac{\frac{1}{S_{j11}^+}}{1 + \frac{S_{j12}^+ S_{j21}^-}{S_{j11}^+ S_{j11}^-} e^{i2\xi_j d_j}} \tag{1.43}$$

$$\frac{E_j^-}{E_0^+} = t_j^- = t_j^+ \frac{S_{j21}^-}{S_{j11}^-} e^{i2\xi_j d_j} \tag{1.44}$$

The spatially-varying total electric field at position x in layer j is then given by the summation:

$$E(x) = \left(t_j^+ e^{i\xi_j x} + t_j^- e^{-i\xi_j x} \right) E_0^+ \tag{1.45}$$

accounting for the phase change due to propagation through the layer (**Figure 1.26**a,b).

It is important to note that up to this point, the optical field E_0^+ is incident on the coherent device stack from *within* the incoherent substrate (**Figure 1.25**). Since light is, in fact, incident on the entire structure from free space, a correction to the electric field intensity must be made to account for reflection and refraction at the air/substrate interface.[58] Due to substrate incoherence however, the phase of propagating light is not continuous throughout the macroscopic structure. As a consequence, scattered fields cannot be related through their magnitude. Instead, a transfer matrix for light *intensity* ($|E|^2$) is derived for the entire structure. Just as before, we can define an incoherent scattering matrix comprised of incoherent propagation ($\bar{L}$) and interface ($\bar{I}$) matrices:

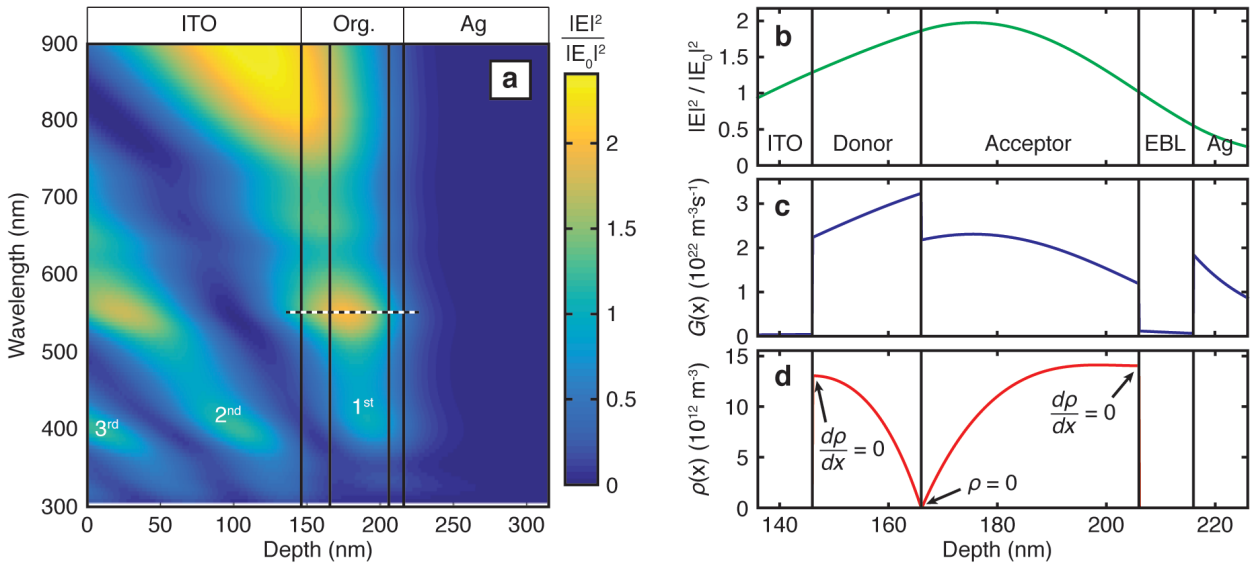

Figure 1.26 (a) Contour plot of the normalized optical field intensity as a function of incident wavelength and position in the coherent layers of a CuPc/C_{60} device. Light is incident from the left in the plot, and the first, second, and third optical interference maxima (relative to the back-reflector) are indicated. (b) Field intensity, (c) exciton generation rate, and (d) steady-state exciton density profiles for the region of interest (dashed line in (a) at 550 nm incident wavelength).

$$\bar{L}_i = \begin{bmatrix} \left|e^{-i\xi_i d_i}\right|^2 & 0 \\ 0 & \left|e^{-i\xi_i d_i}\right|^2 \end{bmatrix} \tag{1.46}$$

and

$$\bar{I}_{i(i+1)} = \begin{bmatrix} \left|S_{11}\right|^2 & -\left|S_{12}\right|^2 \\ \left|S_{21}\right|^2 & \dfrac{\left|\det S\right|^2 - \left|S_{12}S_{21}\right|^2}{\left|S_{11}\right|^2} \end{bmatrix} \tag{1.47}$$

where S is the scattering matrix of the coherent interfaces. In the case of the air/substrate interface, S takes the form of the coherent interface matrix; in the case of the device structure, S represents the total scattering matrix of the coherent stack (Equation (1.36)). We can then define the incoherent scattering matrix of the entire structure ($\bar{S}$):

$$\bar{S} = \bar{I}_{AS}\bar{L}_S\bar{I}_{SD} \tag{1.48}$$

where the subscripts *A*, *S*, and *D* are the air, substrate, and device stack, respectively. Using this result, an intensity correction factor (F_c) for light within the coherent structure can be obtained:

$$F_c = \frac{|S_{11}|^2}{|\overline{S}_{11}|^2} \tag{1.49}$$

where *S* is the coherent device stack's total scattering matrix.

The time-averaged absorbed power (*Q*) per unit volume in layer *j* at a given position is directly related to the field intensity through:

$$Q_j(x) = F_c \cdot \frac{2\pi k_j n_j c\varepsilon_0}{\lambda n_0 \cos\theta_0} |E_j(x)|^2 \tag{1.50}$$

and the time-averaged optical generation rate (*G*) of excitons per unit volume is equivalent to:

$$G_j(x) = \frac{Q_j(x)}{h\nu} \tag{1.51}$$

where *h* is Planck's constant and *v* is the frequency of incident light, assuming 100% of absorbed photons generate excitons (**Figure 1.26**c). The absorption efficiency η_A, summed over the device active layers (*k*), can then be directly calculated by:

$$\eta_A = \sum_k \left(\int F_c \cdot \frac{4\pi n_k k_k}{\lambda} \cdot \frac{|E_k(x)|^2}{|E_0^+|^2} dx \right) \tag{1.52}$$

which is independent of illumination intensity. Note that the above equations all relate to optical fields and absorption at a single wavelength, and this process must be iterated over the spectrum of interest.

1.5.3 Drift-diffusion model

Having calculated the optical generation rate in the active layers, we now apply the drift-diffusion equation[59] to determine the exciton density profile (ρ) in each layer *j*:

$$\frac{\partial \rho}{\partial t} = D_j \frac{\partial^2 \rho}{\partial x^2} - \frac{\rho}{\tau_j} + G_j = 0 \tag{1.53}$$

at steady-state conditions. Note that D_j and τ_j are the one-dimensional diffusivity and exciton lifetime in each layer, as related through Equation (1.8). The drift-diffusion equation can be solved numerically by discretizing the active layers into a mesh with spacing Δx, and using the finite-difference approximation:

$$\frac{\partial^2 \rho}{\partial x^2} = \frac{\rho_{i+1} + \rho_{i-1} - 2\rho_i}{\Delta x^2} \tag{1.54}$$

for each mesh point i in the layer. The three terms in Equation (1.53) can be understood as the steady-state rate of diffusion into each mesh point, the intrinsic relaxation rate, and the generation rate at each point in the mesh, respectively. By imposing a boundary condition of either exciton quenching ($\rho = 0$) or reflecting ($\frac{\partial \rho}{\partial x} = 0$) at each active layer interface the steady-state exciton density profile can be explicitly solved in each layer (**Figure 1.26**d).[26]

For each active layer k, the EQE contribution is determined by:

$$EQE_k = \frac{2J_k}{c\varepsilon_0 \left|E_0^+\right|^2} \tag{1.55}$$

where J_k is the steady-state exciton flux reaching the heterojunction:

$$J_k = D_k \left|\frac{\partial \rho}{\partial x}\right|_{x=x_{HJ}} \tag{1.56}$$

The total EQE is then the sum of the EQE contributions from each active layer independently:

$$EQE = \sum_k EQE_k \tag{1.57}$$

at a given incidence angle and wavelength, again assuming the condition that $\eta_{CT} = \eta_{CC} = 1$. However, modification of Equation (1.57) can take into account non-unity dissociation and

charge transfer by simply multiplying by their additional efficiencies, as in Equation (1.9). Finally, the IQE can also be predicted by taking the ratio of Equation (1.57) to Equation (1.48), which neglects the effects of parasitic absorption in passive layers such as the electrodes.

1.6 Absorption/diffusion tradeoff

1.6.1 Conflicting length scales

Having introduced the physics of thin-film devices, it is now possible to relate their performance to active material properties. At a fundamental level, there arises a competition between the L_D of excitons in the active layers and the absorption efficiency of the layer. Ideally, active layer thicknesses would be fabricated as thick as possible to maximize light absorption across the visible spectrum. However, as photogenerated excitons must efficiently diffuse to the heterojunction to dissociate, active layer thicknesses in planar device layers are approximately limited to L_D. Neglecting optical interference, the absorption depth (L_A) of a material is related to the attenuation coefficient through:

$$L_A = \frac{1}{\alpha} \tag{1.58}$$

Table 1.1 lists the L_D and L_A values for a selection of donor and acceptor materials at their respective absorption peaks. The corresponding imaginary refractive indices of the materials are plotted in **Figure 1.27**. As can be seen, even at the absorption peaks where absorption is maximized, there is nearly an order of magnitude difference between the two length scales. At wavelengths off the absorption peaks, this effect is exacerbated due to the wavelength-independence of L_D. As most organic molecules used in OPVs exhibit sharp absorption bands with full-width-half-maxima (FWHM) of ~100 nm, this absorption-diffusion tradeoff presents a

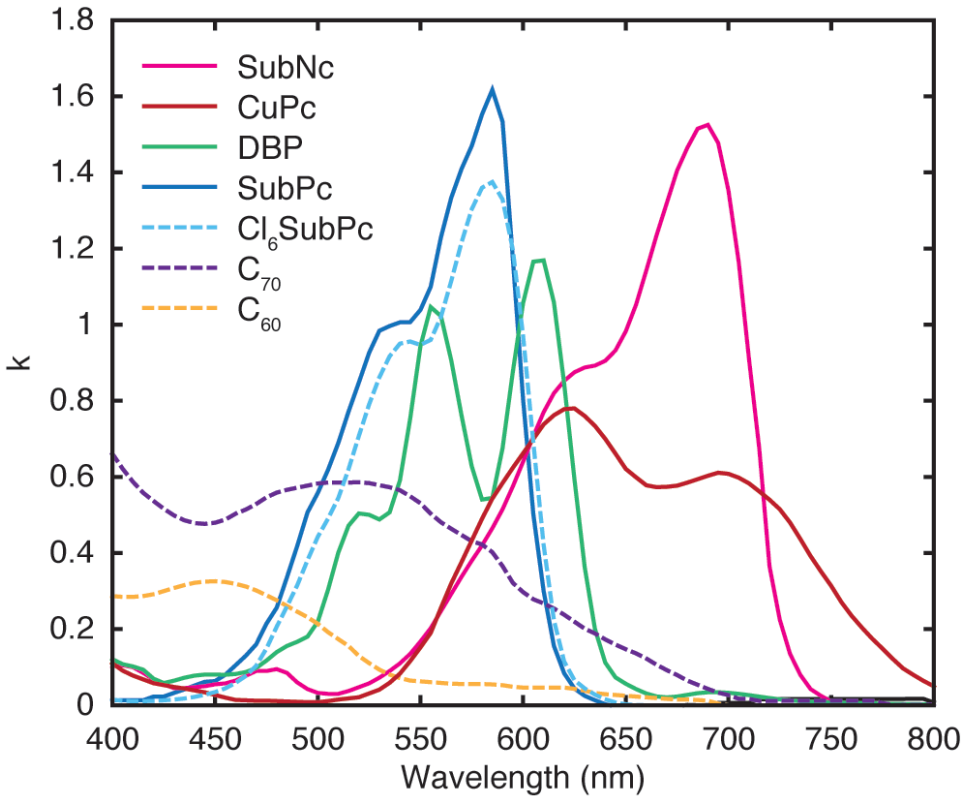

Figure 1.27 Extinction coefficients for a variety of OPV donor (solid lines) and acceptor (dotted lines) molecules in the visible spectrum. The legend lists materials in descending order of absorption peak wavelength for clarity.

Table 1.1 Peak absorption depth (L_A) and diffusion length (L_D) for a selection of donor and acceptor molecules common to OPV devices. Courtesy of Adam Barito.

Material	L_D (nm)	L_A (nm)	L_D/L_A	Abs. Peak (nm)
Electron Donors				
CuPc	15	64	0.24	625
DBP	8	42	0.19	610
SubNc	6	26	0.17	690
SubPc	8.5	29	0.30	585
Electron Acceptors				
C_{60}	17	109	0.16	450
C_{70}	17	70	0.24	520
Cl_6SubPc	4.5	34	0.13	585

substantial limitation to photocurrent generation in OPVs.

While **Table 1.1** relates bulk material properties, in actuality coherent interference effects further complicate the interplay between absorption and diffusion in devices. As a case study, the simulation of a planar OPV employing CuPc and C_{60} as the donor and acceptor layers is presented in **Figure 1.28**. The device structure is:

Glass / ITO (145) / CuPc (20) / C_{60} (40) / BCP (10) / Ag (100)

which was found to maximize J_{sc} output under simulated AM1.5 conditions and normal incidence (layer thicknesses are displayed in nm). In **Figure 1.28**b we model the individual absorption and diffusion efficiencies as a function of donor layer thickness for an illumination wavelength of 700 nm. As can be seen, optical interference causes a modulation of both η_A and η_D, however η_D exhibits a rapid drop from 0 – 50 nm while η_A rises considerably. The small shoulder in η_D at 100 nm corresponds to the positioning of the secondary interference maximum close to the heterojunction (**Figure 1.26**a), so optical generation remains close to the active interface. As is apparent, the optimal thickness that balances both η_D and η_A occurs at a CuPc

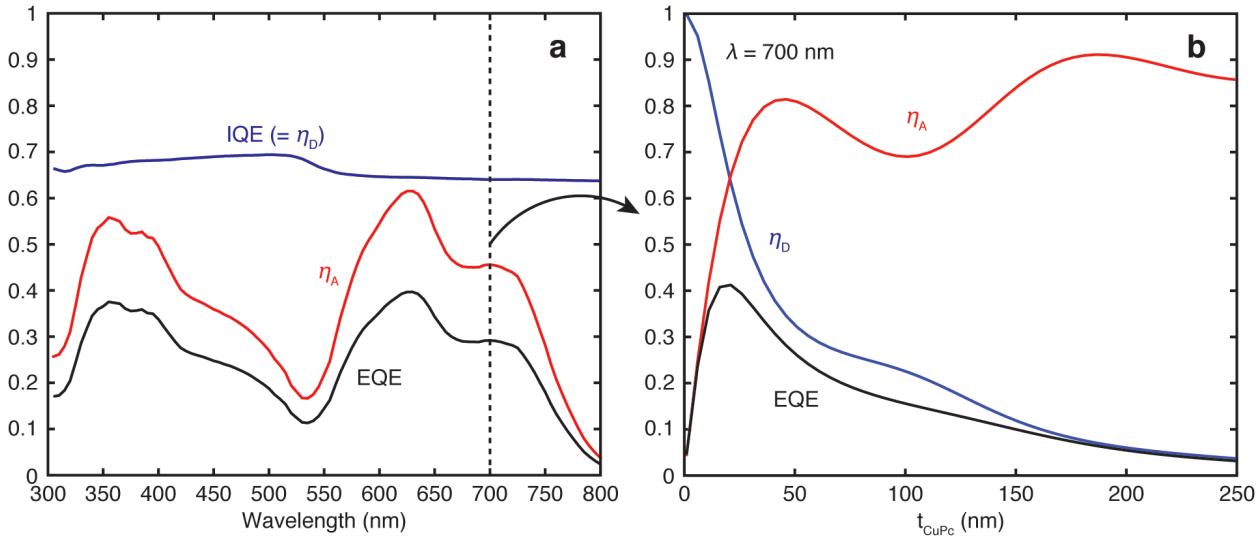

Figure 1.28 (a) EQE, absorption efficiency (η_A), and diffusion efficiency (η_D) spectra for a CuPc:C_{60} planar heterojunction OPV optimized for maximum J_{sc} output. (b) The dependence of the three efficiencies as a function of CuPc donor thickness at a fixed wavelength of 700 nm.

thickness of 20 nm, where the EQE exhibits its maximum. However, absorption is not maximized until a CuPc thickness of 186 nm, more than double L_A (= 92 nm) at this wavelength. Thus, while bulk values would indicate only a factor of 6.1 difference between L_D and L_A at 700 nm, near-field effects increase this value to a factor of 9.3. It is clear from this analysis that the L_D of excitons in OPVs presents a huge barrier to photocurrent generation and overall device efficiency. Indeed, the thermodynamic PCE limit of OPVs is estimated between 22 – 27%,[11] however this assumes perfect absorption and diffusion above the bandgap. As a consequence, OPV performance has been limited thus far to a much more modest 11% efficiency (**Figure 1.5**).

1.6.2 This work

The work presented in this thesis will demonstrate multiple approaches to circumventing the absorption/diffusion tradeoff in OPVs. Modifications to device architecture such as mixed active layers (Chapter 2) and interfacial layers (Chapter 3) are shown to enhance the diffusion efficiency within devices, while a purely optical enhancement of absorption is later demonstrated (Chapter 4). Our work focuses on a small subset of small molecules used in OPVs, however the findings presented herein are considered extendable to any active layer system. Concerning future applications, we will show that a combined approach through active and interfacial layer design and enhanced optical coupling strategies presents the greatest promise for increased OPV performance. No single solution is mutually exclusive from the rest.

Chapter 2

Geometry of exciton diffusion in mixed layers

2.1 Background

The competition between light absorption and exciton diffusion in planar heterojunction (PHJ) OPVs is a result of light propagation and exciton diffusion to the heterojunction occurring in the same direction (**Figure 2.1**a,b). Hence, changes to active layer thicknesses affect both η_A and η_D simultaneously, but in opposing ways (**Figure 1.28**). By far the most successful approach to breaking this tradeoff has been the introduction of the bulk heterojunction (BHJ) by Halls *et al.* and Yu *et al.*, whereby the donor and acceptor layers are blended throughout the active volume (**Figure 2.1**c).[60, 61] Since its demonstration in 1995, the BHJ architecture has become the most common OPV design, and is currently used in nearly all of the highest efficiency devices. Recently, single cell BHJ efficiencies surpassing 10% have been demonstrated for a variety of materials systems.[62-65] However, the precise way in which the length scales of donor-acceptor phase separation (and the extent of their intermixing) affect η_A and η_D remains unclear. In this chapter we explore the effects of active layer mixing on the photocurrent generation process and demonstrate how the dimensionality of mixed-junction architectures increases the probability of diffusion to the heterojunction due to geometric factors (Section 1.2.4), which helps gives rise to their remarkable performance.

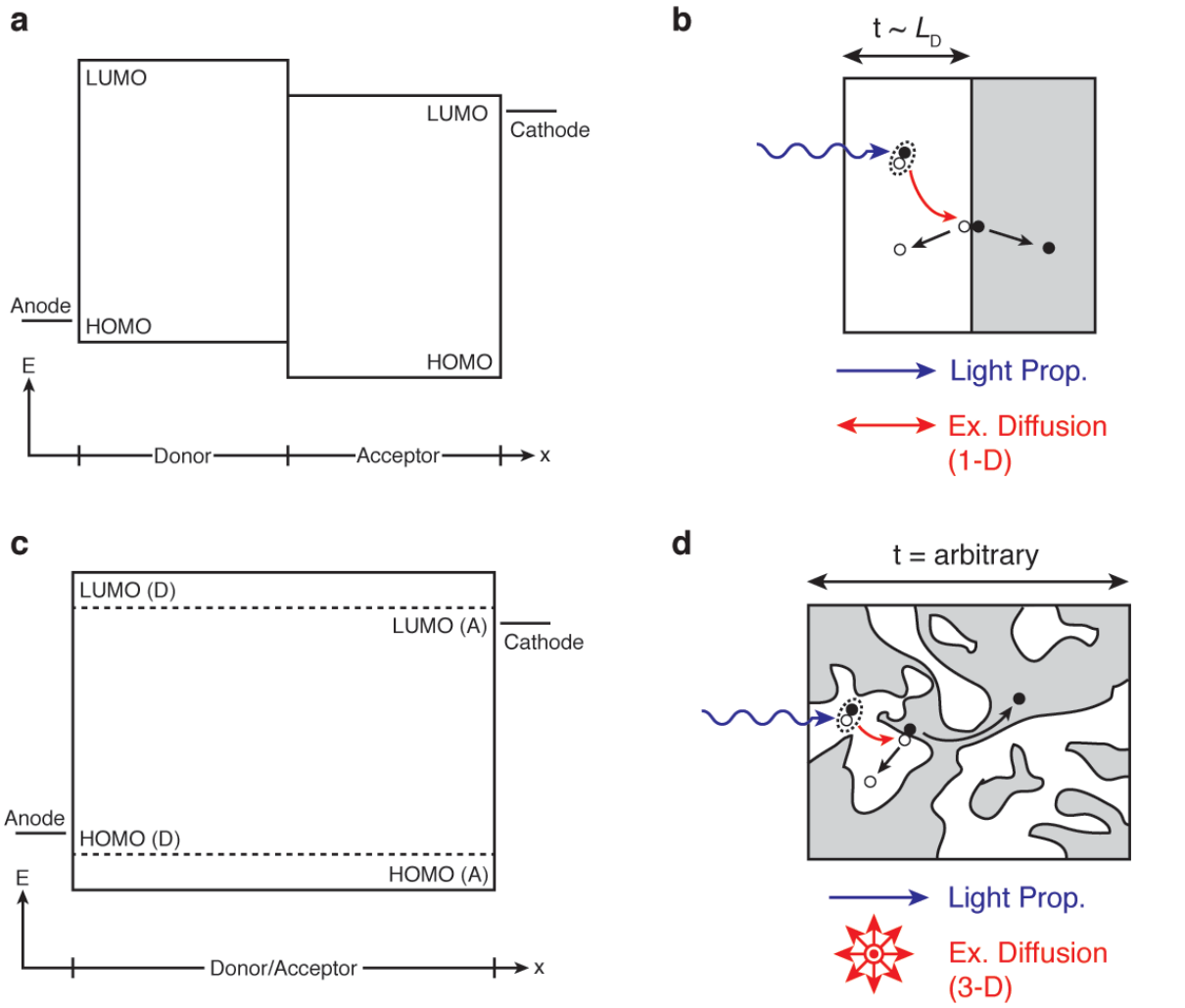

Figure 2.1 Energy level diagrams (a,c) and schematics of exciton generation/diffusion (b,d) in planar and bulk-heterojunction OPVs. Excitons (dashed ovals), CT states (interfacial pairs), holes (empty circles), and electrons (filled circles) are indicated. The three-dimensional distribution of the active layers in the BHJ decouple the directions of light propagation and exciton diffusion, unconstraining the active layer thickness from the L_D. However, exciton diffusion and CT dissociation in (d) are instead influenced by morphology and domain size. Additional losses in free carrier extraction are incurred in the BHJ due to circuitous conducting pathways.

2.1.1 Bulk heterojunctions

The three-dimensional mixing of the donor and acceptor layers in the BHJ architecture decouples the directions of light and exciton propagation in the active layers (**Figure 2.1**d). Excitons generally diffuse isotropically within the active volume, while light propagates unidirectionally under standard illumination conditions (e.g. normal incidence). Thus the distance excitons must

diffuse to the heterojunction becomes independent of active layer thickness and is instead fixed by the domain sizes and morphology of the mixed layer. Therefore bulk recombination losses (relaxation of excitons to heat during the diffusion process) can be minimized, and the active layer thickness can be tailored to maximize light absorption independent of exciton diffusion.

In characterizing and modeling BHJ devices, typically η_D is assumed to be constant (unity) in both donor and acceptor, as well as being wavelength-independent.[66] However, vertical phase segregation and composition gradients in the mixed layer along with mesoscale phase segregation can render this assumption invalid. Often PL quenching techniques[47] are used as an independent means to infer L_D and η_D in blends containing emissive molecules, however the models used for data fitting neglect processes such as FRET between donor and acceptor molecules[48] and make broad assumptions as to the distribution of quenching sites and the blend morphology. Unlike in PHJ devices, mixing of the donor and acceptor creates tortuous pathways that free charges must follow before reaching the electrodes. Additionally, the contact of the donor and acceptor molecules to both electrodes creates large Shottky barriers and built-in field concentration near the electrodes, potentially causing η_{CT} to vary vertically through the device.[67] This can lead to a wavelength-dependent η_{CC} and η_{CT} as the optical interference maxima bias exciton generation to varying depths within the device depending on the incident wavelength.[68] As a result, Equation (1.9) must be modified to reflect this difference in BHJs.

Since EQE measurements are often the primary means of interrogating the individual efficiencies in the photocurrent generation process, the inability to separate the wavelength and voltage dependence of η_D, η_{CT}, and η_{CC} makes studying the internal physics of BHJs difficult. Inevitably, this issue arises from three-dimensional distribution of the heterojunction throughout

the bulk, and complex approaches such as Monte-Carlo modeling[69] or effective medium simulations[70] are required to separate out the individual contributions to photocurrent.

2.1.2 Mixed layer morphology

Until now, the complexity of nanoscale phase separation has made active layer morphologies difficult to measure, predict, and systematically tailor. The estimation of grain sizes, for example, requires techniques such as high energy X-ray diffraction (XRD) using synchrotron sources or energy-filtered transmission electron microscopy (TEM) to resolve structures on the scale of 10 – 100 nm with high precision.[71] To date, the "optimal" BHJ morphology and the effects of nanostructures on the local photogeneration process remain highly debated questions critical to the further improvement of OPV processing, performance, and material design.[72]

The most common acceptors used in BHJs are fullerene derivatives. In most donor/fullerene blends, a three-phase system is often produced, comprising pure nanocrystalline donor and acceptor domains bounded by amorphous mixed regions, regardless of processing strategy.[73, 74] Mixing of donor and acceptor materials at the nanoscale appears to be associated with efficient photocurrent generation[64] due to improved η_D, whereas mesoscale phase separation and fullerene aggregate formation have been linked to lower device efficiencies in multiple materials systems.[75, 76] On the other hand, finely intermixed structures are often associated with reduced η_{CC} and higher bimolecular recombination, suggesting that "corrugated" or finely interdigitated donor-acceptor interfaces with line-of-sight pathways for charges to the respective electrodes are optimal.[77] In addition to compositional variation, the energy landscape can differ substantially between neat and mixed regions due to steric and solvatochromic

reorganization of the molecules.[78] The result is a morphology-dependent competition between η_D, η_{CT}, and η_{CC}, for which the critical length scales are often unclear.

2.1.3 Charge extraction and bimolecular recombination

As stated previously, bimolecular recombination of photocurrent occurs when free carriers from different photoexcitation events relax through the CT state. The process of bimolecular recombination becomes exaggerated in BHJs, as the mixing of the donor and acceptor generates an extremely large heterojunction surface area through which charges may recombine. Often the application of a high reverse bias is used to sweep out carriers from the device faster than they can recombine,[36, 66] however such fields cannot be maintained in a device at forward-bias where power generation occurs.

2.1.4 Planar-mixed heterojunctions

A device structure that combines the benefits of both PHJ and BHJ architectures is the planar-mixed heterojunction (PMHJ), first introduced by Xue *et al*.[79] In a PMHJ, neat donor and acceptor layers cap a central mixed region (**Figure 2.2**). By separating the mixed region from the electrodes, charge selectivity can be maintained, and the formation of a Shottky junction is suppressed. The addition of the planar layers also serves to reduce current leakage and increase R_p within the device, as injected carriers are inhibited from tunneling directly through the device by the HOMO and LUMO offsets at the donor/mixed and mixed/acceptor interfaces.

Unlike BHJ devices, which can be fabricated using both polymers and small molecules, PMHJ devices are generally limited to the latter. The formation of a PMHJ requires the ability to sequentially deposit active layers, which is typically difficult with solution-processed materials

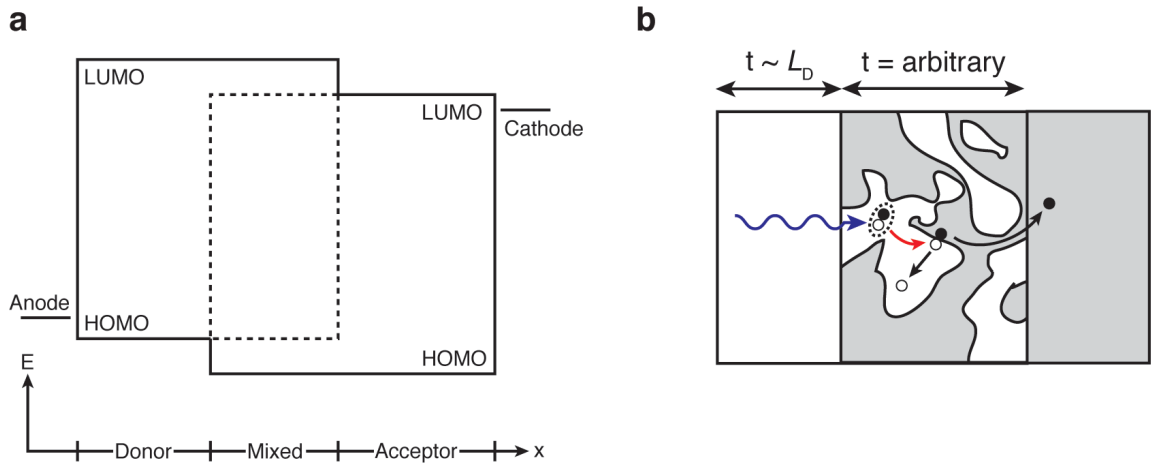

Figure 2.2 (a) Energy level diagram and (b) schematic of exciton generation/diffusion in a PMHJ device.

due to the requirement of solvent orthogonality. However with vacuum deposition techniques, the sequential deposition of organic layers without intermixing is not an issue. To date, small molecular PMHJ OPV cells have been fabricated exhibiting high power conversion efficiencies up to 8.1%.[80-84]

2.2 Diffusion in a 2-D planar-mixed heterojunction

The PMHJ architecture presents an opportunity to study the effects of mixed layer composition and morphology on photocurrent generation in a highly controlled fashion. By employing very thin films, we constrain the mixed layer nanostructures to vary only in-plane (effectively two-dimensional), and are able to directly quantify the dependence of morphology on composition and determine the critical domain sizes necessary for efficient η_D and η_{CT} (**Figure 2.3**).

Here we employ the wide-bandgap molecule bathocuproine (BCP) as a fullerene dopant at the mixed interfacial region between pure boron subphthalocyanine chloride (SubPc) donor and fullerene (C_{60}) acceptor layers in a PMHJ-like cell structure (**Figure 2.4**a). While there is no intermixing between the donor and acceptor layers, BCP serves as a transparent, exciton-

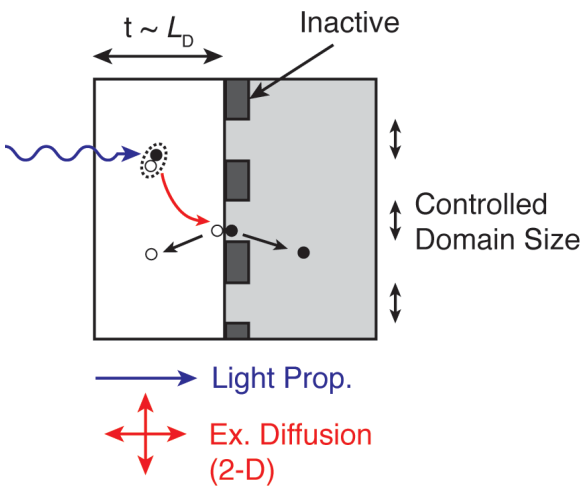

Figure 2.3 Schematic diagram of exciton generation and diffusion in a PMHJ with a two-dimensional distribution of active and inactive domains at the heterojunction interface with a controlled size for interrogating the diffusion/dissociation dependence on domain size independent of free carrier extraction.

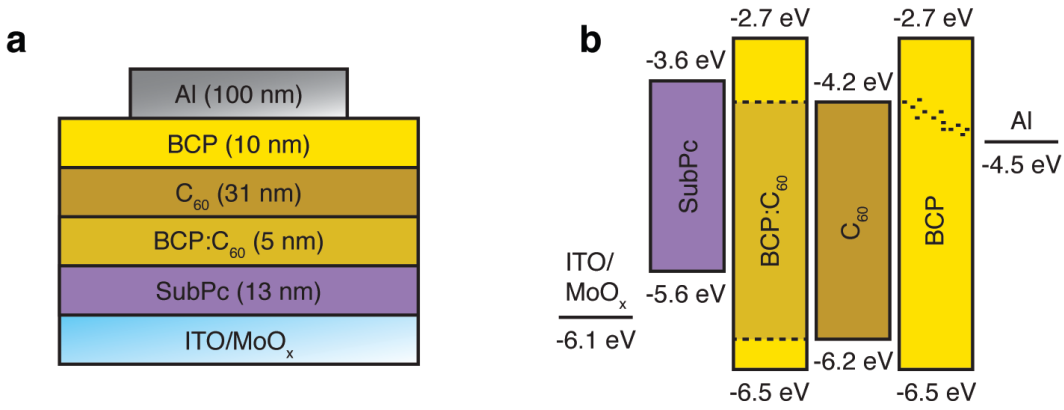

Figure 2.4 (a) Device structure and (b) energy level diagram of the two-dimensional PMHJs being studied. All layer thicknesses are kept constant with ϕ_{BCP} as the only free parameter between devices.

blocking material (**Figure 2.4**b), and when mixed with C_{60} allows for the separation of blending effects on exciton and charge dynamics near the heterojunction. As shown previously by Bartynski *et al.*, the introduction of BCP disrupts the local ordering and aggregation of C_{60} molecules, while still allowing for efficient electron conduction.[85] Here, by restricting the mixed layer thickness to 5 nm, we ensure morphological variations within the mixed layer are constrained in-plane. We control the BCP volume fraction (ϕ_{BCP}) to systematically vary the domain size of C_{60} domains in the mixed layer, and we show the domains exhibit diffusion-limited growth after nucleation. We correlate variations in nanostructure to exciton diffusion efficiency and demonstrate a simple model to describe exciton diffusion between pure and mixed layers. From these data we demonstrate a geometric enhancement of η_D due to the spatial distribution of the heterojunction. Finally we evaluate the kinetics of the charge transfer (CT) state and show the existence of a critical C_{60} domain size necessary for efficient CT dissociation under steady-state conditions, consistent with recent ultrafast spectroscopy evidence of CT delocalization being the primary driver for charge separation.[28, 30, 35]

2.2.1 Experiment

Solar cells were fabricated on ITO-coated glass substrates (R_s < 15 Ω/□), sequentially cleaned using detergent, deionized water, acetone, trichloroethylene, and isopropanol in an ultrasonicator and dried under nitrogen. After cleaning, substrates were UV-ozone treated for 10 min prior to loading into a vacuum thermal evaporator (Ångstrom AMOD) under high vacuum below 5×10^{-7} Torr. MoO_x (Sigma Aldrich, > 99.5%) was deposited at 0.5 Å/s to provide an Ohmic anode contact. The organic layers SubPc, C_{60}, and BCP (Luminescence Technology Corp., > 99%) were then deposited at rates of 0.5, 1.0, and 0.6 Å/s, respectively. In devices containing a mixed

BCP:C_{60} layer between the neat SubPc and C_{60} layers, the net codeposition rate was maintained between 1.0 and 2.0 Å/s depending on ϕ_{BCP}. After the BCP exciton-blocking layer, an Al (Alfa Aesar, 99.9%) cathode was deposited through a shadow-mask at 1 Å/s to define circular devices with a 1 mm nominal diameter. The above rates were kept consistent across all samples in this study, and all depositions were performed under substrate rotation at room temperature.

J-V scans were performed in a nitrogen-filled glovebox with < 1 ppm O_2 and H_2O. Cells were illuminated with an Oriel solar simulator calibrated to AM 1.5G (100 mW/cm^2) using an NREL Si reference cell (Model PVM233 KG5), and data were recorded with an HP 4156B precision semiconductor parameter analyzer. EQE measurements were performed in air using collimated light from a halogen lamp coupled to a Newport 1/8M monochromator. The incident beam was optically chopped at 185 Hz and the device photocurrent was measured with a Stanford Research Systems SR530 lock-in amplifier. A calibrated Si photodetector (Newport 818-SL) was used as a reference. After testing, device areas were measured using an optical microscope and corrected for in all *J-V* and EQE calculations. Reported data were averaged over 9 devices nominally for *J-V* and 6 devices for EQE scans, with error bars representing ±1 standard deviation. For absorption measurements, unmasked samples fabricated in parallel with each device set were measured with a Perkin Elmer Lambda 750 spectrophotometer with Universal Reflectance Accessory under TE-polarization and an 8° incidence angle.

For conductive atomic force microscopy (cAFM) measurements, samples were fabricated with a structure of ITO/MoO_x (5 nm)/SubPc (13 nm)/BCP:C_{60} (5 nm). All cAFM measurements were performed using an Asylum Research MFP-3D stand-alone AFM under a steady purge of argon gas. A PtIr5-coated AFM probe (Nanosensors, ATEC-CONTPt, spring constant 0.2 N/m) was used as the cathode. Measurements were performed in contact mode, tracking topography

and current measurement simultaneously. The contact force was on the order of 10 nN to ensure sufficient contact to track topography with minimal sample damage. Positive (+2.0 to +2.5 V) or negative (-5 V) biases were then applied to the bottom ITO substrate with the AFM probe held at virtual ground, and the AFM's transimpedance amplifier recorded the currents. For each voltage, multiple (~4) areas were scanned at each bias in order to gain a statistical average of the currents, with error bars representing ±1 standard deviation. Relatively large scan sizes of 2 μm^2 were used to ensure images were representative of the entire surface.

For PL quenching measurements, samples with a structure of Glass/SubPc (13 nm)/BCP (5 nm) and ITO/MoO_x (5 nm)/SubPc (13 nm)/BCP:C_{60} (5 nm) were encapsulated under glass microslides using UV-cured epoxy. A Photon Technology International spectrofluorometer was used in both excitation and emission modes to measure PL with the samples illuminated through the substrate at a 30° incidence angle. For L_D measurements, PL excitation scans were performed over excitation wavelengths of 400 – 630 nm on glass samples, with the emission monitored at 650 nm. For η_D measurements, PL emission scans were performed over emission wavelengths of of 550 - 800 nm on both glass and ITO samples, with the excitation fixed at 500 nm. The quenching of SubPc excitons by MoO_x[46, 84] was accounted for in the calculation of diffusion efficiency by using the BCP-capped glass sample as a reference for all ITO samples.

2.2.2 Device modeling

To separate out the effects of varying ϕ_{BCP} on η_A and EQE, we follow the method detailed in Section 1.5.2. This requires a precise knowledge of the refractive indices in each layer of the stack. While this information is known for all of the neat layers (**Figure 2.5**c), it has not been measured for mixed BCP:C_{60} as a function of volume fraction. Generally, optical transitions in

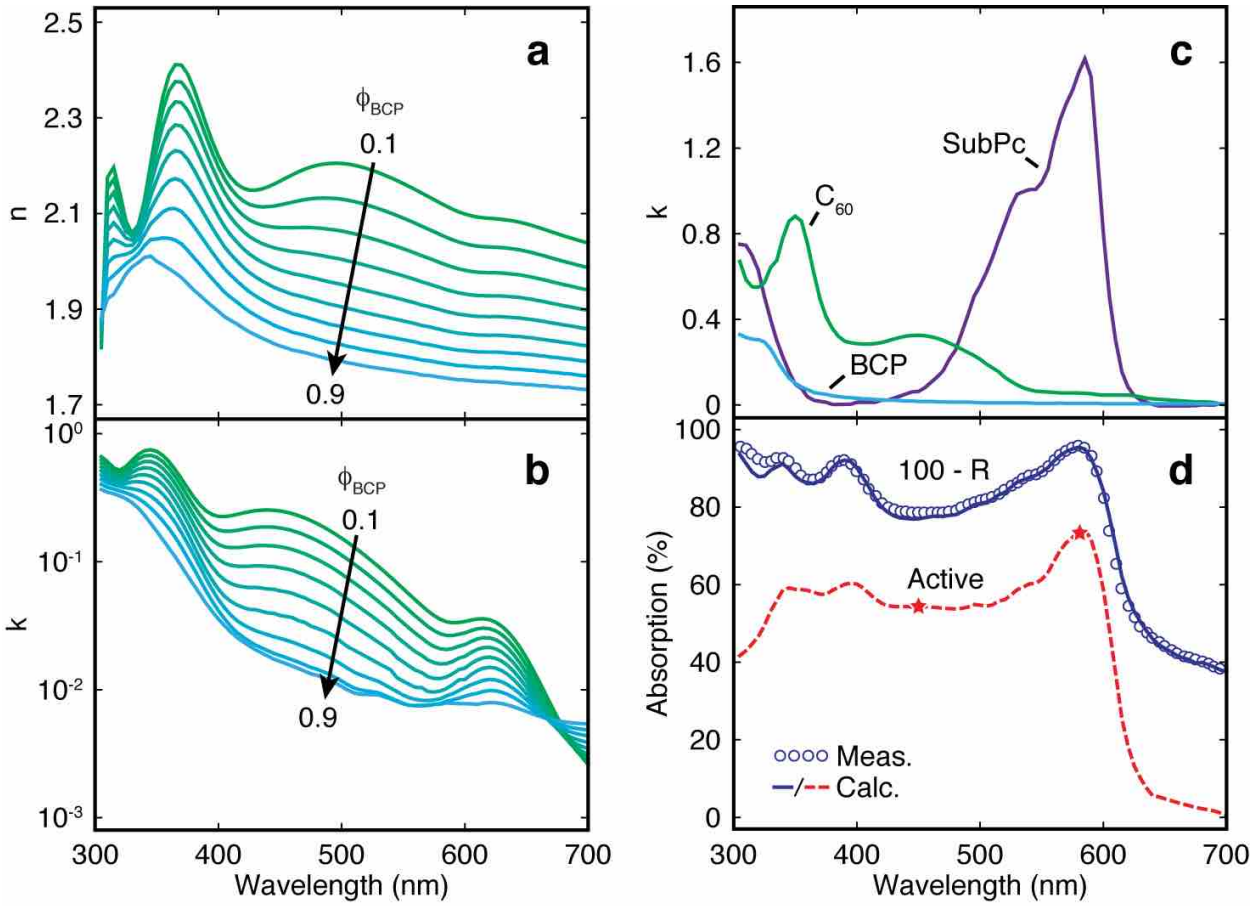

Figure 2.5 (a) Real and (b) imaginary refractive index values used for blended BCP:C60 films for various BCP loading fractions. (c) Imaginary refractive index values for the neat active layers within the devices. (d) Measured and calculated absorption of a complete device stack (ϕ_{BCP} = 0) with active layer absorption indicated by the dashed red line. Points used in IQE calculations for the SubPc and C_{60} layers correspond to their respective absorption peaks in c and are indicated by stars at 580 nm and 450 nm, respectively. In each case, over 95% of the active layer absorption corresponds to the layer of interest. Absorption measurements were performed on samples fabricated simultaneously with tested devices.

small molecular organic films have Frenkel character and are localized on individual molecules. In the case of fullerenes such as C_{60} however, the primary optical transition in the visible spectrum (~450 nm) has significant CT character,[86] and its wavefunction is distributed over a cluster of molecules (**Figure 1.10**). This has a significant impact on the refractive index of doped C_{60} films, as the CT transition doesn't follow a linear rule of mixtures like the Frenkel transitions at ~340 nm and ~615 nm. Indeed Bartynski *et al.* previously showed the extinction coefficient (α) of the CT transition in BCP:C_{60} exhibits a power law dependence with $\alpha \sim \phi_{C60}{}^{M}$ where M =

2.7.[85] We fit the imaginary refractive index (k) of neat BCP and C_{60} films[51, 87] with Lorentzian and Gaussian functions, respectively. The Gaussian fitting was necessary to account for the large amount of inhomogeneous broadening in the absorption spectrum of fullerene films. The real index of refraction (n) contributions from these individual transitions were then calculated through the Kramers-Kronig relation:

$$n_{Trans}(\omega) = \frac{P}{\pi}\int_{-\infty}^{\infty} \frac{k_{Trans}(\omega')}{\omega' - \omega}\, d\omega' \tag{2.1}$$

where P is the Cauchy principal value and ω is the frequency of light. The data was matched to the complete n spectrum *via* an additional Cauchy fitting to third order:

$$n_{Cauchy}(\lambda) = A + \frac{B}{\lambda^2} + \frac{C}{\lambda^4} \tag{2.2}$$

where λ is the wavelength of light. Thus we deconstructed both n and k to the individual contributions of each electronic transition and the background optical dispersion in both BCP and C_{60}. Finally, the complex refractive index was calculated over all ϕ_{BCP} values through a linear interpolation of the Frenkel transitions' contributions and a power law interpolation of the CT transition's contribution using the dependence measured by Bartynski *et al.*, as shown in **Figure 2.5**a,b.

Just as in the case of PHJ devices, we assume in our two-dimensional PMHJ devices that charges encounter a barrier-free path to the electrodes upon dissociation, resulting in $\eta_{CC} = 1$. Additionally η_A can be calculated using the transfer matrix method and factored out from the measured EQE to yield the IQE. Thus we consider the effects of BCP doping on exciton and charge dynamics, independent of changes in absorption. We define η_D as the efficiency with which excitons generated in the neat donor or acceptor layers can reach an active heterojunction (SubPc/C_{60}) site to dissociate. C_{60} excitons have significant CT character and require strong

electronic coupling between neighboring molecules to diffuse.[86] This is in contrast to materials such as SubPc, which support Frenkel excitons that can diffuse *via* self-Förster transfer even through highly dilute or disordered films.[19] As previously shown by Bartynski *et al.*, the introduced disorder from BCP intermixing disrupts the pathways for exciton transport in BCP:C_{60} blends even at low BCP concentrations.[85, 88] For this reason, we expect η_D to be markedly different for excitons originating in the neat SubPc and C_{60} layers; excitons in SubPc can sample the entirety of the heterojunction unhindered, while excitons in originating in C_{60} must first diffuse through the mixed layer before dissociation. Hereafter, we consider η_D in the SubPc layer alone, as its diffusion can be easily characterized. Finally, as detailed in Section 1.4.3, we take a purely phenomenological approach to assessing η_{CT}, using only the relative net rates of dissociation and recombination as a fitting parameter.

2.2.3 Device performance

The *J-V* behavior of PMHJ devices with varying ϕ_{BCP} at the heterojunction under dark and light conditions is depicted in **Figure 2.6**. For $\phi_{BCP} < 0.8$, the shape of the light curves remain consistent, with a slight kink present under high forward-bias ($V > 0.5$ V) for only the highest BCP fractions (likely due to space-charge accumulation). The most profound effect of increasing ϕ_{BCP} is a rapid reduction in J_{sc}, while parameters such as the photoconductivity (S_{pc}) and R_s remain constant at 0.7 – 0.8 $mAV^{-1}cm^{-2}$ and 1 – 3 Ωcm^{-2}, respectively (**Figure 2.7**). From these observations, we can deduce that charge transport isn't significantly affected by the inclusion of the 5 nm BCP:C_{60} layer at zero bias. Indeed, even devices with a neat BCP layer at the interface exhibit some residual photocurrent, which we attribute to charge tunneling and, to a lesser degree, transport through pinholes. Additionally, optical modeling of the absorption

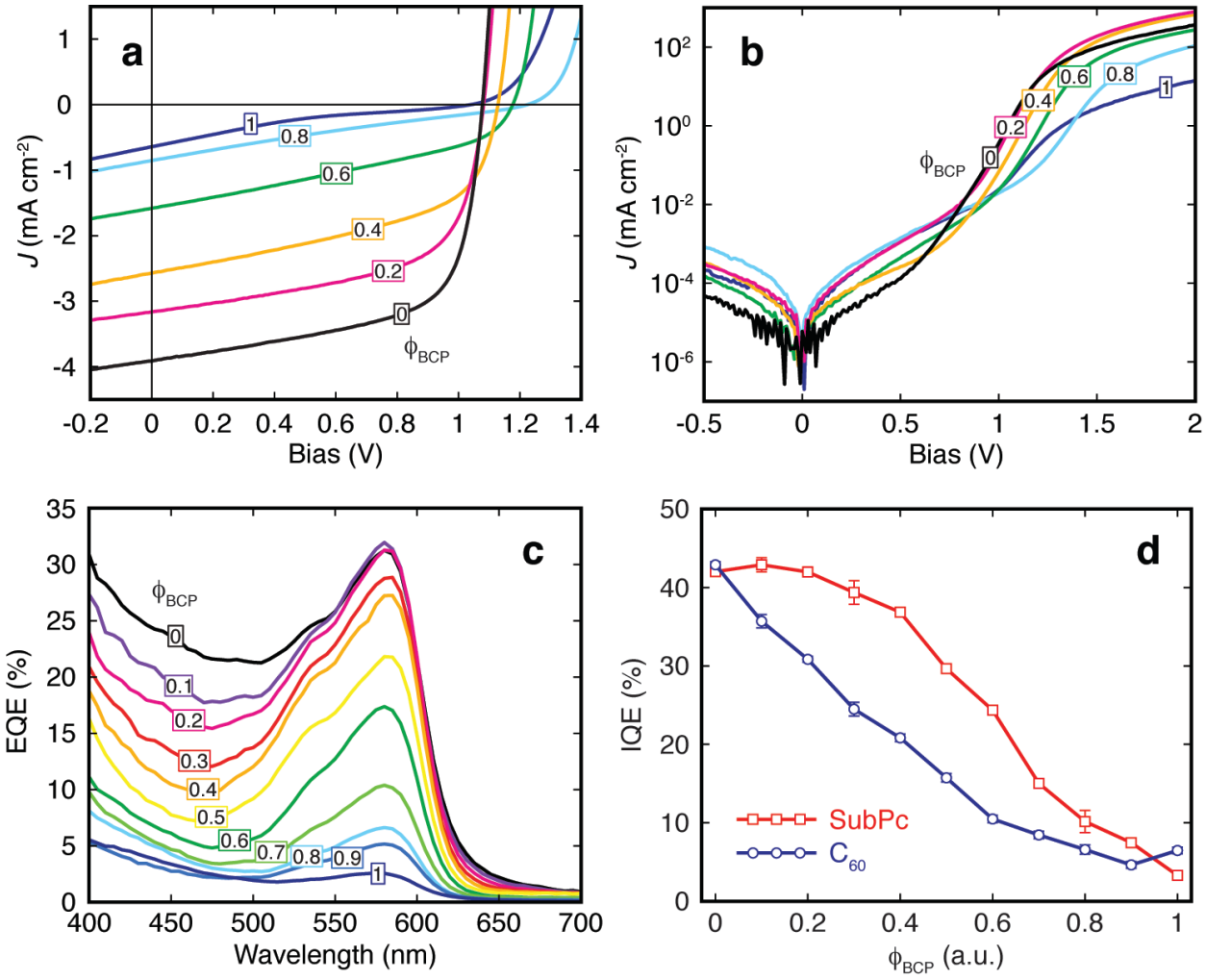

Figure 2.6 Current density-voltage curves under (a) AM 1.5G illumination and (b) dark conditions for select devices. (c) Corresponding EQE spectra for devices over the entire range of ϕ_{BCP}. (d) The IQE values for the SubPc and C_{60} layers at their respective absorption peaks, measured under short-circuit conditions.

spectra (**Figure 2.5**d) indicates a minimal loss in active layer absorption with BCP doping at the heterojunction. Thus the assumption that η_{CC} = 100% appears to hold valid in our PMHJs at zero applied bias, and any measured changes in J_{sc} are attributed to η_D and η_{CT} exclusively. In contrast to the J_{sc}, the V_{oc} increases over 100 mV with BCP doping, reaching a maximum 1.21 ± 0.01 V at a ϕ_{BCP} of 0.7. We attribute this to the reduction in dark current[89] with increasing ϕ_{BCP} (**Figure 2.6**b), resulting from a lowered rate of CT formation by free polarons.[34]

Representative EQE spectra are shown in **Figure 2.6**c for devices over the entire range of ϕ_{BCP}. While the SubPc peak at 580 nm initially remains constant, the C_{60} contribution at 450 nm is immediately reduced upon BCP incorporation. The trends are further clarified in **Figure 2.6**d by comparing the IQE values at their respective peaks to BCP concentration. Photocurrent contributions from C_{60} are linearly attenuated as ϕ_{BCP} increases from 0 to 0.7, at which point η_D in C_{60} becomes zero and the remaining photocurrent saturates at the value for S_{pc}. This result is consistent with previous studies showing the effectiveness of BCP doping for exciton blocking and reflection from pure C_{60}.[83, 85]

In contrast, the SubPc IQE appears insensitive to ϕ_{BCP} up to 0.4, at which point it exhibits a nonlinear reduction reaching a similar value to that of C_{60} at $\phi_{BCP} = 1$, which we attribute to S_{pc}. It is important to note here that Equation (1.9) does not explicitly account for photoconductive contributions to EQE. As mentioned previously, the origin of S_{pc} in OPVs remains a debated topic, with different studies ascribing it to bulk dissociation of excitons[41-43] or exciton-charge annihilation at the active/buffer layer interfaces.[44] This work assumes the former process, which is supported by the large J_{sc} contribution from S_{pc} in the pure-BCP devices ($\phi_{BCP} = 1$, **Figure 2.6**a). In the case of exciton-charge annihilation, S_{pc} would instead be a parasitic loss for photocurrent. To isolate the contribution to EQE from the junction, we subtract the IQE at $\phi_{BCP} = 1$ from the rest of the IQE data.

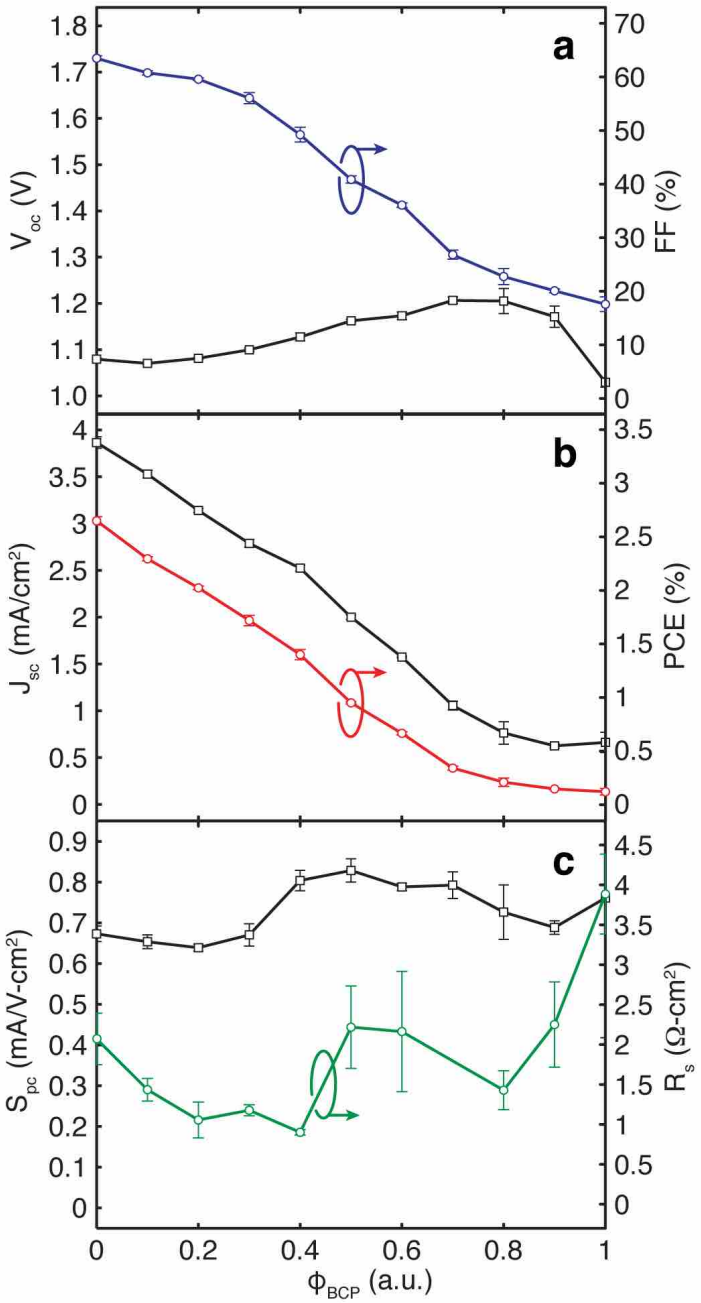

Figure 2.7 (a) Open-circuit voltage (V_{oc}) and fill factor (*FF*) for all devices tested. The V_{oc} exhibits a gradual increase with ϕ_{BCP} due to a reduction in dark current at high bias, while the *FF* shows a concomitant decrease as photoconductivity becomes the dominant source of photocurrent in the devices. (b) Both the J_{sc} and PCE exhibit a nearly identical trend with ϕ_{BCP}. (c) The S_{pc} and R_s exhibit minimal change for all ϕ_{BCP}, indicating overall carrier transport remains unhindered and the parameter variations from (a) and (b) are dominated by effects at the heterojunction itself.

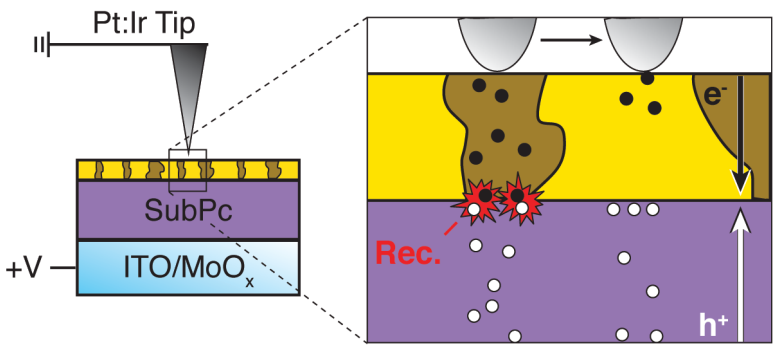

Figure 2.8 Schematic of the cAFM measurement, where holes injected into the SubPc layer via the anode recombine with electrons injected into the mixed layer at the SubPc/C60 heterojunction interfaces. Current is injection-limited from the tip, with BCP regions of the mixed layer (yellow) exhibiting a higher barrier and consequently lower current values.

2.2.4 Imaging domains with conductive atomic force microscopy

To correlate trends in device performance to morphology, we must first image the nanostructure of the mixed layer. We find that conventional AFM imaging provides no clear distinction between small molecules in the mixed layer. Instead, cAFM[90-93] is employed to differentiate the BCP domains from those of C_{60} (**Figure 2.8**). Since their energy levels and electrical properties are intrinsically distinct, the different phases can be resolved by cAFM by effectively mapping electron injection at the tip/organic interface (**Figure 2.9**). For these measurements, samples with the BCP:C_{60} layer exposed are kept in the dark while an electrical bias is applied between the ITO anode and a Pt:Ir coated AFM tip acting as a cathode. At sufficient positive bias, electrons injected from the tip into the C_{60} domains recombine at the heterojunction with injected holes from the anode, while BCP domains exhibit negligible injection current. We employ a relatively low positive bias (+2 V to +2.5 V) to resolve individual phases in the mixed BCP:C_{60} overlayer. This bias range was determined to optimize the signal-to-noise of our measurements while minimizing current tunneling through the film. At higher electrical bias, tunneling is observed to

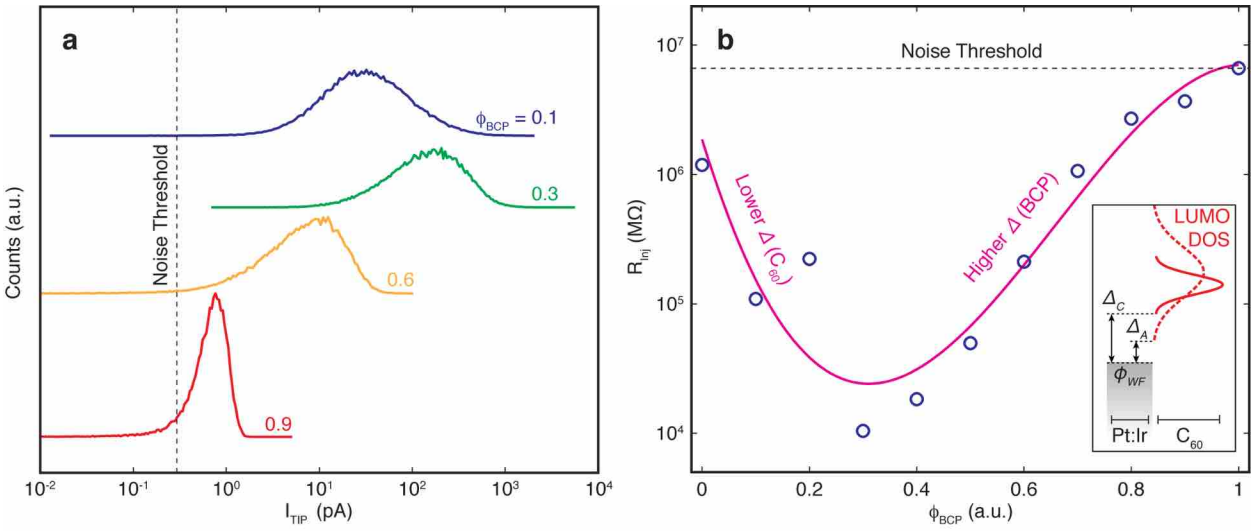

Figure 2.9 (a) Example current histograms for cAFM measurements on samples with varying ϕ_{BCP} under positive bias. Current values (I_{tip}) vary ~4 orders of magnitude, well above the background noise level. Initially the current distributions shift to higher values with the incorporation of BCP at the heterojunction, subsequently followed by a reduction in current at higher loading fractions. (b) Average injection resistance (R_{inj}) calculated from the peak I_{tip} values across all samples. Scans were performed over 3 - 4 distinct regions of each sample. The trend in R_{inj} follows a simple Gaussian (solid line in b), resulting from injection into a variably broadened LUMO DOS (inset in b). Initially, as BCP is incorporated into C_{60}-rich films, the introduced disorder reduces the average injection barrier from the crystalline (Δ_C) to amorphous (Δ_A) C_{60} domains. However for higher ϕ_{BCP}, the average LUMO DOS narrows and Δ increases again as BCP domains begin to regulate charge injection into the mixed layer.

"bleach" the signal and minimal variation in current is observed across the scans.

Our cAFM measurements not only allow us to resolve distinct phases in the mixed film, but also infer changes to the LUMO density of states (DOS) in the mixed layer due to disorder (**Figure 2.9**). The Pt:Ir tip used in this study possesses a workfunction of -5.4 eV, significantly lower than the LUMO level of either C_{60} (-4.2 eV) or BCP (-2.7 eV) relative to vacuum. Thus a large barrier (Δ) is established for charge injection into the Gaussian DOS of the molecules at the free surface. Our results are described by a Fowler-type injection mechanism, consistent with observations in other metal/organic systems.[38, 94] We observe a significant reduction in injection resistance (R_{inj}) by 2 orders of magnitude for $\phi_{BCP} < 0.4$, indicating that the disorder introduced into the mixed layer at low BCP volume fractions effectively broadens the LUMO DOS in the C_{60} matrix by creating deep level traps. The DOS broadening persists even for BCP-rich films, as

the injection resistance does not saturate until ϕ_{BCP} = 1. This provides critical insight into the intermolecular coupling of the C_{60} aggregates in the mixed layer, as the DOS broadening will disrupt the wavefunction delocalization of CT states at the heterojunction.[28]

2.2.5 Mixed layer morphology

A representative current map is presented in **Figure 2.10** for a sample with ϕ_{BCP} = 0.4 in the mixed layer and an applied bias of +0.2 V. As can be seen, regions of both high and low injection current are observed across the sample, exhibiting variations over two order of magnitude. To exclude current leakage through pinholes in the mixed layer as the source of current variations, scans at negative bias were taken for every sample (**Figure 2.11**). Over all measured films, 96 ± 5% of the BCP:C_{60} surface appears to be pinhole-free, confirming that the majority of observed current variation is due to charge injection into the mixed layer.

To resolve individual domains within the mixed layer, a statistical filtering method is applied to the raw current maps obtained by cAFM. Since ϕ_{BCP} is known from deposition conditions, domains are assigned as BCP or C_{60} according to the cumulative distribution function (CDF) of the current histogram, with ϕ_{BCP} as the cutoff value. BCP exhibits a much higher electron injection barrier and orders of magnitude lower injection current for the Pt:Ir tip than C_{60} (**Figure 2.9**). Thus pixels with current values below the cutoff are assigned to BCP domains, producing a binary phase map (**Figure 2.10**c). The BCP:C_{60} layers exhibit a hierarchical nanomorphology typical of organic blends,[95] with domains ranging in size from tens to hundreds of nanometers. We analyze each binary image using the linear intercept method[96] to evaluate the distribution in domain size (**Figure 2.10**d). In all cases the domain sizes follow a Weibull distribution function, and the characteristic domain size for each phase is taken to be the

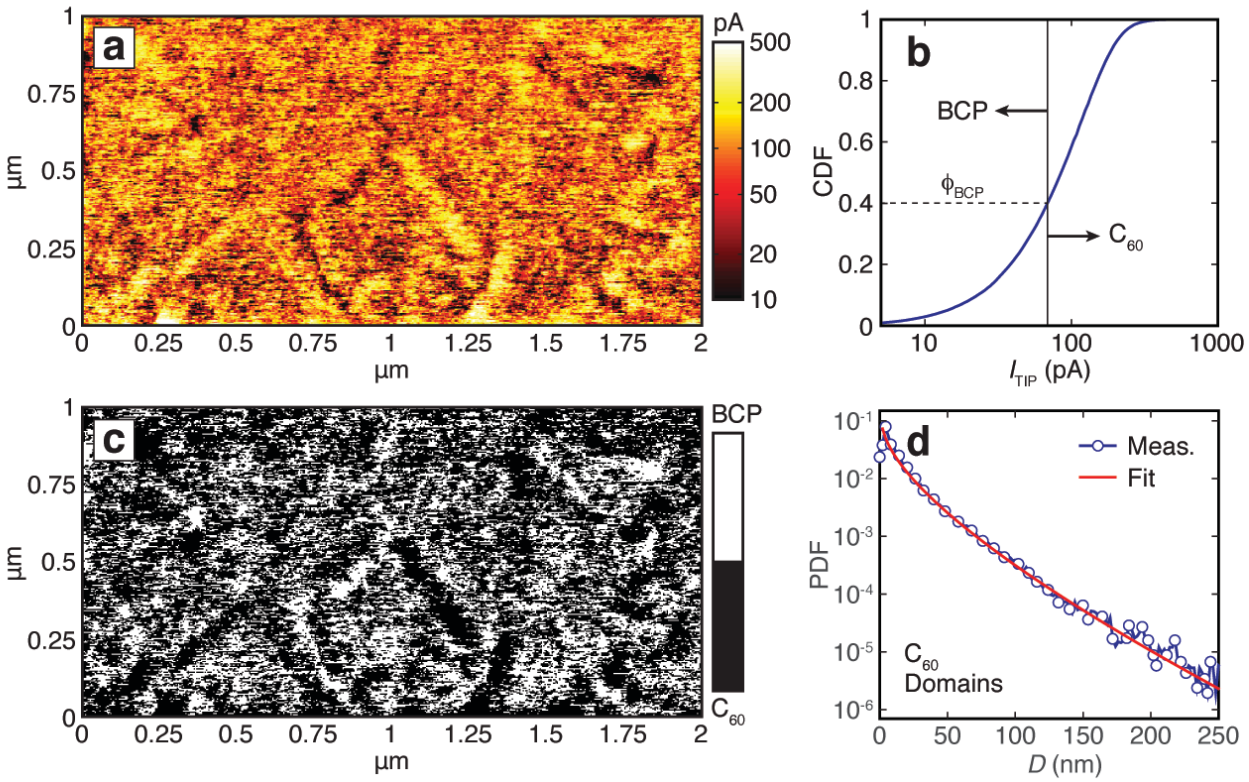

Figure 2.10 (a) Raw current map obtained for ϕ_{BCP} = 0.4 at an applied bias of +2 V exhibiting regions of both high and low injection current. (b) CDF of the raw current values in a used to process the image, with regions above and below the threshold of CDF = ϕ_{BCP} assigned to C_{60} and BCP domains, respectively. (c) Binary phase image extracted from a using the CDF in b exhibiting a hierarchical nanoscale morphology. (d) Measured domain size distribution of the C_{60} phases in (d) fit to a Weibull function, showing excellent agreement over all length scales.

point where the probability distribution function (PDF) decays to 80% of its initial value (D_{80}), as is common practice.[97] We observe a very clear exponential growth of D_{80} for both BCP and C_{60} versus composition (**Figure 2.12**):

$$D_{80} = D^{*} \cdot \exp\left(A \cdot \phi\right) \tag{2.3}$$

where D^* and A are the critical nucleation size (minimum nanocrystal size) and growth factor, respectively. This indicates that domain growth occurs through quasiepitaxial nucleation during the deposition process[98] and not through spinodal decomposition as in many solution-processed material systems.[22, 76, 99] From the fits using Equation (2.3), we extract a D^* of 6.9 nm and 5.8

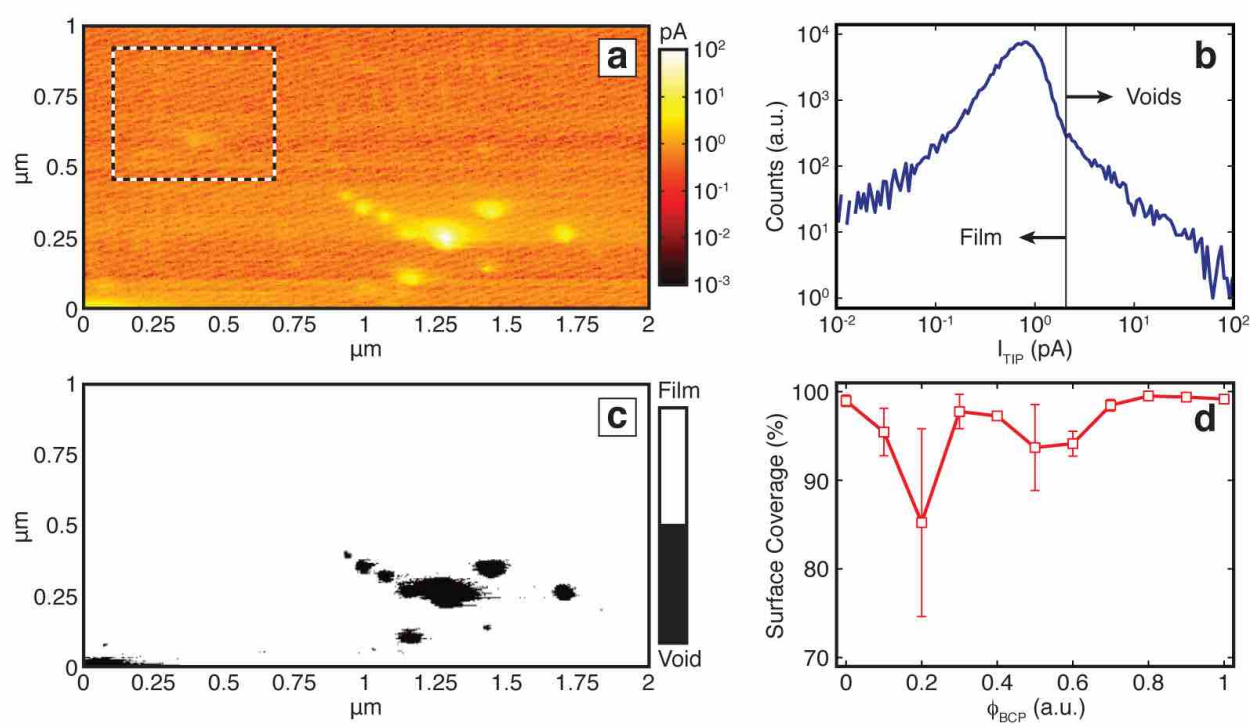

Figure 2.11 (a) Example cAFM scan of the sample in Figure 3a (ϕ_{BCP} = 0.4) taken at a bias of -5V. Due to the high work function of the Pt:Ir tip, under high reverse bias holes from the tip can efficiently inject into any exposed SubPc from the underlying donor film. The dashed box indicates the noise-current region used for background subtraction to determine pinholes/voids in the BCP:C_{60} layer. (b) Histogram of the current over the entire image, with the current threshold for the background noise demarking current originating from voids and the BCP:C_{60} film. (c) Background-subtracted binary image of a indicating the voids in the scan. (d) Average surface coverage for all BCP:C_{60} measured in this study, with error bars indicating ±1 standard deviation. For each sample, scans were taken on 4 distinct regions.

nm for BCP and C_{60}, respectively. Additionally, we observe a much higher growth factor for C_{60} than BCP (2.6 versus 2.2) and extrapolate a polycrystal grain size of 62 nm and 78 nm for neat BCP and C_{60} films, respectively. As shown recently by Bommel *et al*., the nucleation and growth of fullerene domains is a surface diffusion-limited process.[100] From the lower critical nucleation size and higher exponential factor of C_{60}, we infer that BCP exhibits a higher surface diffusivity than C_{60}. Thus BCP domain growth outcompetes fullerene domain growth during the deposition process. This is further reinforced by the shape parameter (less than unity) of the Weibull distributions, which implies a rapid quenching of domain growth after nucleation.

We note the binary phase maps extracted here are an approximation, as the cAFM tip radius (~20 nm) is incapable of molecular-scale resolution. However, since the domain sizes in BCP:C_{60} follow a known distribution, extrapolation to length scales below the tip radius is possible and enhanced resolution can be achieved. Additionally, the CDF filtering method assumes that the extracted morphology extends vertically through the mixed layer, and that scanned areas are sufficiently large to capture the global ϕ_{BCP}. Since the mixed layer itself was restricted to 5 nm thick (below the critical diameter for BCP and C_{60} nanocrystals) and each scan covered a relatively large 2 μm^2 area, both assumptions should be appropriate. Considering the similarities in mechanical properties and atomic composition amongst many van der Waals bound small molecules and polymers, other methods such as energy-filtered transmission electron microscopy (EFTEM) or traditional AFM may not be able to resolve individual domains.[71] We expect the cAFM technique shown here to be a powerful and simple tool for morphological and compositional analysis in a wide range of blended organic thin films.

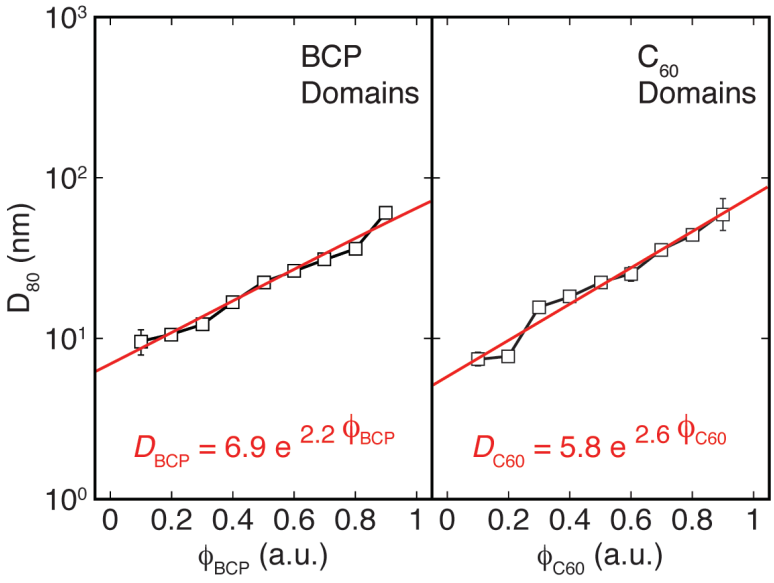

Figure 2.12 Characteristic domain size of BCP and C_{60} phases as a function of ϕ_{BCP} and ϕ_{C60} (= 1 - ϕ_{BCP}) displaying a clear exponential growth with increased volume fraction (Equation (2.3)).

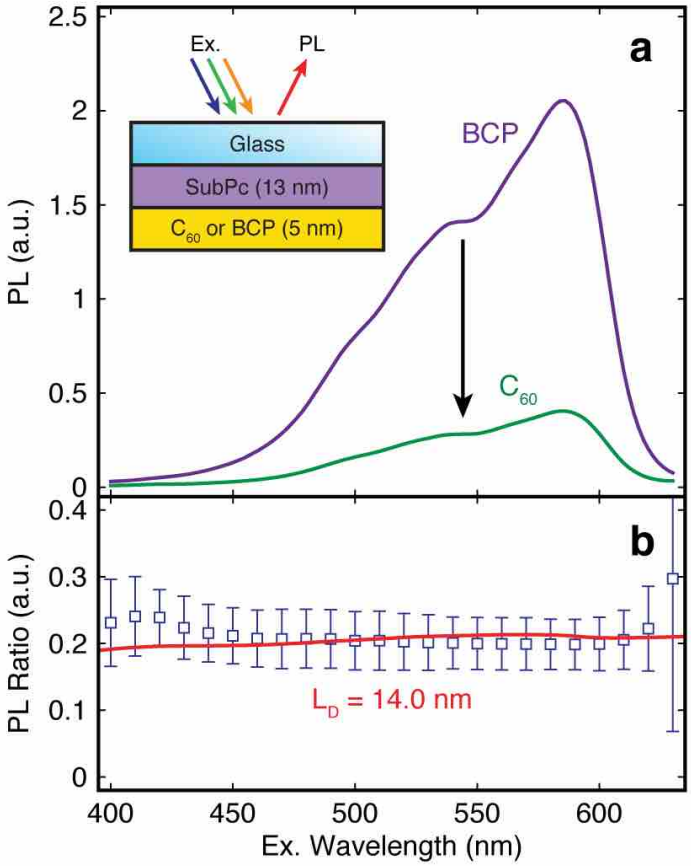

Figure 2.13 (a) PL excitation quenching of SubPc films by a neat C_{60} film relative to an exciton-reflecting BCP film. By comparing the numerically-calculated exciton quenching efficiency to the measured PL ratio (b), the L_D is determined to be 14.0 nm. Measurements are averaged over 5 scans per sample, and error bars represent the propagated error from their standard deviations.

2.2.6 Diffusion efficiency

Having determined the active layer morphology and domain size dependence on composition, we would now like to relate this to device performance and exciton diffusion. First however, it is necessary to characterize the L_D of the SubPc layer for reference. To measure the one-dimensional L_D out-of-plane, identical films of SubPc are deposited on glass substrates and capped by 5 nm of either BCP or C_{60} (**Figure 2.13**). Monochromatic light is used to excite the SubPc films over the visible absorption spectrum, and the photoluminescence (PL) is monitored at a fixed wavelength of 650 nm. As with the OPV devices, the exciton generation profile is

calculated *via* the transfer matrix method and coupled to the drift-diffusion model. The interfaces with glass and BCP are treated as exciton-reflecting, while the C_{60} interface is assumed to be perfectly quenching. By taking the ratio of the steady-state exciton population (C_{60}) to the total generation rate (BCP), the PL ratio is fit to extract an L_D of 14.0 nm.

As shown schematically in **Figure 2.14**, we measure η_D of the donor layer through steady-state PL emission quenching. As can be seen in **Figure 2.14**c, the diffusion efficiency of the donor layer exhibits a slow decay until $\phi_{BCP} = 0.9$. When compared to D_{BCP}, η_D remains approximately constant until the domain size surpasses L_D, at which point it follows a near-exponential slow decay. Surprisingly, even when D_{BCP} is more than $4 \cdot L_D$, the reduction in η_D is less than 50% of its initial value. This result can be understood as follows: what is often termed L_D in OPVs is the one-dimensional, out-of-plane diffusion length for excitons. As the spatial degrees of freedom are increased for two- and three-dimensional diffusion, excitons are capable of traveling a greater distance by a factor of $\sqrt{2}$ and $\sqrt{3}$, respectively (Inset in **Figure 2.14**c). The in-plane nanostructural variations at the SubPc/BCP:C_{60} interface break the uniaxial symmetry of the planar device, and thus reductions in diffusion efficiency follow a two-dimensional trend. We find diffusion to the PMHJ can be accounted for with a very simple model, where in-plane and out-of-plane diffusion is accounted for independently:

$$\eta_D = \eta_D^{in-plane} \cdot \eta_D^{out-of-plane} \tag{2.4}$$

with the in-plane diffusion length equivalent to $\sqrt{2} \cdot L_D$. By separating out the two components, η_D can be approximated by two one-dimensional calculations, drastically simplifying the analysis in systems with complex interfacial morphologies. The quality of the fit in **Figure 2.14**d indicates that the BCP domains are highly pure, as non-percolating C_{60} inclusions (electrically insulated but still capable of exciton quenching) would cause a significant deviation from the

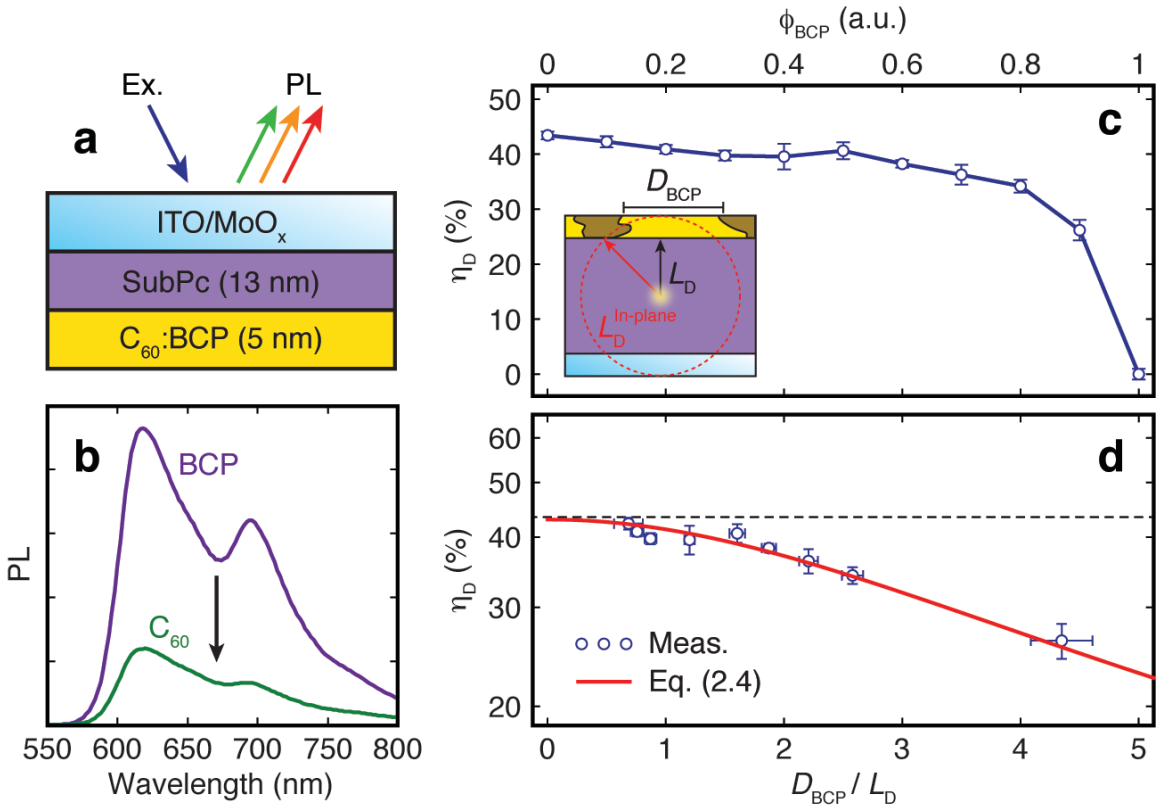

Figure 2.14 (a) Schematic of the PL testing setup for characterizing η_D within the SubPc layer. Note the structure is identical to that measured *via* cAFM. (b) PL spectra of SubPc films with an exciton reflecting (pure BCP) or quenching (pure C_{60}) interface. A reduction in PL intensity corresponds to CT at the heterojunction. η_D of excitons in SubPc to active C_{60} sites at the heterojunction as a function of (c) ϕ_{BCP} and (d) D_{BCP} normalized to L_D. An excellent match to the modeled diffusion (red line) is observed in (d) assuming a two-dimensional L_D in-plane (inset in c).

observed dependence on D_{BCP}.

To confirm the validity of Equation (2.4), we now derive a simple effective medium approach to quantify 2-dimensional diffusion in a neat organic film with periodic boundary conditions in-plane. We begin by evaluating the case of 1-dimensional diffusion and extend this analysis to the 2-dimensional system under consideration. For out-of-plane diffusion, the films and interface boundary conditions are assumed to be uniaxial. Assuming a uniform exciton generation profile, the average distance for an exciton to diffuse to the heterojunction interface is $d = t/2$, where t is the film thickness. This approximation of uniform exciton generation was

confirmed *via* transfer matrix modeling. In the case of a 2-dimensional system such as the SubPc/BCP:C_{60} bilayer, the boundary conditions at the heterojunction interface vary in-plane with a characteristic periodicity according to the domain size and volume fraction of BCP. Regions of the SubPc film underneath C_{60} domains exhibit 1-dimensional diffusion locally, however regions underneath BCP domains must diffuse laterally as well as out-of-plane to reach an active C_{60} site. Thus, when treated as an effective medium, the average overall diffusion distance is:

$$d_{avg} = d_{C60} \cdot \left(1 - \phi_{BCP}\right) + d_{BCP} \cdot \phi_{BCP} \tag{2.5}$$

where $d_{C60} = t/2$ and d_{BCP} is the volumetrically averaged diffusion distance to a C_{60} site from underneath a BCP domain of size D_{BCP} (Inset in **Figure 2.15**). From d_{avg} we can now treat the 2-dimensional system as effectively 1-dimensional, with an effective thickness $t_{eff} = 2 \cdot d_{avg}$ and a characteristic diffusion length of $\sqrt{2}L_D$. Both the 1-dimensional and effective medium methods used here assume quenching at both interfaces, as MoO_x has been shown to quench SubPc excitons.

Comparing the effective medium approach to the linear approximation (Equation (1.24)), the effective diffusion distance is shown to be nearly identical for $D_{\mathrm{BCP}} > L_{\mathrm{D}}$ (**Figure 2.15**a). Below this point, variation of boundary conditions in-plane have minimal effect on diffusion efficiency, as excitons can freely sample the interface until a quenching site is encountered. Thus over the range of domain sizes measured in this study, we find a simple separation of diffusion efficiencies for in- and out-of-plane transport to be within experimental error to that predicted by the more rigorous effective medium approach.

The above result directly confirms one of the most basic assumptions applied to mixed-junction OPVs – that distributing the heterojunction in multiple dimensions drastically improves

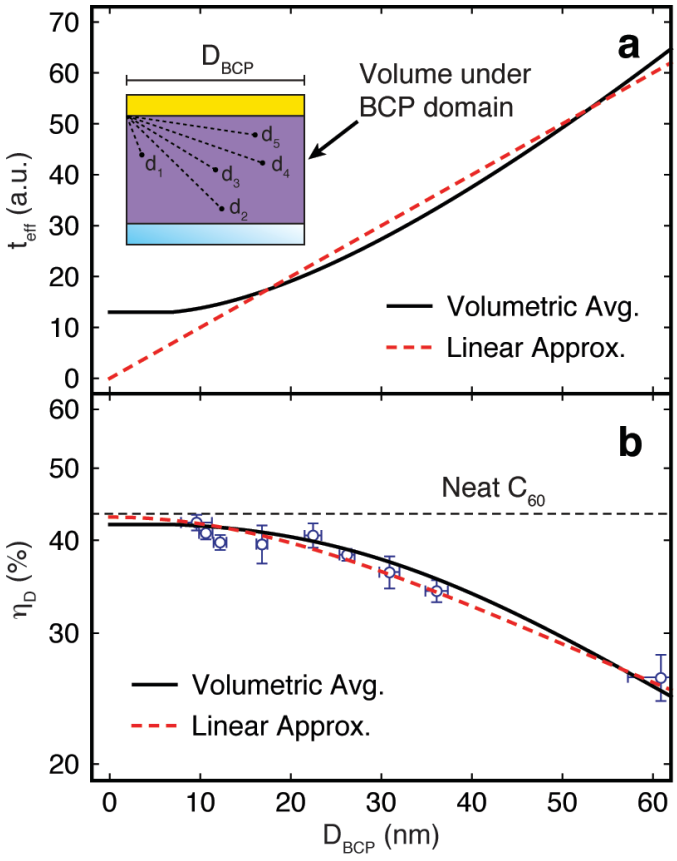

Figure 2.15 (a) Average effective diffusion distance (t_{eff}) to a C_{60} site for the SubPc volume contained under a BCP domain for varying D_{BCP} (Inset). The dimensionality of the system is effectively reduced to one dimension, with a characteristic two-dimensional L_D. This is compared to Equation (2.4), which assumes a linear relationship between D_{BCP} and in-plane diffusion distance. Note that the linear method accounts for in-plane diffusion separate from out-of-plane diffusion, while the volumetric average accounts for both dimensions simultaneously. (b) The calculated diffusion efficiency (η_D) is comparable between both methods, well within the error of our measurements.

η_D to dissociating interfaces. However, we show that the close proximity of the heterojunction to photogeneration sites in mixed-layer architectures is only part of the reason; two- and three-dimensional distributions of the active layers improve the probability of excitons reaching a heterojunction interface due to geometric factors. This indicates in BHJs especially, domain sizes of well over $4 \cdot L_D$ can be tolerated with a minimal reduction in IQE. Furthermore, the ability to separate in-plane from out-of-plane η_D requires the neat layer thickness be on the order of L_D, a condition that is met in most OPV PMHJ devices. Thus, we expect the method embodied by

Equation (2.4) to be generally applicable for modeling excitonic transport at planar-mixed interfaces, as well as a simple optical technique for estimating domain size *in-situ* from PL measurements.

2.2.7 Charge-transfer state dissociation efficiency

Having independently measured η_D, we now consider the dissociation process at the heterojunction. By factoring out η_D from the S_{pc}-corrected IQE, we can experimentally determine the η_{CT} for excitons reaching the heterojunction at zero bias (**Figure 2.16**). Plotted against D_{C60}, a precipitous drop in dissociation efficiency is observed for domain sizes below ~43 nm, above which η_{CT} saturates at ~100%. By comparing the measured values of η_{CT} to those calculated using Equation (1.11), we are able to directly correlate nanostructure and the zero-field kinetics of the CT state (**Figure 2.17**).

In devices with low ϕ_{BCP}, the η_{CT} magnitude is near 100% at zero bias, while variations are within the IQE measurement error. For these points, we consider the full bias-dependent photocurrent curve ($J_{ph} = J_{dark} - J_{light}$) to resolve the minor changes in k_{d0}/k_r (**Figure 2.18**). The voltage-dependent J_{ph} is described by:

$$J_{ph}(V) = -q \cdot \eta_{CT}(V) \cdot J_X - S_{pc} \cdot (V_{bi} - V) \tag{2.6}$$

where J_X is the exciton flux to the heterojunction.

$$J_X = \frac{J_{sc} - S_{pc} \cdot V_{bi}}{\eta_{CT}(V = 0)} \tag{2.7}$$

Thus exciton flux is calculated from the zero bias values of dissociation efficiency, the measured short-circuit current density, and the contribution to photocurrent production from photoconductivity at zero bias. The inclusion of the denominator in Equation (2.7) is necessary

to account for non-unity dissociation yield at zero bias. We assume for simplicity that a uniform field is maintained over a depletion region of width d encompassing the heterojunction:

$$E = \frac{V - V_{bi}}{d} \tag{2.8}$$

and use the series expansion of the first order Bessel function:

$$\frac{k_d(E)}{k_{d0}} = 1 + b + \frac{b^2}{3} + \frac{b^3}{18} + \ldots \tag{2.9}$$

$$b = \frac{q^3 E}{8\pi\varepsilon_r\varepsilon_0 k_B^2 T^2} \tag{2.10}$$

along with Equations (1.11) and (1.15) to solve for the field-dependent η_{CT}. This yields η_{CT} and J_{ph} as a function of bias using only three orthogonal fitting parameters: d, V_{bi}, and $\frac{k_{d0}}{k_r}$. The first two terms determine the field experienced by the CT state, while the final term characterizes the competition between dissociation and recombination under zero-field conditions.

Figure 2.18 displays the fits of Equation (2.6) to the J_{ph}-V curves of devices with ϕ_{BCP} < 0.3, calculated by the subtraction of the dark from light J-V curves (**Figure 2.6**a). However, devices with higher ϕ_{BCP} can not be accurately fit with Equation (2.6), as the contribution from photoconductivity dominates too much of the J_{ph}-V curves to resolve changes to the junction current. Furthermore, above ϕ_{BCP} = 0.5 an additional kink is observed at positive bias, likely due to field-dependent band bending introduced near the heterojunction. Hence we employ Equation (1.11) to directly fit the η_{CT} measured at zero bias from the IQE (**Figure 2.6**d) and η_D (**Figure 2.14**c) to the corresponding $\frac{k_{d0}}{k_r}$ (**Figure 2.17**a), assuming a fixed V_{bi} of 0.98 V and a depletion width of 50 nm (the nominal active layer thickness). Both methods are complementary; at values of $k_{d0}/k_r > 1$, dissociation is highly efficient at zero bias and a range of voltages are required to

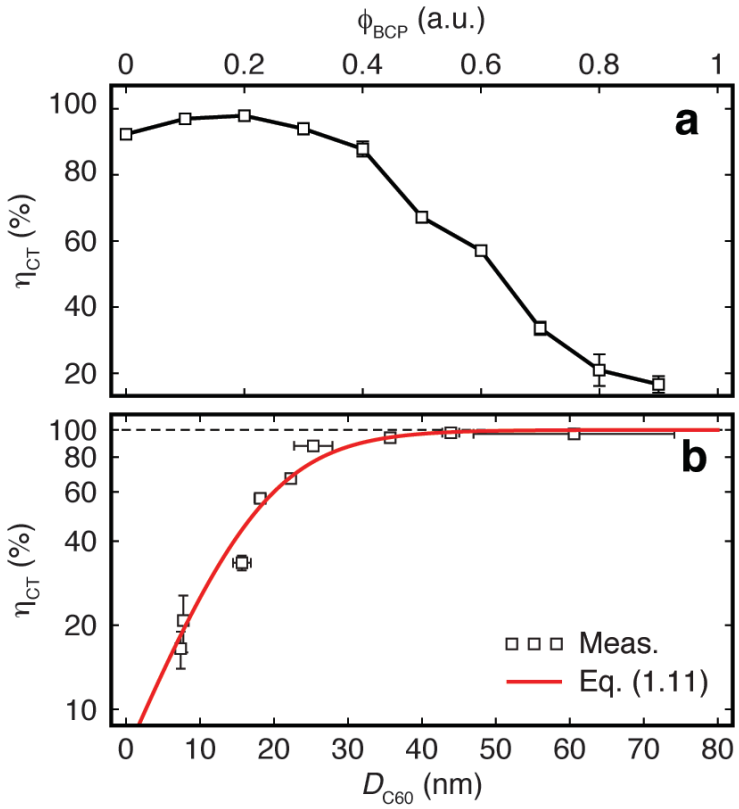

Figure 2.16 η_{CT} at the heterojunction as a function of (a) ϕ_{BCP} and (b) D_{C60}. The trend in b arises from an exponentially decreasing k_{d0}/k_r with C_{60} domain size (red line in b), indicative of a charge delocalization-assisted dissociation process.

track small changes to the CT state kinetics. Below this regime however, small changes to η_{CT} can be accurately discerned from the IQE while avoiding other voltage-dependent terms present in J_{ph}-V scans. We further note that the J_{ph}-V scans presented here are only an approximation of the bias-dependent photocurrent, while the lock-in measurement method of EQE is a direct probe of device photocurrent.

As seen in **Figure 2.17**b, k_{d0}/k_r is exponentially dependent on D_{C60} in the BCP:C_{60} mixed layer. Above D_{C60} = 43 nm, k_{d0}/k_r begins to saturate as η_{CT} approaches 100%. This value represents an upper limit, as the broad distribution in observed domain sizes (**Figure 2.11**) indicates a large population of aggregates with sizes below D_{C60}. However, comparison of the calculated η_{CT} to experiment (**Figure 2.16**b) shows an excellent correlation to within

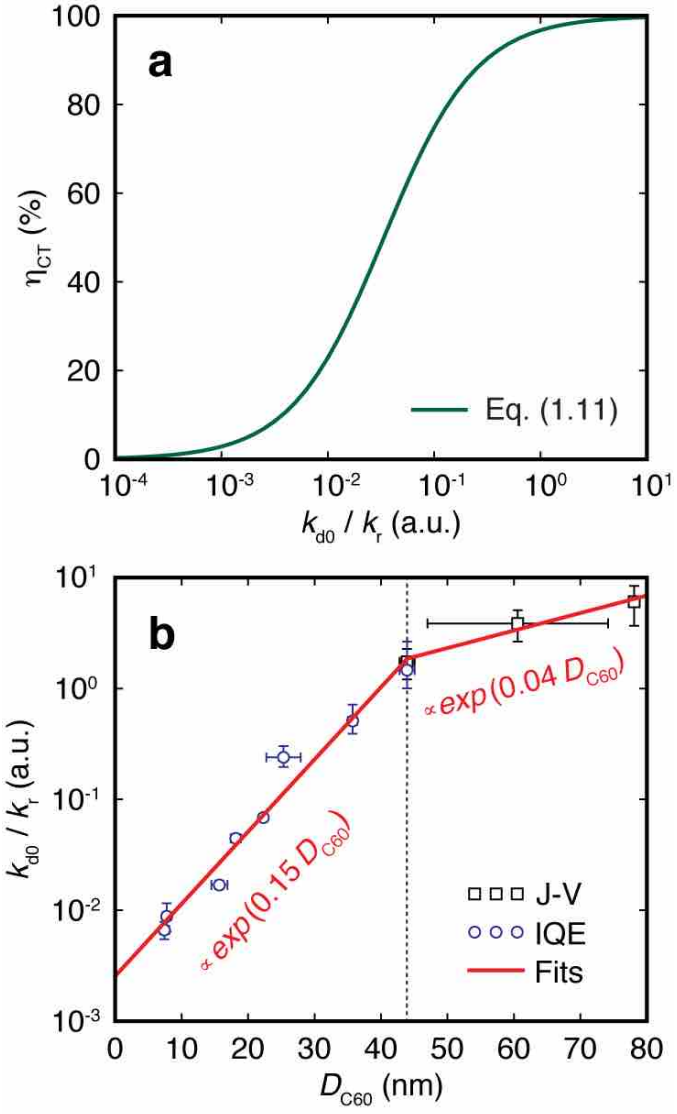

Figure 2.17 (a) Calculated η_{CT} under short-circuit conditions as a function of k_{d0}/k_r and assuming a fixed internal field. (b) k_{d0}/k_r values as a function of C_{60} domain size, extracted from *J-V* and IQE measurements. Two distinct exponential regimes are observed at low (D_{C60} < 43 nm) and high domain sizes, indicating a critical size for efficient dissociation at zero bias. Solid lines in (b) are fit using a least-squares method.

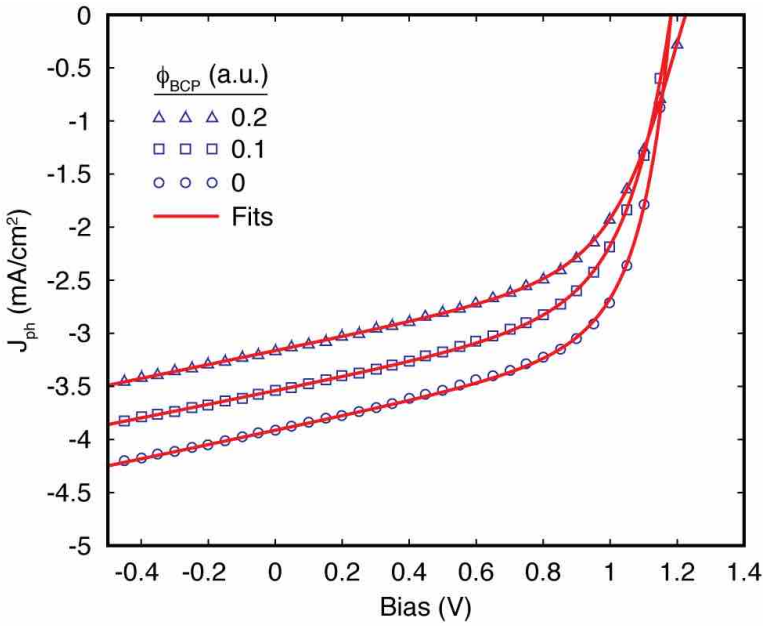

Figure 2.18 Example photocurrent (J_{ph}) curves as a function of electrical bias are shown for the three lowest BCP loading fractions along with their calculated fits to the Equation (1.11). This data corresponds to the "J-V" points of **Figure 2.17**.

experimental error.

We conclude that although the C_{60} domains are capable of CT state formation below D_{C60} = 43 nm (as confirmed by PL quenching measurements), recombination of the CT state progressively outcompetes its dissociation with lower domain size. This result is consistent with recent ultrafast spectroscopy experiments on a variety of polymer/fullerene BHJs, which have indicated the delocalization of the electron wavefunction in fullerene aggregates drives the efficient dissociation of the CT state.[28, 30, 35, 101-103] Our results provide further evidence that charge delocalization in CT states drives the dissociation process at steady-state in fullerene-based devices.

2.3 Conclusions

By confining the mixed layer morphology to two dimensions, we present a unique way to directly probe the heterojunction of OPVs, which is normally a buried interface. The ability to correlate nanostructural changes at the heterojunction to the individual steps of photocurrent generation allows us to quantify a systematic relationship between processing, structure, and performance of PMHJ and BHJ OPVs. We demonstrate that the morphology of vacuum-deposited small-molecular blends such as BCP:C_{60} follows a surface-diffusion limited quasi-epitaxial growth, consistent with observations in pure fullerene films.[100] This results in a hierarchical nanostructure in the mixed layer, with the sizes of aggregates exhibiting an exponential dependence on their corresponding molecular volume fraction. While such morphologies create a highly interconnected network through which charge transport is maintained,[85] the impact on photocurrent generation is demonstrated to be extremely sensitive to aggregate size. Specifically, we show that the relative dissociation rate of the CT state is exponentially dependent on the C_{60} domain size, D_{C60}, which itself exhibits an exponential dependence on the C_{60} loading fraction, ϕ_{C60}. This result explains why vacuum-deposited small-molecular BHJs employing fullerene acceptors must always be kept fullerene-rich, even though the absorption may benefit from higher donor loadings.[104] In contrast, most polymer:fullerene blends undergo spinodal decomposition during film formation[76] and display a linear dependence of domain size on composition,[99] thus we predict an exponential dependence of k_{d0}/k_r on ϕ_{C60} and a higher tolerance for donor loading in polymeric OPVs, as is commonly observed. Furthermore the results here provide further evidence that photocurrent predominantly originates in the pure phases of BHJ devices, as only fullerene aggregates with strong intermolecular coupling will efficiently dissociate the CT state. Finally, our results confirm the

general assumption that volumetrically distributing the donor and acceptor layers in PMHJs and BHJs increases diffusion efficiency. This is accomplished not only through the close proximity of the heterojunction to photogeneration sites, but also through an increased probability for excitons to reach the two- or three-dimensionally distributed heterojunction due to geometric factors. Indeed, we predict that viable domains sizes can far exceed the one-dimensional L_D without significantly reducing η_D. These new insights can guide the future rational design of OPV device morphologies and provide a deeper understanding of their impact on device operation.

2.4 Future work

The cAFM and PL methods presented in this Chapter provide new means for interrogating the structure of binary mixed layers. The use of cAFM, in combination with Kelvin-probe force microscopy for example, would enable the spatial correlation of the local DOS, morphology, and charge injection behavior with high resolution (~5 nm). Furthermore, deriving the composition-dependent parameters of Equation (2.3) for a variety of molecular systems and substrates would provide insight into the growth and surface diffusion kinetics of small molecules as a function of intermolecular bonding and substrate surface energy. As for PL quenching, we anticipate this method to provide a simple and rapid means of estimating domain size in blended organic films using Equation (2.4). Using an isotropic film as a fluorescence probe, domains at the interface of an adjacent mixed layer can be interrogated from PL quenching measurements. With proper selection of the probe material, exciton quenching can be constrained to a single phase in the mixed layer. An accurate measurement only requires prior knowledge of the probe's L_D and the avoidance of significant Förster transfer to the mixed layer. Finally, while we have extrapolated

guidelines for device design from our two-dimensional PMHJ devices, a systematic extension of this work to small molecule BHJs would be the next logical step in developing a general process-structure-performance relationship for mixed-layer OPVs.

Chapter 3

Interface modification and exciton dissociation layers

3.1 Background

Interfaces are critical to the performance of organic photovoltaic devices. Apart from the organic heterojunction where dissociation occurs, interfaces at the anode and cathode often include additional layers to assist in charge injection/extraction and enhance the built-in field provided by the electrodes. On the cathode side of the device, buffer layers such as BCP are often employed to inhibit metal diffusion into the active layers during cathode deposition[85, 88, 105-108] and reduce exciton quenching by the conducting metal electrode through physical separation.[109] On the anode side, high work function transition metal oxides and conducting polymers such as MoO_3 and PEDOT:PSS, respectively, are commonly used to improve V_{oc} and FF.[110-115]

While exciton behavior at cathode buffers (e.g. BCP) was studied previously, little attention until recently has been paid to anode buffers. In this chapter we will demonstrate that the presence of MoO_3 quenches excitons in the adjacent layer and introduce a new concept, the exciton dissociation layer (EDL), for mitigating exciton quenching at the anode and significantly improving diffusion efficiency within devices without affecting absorption. By providing an additional interface for dissociation, the inclusion of an EDL creates a "cascade heterojunction"

(CHJ), which we will show to have superior performance to traditional planar heterojunction OPVs when properly engineered.

3.1.1 Exciton blocking layers

In the conventional device geometry, the anode is positioned on the substrate (typically ITO) and the cathode consists of a thermally evaporated metal film (typically Ag or Al). In small molecule organics especially, penetration of the metal occurs deep into the underlying organic layers forming metallic nanoparticle inclusions.[109, 116] In addition to the acceptor/cathode interface itself, these conducting metal clusters rapidly quench excitons in their vicinity and can cause a sharp drop in photocurrent production from the surrounding volume. Additionally, their presence can create electrical shorts through the device, reducing *FF* substantially. For these reasons, the concept of an EBL was introduced by Peumans *et al.*, where a wide bandgap small molecule such as BCP is inserted below the cathode layer (**Figure 3.1**).[107, 117] The presence of the EBL, which is typically non-absorbing, shields the underlying active layers from metal penetration and

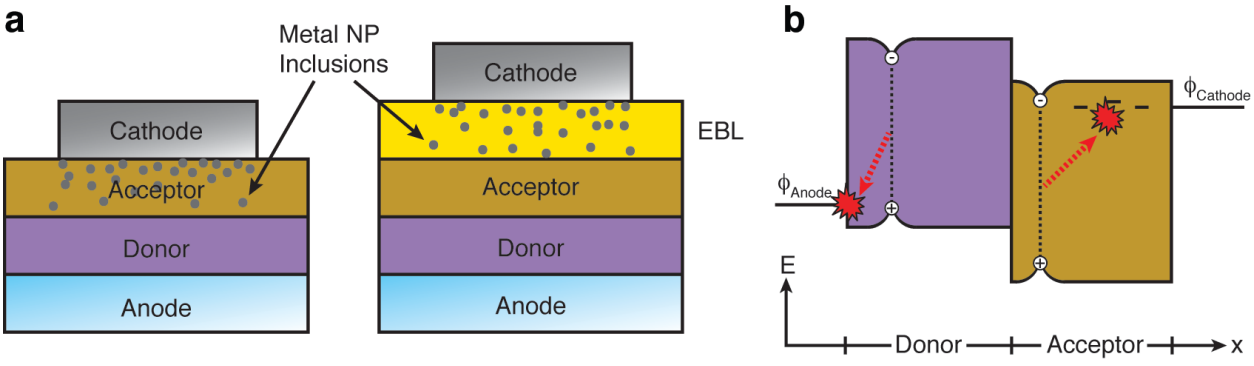

Figure 3.1 (a) Metallic cluster (nanoparticle) inclusions form in the underlying organic layer during metal deposition. Incorporation of an EBL protects the underlying active layers from metal penetration. (b) Energy level diagram showing exciton quenching electrode interfaces and metal NP inclusions.

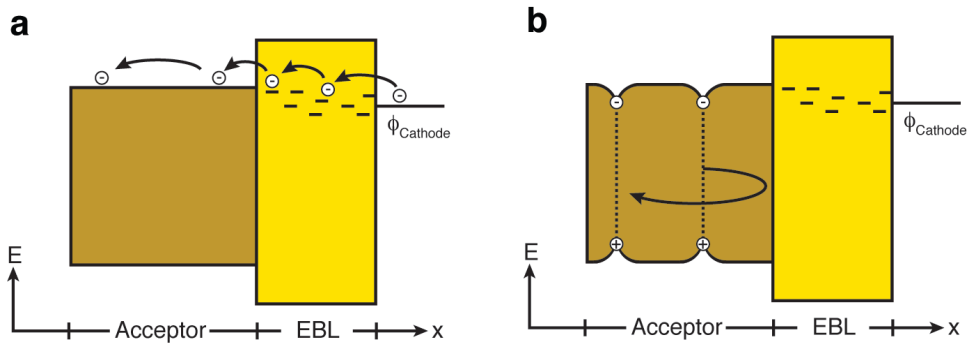

Figure 3.2 (a) Defect states induced in the EBL from metal deposition allow for barrier-free charge injection/extraction between the cathode and acceptor. (b) The larger bandgap of the EBL relative to the acceptor causes excitons to "reflect" from the interface during diffusion.

physically separates the exciton population from the cathode interface.

The direct effects of the EBL are twofold: the physical separation of the exciton population in the acceptor eliminates exciton quenching at the neighboring acceptor interface, and the confinement of metallic inclusions to the EBL reduces shorts through the device, improving *FF*. In the case of wide-bandgap materials such as BCP, the metal penetration into the EBL is advantageous, as it produces mid-gap defect states through which charges can be injected into (and extracted from) the LUMO of the acceptor layer (**Figure 3.2**).[105, 109] Otherwise, the larger EBL bandgap would introduce a substantial injection and extraction barrier for electrons. Due to the conductivity dependence on these metal-induced gap states, blocking layers such as BCP are typically constrained to 10 nm or less. Above this thickness, gap states do not extend throughout the film, and conductivity suffers. More recent work by Lassiter *et al.* has demonstrated EBLs with LUMO levels aligned to that of the acceptor, which provide a lower series resistance and improved FF for thicker layers.[106] However, due to uncertainty in energy level measurements and the requirement of LUMO matching to each specific acceptor material, the wide bandgap approach is more common.

As a consequence of eliminating quenching at the acceptor/cathode interface, the steady-state exciton flux to the heterojunction increases significantly. Not only are excitons generated in the vicinity of the cathode contributing to photocurrent, but excitons diffusing towards the cathode are capable of being reflected and contributing to J_{sc}. Combined with its dual use as an optical spacer, which can improve the positioning of the optical interference maxima closer to the heterojunction, the overall impact of EBL incorporation is the improvement of η_D.

3.1.2 Exciton quenching at the anode

While the issue of exciton quenching at the cathode was solved early on with the introduction of cathode EBLs, anode quenching remained unaddressed until recently. As mentioned previously, transition metal oxides such as NiO and MoO_3 (also denoted MoO_x) or conducting polymers such as PEDOT:PSS are commonly used to increase the work function of the anode. It had been generally assumed that such films were exciton-reflecting, as they are not traditional metallic conductors.[113, 118] Recent work however has shown this not to be the case for either transition metal oxides[46, 84] (**Figure 3.3**) or conducting polymer films[119] (**Figure 3.4**). Indeed, it is a safe assumption that any conductor/organic interface will provide ample surface states for exciton quenching.

Ideally, the EBL concept could be extended to the anode side of the device. However, unlike cathode EBLs, there is no subsequent metal deposition step during device fabrication to enable conduction through a high bandgap layer at the anode side. Furthermore, it is unclear whether such an approach would produce deep level traps aligned to the HOMO of the donor layer – a requirement for efficient charge injection and extraction. Some limited success has been achieved using EBL/donor combinations with aligned HOMO levels, such as

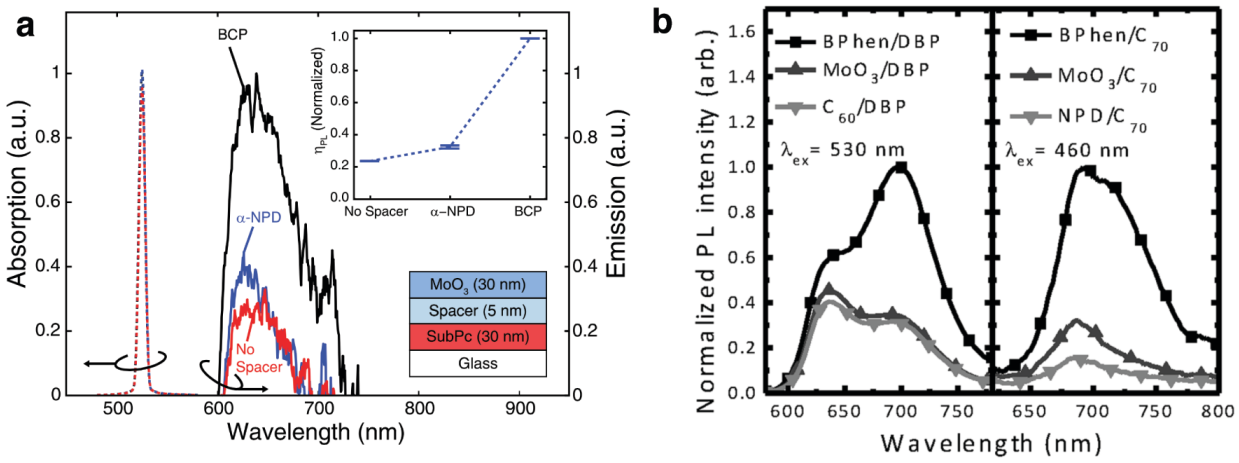

Figure 3.3 Exciton quenching of (a) SubPc and (b) DBP and C_{70} by MoO_3 films probed through PL quenching. The presence of MoO_3 yields a drop in PL intensity, correlated with parasitic exciton recombination at the interface. [46, 84]

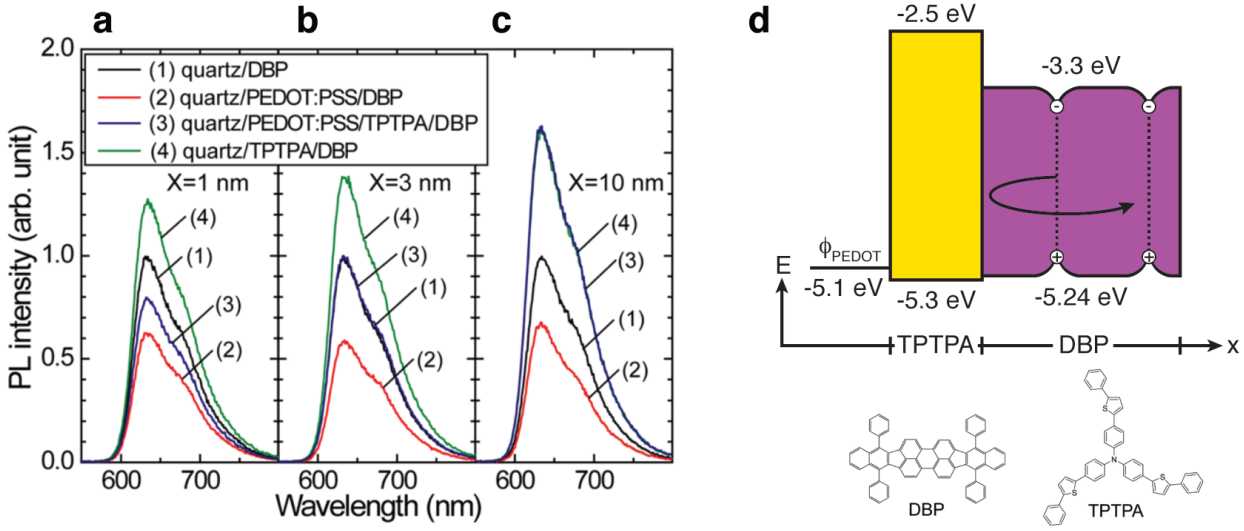

Figure 3.4 PL quenching data for films of DBP on inert (glass) and quenching (PEDOT:PSS) substrates with (a) 1 nm, (b) 3 nm, and (c) 10 nm of TPTPA buffer excited at 530 nm. (d) Energy level diagram of the TPTPA/DBP bilayer and their corresponding molecular structures. [119]

tris{4-(5-phenylthiophen-2-yl)phenyl}amine (TPTPA) with tetraphenyldibenzoperiflanthene (DBP) as the EBL and donor, respectively (**Figure 3.4**).[119] This work demonstrated the large performance enhancements potentially afforded by an anode EBL: J_{sc} was increased from 5.82 ± 0.08 mA/cm^2 to 7.15 ± 0.25 mA/cm^2 upon optimization, without affecting either *FF* or V_{oc}. Additional studies have used various other small molecule EBL compounds at the anode, with varying success.[120-122] Just as in the case of LUMO-aligned cathode EBLs, the constraint of HOMO level alignment makes it difficult to find suitable buffer layers, and no single molecule can be applied as an anode EBL universally. However, recent work by Zimmerman *et al.* has shown phosphonic acid monolayers can function with a variety of donors on NiO.[123]

3.1.3 Structural templating layers

Polycrystalline small molecule films have the ability to template to an underlying organic layer through quasi-epitaxial growth.[124-134] This effect can be advantageous, as most organic molecules are tilted relative to the substrate in thin films, and the incorporation of a templating layer can force them to lie flat relative to the substrate. Such an orientation imposes the transition dipole of the molecular absorption bands in-plane, which can significantly enhance light absorption at normal incidence. However, the reorganization of molecules in a film can additionally affect its electrical and excitonic properties, particularly charge mobility and exciton diffusivity/lifetime. Preferential orientation of the molecules can increase the L_D along the crystallographic axis. For example, a study by Lunt *et al.*[135] demonstrated a nearly fourfold increase in L_D with crystalline order in PTCDA films. Additionally, the change in molecular orientation affects the intermolecular orbital overlap, modifying the polarizability, refractive index, and exciton lifetime. Typically in PL quenching studies of exciton diffusion, it is assumed

the active film morphology (and absorption) remains constant.[47] This enables the determination of the quenching/reflecting boundary conditions imposed by the neighboring layers along with the exciton L_D. However, in the case of templating layers, this assumption may be invalid and L_D determination, as well as boundary condition determination, is much more difficult. It is imperative when studying the effectiveness of anode buffer layers to account for such effects, as increases in absorption or L_D from templating can be easily misconstrued as J_{sc} contributions resulting from reduced exciton quenching.

3.2 Exciton dissociation layers

3.2.1 Concept

By introducing an entirely "passive" EBL that only reflects excitons, the net flux of excitons at the single heterojunction (SHJ) is increased only slightly, while a large portion of excitons generated nearest the EBL interface will still recombine parasitically in the bulk. As an alternative approach to the EBL, we introduce the concept of an exciton dissociation layer (EDL). The principal difference between an EDL and a conventional EBL is that the EDL material is chosen such that its HOMO and LUMO levels enable cascade-energy-level-alignment[136-139] with the donor layer, facilitating exciton dissociation at the EDL/donor interface (**Figure 3.5**b). With the incorporation of such an EDL, the exciton concentration profile within the active layer remains identical to the profile in the case of quenching at the electrode, but instead of being lost to parasitic recombination, the excitons at the EDL/active layer heterojunction also contribute to photocurrent (**Figure 3.6**c). The second heterojunction operates in parallel (current additive) with the original junction, thus we term this a cascade heterojunction (CHJ) structure. In principle, by effectively decreasing the distance excitons need

to diffuse before dissociation, the EDL/donor heterojunction relaxes the requirement for long exciton diffusion lengths and improves the η_D and IQE of any adjacent layer. Note the CHJ is not to be confused with what are commonly termed "energy cascade" OPVs, in which one or more buffer layers act as a sensitizer by transferring their absorbed photons into the active layers through FRET.[140-143] Such devices only employ a single heterojunction, so they their operation is fundamentally different from CHJs.

We validate the EDL concept by fabricating devices with N,N'-bis(naphthalen-1-yl)-N,N'-bis(phenyl)-2,2'-dimethylbenzidine (α-NPD) inserted between SubPc and MoO_3 in an archetypal SubPc/C_{60} heterojunction OPV cell. This approach increases the photocurrent contribution of SubPc by 66% (leading to a 27% enhancement in device J_{sc}), without changing the number of photons absorbed by SubPc. In other words, inserting the EDL substantially boosts the IQE of the SubPc layer. The EDL functionality is further confirmed with a rigorous physical model of EQE and IQE in CHJ structures.

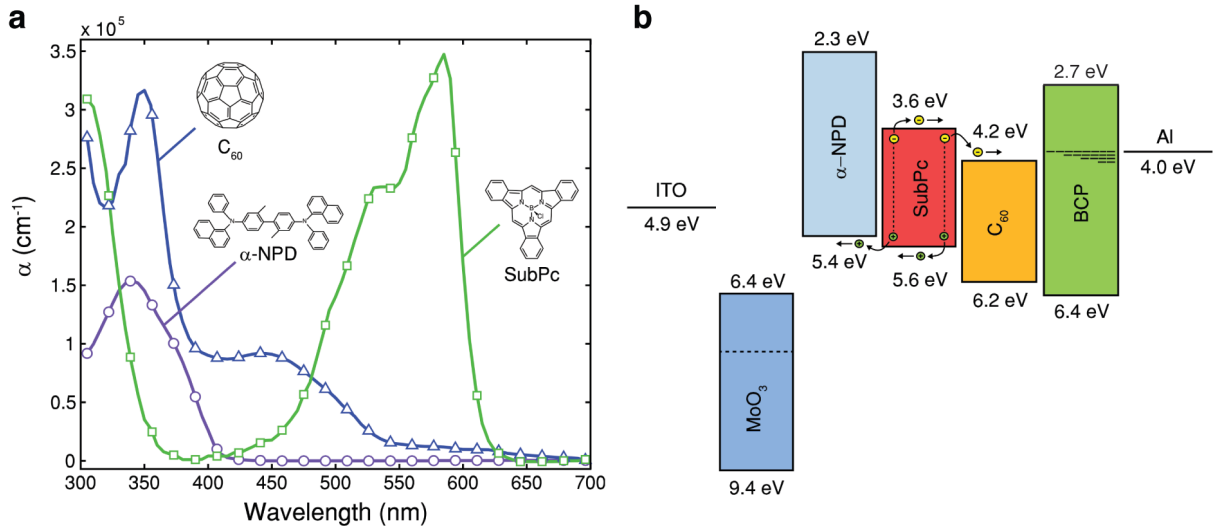

Figure 3.5 (a) Active molecules used within this study and their absorption spectra calculated from refractive index values measured by spectroscopic ellipsometry. (b) An energy level diagram for a SubPc/C_{60} device with an α-NPD EDL inserted between the SubPc and MoO_3 layers. [46]

3.2.2 Theory

The molecules used in this study and their respective absorption coefficients are shown in **Figure 3.5**a. The reference device structure employed is an archetypal SubPc/C_{60} PHJ, which has been extensively characterized in the literature.[144, 145] In **Figure 3.5**b, an energy level diagram is shown for the devices under investigation.[146-149] Optical analysis (Section 1.5.2) shows negligible light absorption in the EDL, allowing us to isolate its ability to increase the IQE of SubPc.

We first consider the physical model of an archetypal SHJ planar OPV cell as detailed in Section 1.5. At steady-state conditions, we can assume $d\rho/dt$ to be zero, allowing us to determine a numerical solution for the exciton population profile by imposing boundary conditions at the active layer interfaces (**Figure 3.6**c). For each case, we assume 100% dissociation at the SubPc/C_{60} heterojunction, consistent with standard practice.[26] Because BCP is a large bandgap EBL, the C_{60}/BCP interface is treated as an exciton reflector ($d\rho/dx = 0$ at the interface). In the case of a reflecting anode (e.g. EBL), the interface behaves identically and $d\rho/dx = 0$. However, as the MoO_3/SubPc interface has been shown to be exciton-quenching, we impose a zero value for the population density ($\rho = 0$). The same condition applies if an EDL is present, as the EDL/donor heterojunction also quenches excitons *via* the formation of CT states. Unlike the MoO_3 interface however, exciton flux at the EDL/donor heterojunction contributes to the total photocurrent of the device; in its absence, the same exciton flux is instead lost to interfacial recombination.

The integrated area under the two curves in **Figure 3.6**c represents the population of excitons lost to bulk recombination during diffusion. As can be seen, the introduction of an EDL significantly decreases bulk recombination over the EBL case, as more excitons are capable of

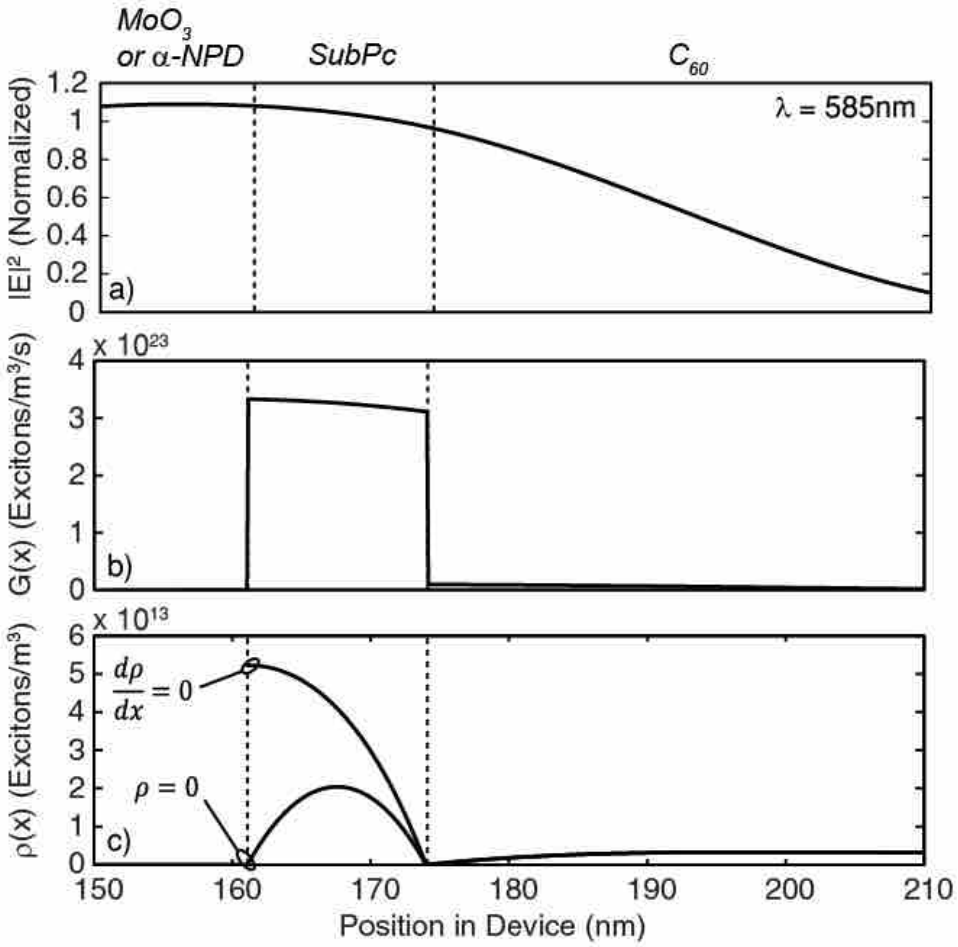

Figure 3.6 Modeled (a) electric field, (b) exciton generation, and (c) exciton population density profiles within the OPV device used in this study. Boundary conditions (which only affect the exciton population density) at the MoO_3/SubPc or α-NPD/SubPc interface are shown for both perfect exciton reflection ($d\rho/dx = 0$) and 100% exciton quenching or dissociation ($\rho = 0$). [46]

reaching an active heterojunction, and η_D is subsequently improved. While it would appear that recombination is similarly reduced in the case of a quenching anode, this is in fact not the case. Although bulk recombination decreases relative to the EBL condition, it is directly offset by interfacial recombination at the anode, and the net recombination rate remains the same. However, the shift from bulk (EBL) to interfacial recombination (anode quenching) reduces the flux reaching the SHJ, and reduces η_D as a result.

In the device containing an EDL, a second heterojunction is operating in addition to the conventional donor/acceptor junction. To predict the EQE spectrum, we must make an assumption as to whether the two heterojunctions are operating as diodes connected in series or parallel. Previously, CHJs have been described in literature as individual diodes connected in series.[136, 139] However, our results indicate that while the layers themselves are spatially positioned in series, they behave electrically as parallel photodiodes. Due to their energy level alignment, charges dissociated from one interface experience a barrier-free transit to the electrodes, regardless of their position within the structure (**Figure 3.5**b). Thus our modeling treats the photocurrents from each junction as additive (electrically in parallel), with the caveat that there is negligible bimolecular recombination of non-geminate carriers within the bulk of the central device layers (consistent with previous findings for cascade devices with SubPc used as an ambipolar interlayer).[136]

While our model focuses primarily on exciton and charge transport at short-circuit conditions, it is important to note that current injection under applied bias in a CHJ device will differ from current injection in a SHJ device. Although photocurrent extraction remains unimpeded, the extra heterojunction contributes an additional barrier to current injection that increases the total series resistance of each HJ in the cascade device over that in its SHJ counterpart. Additionally, in the case of strongly unipolar materials, internal layers can also become transport limiting and exhibit space-charge limited (SCL) current behavior. This non-ideal case should result in a lower *FF* relative to the case of a SHJ device, due to a large difference in the internal electric field at each heterojunction.

3.2.3 Experiment

Devices and samples were fabricated on commercially available ITO (Delta Technologies, R_s < 15 Ω/□, 150 nm thick). Substrates were cleaned via heated (40 °C) sonication in detergent, water, acetone, trichloroethylene, and isopropanol, followed by boiling in isopropanol and 10 min of UV-ozone treatment to remove carbon residues and increase the anode work function. Device layers were deposited *via* vacuum thermal evaporation (VTE) using an Ångstrom AMOD deposition system. Fabrication was performed in a glovebox filled by an inert nitrogen environment (<1 ppm O_2 and H_2O), and samples were only exposed to atmosphere during testing. To minimize degradation in atmosphere during testing, devices were deposited on three substrates simultaneously, so that one of each could be used for testing J-V, EQE, and absorption, respectively. Devices were kept in the glovebox until immediately before testing.

All organic materials were purchased from Luminescence Technology Corp. and deposited with no further purification. SubPc, BCP, and α-NPD (all >99%) and C_{60} (>99.5%) were all sublimed grade. MoO_3 (>99.99%) was purchased from Sigma Aldrich. Aluminum island electrodes were deposited through a shadow mask with a diameter of 1 mm, defining a nominal device area of 0.7865 mm^2, and contacted by a thin gold wire for testing.

J-V data for all devices were recorded using an HP 4156B precision semiconductor parameter analyzer. The cells were illuminated with a Newport solar simulator (model# 91191-1000) calibrated to AM 1.5 (100 mW/cm^2) using an NREL Si reference cell (Model PVM233 KG5). EQE was measured by directing a collimated beam of optically chopped light (185 Hz) from a halogen lamp coupled to a Newport 1/8 m monochromator (5 nm FWHM) incident on the sample. The photocurrent was measured using a Stanford Research Systems SR530 Lock-in Amplifier and compared to the output from a calibrated Si photodiode. Total absorption of

devices was measured using a Perkin Elmer Lambda 750 UV/Vis/NIR spectrometer. IQE was calculated by dividing EQE by experimental absorption at each wavelength. All device areas were measured using a Carl Zeiss Scope A.1 optical microscope and included explicitly in calculating EQE, J_{sc}, and PCE.

PL quantum yield (QY) measurements were taken with a Photon Technology International QuantaMaster spectrofluorometer. Luminescence between 550 and 800 nm was measured in an integrating sphere under 530 nm (<10 nm FWHM) illumination from a Xenon lamp. All AFM measurements were performed on ITO-coated glass substrates using an Asylum Research Labs MFP-3D standalone system in tapping mode. XRD measurements were performed using a Rigaku Rotating Anode X-Ray Diffractometer in θ-2θ geometry with Cu-Kα radiation (wavelength of 1.5418 Å). Sample materials were deposited onto <100> Si. The SubPc control sample for XRD was annealed post-deposition for 15 min at 95 °C to induce crystallization.

3.2.4 Results

We first examine an archetypal SHJ SubPc/C_{60} device deposited on ITO, with MoO_3 implemented as a work function modifier (**Figure 3.7**). The J_{sc} is slightly lower than the highest reported values for the same material system, likely due to variances among labs in material purity and instrument calibration.[145] Because of these variations, a common practice is to fit L_D of each active material to experimental EQE curves. Alternatively, L_D can be treated as a constant material property (when morphology is consistent), allowing EQE fitting to be accomplished by modifying boundary conditions within the device. Using L_D values from literature[48, 49, 150-152] (**Table 3.1**), we note that EQE curves with the best fit to experiment are

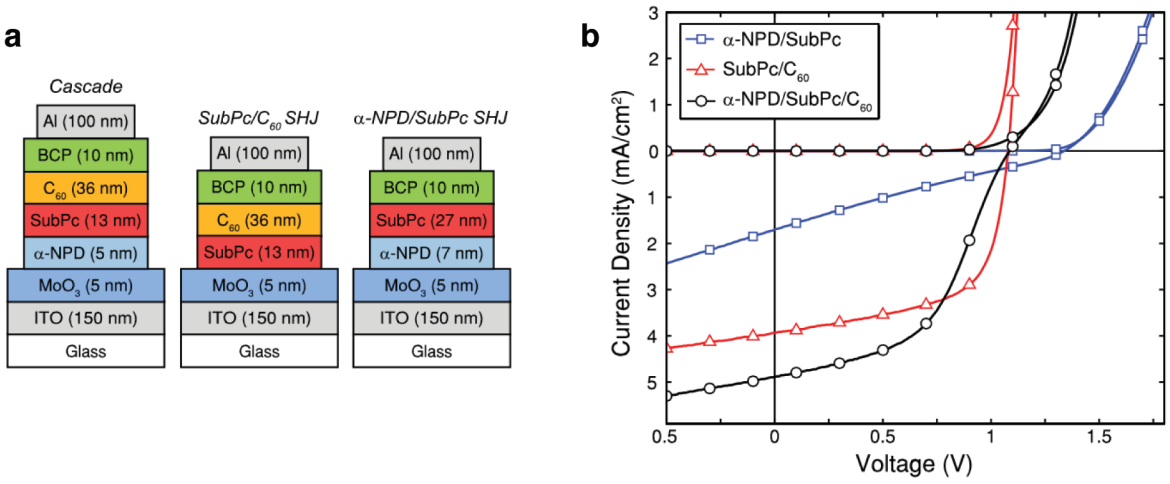

Figure 3.7 (a) Device structures for α-NPD/SubPc/C_{60}, SubPc/C_{60}, and α-NPD/SubPc OPV cells. (b) *J-V* data under 1-sun illumination for α-NPD/SubPc (squares), SubPc/C_{60} (triangles), and α-NPD/SubPc/C_{60} (circles) devices. [46]

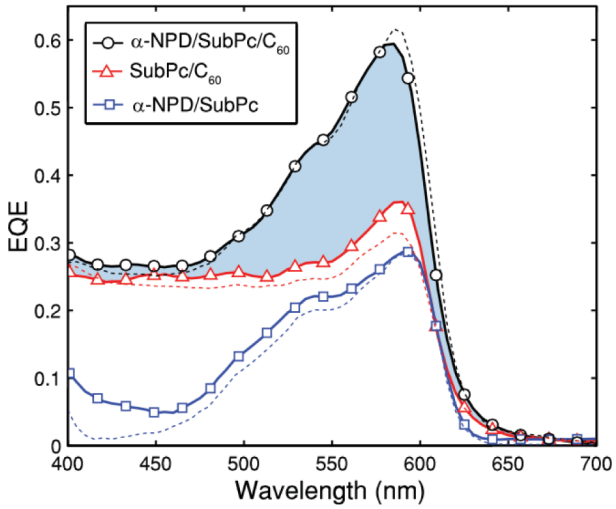

Figure 3.8 For each device in **Figure 3.7**, experimental EQE data (solid lines) are compared to the model (dashed lines). [46]

consistent with exciton quenching at the MoO_3/SubPc interface. The value of L_D = 8.5 nm for SubPc deduced from our fits is consistent across all devices in this study and closely approximates SubPc diffusion lengths measured independently by Luhman *et al.*[48] and Lunt *et al.*[49]

To validate our hypothesis that α-NPD would enable exciton dissociation, we created a SHJ device with α-NPD acting as the donor and SubPc as the acceptor. Previous reports have shown that SubPc can act as an acceptor in SHJ devices or as both a donor and acceptor interlayer in CHJ devices.[136] The α-NPD/SubPc SHJ device (**Figure 3.7**a) exhibits a J_{sc} of 1.72 mA/cm^2, indicating that it indeed enables exciton dissociation and photocurrent generation. The majority of the photocurrent in the device is due to contributions from the SubPc layer, as indicated by the modeled and experimental EQE curves in **Figure 3.8**. Although the HOMO-LUMO gap of the heterojunction is nearly equivalent to that of SubPc/C_{60} (1.8 eV vs. 1.9 eV, respectively), the device exhibits an unusually high V_{oc} of 1.34 V. This V_{oc} seems to indicate a higher k_{d0}/k_r of the CT state, likely due to a different molecular separation distance between SubPc and α-NPD as compared to SubPc and C_{60}.[34]

While SubPc is capable of transporting electrons, devices tested in this study appear to be electron transport-limited. Due to a low electron mobility (compared to hole mobility) in

Table 3.1 Literature and fitted values of exciton lifetimes and diffusion lengths for active materials used in this study. [46]

Material	L_D (Ref.) (nm)	L_D (Fit) (nm)	τ (Ref.) (ns)	τ (Fit) (ns)
SubPc	7.7 [48], 8.0 [49]	8.5	<1 [49]	0.3
C_{60}	11 [151]	14	1.2 [150]	1
α-NPD	5.1 [49]	5	3.5 [152]	5

SubPc,[73] the device exhibits SCL current behavior under forward bias, described by the Mott-Gurney Law.[153] Because both α-NPD and SubPc exhibit high hole mobilities,[154] the device experiences a large drop in R_p due to photoconductivity,[43] resulting in a *FF* of 23.5%. Minority carrier mobility can be especially sensitive to material impurities, and the low electron mobility in our SubPc may be due to differences in impurity concentration from that used by Beaumont *et al.*[155] (Impurities affecting electron conductivity do not necessarily influence exciton diffusion.) The *FF* of this device may be improved either by choosing another acceptor material with higher electron mobility or by improving the electron mobility of SubPc *via* purification, doping, or molecular ordering. We note that when this junction is examined in the MoO_3/α-NPD/SubPc/C_{60} cascade device, the charge transport limitation is partially mitigated by a more favorable electric field profile.

From **Figure 3.8**, it is clear that the addition of the 5 nm α-NPD layer to the SubPc/C_{60} device substantially increases both EQE and J_{sc}. To further probe the transition from quenching

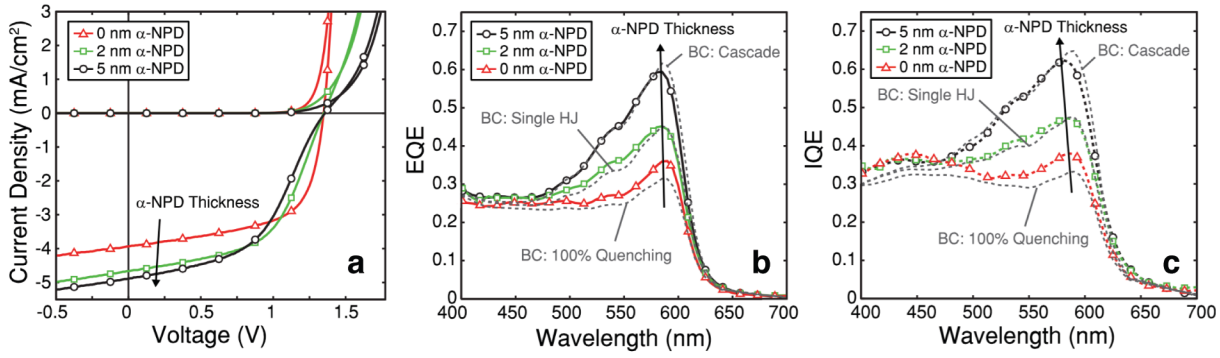

Figure 3.9 Experimentally determined (a) *J-V*, (b) EQE, and (c) IQE data for glass/ITO/MoO_3 (5 nm)/α-NPD (x nm)/SubPc (13 nm)/C_{60} (36 nm)/BCP (10 nm)/Al (100 nm). Three α-NPD thicknesses are shown: 0 nm (triangles), 2 nm (squares), and 5 nm (circles). Modeled EQE and IQE (dotted lines) are shown with three possible boundary conditions at the SubPc/MoO_3 or SubPc/α-NPD interface: 100% quenching, exciton reflection (Single HJ), and 100% dissociation (Cascade). [46]

to exciton dissociation in these structures, we studied CHJ devices with a varying α-NPD EDL thickness from 0 to 5 nm. Because there is minimal optical cavity confinement within the device and the α-NPD layer is located furthest from the reflective cathode, increasing the α-NPD thicknesses from 0-5 nm has a negligible effect on the optical field profile within the active layers. Therefore, all noticeable effects on device performance can be attributed to interfacial properties at the SubPc/α-NPD junction. **Figure 3.9** shows select *J-V* and spectroscopic characteristics of devices as the α-NPD thickness is increased, with each device demonstrating an EQE spectrum corresponding to modeled EQE for one of three boundary conditions at the SubPc/α-NPD or SubPc/MoO_3 interface (quenching, exciton reflection, and exciton dissociation). With increasing α-NPD thickness, there is a notable increase in photocurrent as well as a concomitant decrease in the *FF* due to the Mott-Gurney behavior and low R_p of the α-NPD/SubPc junction under illumination (**Figure 3.10**). Cnops *et al.* see a similar decrease in FF for thick SubPc layers used in CHJ devices, also attributing the drop to low charge carrier mobilities in SubPc.[136] The EQE contribution from the SubPc layer (peak at λ = 585 nm) increases with α-NPD thickness, as seen in **Figure 3.10**a. We observe a reasonable fit for the quenching boundary condition at the SubPc/MoO_3 interface (**Figure 3.9**b). Note that while devices with 2 nm of α-NPD do approximate the modeled EQE with exciton reflection as the boundary condition at the SubPc/α-NPD interface, this would require a sudden and temporary change in the fundamental properties of the materials involved. Instead, it is more likely that at 2 nm, coverage of the electrode by the EDL is incomplete, resulting in only partial exciton dissociation at the α-NPD, offset by parasitic quenching at the MoO_3. The experimental EQE for the 5 nm α-NPD device is much higher than the predicted EQE for a SHJ device, corroborating the functionality of α-NPD as an EDL. If the two heterojunctions in the CHJ structure are

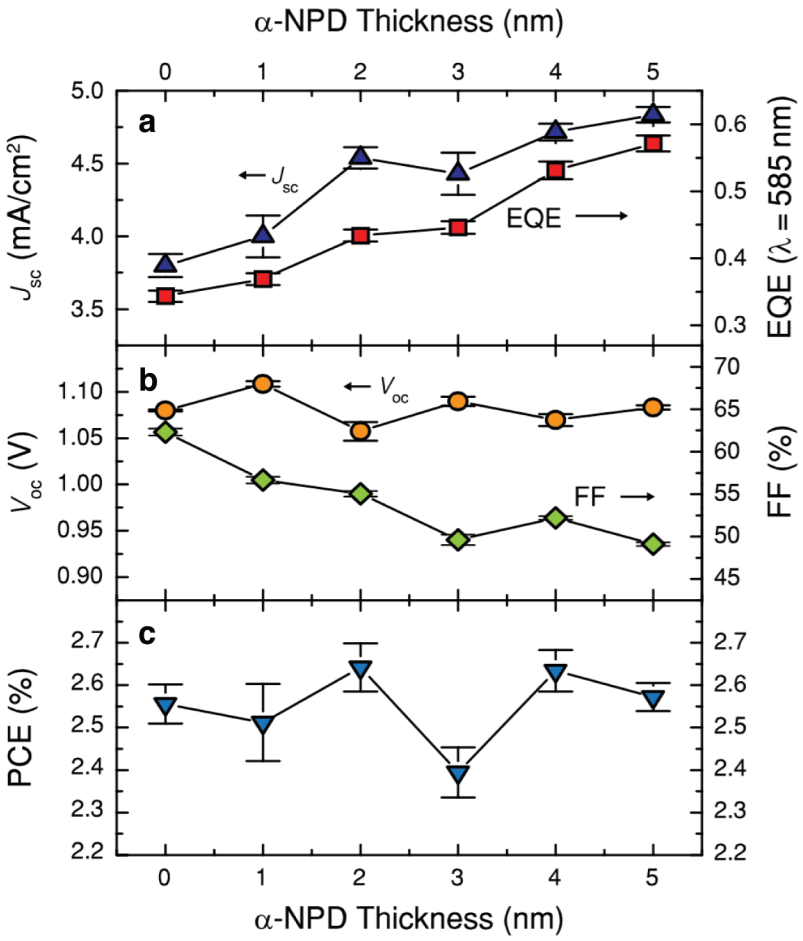

Figure 3.10 Dependence of (a) Jsc, EQE at λ = 585 nm, (b) V_{oc}, *FF*, and (c) PCE on α-NPD layer thickness for a device comprising glass/ITO/MoO_3 (5 nm)/α-NPD (x nm)/SubPc (13 nm)/C_{60} (36 nm)/BCP (10 nm)/Al (100 nm). Error bars represent standard deviations calculated from a sample size of >8 devices. [46]

treated as current-additive in the model, the fit is nearly perfect for the device with 5nm α-NPD. Experimental and modeled IQE plots (**Figure 3.9**c) are well matched, further confirming that the observed increase in J_{sc} is not due to changes in the optical field profiles or additional absorption from α-NPD, but rather from changes in boundary conditions at the SubPc/MoO_3 or SubPc/α-NPD interfaces.

We observe a stable V_{oc} in all devices versus α-NPD thickness (**Figure 3.10**b), in agreement with the assumption that both heterojunctions are operating in parallel, limiting the

V_{oc} to that of the lowest-voltage (SubPc/C_{60}) heterojunction. There is a steady increase in both the J_{sc} and EQE at λ = 585 nm versus α-NPD thickness, consistent with the creation of a conformal layer for exciton dissociation. AFM images of 5 nm MoO_3 on ITO show a root mean squared roughness (R_{rms}) of 3.52 nm (**Figure 3.11**). Therefore, we expect that as the α-NPD layer thickness is increased from 0 to 5 nm, the substrate coverage becomes more complete, resulting in a monotonic increase in photocurrent.

As the thickness of the α-NPD layer is increased, we note that while the average J_{sc} increases at a similar rate to that of the EQE at 585 nm, there is a small "jump" in the J_{sc} that occurs at 2 nm α-NPD. For the device with 2 nm α-NPD, the V_{oc} also decreases. Because there is no visible trend in the V_{oc} of each device from 0 to 5 nm α-NPD, and because *J-V* and EQE tests are performed on different devices and substrates, we assume these deviations to be due to small variations in material purity or work function of the ITO substrate, both of which could influence

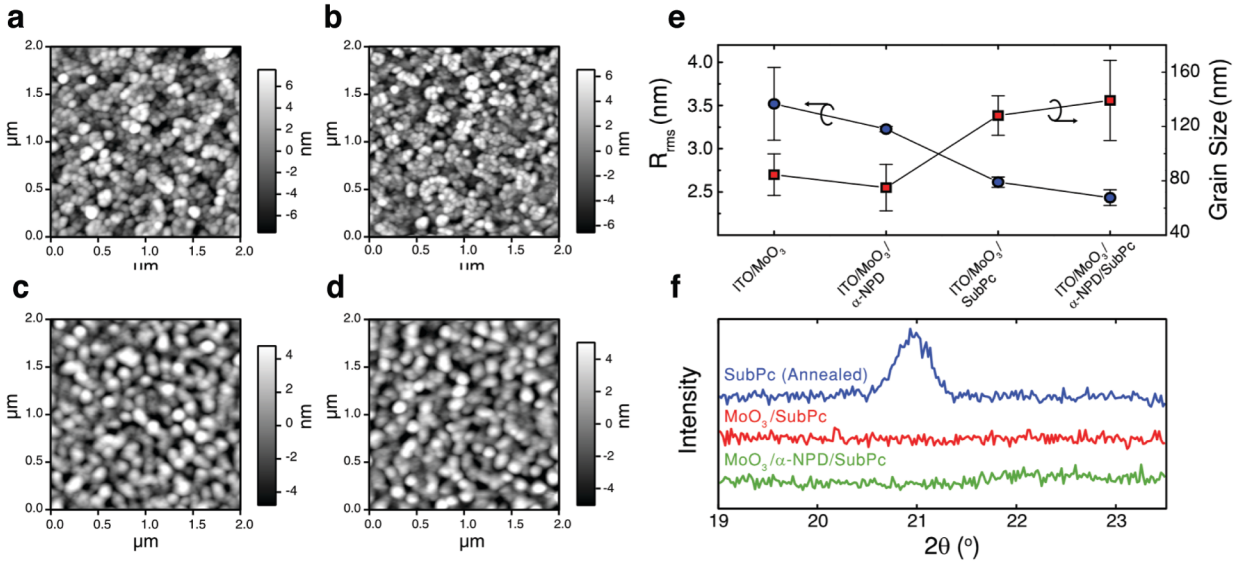

Figure 3.11 AFM images of (a) ITO/MoO_3 (5 nm), (b) ITO/MoO_3 (5 nm)/α-NPD (5 nm), (c) ITO/MoO_3 (5 nm)/SubPc (13 nm), and (d) ITO/MoO_3 (5 nm)/α-NPD (5 nm)/SubPc (13 nm). (e) Grain size and R_{rms} values for each sample and (f) XRD scans of MoO_3 (5 nm)/SubPc (13 nm) and MoO_3 (5 nm)/α-NPD (5 nm)/ SubPc (13 nm), as well as a crystalline control sample of 13 nm SubPc annealed for 15 min at 95 °C. [46]

V_{oc} and J_{sc} (**Table 3.2**).

Atomic force micrographs (**Figure 3.11**) show no discernible change in roughness of the SubPc layer with and without a 5 nm α-NPD spacer layer added. We see little change in the grain size or roughness of the SubPc layer (**Figure 3.11**e) deposited on different surfaces under our experimental conditions. Additionally, XRD shows no sign of induced crystallinity in SubPc, so the increase in EQE cannot be explained by an increase in L_D due to templating in the SubPc layer. This confirms our assumption that changes to the EQE occur from modification of the boundary condition at the α-NPD/SubPc interface.

Table 3.2 Champion solar cell performance data for the structure: Glass/ ITO/MoO3 (5 nm)/α-NPD (x nm)/SubPc (13 nm)/C_{60} (36 nm)/BCP (10 nm)/ Al (100 nm) under simulated 1-sun, AM 1.5G illumination. [46]

α-NPD Thickness (nm)	J_{sc} (mA/cm^2)	V_{oc} (V)	*FF* (%)	PCE (%)
0	3.94	1.08	61.5	2.61
1	4.20	1.10	55.9	2.75
2	4.67	1.08	54.4	2.74
3	4.77	1.08	49.0	2.53
4	4.74	1.08	52.3	2.67
5	4.90	1.09	49.2	2.61
ITO/MoO_3 (5)/α-NPD (7)/ SubPc (27)/BCP (10)/Al (100)	1.72	1.34	23.5	0.54

3.2.5 Conclusions

By introducing the EDL, an additional interface for exciton dissociation was created, resulting in a 66% increase in IQE and EQE of the SubPc layer and a 27% increase in photocurrent of the

device. Because the SHJ α-NPD/SubPc device exhibits a high V_{oc} (1.34 V), the α-NPD/SubPc/C_{60} device is able to maintain the 1.1 V open-circuit voltage of the SubPc/C_{60} system. The observed decrease in *FF* (an inherent problem for CHJ devices with a thick SubPc interlayer) will need to be addressed in future work, likely by choosing a more ambipolar donor material or by improving the electron mobility of SubPc *via* doping and/or molecular ordering.

The EDL in this study is defined such that it improves the overall EQE of the OPV device, but it does so specifically by reducing diffusion losses in the adjacent active layer (i.e., absorption changes in the device are negligible). This makes the EDL-containing device different from energy cascade devices where multiple photon-harvesting layers are used - the EQE of a given device might be improved by adding a third absorbing layer in a CHJ geometry, but the IQE of the outermost absorbing layers will still be lower than if a transparent EDL were inserted between the electrode and outermost active layer. Furthermore, the EDL concept is not limited to the α-NPD/SubPc/C_{60} system, nor is it limited to the anode side of the device - adding an EDL to any planar OPV cell will substantially increase its IQE by preventing quenching at the electrode and reducing bulk recombination. The use of the CHJ architecture promises to be a viable alternative approach to BHJs for circumventing the trade-off between exciton diffusion and optical absorption efficiencies in OPV active layers.

3.3 High fill factor cascade heterojunctions

3.3.1 Introduction

Having demonstrated the ability of the EDL to increase both diffusion efficiency and IQE, we now focus on improving the overall PCE output of devices employing an EDL (and cascade

heterojunction devices in general). For clarity, we first define some new terminology to describe CHJ architecture.

In the simplest case, a planar CHJ employs a three-layer architecture consisting of a donor/interlayer/acceptor stack: the interlayer is sandwiched between two heterojunctions, enabling exciton dissociation on both the donor and acceptor sides, thereby reducing the distance excitons must travel before dissociating. This reduced diffusion distance can substantially increase the IQE of the interlayer, resulting in a higher EQE and overall device J_{sc}. Compared to BHJs, planar devices can offer nearly 100% η_{CC}, more straightforward optimization of optical absorption, and more refined control over individual layer morphologies.[156] Due to the nature of CHJ device design, it is also possible to broaden spectral coverage by using three (or more) active layers with absorption peaks in non-overlapping regions of the spectrum, providing an alternative or complementary approach to series tandem configurations. However, efficient charge collection in CHJs does not automatically translate to a high FF.[46, 136]

Here we perform an extensive, highly systematic study of the EDL/interlayer/acceptor system to probe the underlying mechanisms that cause low FF in CHJ devices. By definition, the FF is a simple way of relating J_{sc} and V_{oc} to the maximum power point:

$$FF = \frac{V_{MPP} J_{MPP}}{V_{oc} J_{sc}} \tag{3.1}$$

where V_{MPP} and J_{MPP} are the voltage and current at the MPP, respectively. However, while FF can be a useful metric for describing device performance, it can be imprecise or misleading if both J_{sc} and V_{oc} vary between the devices under consideration. We instead focus on the MPP for comparisons between devices with the understanding that if V_{MPP} and J_{MPP} are maximized, then FF and PCE will also be maximized.

We begin by evaluating the charge buildup in CHJs as a function of built-in field, and show a direct correlation between V_{MPP} reduction, s-kink formation, and field inversion in the interlayer. We then perform a combinatorial study using 12 different EDLs coupled with SubPc or boron subnaphthalocyanine chloride (SubNc) as interlayers and use C_{60} as the acceptor. We demonstrate that the two active heterojunctions (which we term "subjunctions") in the CHJ operate electrically in parallel,[46] with the maximum possible V_{MPP} of the CHJ limited by the lowest V_{MPP} of the two subjunctions. We then show that space charge accumulation from field inversion further reduces V_{MPP} of a CHJ and is dependent on the energy offset between the HOMO levels (ΔE_{HOMO}) of the EDL and interlayer. Finally we introduce general design principles for engineering CHJs with both high FF and enhanced PCE over single junctions, and demonstrate champion devices with up to 46% improvement in PCE and nearly 100% IQE in the interlayer with the introduction of a transparent EDL.

3.3.2 Experiment

HOMO levels for all interlayer and EDL materials were measured *via* cyclic voltammetry. Each material was dropcast from chloroform onto a 3 mm diameter glassy carbon working electrode. Using 0.1 M tetrabutylammonium hexafluorophosphate in acetonitrile as an electrolyte, samples were scanned at a rate of 0.1 V s^{-1} relative to an $Ag/AgNO_3$ reference electrode with a Pt wire counter electrode. Scans were normalized to the onset of oxidation of ferrocene, taken as -4.8 eV. The bandgap was estimated from the onset of absorption, and the LUMO level was calculated by adding the bandgap to the HOMO level.

Devices were deposited on commercially available ITO (Delta Technologies, 150 nm thick, R_s<15 Ω/□). Substrates were cleaned *via* heated (40°C) sonication in detergent, water,

acetone, trichloroethylene, and isopropanol, followed by boiling in isopropanol and 10 minutes of ultraviolet/ozone treatment to remove carbon residues and increase the anode work function. Device layers were deposited through VTE using an Ångstrom AMOD deposition chamber. Fabrication and *J-V* testing was performed in a glovebox filled with an inert nitrogen environment (<1 ppm O_2 and H_2O). To minimize degradation in atmosphere during testing, devices were simultaneously deposited on three substrates, so that one of each could be used for testing *J-V*, EQE, and absorption. Only samples for EQE and absorption measurements were exposed to atmosphere. For EQE and *J-V* testing, aluminum island electrodes were deposited through a shadow mask with a diameter of 1 mm. All device areas were measured using a Carl Zeiss Scope A.1 optical microscope and included explicitly in calculating J_{sc}, EQE, IQE, and PCE. All organic materials were purchased from Luminescence Technology Corp. and deposited with no further purification. SubPc, SubNc, BCP, and all EDL materials (>99%) and C_{60} (>99.5%) were sublimed grade. MoO_3 (>99.99%) was purchased from Sigma Aldrich and Al (99.9%) was purchased from Alfa Aesar.

Device *J-V* data were recorded using an HP 4156B precision semiconductor parameter analyzer. The cells were illuminated with a Newport solar simulator (model# 91191-1000) calibrated to AM 1.5G (100 mW/cm^2) using an NREL Si reference cell (Model PVM233 KG5). Impedance spectra were measured using a 10 mV AC voltage applied at 100 Hz over a swept DC bias with a Solartron Modulab 2100A under both dark and illumination. EQE was measured by directing a collimated beam of optically chopped light (185 Hz) from a halogen lamp coupled to a Newport 1/8m monochromator (5 nm FWHM) incident on the sample. The photocurrent was measured using a Stanford Research Systems SR530 Lock-in Amplifier and compared to the output from a calibrated Si photodiode. The spectrum of the solar simulator was measured with

an Ocean Optics USB2000 spectrometer and convoluted with the experimental EQE to determine the spectral mismatch factor for each device with respect to the AM1.5G spectrum (All mismatch factors were determined to be 1 ± 0.05).[157] Absorption in the completed devices was measured in reflection mode using a Perkin Elmer Lambda 750 UV/Vis/NIR spectrometer at an incidence angle of 7.5°. The absorption spectrum for each device was then compared to a transfer matrix optical model to confirm device layer thicknesses. IQE was calculated by dividing experimental EQE by modeled active layer absorption at each wavelength at normal incidence.

The thicknesses and optical properties of all materials were measured using a variable angle spectroscopic ellipsometer (M-2000, J.A. Woollam Co.). Measurements were performed in both transmission mode and reflection mode at angles of 55°, 65°, and 75° for each of the materials on a glass substrate. The film thickness and surface roughness were first determined by fitting the acquired ellipsometric angles Δ and Ψ to a Cauchy model over the wavelength range in which the material is transparent. The refractive index values were then determined by fixing the film thickness as well as surface roughness and parameterizing the material as a B-Spline layer. The wavelength range was gradually increased, in increments of 0.1 eV, until it included the entire measured spectral range. The resultant values were then verified to be Kramers-Kronig (KK) consistent.

For hole mobility measurements, samples were fabricated with the structure ITO/PEIE(10 nm)/EDL(800 nm)/Au(80 nm). PEIE (0.4 wt% in methoxyethanol) was spin-coated at 5000 rpm for 60 s and subsequently baked at 100°C for 10 minutes prior to VTE deposition of the EDL at 1 Å/s. Circular gold contacts were deposited at 1 Å/s and defined by a shadow mask. Time-of-flight measurements were performed using a nitrogen laser (VSL337

from Newport) with a wavelength of λ = 337.1 nm, an intensity per pulse of ~120 μJ, and a pulse duration less than 4 ns, for photo-generation of charge carriers in the films (illuminated through the ITO substrate). A Keithley 2400 SourceMeter was used to apply constant voltage over devices, with the ITO cathode under positive bias to prevent charge injection. The current transients were then amplified using a FEMTO DLPCA-200 low noise current amplifier and recorded with a Tektronix TDS3052C digital oscilloscope.

3.3.3 Space charge accumulation and field inversion

There are two common sources of space charge accumulation in OPVs: charge accumulation due to poor (non-Ohmic) electrode injection, and space charge accumulation at organic-organic interfaces.[158-160] To rule out contact effects at the electrode as a source of the observed s-kink behavior in CHJs, we begin by considering the capacitance of a SHJ with different workfunction anodes:

Anode/SubPc (11)/C_{60} (27)/BCP (10)/Al (100)

Where the anode was either untreated ITO or UV-ozoned ITO with a 5 nm MoO_x buffer layer. For the bare ITO devices, the anode surface was left untreated (no UV-ozone) to maintain its workfunction at 4.3 eV, which is identical to that of the Al cathode. Thus the built-in field should be negligible, assuming no strong interfacial dipoles exist at the electrode/organic contacts.

Device capacitance was measured through impedance spectroscopy in the dark and under AM 1.5G illumination. As can be seen in **Figure 3.12**a, we observe very different performance between the two electrodes. For the ITO/MoO_x devices, a typical capacitance-voltage (*C*-*V*) is obtained where *C* is fixed at the geometrical capacitance (C_g) until high forward-bias, at which point injected charge accumulation in the active layers with increasing quasi-Fermi level offset

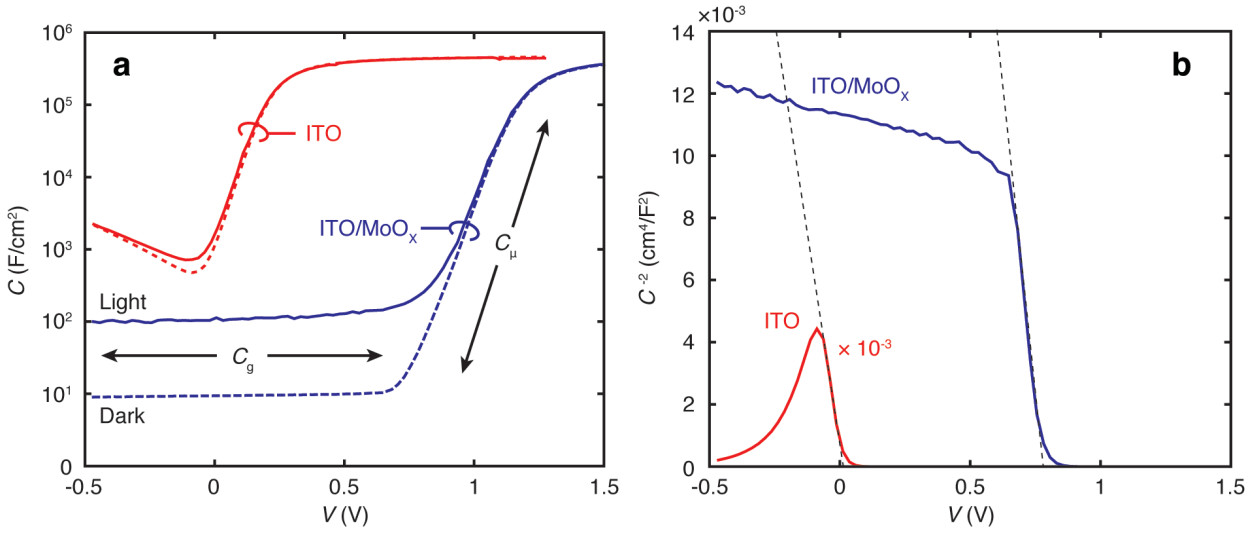

Figure 3.12 (a) *C*-*V* curves of a SHJ device with (blue) and without (red) charge selective contacts. Solid lines indicate scans taken under illumination. In the ITO/MoO_x device, a clear transition is observed between the geometric (C_g) and chemical capacitance (C_μ) regimes. (b) Mott-Shottky plots for both devices as measured in the dark. Extrapolation of the linear regions to zero provides a measure of the V_{bi} within devices.

causes the chemical capacitance (C_μ) to increase exponentially.[161] In contrast, the untreated ITO devices exhibit an asymmetrical C_μ under both forward- and reverse-bias. This indicates the anode is not charge-selective; it injects electrons into the adjacent SubPc layer effectively even at low reverse bias. Furthermore as there is negligible V_{bi} between the two electrodes, the applied field is not opposed by an internal field (**Figure 1.21**), and the onset of C_μ occurs close to zero bias. As a result, the C_g is not observable in the bare ITO devices.

By fitting the linear portion of the Mott-Shottky curves (C^{-2}-V) in the dark (**Figure 3.12**b) it is possible to extract the V_{bi} for each device from the x-intercept.[162] As anticipated, the untreated ITO devices exhibit a low V_{bi} of 0.021 ± 0.002 V, while the inclusion of UV-ozone treatment and a MoO_x buffer increase this value to 0.780 ± 0.007 V. Although there is a negligible built-in field and the devices exhibit poor charge selectivity, this does not create an s-kink or a non-Ohmic contact to the SubPc layer. As a result, a high *FF* is maintained between

both device sets, with the untreated anode producing a lower V_{oc} and V_{MPP} but similar J_{sc} (**Figure 3.13**a).

Unlike the SHJ devices however, a markedly different *J-V* behavior is observed using a CHJ architecture (**Figure 3.13**b). Devices with the structure:

Anode/TPTPA (5)/DBP (10)/SubPc (13)/C_{60} (30)/BCP (10)/Al (100)

were fabricated, with DBP acting as a donor for the SubPc interlayer. A range of UV-ozone treatment times (0 s, 30s, 1 min, 2 min, 10 min) were used to vary the bare ITO workfunction, while MoO_x and PEDOT:PSS were also used as high-workfunction buffer layers. UV-ozone treatment has been previously shown to increase the oxygen termination of the In atoms at the ITO surface and remove adsorbed carbon residue, yielding an increase in workfunction up to 4.9 eV.[163-165] In the CHJ structure, decreasing V_{bi} has little effect on the V_{oc} output of the cells. Instead, the V_{MPP} appears to decrease along with V_{bi} as photocurrent production is progressively shut off at lower bias. Also dissimilar from the SHJs tested, a large V_{bi} of 0.603 ± 0.084 V is produced from devices with untreated ITO (**Figure 3.14**b), and charge selectivity appears to be maintained. This is likely due to the formation of a strong interfacial dipole at the ITO/TPTPA interface, increasing the Fermi level at the anode. Most importantly, we observe the formation of two distinct capacitance peaks in CHJ devices at voltages below the onset of C_{μ} (**Figure 3.14**a). These peaks are produced only under illumination; in the dark, the *C-V* curves saturate at the C_g value in the same voltage range. To the best of our knowledge, this behavior is unique to CHJs and is indicative of the internal processes occurring within the device. We ascribe the two peaks, which we fit to Gaussian distributions, to photocurrent-supplied space charge accumulation at the two subjunctions. As has been modeled in detail previously,[160] the introduction of an energetic barrier to charge injection (e.g. ΔE_{HOMO} at the donor/interlayer interface) can produce

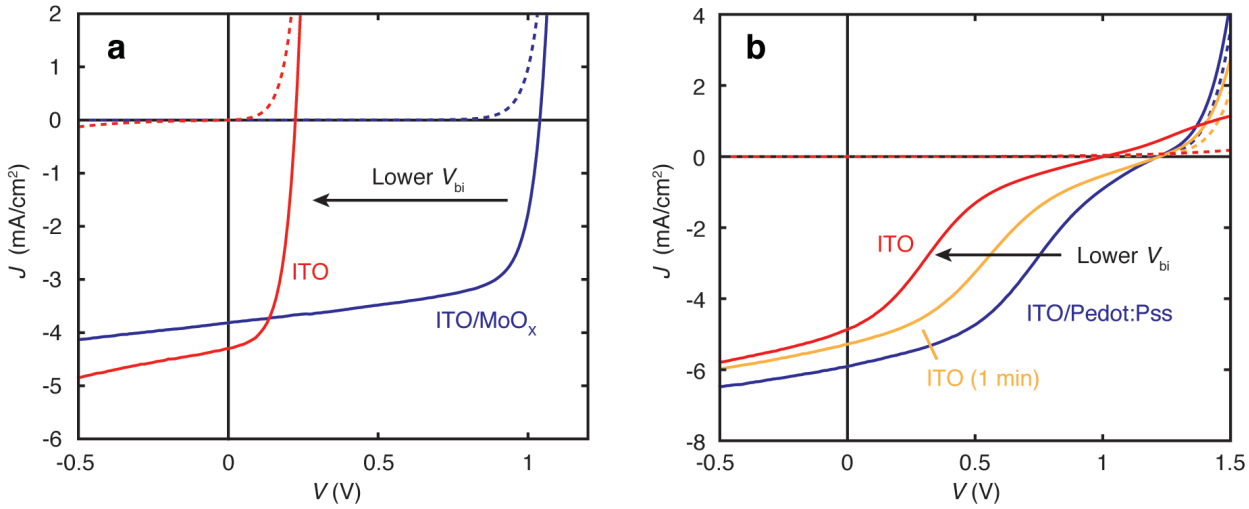

Figure 3.13 Current density-voltage curves of (a) SHJ devices and (b) CHJ devices with varying anode treatments. In the SHJ devices, V_{bi} is shown to predominantly affect the V_{oc}, while the V_{mpp} is most affected in the CHJ architecture.

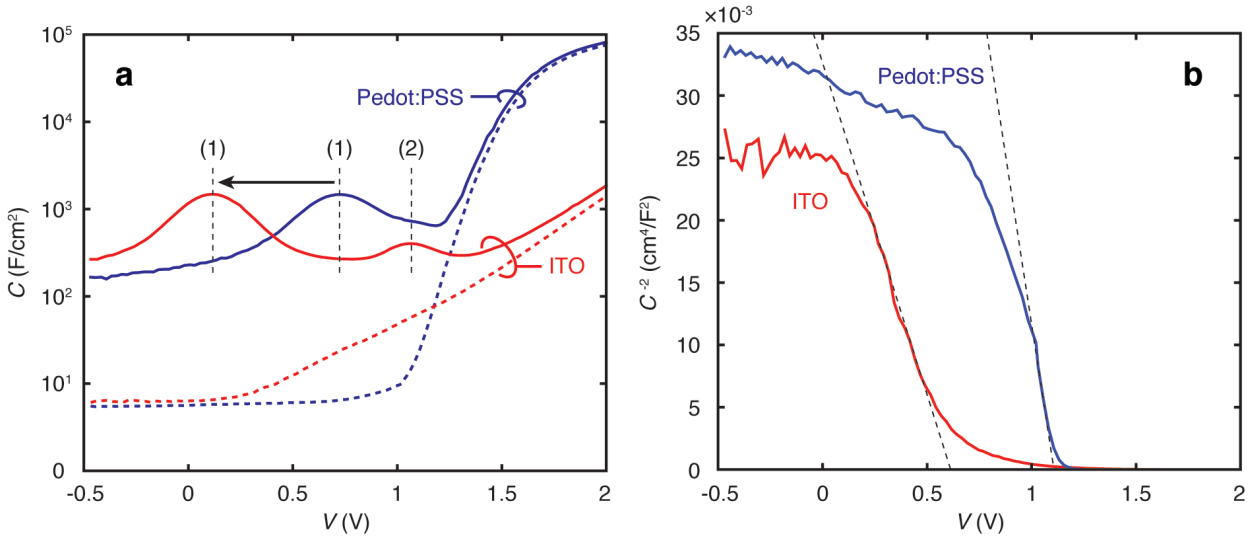

Figure 3.14 (a) *C-V* curves of CHJ devices with high (blue) and low (red) V_{bi} provided by the anode. In both cases, two additional capacitance peaks are observed under illumination (solid lines), which we attribute to space charge buildup at the two subjunctions. (b) Mott-Shottky plots for both devices under dark conditions.

field inversion in the interlayer at biases below V_{bi} (**Figure 3.15**). The lower field at the two heterojunctions then causes a premature shutdown of the CT dissociation process. This field inversion is not anticipated to be symmetric about the two subjunctions, hence we expect one to be more sensitive than the other, depending on active layer properties such as charge mobility and the value of ΔE_{HOMO} itself.[46] Furthermore, as the V_{bi} of the contacts determines the internal field at zero bias, any reduction in V_{bi} serves to reduce the applied bias at which field inversion will occur.

Indeed, we observe the first peak to be highly sensitive to the V_{bi} over the entire range tested (**Figure 3.16**). As this correlates to the voltage range where the majority of photocurrent is suppressed, and the SubPc/C_{60} subjunction is responsible for most of the photocurrent production (as confirmed through modeling), we attribute this peak to charge accumulation at the SubPc/C_{60} interface. The second peak at $V \sim 1.1$ V is attributed to the DBP/SubPc subjunction, whose current output appears to be less sensitive to the magnitude of the built-in field. The FWHM and height of the two peaks appear independent of the V_{bi}, further indicating this phenomenon is not due to the C_{μ} of injected charge carriers. While this behavior does not appear to manifest in SHJdevices (**Figure 3.12**), we expect it does occur at higher biases. However, in most cases it appears the range at which junction capacitance should contribute in SHJ devices is masked within the C_{μ} regime. Through a combination of field inversion and a suppressed dark current characteristic of CHJ devices,[89] junction capacitance peaks are observable in the materials system studied here. For additional reference, the complete list of parameters measured for SHJ and CHJ devices can be found in **Table 3.3**.

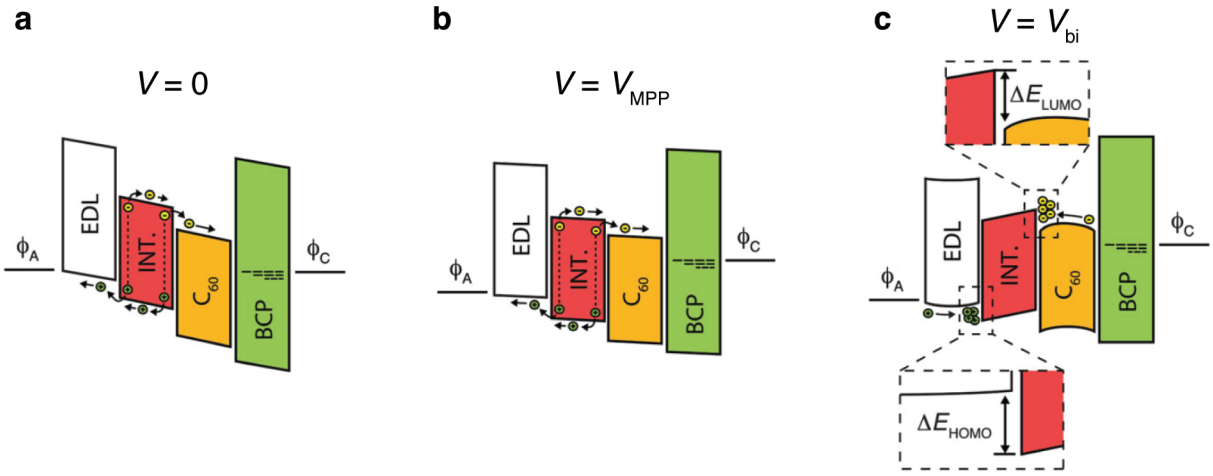

Figure 3.15 Schematic band diagrams of (a) CT dissociation in a CHJ at short-circuit conditions ($V = 0$), (b) at V_{MPP}, where flat-band conditions have not been met, and (c) field inversion at V_{bi} due to the introduced hole-injection barrier with energy ΔE_{HOMO}. [89]

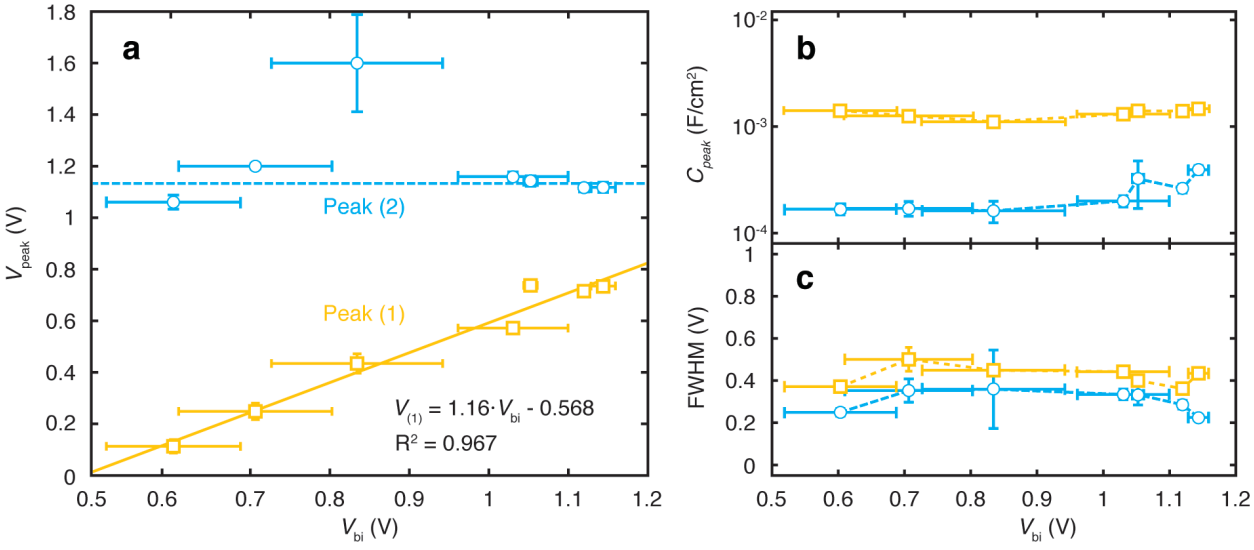

Figure 3.16 (a) Location of the capacitance peaks corresponding to space charge accumulation at the (1) SubPc/C_{60} and (2) DBP/SubPc subjunctions as a function of V_{bi}. A linear dependence is fit to the first peak voltage ($V_{(1)}$) with high confidence, while the second peak voltage remains constant (the third data point is an outlier). No appreciable V_{bi}-dependence is observed in the (b) magnitude or (c) FWHM of the two subjunction capacitance peaks.

Table 3.3 Solar cell parameters extracted from *C-V* and *J-V* measurements of both SHJ and CHJ devices with varying anode surface treatments. Nominally 6 or more devices were measured per sample (data in parentheses are standard deviations).

Anode	V_{bi} (V)	V_{MPP} (V)	V_{oc} (V)	J_{sc} (mAcm^{-2})	FF (%)	PCE (%)
SHJs						
ITO	0.021 (0.002)	0.149 (0.009)	0.210 (0.013)	4.258 (0.082)	54.25 (1.12)	0.487 (0.049)
ITO/MoOx	0.780 (0.007)	0.884 (0.005)	1.039 (0.003)	3.804 (0.038)	67.46 (0.20)	2.667 (0.033)
CHJs						
ITO	0.603 (0.084)	0.308 (0.048)	0.979 (0.081)	4.881 (0.309)	18.87 (2.41)	0.919 (0.251)
ITO (30 s)	0.706 (0.096)	0.406 (0.029)	1.142 (0.040)	5.349 (0.239)	22.83 (1.57)	1.402 (0.199)
ITO (1 min)	0.834 (0.108)	0.460 (0.035)	1.204 (0.016)	5.293 (0.195)	25.63 (2.46)	1.638 (0.222)
ITO (2 min)	1.052 (0.008)	0.587 (0.005)	1.189 (0.020)	5.853 (0.096)	35.02 (0.62)	2.436 (0.035)
ITO (10 min)	1.030 (0.069)	0.551 (0.029)	1.221 (0.009)	5.636 (0.124)	31.84 (2.02)	2.192 (0.178)
ITO/MoOx	1.120 (0.006)	0.573 (0.005)	1.200 (0.002)	5.417 (0.088)	34.21 (0.25)	2.224 (0.033)
ITO/PEDOT:PSS	1.144 (0.015)	0.591 (0.006)	1.217 (0.004)	5.894 (0.053)	34.48 (0.33)	2.473 (0.016)

3.3.4 Material selection and device design

Having demonstrated the origin of V_{MPP} loss in devices, we now take a combinatorial approach to finding empirical design criteria to mitigate PCE loss in CHJs. Twelve different triphenylamine derivatives are used in this study as EDLs, selected based on their high hole mobilities, transparency in the visible spectrum, and HOMO levels varying from ~4.9 eV to ~5.5 eV. **Figure 3.17** depicts a schematic energy level diagram and the molecular structure for all materials used.[146-148] In **Figure 3.18** we show the absorption coefficients for each material, with

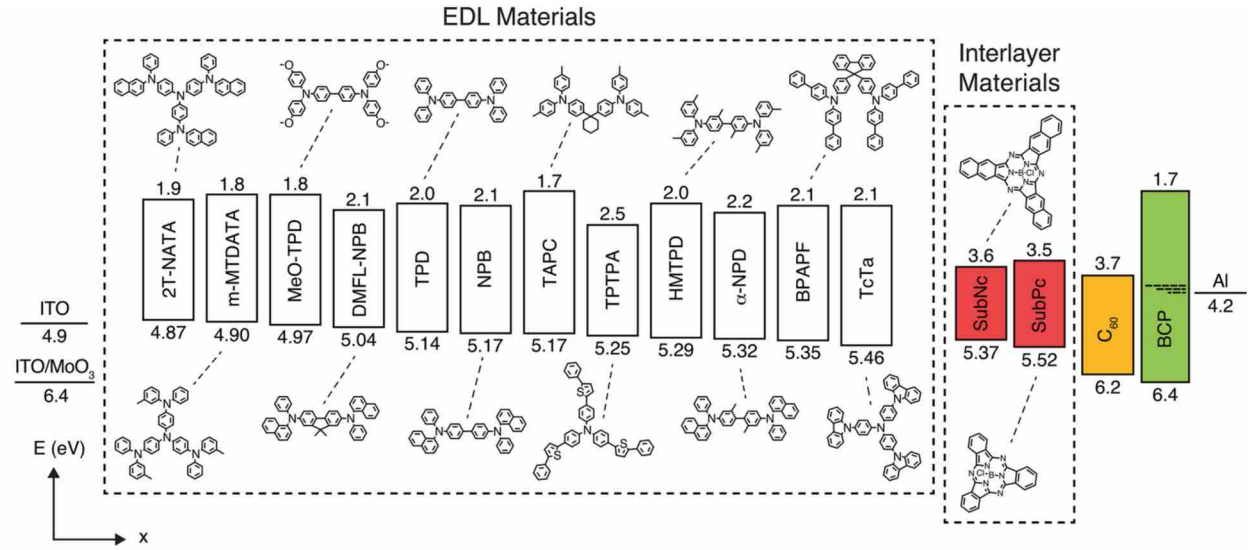

Figure 3.17 Energy levels and molecular structures for all materials used in the combinatorial study. HOMO levels of EDL and interlayer materials were measured using cylic voltammetry, and bandgap energies were estimated from the absorption onset. The prospective EDL materials were chosen such that their HOMO levels ranged semicontinously from approximately 4.9 eV to 5.5 eV. The two interlayers were chosen based on their differences in V_{MPP} when in SHJ configurations with C_{60}. [89]

only the interlayers and C_{60} acceptor having absorption peaks in the visible spectral region. The two interlayer materials were chosen primarily due to their different characteristic V_{MPP} when paired with C_{60} in a SHJ configuration. As demonstrated below, the EDL/interlayer V_{MPP} often limits the CHJ V_{MPP}, so choosing a reference SHJ with a lower V_{MPP} can help match the V_{MPP} between the EDL/interlayer and interlayer/C_{60} subjunctions.

To correlate trends in performance to charge transport, we used the time-of-flight method to measure the hole mobility of select EDL materials (**Figure 3.19**a). The remaining mobilities were taken from time-of-flight measurements reported in literature.[166-169] In **Figure 3.19**b, we plot the room-temperature zero-field hole mobilities (Equation (1.1)) of each EDL material versus its HOMO level energy; from this plot, there is a clear trend between μ_{h0} and the HOMO level. To the best of our knowledge, this is the first study to show such a correlation. We hypothesize it arises from dependence of both HOMO levels and mobility on the phonon modes and charge delocalization of the molecular orbitals. This is an important observation, as we must

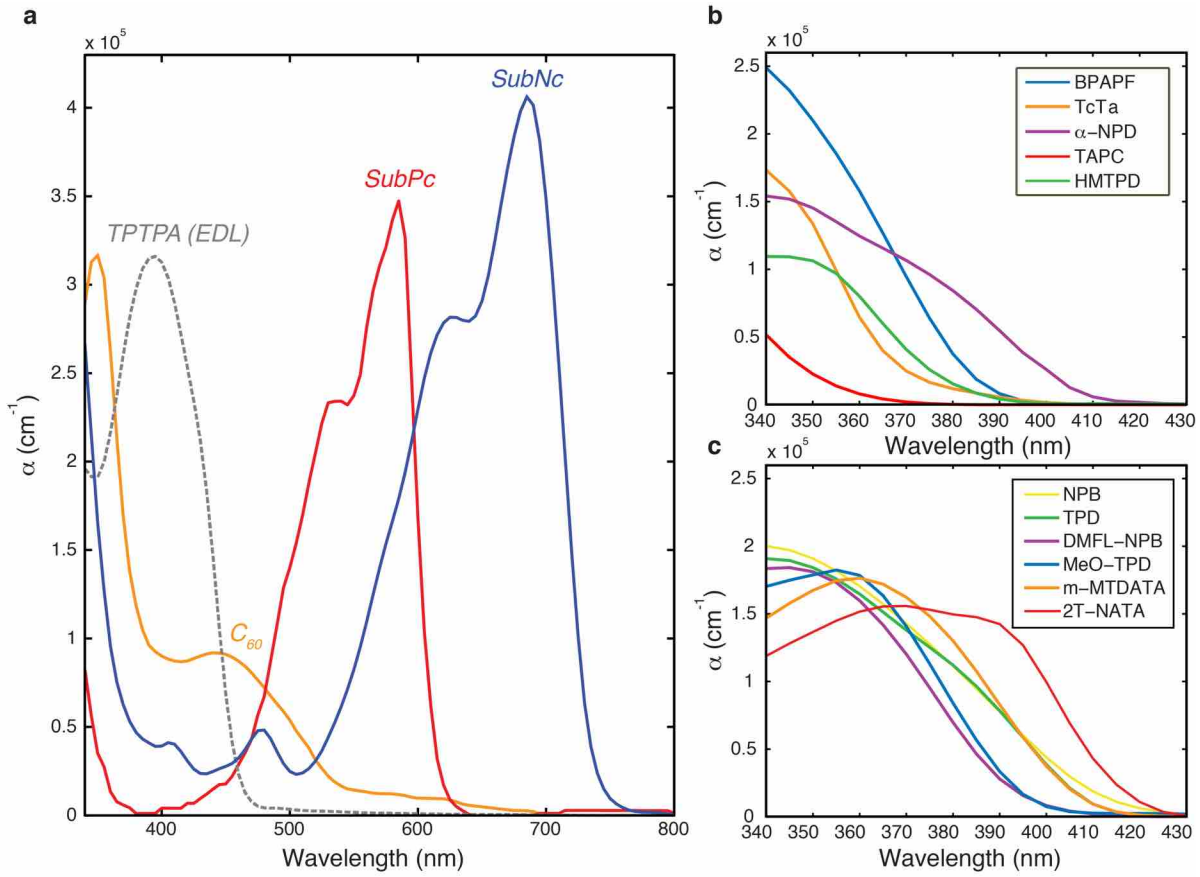

Figure 3.18 Absorption coefficients for the active materials used in the combinatorial study, corresponding to (a) the absorbing acceptor and interlayers molecules and (b,c) the transparent EDL molecules as determined by spectroscopic ellipsometry. [89]

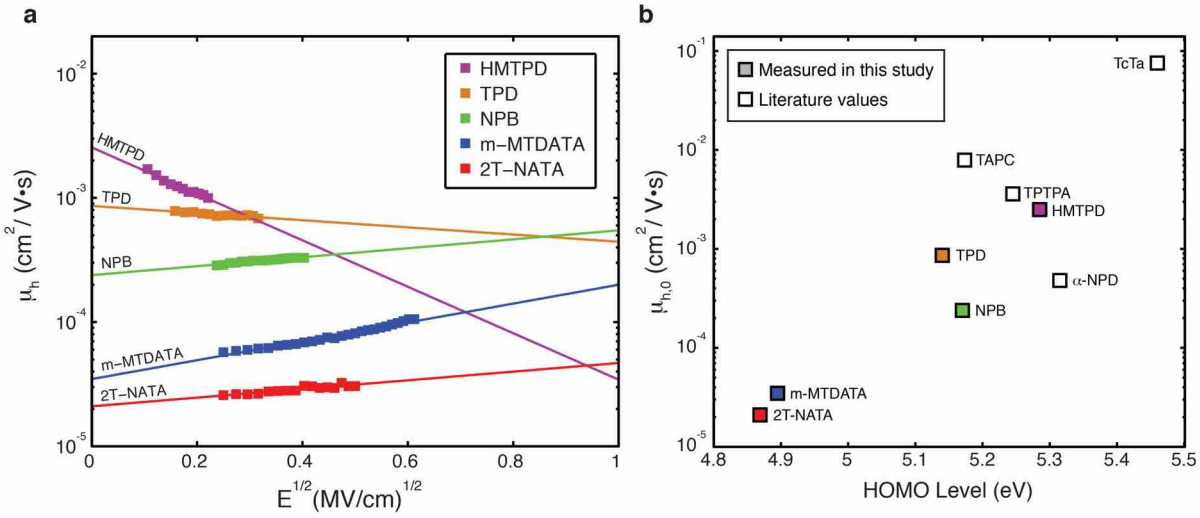

Figure 3.19 (a) Field-dependence of hole mobilities for select EDLs, fit to the Poole-Frenkel relation (Equation (1.1)). (b) Comparison of the zero-field mobilities to HOMO level, with colored squares indicating measured values and empty squares taken from the (time of flight) literature. [89]

confirm that trends correlating V_{MPP} changes to ΔE_{HOMO} do not, in fact, erroneously arise from mobility variations. For further reference, HOMO levels and mobility parameters are provided in **Table 3.4**.

MoO_3 was used as an anode buffer layer in all SHJ and CHJ devices employing SubPc as an active layer. While MoO_3 quenches excitons in SubPc and other common OPV materials, its high work function is necessary for sustaining the ~1.1 V open-circuit voltage of SubPc/C_{60} devices (**Figure 3.13**a). Moreover, MoO_3 causes virtually no changes to the optical field profiles within the device, unlike other commonly used buffer layers such as PEDOT:PSS.[170] Because MoO_3 is not required for the lower V_{oc} (~0.8 V) of SubNc/C_{60} devices, it was not used in any devices employing a SubNc/C_{60} heterojunction. However, MoO_3 was used for all EDL/SubNc SHJ devices. The choice of high workfunction contacts ensures the devices are not V_{bi}-limited (Section 3.3.3), hence all following trends in device performance are shown to be independent of the anode.

Table 3.4 Mobility parameters for all EDL materials, as determined by time-of-flight measurements. Mobility values taken from literature are noted. All other mobility values and HOMO levels were measured in this study. [89]

Material	HOMO Level (eV)	μ_{h0} ($cm^2\ V^{-1}\ s^{-1}$)	γ $(cm\ V^{-1})^{1/2}$	Source
TcTa	5.46	7.56E-02	5.62E-04	[169]
BPAPF	5.35	-	-	-
α-NPD	5.32	4.80E-04	5.30E-04	[167]
HMTPD	5.29	2.50E-03	-4.30E-03	This work
TPTPA	5.25	3.60E-03	2.90E-03	[168]
TAPC	5.17	7.90E-03	8.81E-04	[166]
NPB	5.17	2.39E-04	8.30E-04	This work
TPD	5.14	8.622E-04	-6.632E-04	This work
DMFL-NPB	5.04	-	-	-
MeO-TPD	4.97	-	-	-
m-MTDATA	4.90	3.478E-05	1.700E-03	This work
2T-NATA	4.87	2.100E-05	8.028E-04	This work

3.3.5 Single heterojunction performance

Considering the subjunctions of a CHJ act electrically in parallel (current-additive),[46] we now investigate how this impacts their *J–V* characteristics. In series-connected tandem structures, the J_{MPP} of the complete device will be limited by the lowest J_{MPP} of its subcells following Kirchoff's law.[171] Analogously, the V_{MPP} of a CHJ device will be limited by the lowest V_{MPP} of its constituent, electrically-parallel subjunctions. Due to CHJ device geometry, it is difficult to measure the V_{MPP} of each subjunction *in situ*. However, it is instead possible to estimate the V_{MPP} of each subjunction by measuring their *J–V* characteristics in separate SHJ configurations. These concepts are illustrated in **Figure 3.20**a, where equivalent circuit diagrams are provided for each SHJ device and the CHJ device comprised of the two corresponding subjunctions. Experimental *J–V* curves for a CHJ (TAPC/SubPc/C_{60}) and its corresponding SHJs are shown in **Figure 3.20**b, with a star marking the maximum power point for each device. From this plot, we can see that the V_{MPP} of the EDL/interlayer subjunction will limit the theoretical maximum V_{MPP} of the CHJ device. However, due to field inversion and space charge accumulation (**Figure 3.15**), the CHJ is often lower than predicted. Measured parameters for all SHJs and CHJs tested in this study can be found in **Table 3.5** and **Table 3.6** for devices employing SubPc and SubNc, respectively.

To provide an estimate for their subjunction performance in a CHJ, reference SHJ devices were fabricated with the following structures:

ITO/MoO_3 (5)/EDL (10)/SubPc or SubNc (30)/ BCP (10)/Al (100)

ITO/MoO_3 (5)/SubPc (13)/C_{60} (36)/BCP (10)/Al (100)

ITO/SubNc (8.5)/C_{60} (36)/BCP (10)/Al (100)

We find that charge transfer occurs for EDL/interlayer interfaces with ΔE_{HOMO} as low as 0.02 eV. Some may find this result surprising, as it was assumed for many years that the energy level

offset at the heterojunction provides an energetic driving force for charge transfer, and offset values of E_g - ΔE_{HL} > 0.3 were assumed necessary.[172] However, in light of recent developments indicating CT formation is entropically-driven, this constraint is not a requirement.[35, 173] Furthermore, the ΔE_{HOMO} values reported here serve only as an estimate, as the HOMO levels measured are bulk values, and interfacial dipole formation at the heterojunction may increase their offset. Our results are supported by other recent findings that materials exhibiting E_g - ΔE_{HL} values as low as 0.06 eV are sufficient to drive CT formation and function as heterojunctions.[174] All EDL/interlayer SHJs tested exhibit high J_{sc} values (over 1.5 mA/cm^2), consistent with model

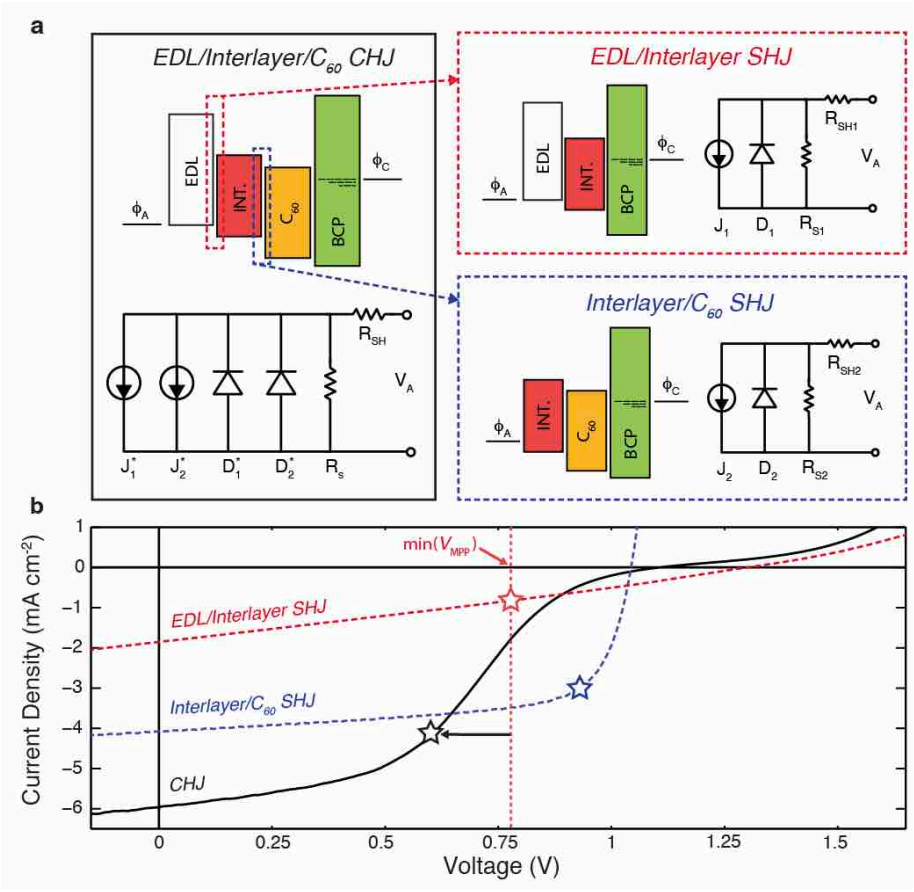

Figure 3.20 (a) Schematic energy level and circuit diagrams for CHJ devices. The characteristic performance of each subjunction can be estimated by considering the *J–V* curves of corresponding SHJ devices. (b) Characteristic experimental *J–V* curves of an EDL/interlayer SHJ, an interlayer/C_{60} SHJ, and an EDL/interlayer/C_{60} CHJ. The MPP for each device is marked by a star. From the two SHJs, it is clear the V_{MPP} of the EDL/interlayer will limit the maximum V_{MPP} of the CHJ device. [89]

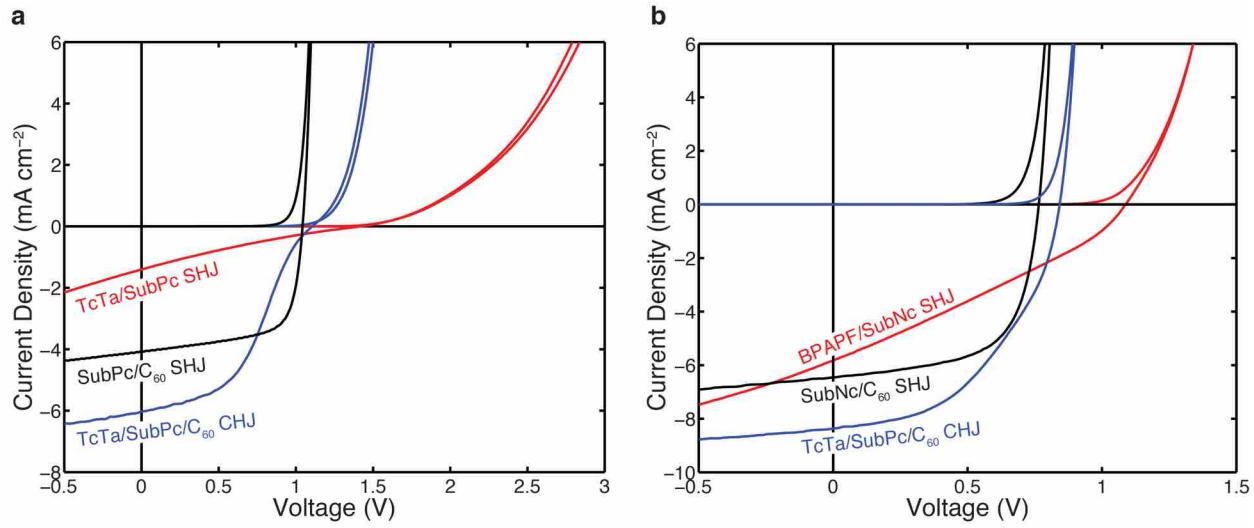

Figure 3.21 *J-V* curves for (a) TcTa/SubPc SHJ, SubPc/C_{60} SHJ, and TcTa/SubPc/C_{60} CHJ devices; and (b) BPAPF/SubNc SHJ, SubNc/C_{60} SHJ, and BPAPF/SubNc/C_{60} CHJ devices. [89]

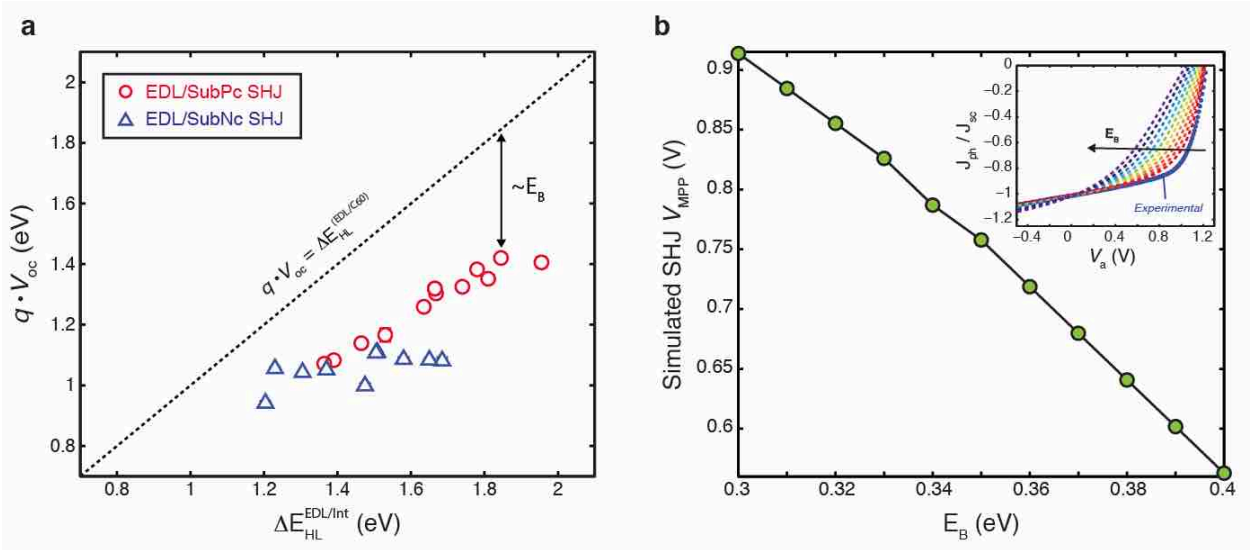

Figure 3.22 (a) V_{oc} of every EDL/interlayer SHJ device in this study versus ΔE_{HL}. Error bars were calculated as one standard deviation of measurements from at least six devices, but are too small to show up in the plot. (b) Simulated V_{MPP} for a SubPc/C_{60} SHJ as a function of the "effective" CT binding energy, E_B. Inset: Normalized calculated J_{ph}-V for varying E_B. [89]

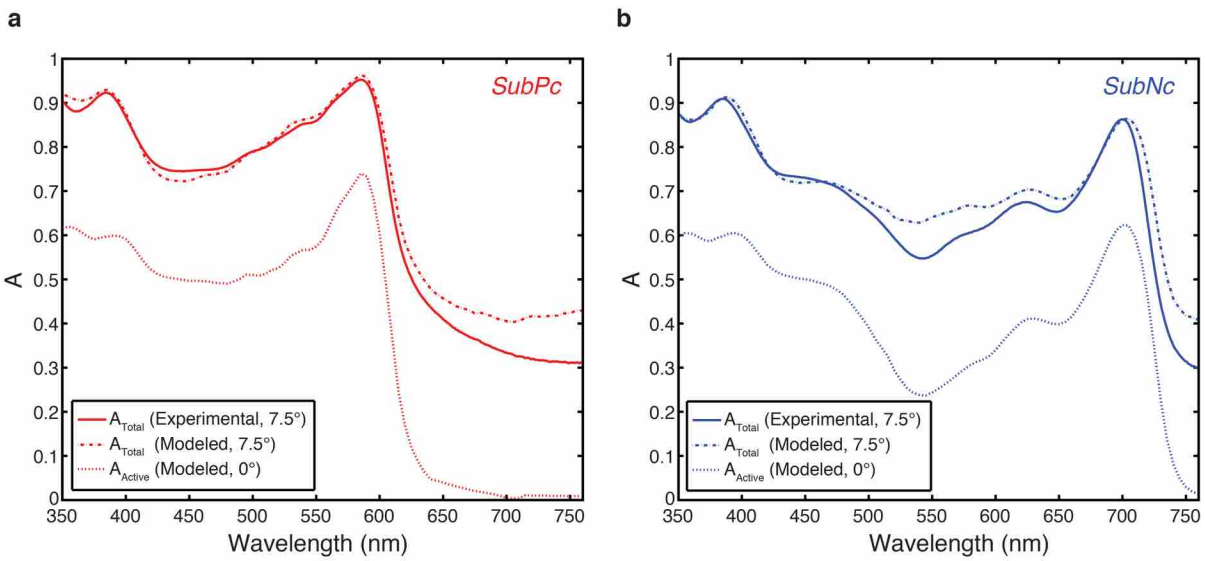

Figure 3.23 Experimental and modeled absorption spectra of (a) SubPc/C_{60} and (b) SubNc/C_{60} CHJ devices. [89]

predictions and indicating efficient CT dissociation occurs (**Figure 3.21**). However, as observed previously with the α-NPD/SubPc system (Section 3.2.4), the EDL/Interlayer single junctions also exhibit significant photoconductivity and subsequently low FFs (~30%). Of particular interest however is their V_{oc} output, as shown in **Figure 3.22**a.

By comparing the V_{oc} to the ΔE_{HL}, an average effective "binding energy" of the CT state can be approximated (Section 1.4.4), equivalent to the average voltage lost during the dissociation process. As previously discussed, many CT states are delocalized and not Coulombically-bound ($E_B = 0$), however the relative proportion of localized CT states shifts the average E_B of the system. We observe a net *increase* in the effective E_B with increasing ΔE_{HL} (lower ΔE_{HOMO}), as a higher fraction of polarons become electrostatically bound in localized CT states. A linear trend in E_B has been previously shown by Zhang *et al.*,[175] and can be attributed to a reduction of the energetic width of delocalized CT states accessible to excitons reaching the heterojunction ("B-W" in **Figure 1.18**a).[30] Qualitatively, this increase in the effective binding energy will cause a net reduction in the V_{MPP} produced by the subjunction (**Figure 3.22**b).[34]

Thus, a balance must be struck between the need to minimize ΔE_{HOMO} and charge buildup and the need to maximize the V_{MPP} output of EDL/interlayer subjunction (Section 3.3.5).

In the case of the SubPc/C_{60} and SubNc/C_{60} SHJs, we observe a V_{MPP} of 0.89 V and 0.59 V, respectively, with efficiencies of ~2.7 % (**Figure 3.21**). A high FF ~65% is produced in both devices, and a close match between optical modeling and measured device reflectivity indicates the validity of the refractive indices used (**Figure 3.23**). These two device sets represent the reference standard for all CHJs in this study, as the introduction of a 5 nm EDL produces no change to their optical absorption.

3.3.6 Cascade heterojunction performance

In CHJs, injected holes and electrons could in principle recombine at either the EDL/interlayer heterojunction or the interlayer/acceptor heterojunction. In practice, however, asymmetric injection barriers and carrier mobilities will force recombination to preferentially occur at one of the subjunctions, which will in turn determine the overall diode behavior of the CHJ.[172, 175] For devices in this study, and the majority of CHJs shown previously in literature, phthalocyanines have been used as the interlayer, resulting in a large mismatch between interlayer hole (μ_h) and electron (μ_e) mobilities. Because $\mu_h > \mu_e$ for most phthalocyanines, recombination of injected charges will preferentially occur at the interlayer/acceptor interface. Recombination at that interface is favored even more if the electron injection barrier from the acceptor into the interlayer (ΔE_{LUMO}) exceeds the hole injection barrier from the EDL into the interlayer (ΔE_{HOMO}), as is the case for devices in this study with $\Delta E_{HOMO} < 0.2$ eV (**Figure 3.15**c).

If recombination occurs at the interlayer/acceptor interface, we must then consider the effect of ΔE_{HOMO}, specifically its impact on CHJ V_{MPP} as a consequence of space charge

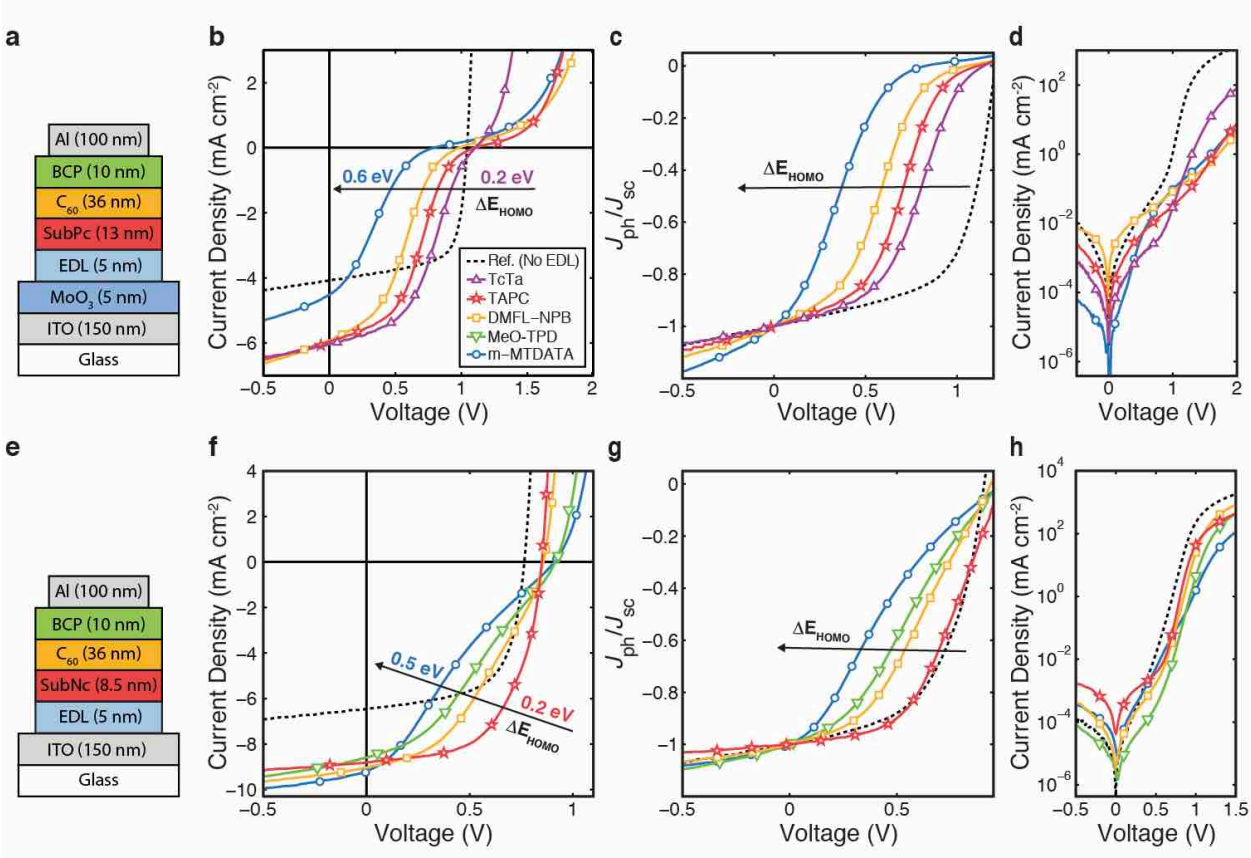

Figure 3.24 The effect of ΔE_{HOMO} on the *J–V* performance of CHJ devices. (a–d) The CHJ device structure, *J–V*, normalized photocurrent, and dark current for devices using SubPc as the interlayer. (e–h) The same data for devices using SubNc as an interlayer. [89]

accumulation and field inversion.[160] In **Figure 3.24**, we show how ΔE_{HOMO} can affect *J–V* performance by varying the material used for the 5 nm transparent EDL. The black dashed line in each plot represents the reference interlayer/C_{60} SHJ device without an EDL. The onset of s-kink behavior is most apparent in **Figure 3.24**c,g, where we normalize the photocurrent for each device to its J_{sc}. This provides a useful metric for the shape of the device curve regardless of the J_{sc} and more clearly illustrates changes to the s-kink behavior. Furthermore, we note that the dark current at V_{oc} is 10 – 100× lower in the CHJs than in the SHJ reference device. Lower dark currents at biases close to V_{oc} indicate a decrease in recombination of injected charges at the dominant heterojunction, providing further evidence for a buildup of holes at the EDL/interlayer

interface. If injected holes are unable to reach the interlayer/C_{60} interface, they cannot recombine with injected electrons and contribute to dark current.

Figure 3.25a plots the normalized V_{MPP} of each CHJ against ΔE_{HOMO}, with the normalization factor (f) defined by:

$$f = \frac{1}{\min\left(V_{MPP}^{EDL/\text{int}}, V_{MPP}^{\text{int}/C60}\right)} \tag{3.2}$$

where f is the inverse of the minimum V_{MPP} of either subjunction operating in the CHJ. Remarkably, the data collapse onto a universal linear trend:

$$f \cdot V_{MPP}^{CHJ} = 1.08 - 0.78 \cdot \Delta E_{HOMO} \tag{3.3}$$

with the caveat that the cascade V_{MPP} will not exceed the V_{MPP} of either subjunction. This result indicates that for $\Delta E_{HOMO} < 0.2$ eV, the CHJ is primarily limited by the lowest subjunction V_{MPP} and operates purely as a set of parallel diodes. However, for $\Delta E_{HOMO} > 0.2$ eV, the hole injection barrier becomes significant enough to shut down photocurrent production before V_{oc} is reached, decreasing V_{MPP} below that of either subjunction. This 0.2 eV threshold is consistent with what has been shown in bilayer organic light-emitting diodes, where efficient hole injection into the electron transport layer occurs only when ΔE_{HOMO} is less than 0.1–0.3 eV.[176-178] Thus, **Figure 3.25**a encompasses the critical parameters that will determine the MPP (and PCE) of a CHJ device. From the plot, we conclude that for a high efficiency CHJ, the V_{MPP} of each subjunction must be closely matched and ΔE_{HOMO} between the EDL and interlayer should be kept below 0.2 eV. Finally, from comparing the two contour plots (**Figure 3.25**b,c), we can see that a much lower EDL/interlayer V_{MPP} is required to achieve the maximum V_{MPP} in the SubNc CHJ as compared to the SubPc CHJ. In many cases, the simplest route to a high-performance CHJ device may be choosing a base device system with higher J_{sc} and lower V_{oc} or V_{MPP}. By "trading"

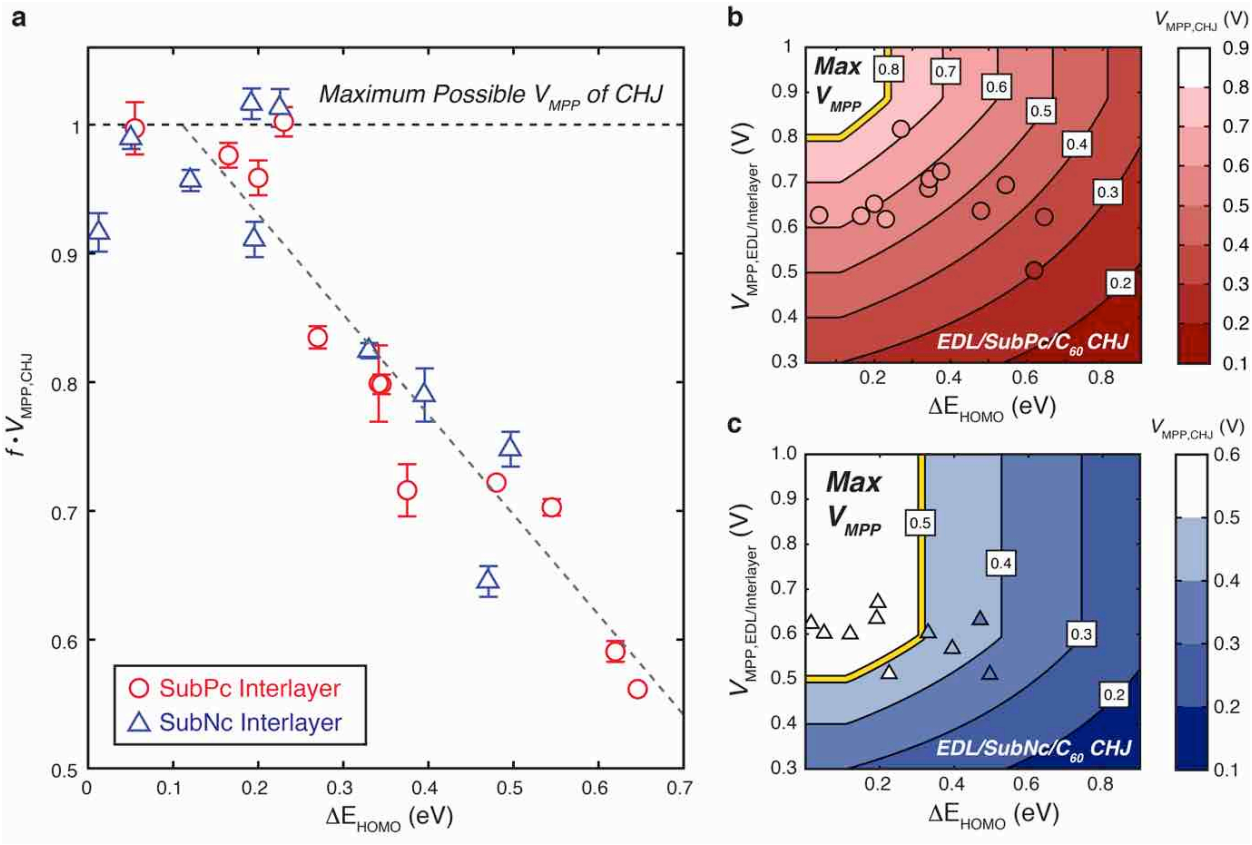

Figure 3.25 (a) A plot of each CHJ V_{MPP} normalized by the minimum V_{MPP} of its constituent subjunctions versus ΔE_{HOMO} (Equation (3.2)). Beyond ΔE_{HOMO} ~ 0.2 eV, the CHJ V_{MPP} is reduced due to progressive field inversion (Equation (3.3)). Error bars represent standard deviations calculated from six or more devices. (b,c) Contour plots of simulated V_{MPP} for CHJ devices with SubPc and SubNc interlayers, respectively, according to Equation (3.3). Experimental data points (circles and triangles) for CHJ devices are plotted and colored corresponding to measured V_{MPP} values. [89]

J_{sc} for V_{MPP}, the PCE of the reference SHJ device can remain high, while lowering the necessary V_{MPP} of the EDL/interlayer subjunction in the CHJ.

We note that the HOMO levels of the EDL and interlayer materials were obtained via cyclic voltammetry on individual materials. Within the devices, however, the HOMO levels and offset energies could conceivably vary due to band bending or intermixing at the active layer interfaces. Therefore, as with the estimation of each subjunction's V_{MPP} from the V_{MPP} of its SHJ counterpart, the measured energy levels provide an approximate value that can be used for

predicting CHJ device performance. It is likely that the variations in energy levels and V_{MPP} of each subjunction within the CHJs account for some of the data spread seen in **Figure 3.25**a.

Since μ_h is correlated with ΔE_{HOMO} (**Figure 3.19**), we also varied the EDL thickness for each CHJ device set from 5 nm to 10 nm to deconvolve any effects the two properties may have on device performance. Because the injection barrier remains constant regardless of EDL thickness, any changes in performance versus thickness could be attributed to mobility differences in the EDL layer. The normalized V_{MPP} for both sets of CHJ devices can be seen in **Figure 3.26**a. While the EDL thickness variation introduces an additional spread to the data set, the trend remains consistent. Furthermore, as can be seen from **Figure 3.26**b, there is no clear trend in V_{MPP} as a function of EDL thickness. In fact, some CHJ devices experience an *increase* in V_{MPP} with a thicker EDL layer. While the physical reasons for variations in CHJ performance versus EDL thickness warrant further investigation, they are outside the scope of this study. However, we conclude that any effects due to changes in mobility are secondary to ΔE_{HOMO}.

Recently, Cnops *et al.* suggested that the V_{oc} of CHJs should be limited by the energy levels of the outermost active layers.[179] This limitation on the V_{oc} would occur due to the additional losses in energy as the free charges are extracted from the device. In **Figure 3.27**, we plot the V_{oc} of each CHJ versus the HOMO-LUMO offset between the EDL and acceptor layers, and indeed show that the V_{oc} can be limited by the outermost active layers. In the CHJ devices employing a SubPc interlayer, we observe a crossover point around 1.45 eV (ΔE_{HOMO} = 0.35 eV), above which the V_{oc} remains relatively constant, and below which the V_{oc} decreases monotonically with HOMO-LUMO offset. A similar transition is inferred at ~1.18 eV (ΔE_{HOMO} = 0.48 eV) for devices with a SubNc interlayer, however the limited data below this value makes it more approximate. Critically, any limitations in V_{oc} only occur for very small HOMO-LUMO

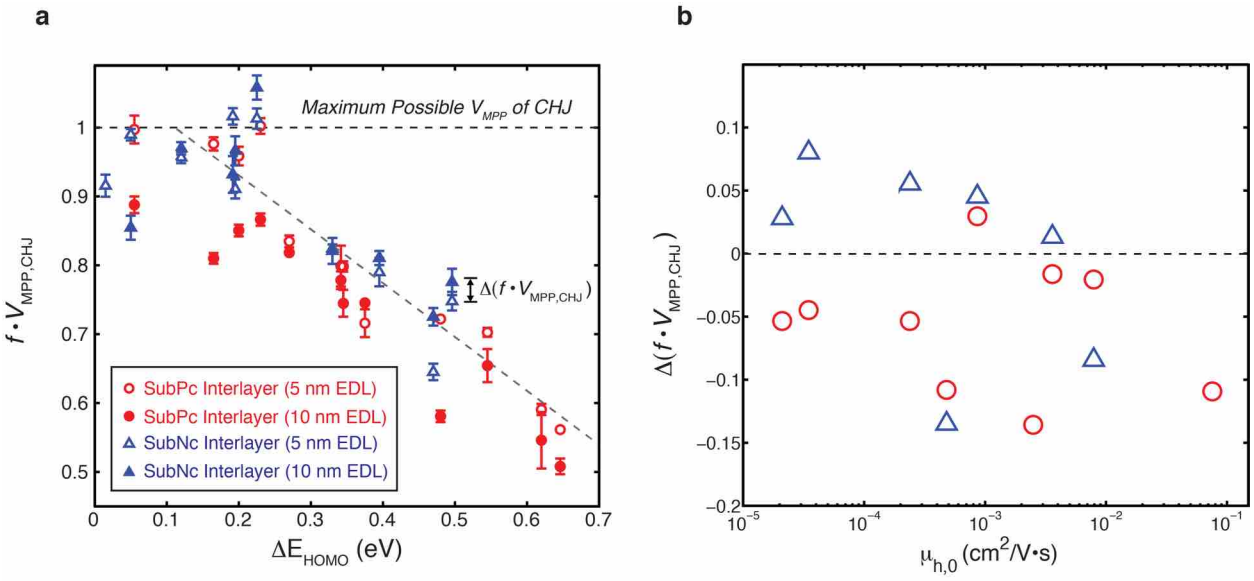

Figure 3.26 (a) Plot of the normalized V_{MPP} for CHJs with EDL thicknesses of 5 and 10 nm. (b) The difference in normalized V_{MPP} for CHJs with 5 nm and 10 nm EDL thicknesses vs. the zero-field hole mobility of each EDL material. Because there is no clear dependence of V_{MPP} on EDL thickness, we conclude that the effects of mobility variation on V_{MPP} are either negligible or secondary. [89]

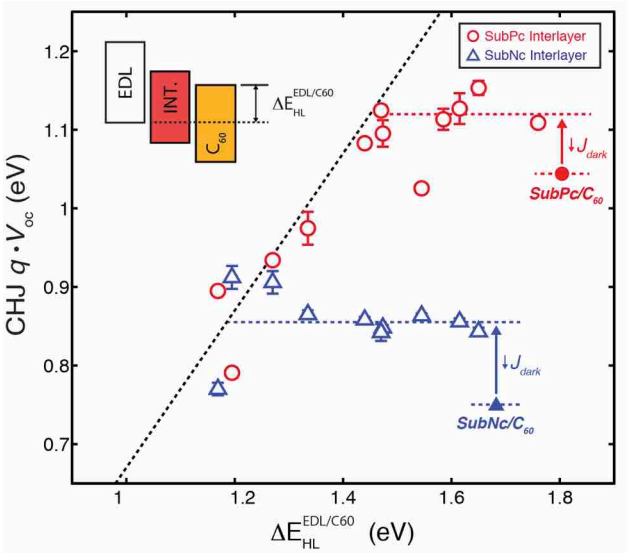

Figure 3.27 The V_{oc} for each CHJ device versus HOMO-LUMO offset of the EDL and C_{60} layers, respectively. The V_{oc} of CHJ devices increases initially upon insertion of an EDL due to a decrease in the dark current. As the HOMO-LUMO offset decreases, the V_{oc} of the CHJs remains relatively constant until it becomes limited by Equation (3.4). [89]

offsets (large ΔE_{HOMO} values). Conversely, for larger HOMO-LUMO offsets, the CHJ devices actually exhibit an *increase* in V_{oc} compared to the reference interlayer/C_{60} SHJ, which we attribute to a decrease in dark current (**Figure 3.24**d,h). The black dotted line in **Figure 3.27** represents:

$$qV_{oc} = \Delta E_{HL}^{EDL/C60} - 0.3 \tag{3.4}$$

indicating that the maximum possible V_{oc} of the CHJs is limited by HOMO-LUMO offset between the outermost layers of the CHJ and reduced by an effective binding energy of ~0.3 eV for the total structure (consistent with that of the SubPc/C_{60} and SubNc/C_{60} SHJs). Since a majority of photocurrent in the CHJ is generated at the interlayer/C_{60} interface,[46] it is not surprising that the effective E_B of the CHJ is close to that of the interlayer/C_{60} subjunction.

As demonstrated by the EDL/SubNc/C_{60} devices, CHJs with interlayer/acceptor subjunctions exhibiting high recombination losses can employ donor layers with a larger ΔE_{HOMO} before V_{oc} begins to drop. However, as we have already established that ΔE_{HOMO} should be kept to less than 0.2 eV to minimize charge injection barriers in the devices, properly designed CHJs will not be V_{oc}-limited. Instead, CHJ operation can substantially reduce recombination losses and bring the V_{oc} closer to the theoretical maximum.

3.3.7 Champion device performance

In **Figure 3.28**, we show the champion device results for CHJs using either a SubPc or SubNc interlayer. Both data sets are compared to the reference interlayer/C60 SHJ devices, which are plotted with dashed lines. Impressively, the IQE of the SubNc interlayer within the cascade approaches 100%, meaning that nearly all photogenerated excitons in the SubNc are converted to

electrical current, and η_D is near-unity within the interlayer. Furthermore, the V_{MPP} of the SubNc CHJ is insensitive to the insertion of a 5 nm TAPC EDL between the ITO anode and the SubNc layer, while the SubPc CHJ still exhibits a large drop in V_{MPP}. Consequently, the FF of the SubNc/C_{60} SHJ (62%) is largely maintained in the TAPC/SubNc/C_{60} CHJ (58%), whereas the FF of the TcTa/SubPc/C_{60} CHJ (44%) is decreased significantly compared to the SubPc/C_{60} SHJ reference (67%). This makes empirical sense: since ΔE_{HOMO} is less than 0.2 eV in both cases, the V_{MPP} of each CHJ should be limited to the minimum subjunction V_{MPP}. In the case of the SubPc interlayer, the TcTa/SubPc subjunction outputs 0.63 $\pm$ 0.01 V while the SubPc/C_{60} subjunction outputs 0.89 $\pm$ 0.01 V. Hence the overall V_{MPP} of the CHJ is restricted to 0.63 $\pm$ 0.01 V. On the other hand, the V_{MPP} of each SubNc subjunction is closely matched (0.63 $\pm$ 0.01 V for the TAPC/SubNc and 0.59 $\pm$ 0.01 V for SubNc/C_{60}), leading to an overall CHJ V_{MPP} = 0.60 $\pm$ 0.01 V. The final result is an observed 46% improvement in PCE for the SubNc CHJ over the reference SHJ device, purely through an improvement in η_D and consequently J_{sc}.

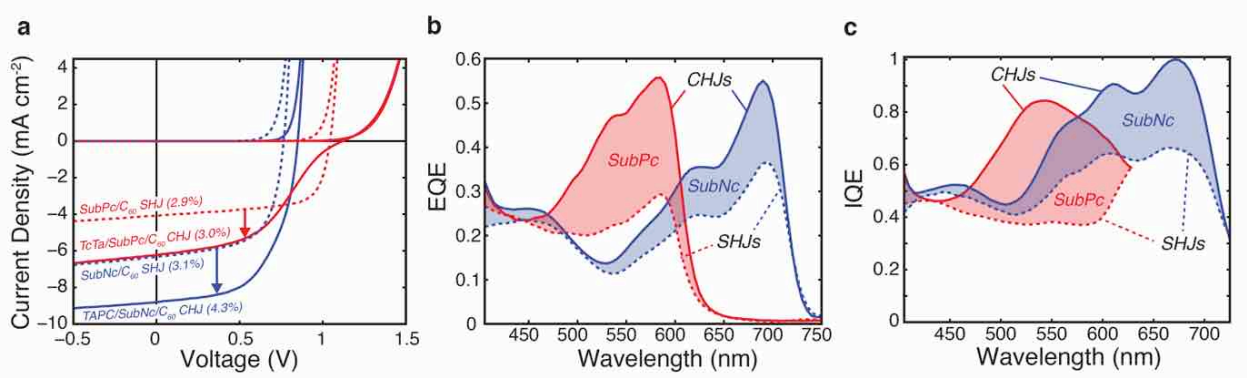

Figure 3.28 (a) *J–V* curves, (b) EQE, and (c) IQE of optimized CHJ devices and the corresponding reference SHJ devices with no EDL. In the SubNc interlayer, the peak IQE is >99%. The pronounced s-kink behavior in the SubPc CHJ is due to the limiting V_{MPP} of the TcTa/SubPc subjunction. [89]

Table 3.5 Performance parameters for SHJ and CHJ devices utilizing SubPc in this study. Standard deviations, as calculated from at least six different devices, for V_{oc}, J_{sc}, FF, PCE, and V_{MPP} were all less than 3%, 11%, 6%, 12%, and 4%, respectively. [89]

Device	**ΔE_{HOMO} (eV)**	**V_{oc} (V)**	**J_{sc} (mA cm^{-2})**	**FF (%)**	**PCE (%)**	**V_{MPP} (V)**
SubPc/C_{60} SHJ	-	1.04	3.9	67	2.74	0.89
TcTa/SubPc SHJ	0.05	1.41	1.5	21	0.44	0.63
TcTa/SubPc/C_{60} CHJ		1.11	5.8	44	2.81	0.63
BPAPF/SubPc SHJ	0.17	1.42	1.3	20	0.38	0.63
BPAPF/SubPc/C_{60} CHJ		1.15	5.7	41	2.70	0.61
α-NPD/SubPc SHJ	0.20	1.35	1.9	23	0.60	0.65
α-NPD/SubPc/C_{60} CHJ		1.13	5.7	43	2.76	0.63
HMTPD/SubPc SHJ	0.23	1.38	1.4	21	0.40	0.62
HMTPD/SubPc/C_{60} CHJ		1.11	5.7	42	2.69	0.62
TPTPA/SubPc SHJ	0.27	1.33	3.1	38	1.58	0.82
TPTPA/SubPc/C_{60} CHJ		1.03	5.3	51	2.79	0.68
TAPC/SubPc SHJ	0.34	1.30	1.9	27	0.65	0.69
TAPC/SubPc/C_{60} CHJ		1.10	5.8	38	2.42	0.55
NPB/SubPc/SHJ	0.35	1.32	1.9	28	0.71	0.71
NPB/SubPc/C_{60} CHJ		1.12	6.0	38	2.60	0.57
TPD/SubPc SHJ	0.38	1.26	2.0	30	0.77	0.72
TPD/SubPc/C_{60} CHJ		1.08	5.8	36	2.25	0.52
DMFL-NPB/SubPc SHJ	0.48	1.17	1.9	31	0.65	0.64
DMFL-NPB/SubPc/C_{60} CHJ		0.97	5.6	34	1.85	0.46
MeO-TPD/SubPc SHJ	0.55	1.14	1.6	34	0.62	0.69
MeO-TPD/SubPc/C_{60} CHJ		0.93	5.1	39	1.86	0.49
m-MTDATA/SubPc SHJ	0.62	1.08	1.2	24	0.33	0.51
m-MTDATA/SubPc/C_{60} CHJ		0.79	4.4	23	0.80	0.30
2T-NATA/SubPc SHJ	0.65	1.07	2.0	33	0.70	0.62
2T-NATA/SubPc/C_{60} CHJ		0.89	5.2	28	1.31	0.35

Table 3.6 Performance parameters for SHJ and CHJ devices using SubNc in this study. Standard deviations, as calculated from at least six different devices, for V_{oc}, J_{sc}, FF, PCE, and V_{MPP} were all less than 2%, 9%, 7%, 10%, and 3%, respectively. [89]

Device	ΔE_{HOMO} (eV)	V_{oc} (V)	J_{sc} (mA cm^{-2})	FF (%)	PCE (%)	V_{MPP} (V)
SubNc/C_{60} SHJ	-	0.75	5.9	62	2.76	0.59
BPAPF/SubNc SHJ	0.02	1.08	5.1	30	1.64	0.62
BPAPF/SubNc/C_{60} CHJ		0.84	8.0	47	3.18	0.54
α-NPD/SubNc SHJ	0.05	1.08	4.7	29	1.50	0.60
α-NPD/SubNc/C_{60} CHJ		0.86	8.0	53	3.59	0.59
TPTPA/SubNc SHJ	0.12	1.09	5.1	29	1.63	0.60
TPTPA/SubNc/C_{60} CHJ		0.86	8.2	51	3.65	0.57
TAPC/SubNc SHJ	0.19	1.11	5.2	30	1.73	0.63
TAPC/SubNc/C_{60} CHJ		0.85	8.3	58	4.05	0.60
NPB/SubNc/SHJ	0.20	1.11	5.6	34	2.10	0.67
NPB/SubNc/C_{60} CHJ		0.84	8.2	50	3.46	0.54
TPD/SubNc SHJ	0.23	1.00	1.9	25	0.48	0.51
TPD/SubNc/C_{60} CHJ		0.86	7.2	44	2.70	0.52
DMFL-NPB/SubNc SHJ	0.33	1.05	4.0	29	1.21	0.60
DMFL-NPB/SubNc/C_{60} CHJ		0.87	7.9	41	2.79	0.49
MeO-TPD/SubNc SHJ	0.40	1.04	3.1	28	0.93	0.57
MeO-TPD/SubNc/C_{60} CHJ		0.91	7.4	33	2.21	0.45
m-MTDATA/SubNc SHJ	0.47	1.06	4.9	32	1.63	0.63
m-MTDATA/SubNc/C_{60} CHJ		0.91	8.2	23	1.74	0.38
2T-NATA/SubNc SHJ	0.50	0.94	1.8	27	0.44	0.51
2T-NATA/SubNc/C_{60} CHJ		0.77	5.2	28	1.12	0.38

3.3.8 Conclusions

We have shown that CHJ architectures are viable options for high-efficiency planar OPVs, primarily due to their nearly 100% IQE within the interlayer. To ensure high fill factor, the V_{MPP} of each subjunction must be matched and the HOMO level offset between the EDL and interlayer should be < 0.2 eV. This ensures that space charge accumulation in the active layers does not prematurely shut off photocurrent production from either subjunction. Using these empirical design rules, we demonstrated a 46% increase in the PCE of a SubNc/C_{60} planar device by introducing a transparent EDL between SubNc and the ITO anode (from 2.8% ± 0.2% to

4.1% ± 0.2%). By introducing the 5 nm layer of TAPC, the IQE of the SubNc layer increased from 66% to >99% at its peak while maintaining a high FF.

3.4 Future work

Although the PCE was significantly enhanced in CHJ devices employing an EDL, J_{sc} could be improved further through increased active layer absorption. Because the presence of two heterojunctions relaxes the tradeoff between absorption and exciton diffusion, the interlayer thickness can be increased to optimize absorption and EQE. Some material combinations are more suitable for this than others; Verreet *et al.* recently showed that replacing C_{60} with hexachlorinated SubPc allowed the SubNc layer thickness to increase upwards of 20 nm.[37] Furthermore, by using a smaller bandgap material in place of the transparent EDL to increase spectral coverage, device J_{sc} should increase without any additional drop in V_{oc}, V_{MPP}, or FF. Because the CHJ devices have such high IQE, they are also ideal candidates for use as sub-cells in series-connected tandems, potentially allowing for high efficiency OPVs comprising six or more active layers with complementary absorption peaks.

Furthermore, the impedance spectroscopy work presented here presents the opportunity to directly probe steady-state recombination at each subjunction. By registering intensity-dependent changes in the junction capacitance, new insights into space charge accumulation, dissipation, and field inversion in CHJs can be drawn. As such processes occur at buried interfaces, few other techniques provide the ability to directly probe polarons in the CT state under steady-state conditions.

Chapter 4

Plasmonic absorption enhancement

4.1 Background

In OPVs and organic photodetectors (OPDs), surface plasmon polaritons (SPPs) have been explored for their enhancement of optical fields and large scattering cross-sections, both of which can give rise to significant absorption enhancement on- and off-surface plasmon resonance (SPR).[180, 181] Such SPP modes have an extremely high optical density of states, exhibit high spatial confinement due to their evanescent character, and can efficiently couple to absorbers in the near-field.[182] Due to the strong confinement of SPP modes, optical coupling at SPR provides not only an effective means for improving absorption but also the ability to transduce optical signals in photonic circuits.[183-185] Typically, plasmonic OPVs and OPDs employ metal nanoparticles[57, 116, 186-191] or nanostructured electrodes[192-197] exhibiting localized surface plasmon resonance (LSPR) to improve active layer absorption. While enabling optical field enhancements, however, the inclusion of metallic nanostructures can produce unintended consequences such as free carrier trapping, exciton quenching, and morphological changes, which limit the overall performance enhancement.[188, 198-201] Thus, while absorption can easily be improved through LSPR coupling, efficient extraction of the additional generated charges to photocurrent remains a challenge.

In this chapter, we present an alternative approach to improving absorption in OPVs (and OPDs) using SPP coupling in a planar metallic nanocavity. By positioning the plasmon-supporting interfaces external to the active organic layers, we are able to avoid many of the drawbacks inherent to embedded nanoparticles. Through both experiment and simulation, we demonstrate large enhancements of both the absorption *and* EQE at SPR across the entire visible spectrum, without affecting the exciton diffusion efficiency.

4.1.1 Drude model

Electrons in the conduction band of a metal, unlike those in tightly-bound covalent or ionic materials, are free-flowing and distributed throughout the volume. This "sea of electrons" can be physically described as a free electron gas (FEG), or plasma, with a characteristic plasma frequency (ω_p). The bulk plasma frequency represents the natural resonance frequency of the electrons, and for noble metals such as Au or Ag it exists at optical frequencies in the visible spectrum. To first order, ω_p can be approximated using the Drude model[202]:

$$\omega_p = \sqrt{\frac{nq^2}{m\varepsilon_0}} \tag{4.1}$$

where n is the free electron density, q is the elementary electron charge, m is the effective mass of electrons, and ε_0 is the free-space permittivity. Using the Drude formalism, the relative frequency-dependent permittivity of a metal can then be described by:

$$\varepsilon_r(\omega) = 1 - \frac{\omega_p^2}{\omega^2 + \gamma^2} + i\frac{\omega_p^2 \gamma}{\omega\left(\omega^2 + \gamma^2\right)} \tag{4.2}$$

where γ is the dampening factor of the metal defined by:

$$\gamma = \frac{nq^2}{m\sigma} \tag{4.3}$$

and σ is the DC conductivity of the metal. In most cases such as noble metals, $\gamma << \omega_p$ and the imaginary component of Equation (4.2) is neglected. As is apparent from Equation (4.2), light incident on a metal at frequencies below ω_p are strongly attenuated, while above ω_p the metal becomes transparent to electromagnetic radiation. Below ω_p, the collective oscillatory response of the FEG is more commonly known as a "plasmon". Multiple types of plasmon modes exist in metals, which can be divided into those confined to the bulk of the material and plasmons at the surface of the metal. This chapter focuses on the latter, termed "surface plasmons," and their unique ability to confine and focus electromagnetic radiation to subwavelength volumes near the metal surface to enhance absorption in the neighboring medium.

4.1.2 Surface plasmon polaritons

In all cases, surface plasmons are evanescent fields confined to the metal surface. They exhibit an exponential decay in intensity with distance from the metal/dielectric interface with a maximum in optical field intensity at the interface itself. When the metal surface is flat and effectively unbounded, such collective oscillations freely propagate as both a photon (polariton) mode in the neighboring dielectric medium and as out-of-plane oscillations in the FEG, in what are termed "surface plasmon polaritons" (SPPs). SPPs can be stimulated for any frequency below the characteristic surface plasmon frequency, assuming proper matching of the incident light wavevector. In contrast, metals with a surface texturing or nanostructuring on the order of the wavelength of light exhibit quantized resonance modes, which are termed "localized surface plasmons" (LSPs). **Figure 4.1** shows a cartoon depicting the two types of surface plasmon mode.

SPPs follow a dispersion relation typical of waveguided modes. In the simplest case of a metal/dielectric interface with semi-infinite media on both sides, the dispersion relation can be approximated by the solving Maxwell's equations for an electromagnetic plane-wave propagating in the x-z plane with an electric field:

$$\vec{E} = E_0 \exp\left(i\left(k_x \hat{x} + k_z \hat{z} - \omega t\right)\right) \tag{4.4}$$

where k_x and k_z are the plane-parallel and plane-perpendicular components of the electric field's wavevector (k) relative to the interface. Recall that the polarization of such fields is denoted "transverse-magnetic" (TM), as the magnetic field component of the photon is maintained parallel to the metal-dielectric interface (in the +y direction). Conversely, a "transverse-electric" (TE) polarization describes an electromagnetic wave whose electric field is maintained in-plane (e.g. in the +y direction for a wave propagating in the +x/-z plane). However, no SPP modes can be stimulated in the TE polarization, as the electric field is incapable of driving oscillations of the FEG out-of-plane in this orientation.

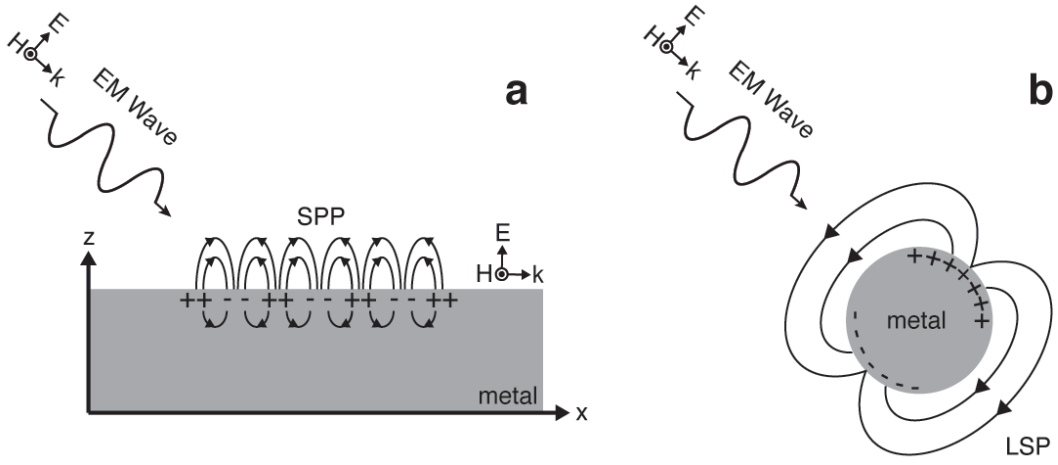

Figure 4.1 (a) Conversion of a TM-polarized electromagnetic (EM) wave to a propagating SPP mode at a semi-infinite metal/dielectric interface. (b) Generation of the fundamental dipolar LSP resonance in a conducting metal nanoparticle in a non-conducting dielectric medium, stimulated by an incident EM wave.

The solution to the dispersion relations for TM-supported SPP modes is then solved by the following boundary conditions:

$$\varepsilon_1 k_{z1}^2 + \varepsilon_2 k_{z2}^2 = 0 \tag{4.5}$$

$$k_x^2 = \frac{\varepsilon_1 \omega^2}{c^2} - k_{z1}^2 = \frac{\varepsilon_2 \omega^2}{c^2} - k_{z2}^2 \tag{4.6}$$

due to the continuity of Maxwell's relations between the dielectric (medium 1) and metal (medium 2). As can be seen in Equation (4.6), the in-plane wavevector k_x remains constant across the interface. Solving these two sets of equations yields the dispersion relation:

$$k_x = \frac{\omega}{c}\left(\frac{\varepsilon_1 \varepsilon_2}{\varepsilon_1 + \varepsilon_2}\right)^{1/2} \tag{4.7}$$

as plotted in **Figure 4.2**a for a Ag/air interface. The real (n) and imaginary (k) components of the Ag refractive index, $\tilde{\varepsilon} = (n + ik)^2$, are displayed in the inset with the refractive index of air assumed to be 1. The SPP dispersion curve asymptotically approaches an infinite k_x near the surface plasma frequency, $\omega_{sp} = \omega_p (1 + \varepsilon_1)^{-1/2}$, where there exists a discontinuity in the response

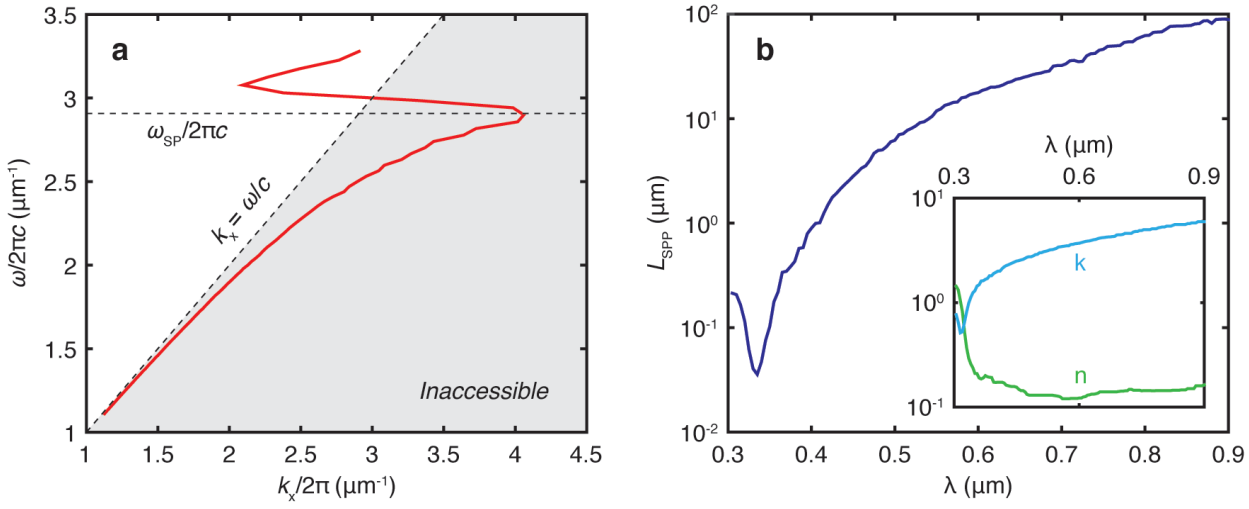

Figure 4.2 (a) Dispersion curve calculated for a semi-infinite Ag/air interface, also showing the light line for air ($k_x = \omega/c$). (b) Corresponding SPP propagation length for (a) as a function of the free space wavelength. (*Inset*) Refractive index values used for Ag, adapted from Palik. [203]

function. As should be clear from the above derivations, the SPP dispersion is highly sensitive to variations in the local dielectric environment that modify the local refractive index near the interface. Such interactions invariably tune the plasmonic response of SPP and LSP-supporting structures, and must be accounted for when designing systems for the resonant absorption enhancement of the local medium through plasmon-coupling.

Coupling to SPPs such as the Ag/air mode in **Figure 4.2**a can only occur when the k_x of the incident light is matched, which defines the condition for SPR. Unfortunately, this poses an issue in planar films, as the modes accessible to light in a given medium are limited to wavevectors at or below the "light line" ($k_x = n\omega/c$), as shown in **Figure 4.2**a. As explained in Section 1.5.1, Snell's law defines the range of angles accessible to photons in a given medium based on the refractive index. Hence, angles (wavevectors) beyond the light line are generally inaccessible to incident photons. According to Equation (4.7), SPPs generated at the interface with a medium M of refractive index n_M below the surface plasma frequency will always exist beyond the light line for M ($k_{SPP} > n_M\omega/c$). Hence to couple to SPPs at a metal/dielectric interface, light must be incident from a higher-index dielectric medium such that k_{SPP} is accessible. This can be accomplished through various techniques, the most common of which is the Kretschmann geometry (**Figure 4.3**a).[204] In this configuration, light from free space (e.g. air) is coupled into a high-index prism (e.g. glass), through which it is incident on a thin metal film. The air/glass interface is maintained at close to normal incidence, so minimal refraction occurs during incoupling. As a consequence, the angle of propagation in free space *relative to the metal interface* is matched to that in the higher index prism, and the larger range of k_x within the prism becomes accessible. As the light line of the prism extends past the air light line, the SPP mode at the Ag/air interface may be directly stimulated (**Figure 4.3**b).

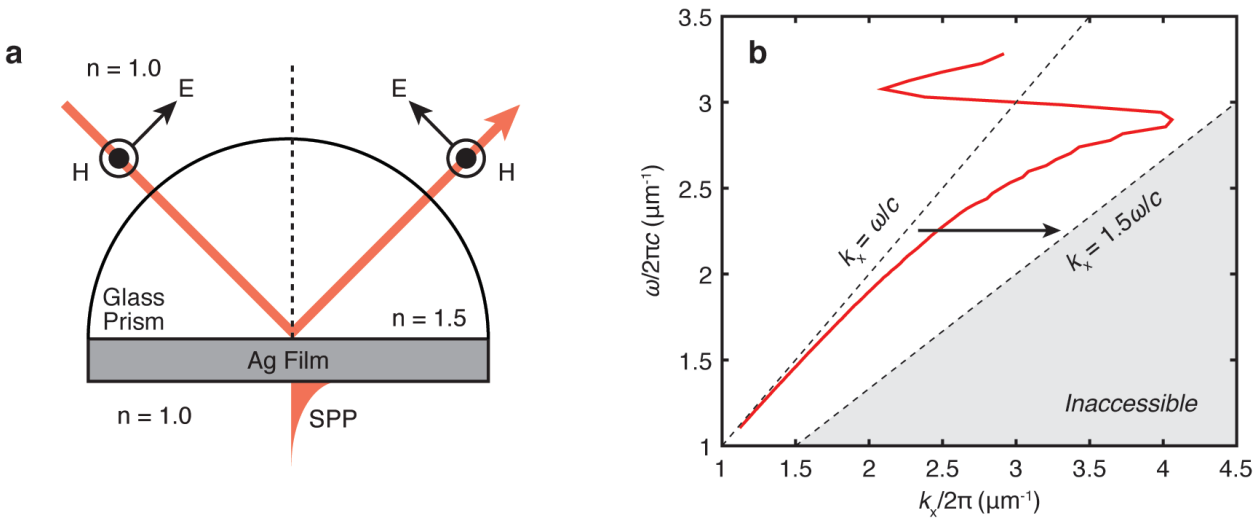

Figure 4.3 (a) Diagram of the Kretschmann coupling geometry, in which light is coupled through a high-index prism (e.g. glass) to access larger wavevectors. (b) Dispersion diagram for the Ag/air SPP mode, indicating a shift in the accessible k_x through Kretschmann coupling including matching to SPR.

The evanescent character of SPPs enables localized absorption enhancement two-fold: through an increase in the local electric field intensity near the interface due to spatial confinement of the electromagnetic field (near-field enhancement), and *via* a significant enhancement of the propagation length of light through the neighboring medium. Consider for example a dielectric medium of finite thickness t bounded by a semi-infinite metal slab. For light propagating perpendicular to the interface, the propagation distance through the dielectric is at most $2t$, assuming perfect reflection at the boundary. If $t << L_A$, light absorption is inefficient under these conditions. Such is the case for most organic films, which are generally confined to thicknesses below the wavelength of light (Section 1.6.1). When, however, the incident light is coupled to an SPP mode, the propagation length (L_{SPP}) along the metal/dielectric interface can be orders of magnitude longer than the wavelength:

$$L_{SPP} = \frac{1}{2k_x''} \tag{4.8}$$

where k_x'' is the imaginary component of the in-plane wavevector for the solution to Equation (4.7). At the Ag/air interface for example, L_{SPP} can be up to 100 μm at visible frequencies (**Figure 4.2**b), over 2 orders of magnitude larger than the corresponding free-space wavelength of the incident light. Thus, photons converted to SPPs sample a substantially larger volume of the neighboring dielectric medium than those propagating at normal incidence and have a much higher probability of absorption ($L_{SPP} >> L_A$).

4.1.3 Localized surface plasmons

We now consider LSPs, specifically those supported by conducting metal nanoparticles (NPs). In contrast to the propagating SPP modes described above, the confined modes on such particles do not increase the path length of the incident light on-resonance directly. Instead absorption can be enhanced locally by either near-field enhancement of the optical field or through scattering of the LSPs to higher order waveguided modes than the incident light would normally couple to (**Figure 4.4**).

The strong scattering exhibited by metal nanoparticles can be accurately described using Mie theory.[205] While the full details of this analysis are outside the scope of this thesis, it is sufficed to mention that in the simplest case of a spherical particle excited by a plane wave, the radiated (scattered) fields are described by spherical Bessel and Hankel functions, and the total absorbed power (W_{abs}) at some radius R from the center of the particle can be evaluated by:

$$W_{abs}(R) = -\frac{1}{2}\mathrm{Re}\oint_{r=R}\left[\left(E_i + E_s\right)\times\left(H_i^* + H_s^*\right)\right]\cdot ds = W_i(R) - W_s(R) + W_{ext}(R) \tag{4.9}$$

where the subscripts *i*, *s*, and *ext* correspond to the incident, scattered, and cross-term of the optical fields. From the solution to Equation (4.9), an upper bound to the near-field absorption

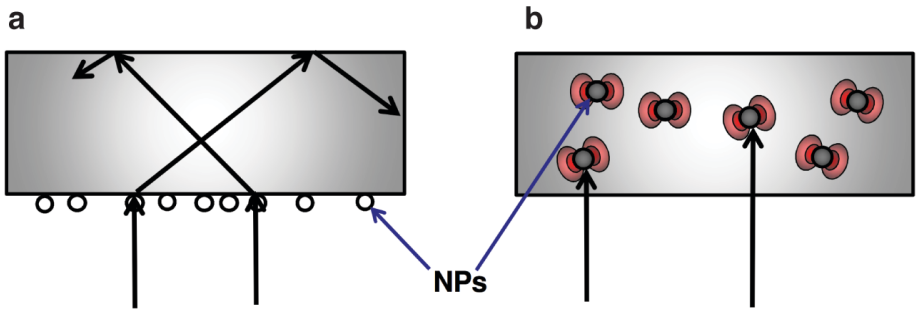

Figure 4.4 (a) Schematic of a photovoltaic cell with metal NPs placed on the surface. Enhancement of optical absorption is a *far-field* effect caused by the redirection of light into guided or trapped modes. (b) Schematic of a photovoltaic cell with NPs embedded in the active layer. In this case, enhancement of optical absorption results from *near-field* coupling which exploits the locally enhanced optical electric fields. [188]

enhancement (η_{enh}) from the particle scattering is found to be:

$$\eta_{enh}(r) = 1 + \left| 2\left(\frac{a}{r}\right)^3 \frac{\tilde{n}_{NP}^2 - \tilde{n}^2}{\tilde{n}_{NP}^2 + 2\tilde{n}^2} \right|^2 \tag{4.10}$$

averaged over a spherical shell volume between the NP radius a and the chosen radius r from the center of the particle.[188] The two complex refractive indices correspond to that of the nanoparticle and embedding medium, respectively. A clear size-dependence can be seen from Equation (4.10), indicating scattering is enhanced with particle size. Typically however, metal nanoparticles are limited by the organic layer thicknesses within a device, and must be kept on the order of 10 – 20 nm to prevent the formation of electrical shorts.

An alternative means of generating LSPRs without nanoparticles is through surface texturing of the metal electrode(s).[206] By introducing a periodic grating with some characteristic wavelength (λ_g), the dispersion curve can be shifted by $k_g = 2\pi/\lambda_g$ (**Figure 4.5**). In such a case, the wavevector corresponding to SPR crosses the air light line (or light "cone" in 3-dimensions) to become accessible to coupling from free space. With a sufficient periodicity, e.g. $k_g = k_{SPP}$, the SPP mode can be directly excited at normal incidence. Unlike the case of a planar film however, the introduced roughness from surface texturing reduces L_{SPP}, thus absorption enhancement

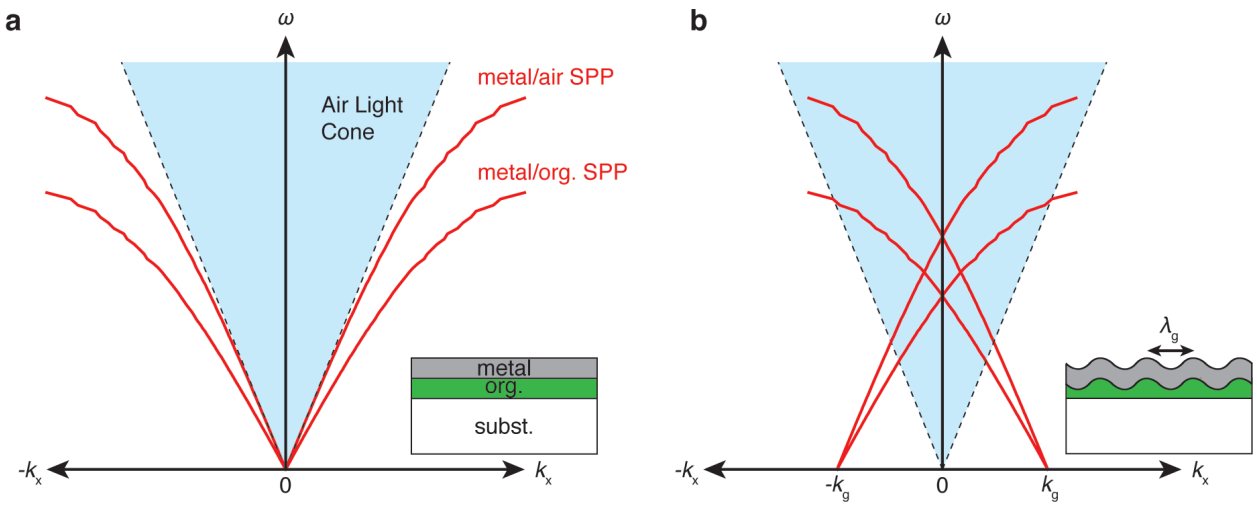

Figure 4.5 Dispersion diagrams of (a) flat and (b) surface textured electrodes in an OPV structure. As in **Figure 4.2,** light incident from free space is incapable of coupling to SPPs at either metal interface. With the introduction of periodic nanostructuring, the SPP wavevectors are shifted into the air light cone, and become accessible directly from free space.

through increased propagation length is traded for an enhancement in the near-field optical intensity.

4.1.4 Surface plasmon polariton modes in a metal nanocavity

Unlike the case of a semi-infinite metal slab as calculated in Section 4.1.2, in practice SPP-supporting metal films are finite in thickness. When the film thickness is on the order of the metal's skin depth, the penetration depth at which the SPP's electric field magnitude decays to 1/*e* of its surface value, oscillations in the electron density at both surfaces become coherently coupled. In general, we can define the penetration depth (δ) of the SPP as:

$$\delta_i = \frac{c}{\omega}\sqrt{\frac{\varepsilon_1 + \varepsilon_2}{\varepsilon_i^2}} \tag{4.11}$$

where the choice of i = 1 or 2 determines penetration in the (1) dielectric or (2) metal (skin depth). As the permittivity is itself frequency-dependent and it depends on the neighboring

medium, δ cannot be considered a material constant. However in the case of Ag it is approximately 20 nm at visible frequencies.

The close proximity of the metal surfaces and the coupling of their free electron oscillations result in two fundamental SPP modes in a thin metal film: an antisymmetric mode (A) and a symmetric mode (S). As can be seen in **Figure 4.6**, these modes are defined by the symmetry of their electric field at the two metal interfaces. In the S mode, the electric field has a much higher value inside of the bulk of the film, increasing its dissipation, whereas the electric field of the A mode is more effectively confined to the film surfaces. Thus the long-range antisymmetric mode has been shown to exhibit much larger L_{SPP} values than the short-range symmetric mode.[207-209] It is also useful to understand the inverse of the single thin-film geometry – a finite gap within a semi-infinite metallic medium. We can define two fundamental modes within such a gap – a symmetric (S_0) and antisymmetric (A_0) SPP (**Figure 4.6**c,d).

When two thin metal films are brought into close proximity (i.e. within the dissipation length of the separating dielectric), the fundamental S and A modes in each film become coupled. In the simplest case of a symmetric metal nanocavity within a dielectric medium, there exist four SPP cavity modes supported by the structure. We can define these modes according to

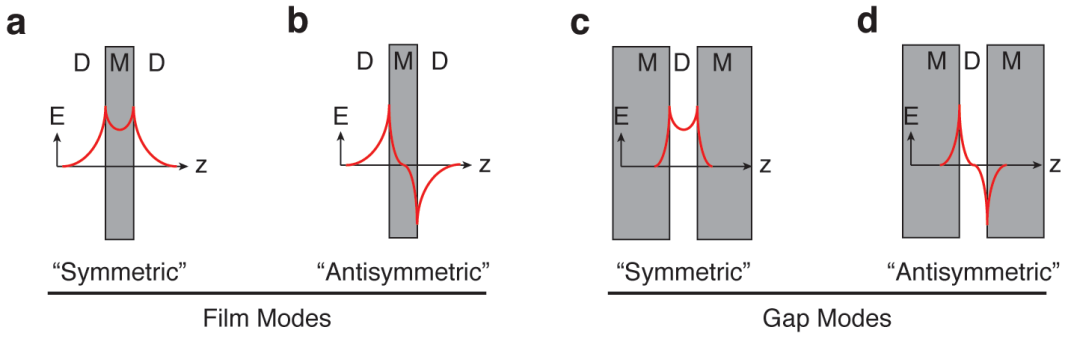

Figure 4.6 In-plane electric field profiles of the fundamental (a) symmetric and (b) antisymmetric SPP modes supported in a thin metallic film (M) bounded by a dielectric (D) and those supported in a finite dielectric gap within a semi-infinite metal slab (c,d).

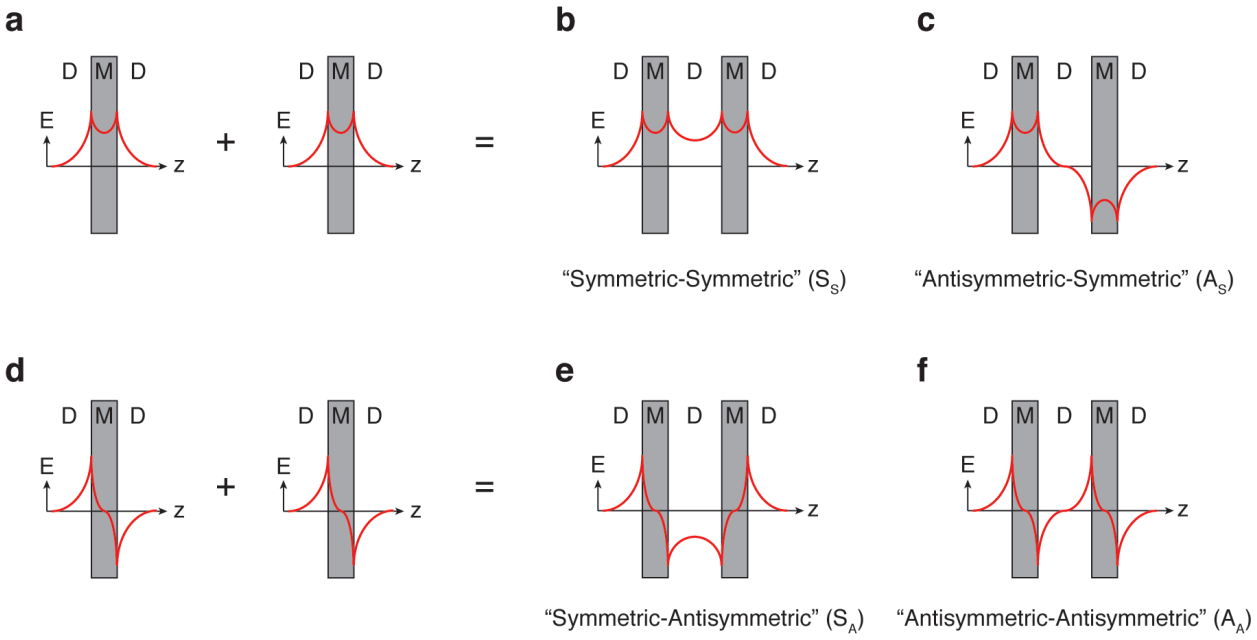

Figure 4.7 SPP modes supported in a dielectric-embedded metal nanocavity can be understood as the summation of two (a) symmetric or (d) antisymmetric SPPs in each individual film. The combinations yield a set of symmetric (b,e) and antisymmetric (c,f) SPP modes, whose subscripts denote the symmetry of the constituent SPPs. Adapted from [209]

their optical field symmetry within the cavity, and the symmetry within each film. By combining the S modes of each film, a symmetric (S_S) or antisymmetric (A_S) SPP is produced. Alternatively, coupling of the A modes within each film yields an additional symmetric (S_A) or antisymmetric (A_A) SPP within the structure (**Figure 4.7**).[207, 209] The modes S_S and A_S have been shown to exhibit resonance at lower frequencies (energies) and higher wavevectors than the S_A and A_A modes, as their constituent S modes are of lower energy and are more lossy (higher k_x).[207] Furthermore, the S_A mode is closely correlated to the fundamental gap mode S_0 and exhibits a similar dispersion.

In many cases it is advantageous to use semitransparent metal contacts for one or both electrodes in a device.[210] In the case of OLEDs, thin metal top contacts have been used to reduce substrate waveguiding and emit directly into free space[211-214] or to couple to external dyes for harnessing energy typically lost to heat in cavity-guided SPP modes.[215] Metallic cavity

structures have also been shown to enhance optical field intensities within OPV active layers compared to traditional ITO-based devices[55, 57, 216-219] and enable efficient, semi-transparent OPVs for window-based solar energy conversion.[220-222] In the case of OLEDs, the radiation produced by electrically-pumped excitons intrinsically couples to all modes within the cavity structure, including the SPP cavity modes. Due to the high quantum yield of the materials used in OLEDs, dissipative losses to heat through SPP modes can be a dominant factor in determining performance.[223] In contrast, quantum yields of the active materials used in OPVs are generally only ~1% or less, and therefore radiative coupling[224] between photogenerated excitons and SPPs within the device has a negligible effect on overall exciton lifetime and L_D. However, light absorption can be significantly modified through the incoupling to such modes.

It is important to note that the SPP cavity modes discussed above are modified when the symmetry of the nanocavity structure is broken. Differences in thickness between the two metal films or variations in the dielectric layers within and without the structure will adjust the dispersion of the cavity modes and, in some instances, render some of them forbidden. For this reason, **Figure 4.7** provides only the most basic foundation for understanding the plasmon modes within a working device.

4.2 SPP enhancement in OPV-embedded metal nanocavities

4.2.1 Plasmonic coupling in the Kretschmann configuration

As an alternative to LSPR-supporting nanostructures, we now consider plasmon-enhanced absorption in OPVs accomplished using a planar metal-dielectric-metal (MDM) structure coupled to SPPs (**Figure 4.8**a).[182] This type of device exhibits highly tunable spectral and angular selectivity, and can be reliably modeled (Section 1.5) to deconvolute the photocurrent

generation process at SPR. Unlike radiative and waveguide modes, SPPs in metal films exhibit high field concentrations and propagate purely in-plane. This evanescent character increases the optical path length from the device thickness at normal incidence (~100 nm) to L_{SPP} ~ 10 μm (**Figure 4.2**b). Thus, coupling to SPP modes can further improve absorption beyond what is possible in conventional planar device geometries.[225, 226] Additionally, since the plasmon-supporting interfaces are external to the active layers, the MDM structure avoids changes to internal charge and exciton transport and active layer morphology from embedded nanostructures. Previous work on SPP-based OPDs in a MDM geometry has demonstrated that SPP fields can be effectively coupled to the device active layers and efficiently harvested as photocurrent.[227-231] The earlier studies by Kume *et al.* explored the wavelength and angular dependence of SPP-based photocurrent in single-layer CuPc Shottky diodes, while later work by Mapel *et al.* and Bora *et al.* on bilayer CuPc/C_{60} devices focused on the angular response at a single wavelength. However, none evaluated the full spectroscopic and angular dispersion of SPP-enhanced photocurrent generation in more efficient, bilayer OPVs.

Here we explore the broadband response to plasmon-enhanced absorption in planar OPVs with a MDM geometry using an attenuated total reflection (ATR) method in the Kretschmann configuration (**Figure 4.8**a).[204] Using an archetypal SubPc/C_{60} heterojunction, our experiments demonstrate broadband, direct conversion of SPPs to photocurrent with the EQE performance at SPR reaching 4.3x that at normal incidence. This increase is attributed to a simulated 9-fold enhancement in absorption efficiency within the ultrathin active layers. In addition, we show that absorption efficiency is maximized using near-field SPR coupling in the MDM geometry and is insensitive to the active layer deposition sequence. To provide further quantitative support for these conclusions, we employ rigorous device modeling to calculate the absorption, EQE, and

IQE spectra. As an extension of our results, we find that absorption efficiency in plasmonic MDM structures is relatively insensitive to active layer thicknesses down to a few monolayers, suggesting new means of probing photovoltaic energy conversion processes at the molecular-scale.

4.2.2 Experiment

1 mm thick glass substrates (Fisher Sci.) were cleaned via heated (40° C) sonication in detergent, deionized water, acetone, trichloroethylene, and isopropanol followed by boiling in isopropanol to remove any surface contaminants. A polyethylenimine ethoxylated (PEIE) layer was then spin-cast from a 0.4 wt% solution in water and methoxyethanol at 5000 rpm for 60 s and annealed at 100° C for 10 min to create a 10 nm thick wetting layer with a refractive index matching that of glass. For the bottom electrode, a thin Ag film was deposited using VTE at a rate of 5 Å/s to ensure an optically smooth film. For inverted devices, a second layer of PEIE was then spin cast to form a 10 nm layer on the cathode and act as a work function modifying layer. Next the small molecular active materials, C_{60} and SubPc, and the MoO*x* buffer layer were VTE deposited at deposition rates of 1, 0.5, and 0.5 Å/s respectively. Devices were shadow masked and a thin Ag top electrode was deposited with a diameter of 1 mm at a rate of 1 Å/s to prevent shorting. Depositions by VTE were all carried out at pressures below 5×10^{-7} Torr, with a rotating substrate held at room temperature; the entire device fabrication sequence was performed within a nitrogen-filled glove box containing less than 1 ppm O_2 and H_2O.

The organic materials SubPc (>99%), C_{60} (>99.5%), and BCP (>99%) were purchased from Luminescence Technology Corp., while MoO_3 (>99.99%) and Ag (>99.99%) were

obtained from Sigma Aldrich and Kurt J. Lesker, respectively. The active layer materials SubPc and C_{60} were additionally purified once through vacuum thermal gradient sublimation.

Transmissivity and reflectivity spectra (at normal and 7.5° incidence, respectively) were collected using a Perkin Elmer Lambda 750 UV/Vis/NIR spectrophotometer and used to confirm layer thicknesses. In both configurations, illumination was incident on the samples through the glass substrate. AFM measurements were performed in air with an Asylum Research Systems MFP-3D standalone system in tapping mode. Surface roughness measurements were averaged over 4 μm × 4 μm areas on each sample.

EQE measurements were carried out in ambient using a custom ATR Kretschmann setup (detailed in Section 4.2.5). Devices were tested at normal incidence before and after the ATR EQE scans to confirm there was no device degradation or change in spectral response. For reflectivity measurements, the specularly reflected beam off each sample was compared to the reflected beam of the same polarization from a thick (150 nm) silvered mirror as a baseline. For both reflectivity and EQE Kretschmann measurements, a 5 nm wavelength increment and an angular step size of 0.5° were used.

J-V testing was performed in a glove box without exposure to air. Devices were illuminated through the glass substrate with an Oriel solar simulator (Model 91191–1000) with an AM 1.5 filter and calibrated to 100 mW/cm^2 using an NREL-certified Si reference cell (Model PVM233 KG5). Data was collected using a Hewlett-Packard scanning parameter analyzer (Model 4156B). All device areas were measured using a Carl Zeiss A.1 optical microscope and included explicitly in calculating EQE, J_{sc}, and PCE.

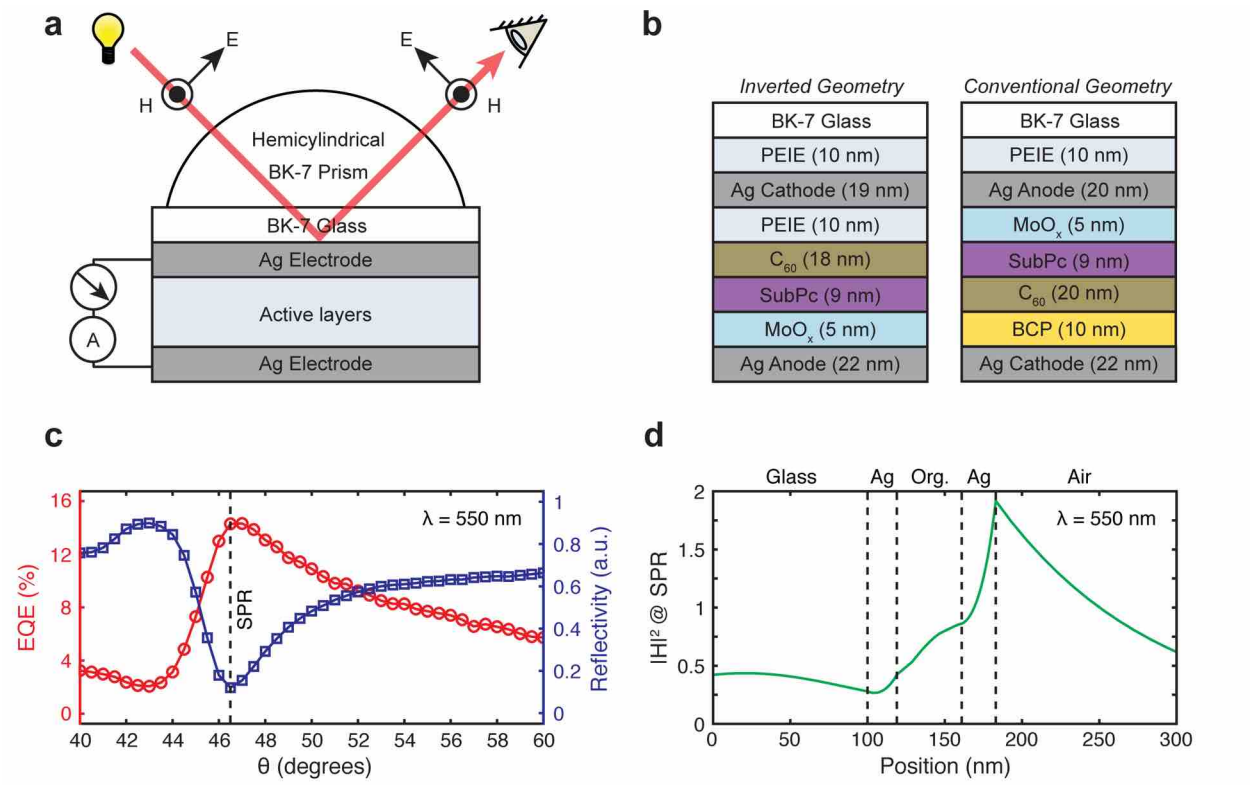

Figure 4.8 (a) Measurement setup of MDM devices in the Kretschmann configuration using monochromatic TM-polarized light incoupled to the device *via* a hemicylindrical prism and index-matching fluid. (b) Device structures used in this study, displayed in the same orientation as the testing setup in (a). (c) Angular scan of reflectivity and EQE at a single wavelength for the inverted device in (b), exhibiting a sharp drop in reflectivity and concomitant increase in EQE upon reaching SPR. (d) Calculated H-field at the SPR condition indicated in (c), exhibiting enhanced field magnitude and an exponential decay of the evanescent SPP mode localized at the Ag/air interface. As shown in (a), light is incident from the glass substrate in all measurements. [232]

4.2.3 OPVs with symmetric metal contacts

Two types of devices are studied (**Figure 4.8**b): a conventional and an "inverted" layer configuration. In the conventional device structure, the anode and MoO_x layers are deposited first, followed by the donor, acceptor, exciton blocker, and cathode layers. In the "inverted" structure, the cathode is deposited onto the substrate first, followed by PEIE, the acceptor, donor, MoO_x, and anode layers. Layer thicknesses are maintained to within experimental precision between the two structures, with only the active layers' order changing relative to the SPP-

supporting electrode. A similar separation distance between the silver electrodes is maintained in both geometries. In both structures, 5 nm of MoO_x is used as a work function modifying buffer layer at the anode[113] to provide the necessary built-in potential difference for efficient charge separation at the donor-acceptor heterojunction (**Figure 3.12**). Additionally, a low-workfunction PEIE layer is applied to the cathode in place of BCP in inverted devices to further improve V_{bi}.[23] This approach permits the selection of metal contacts for their plasmonic properties with less regard to their work functions.

Reflection and transmission spectra of devices at 7.5° and normal incidence, respectively, are shown in **Figure 4.9**. In all samples tested, we observe an excellent match between predicted and measured values. For these measurements, several substrates are placed in the deposition chamber and removed at incremental stages of the device fabrication process (illustrated in the insets of **Figure 4.9**), yielding a sample set from the same batch. This procedure enables fitting of layer thicknesses with nanometer precision, as slight variations between batches can have an enormous effect on the optics in MDM structures.

To confirm the rectifying behavior of the OPV devices, we tested the current density-voltage dependence under simulated AM 1.5 conditions (**Figure 4.10**). As expected for MDM devices with semitransparent electrodes at normal incidence, low PCEs of 0.48 ± 0.04 % and 0.95 ± 0.08 % were obtained for inverted and conventional devices, respectively. This result is almost entirely due to low photocurrent generation; without a thick back-reflector, optical interference within the active layers is suboptimal for absorption at normal incidence. However, the diode behavior confirms that even with symmetric metal contacts in the MDM configuration, we are able to achieve a functioning OPV and maintain a high open-circuit voltage (0.89 ± 0.05 V to 1.05 ± 0.02 V) characteristic of SubPc/C_{60} SHJ devices.[149]

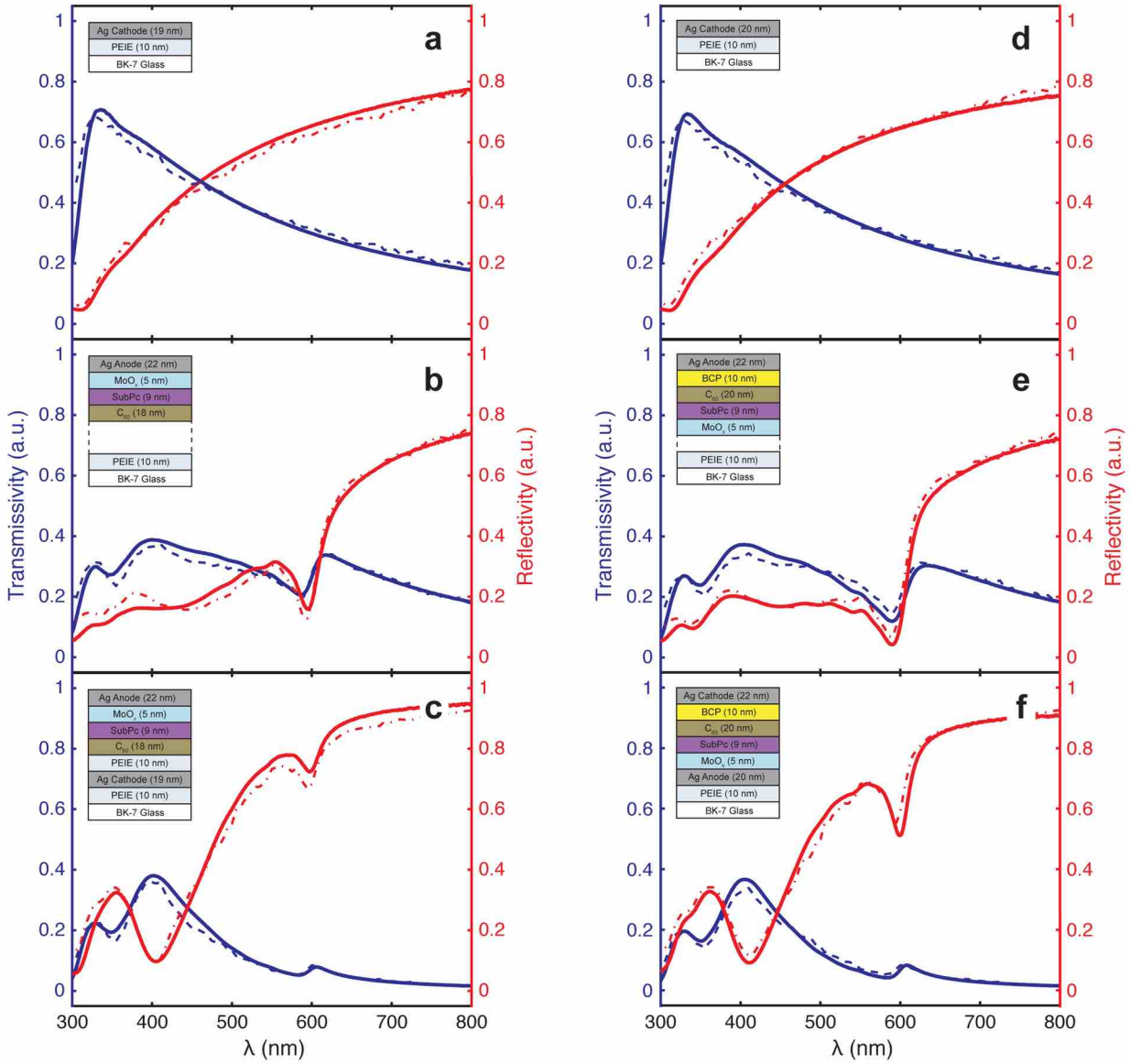

Figure 4.9 Reflectivity (red lines) and transmissivity (blue lines) spectra taken for sequentially deposited layers of both devices, measured at 7.5° and normal incidence respectively. Plots include (a,d) the silver cathode/anode, (b,e) organic layers and anode/cathode, and (c,f) complete inverted/conventional device structure. Modeled reflectivity (dash) and transmissivity (dot dash) spectra are included, showing the accuracy of the optical transfer-matrix model used in this study. Insets show the sample structures corresponding to each set of spectra, with dotted lines indicating the omitted layers. [232]

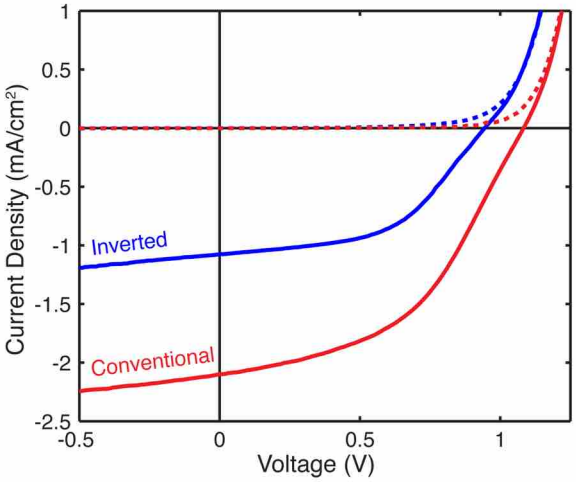

Figure 4.10 Current density-voltage characteristics of both inverted and conventional devices under illumination through the glass substrates with an AM 1.5 spectrum at an intensity equivalent to one sun. Testing occurred within a nitrogen glove box on devices fabricated in the same batches as those measured with ATR spectroscopy. [232]

4.2.4 Surface roughness measurements with AFM

For accurate device modeling at SPR, it is critical to minimize surface roughness of the electrodes. Roughness both modifies the Fresnel coefficients at the metal/dielectric interfaces and strongly attenuates SPP propagation lengths through dissipative losses *via* inelastic scattering, making the response at SPR difficult to predict.[52, 233] AFM of the cathode and anode indicated an RMS roughness of 0.438 nm and 2.85 nm for inverted devices and 0.467 nm and 0.988 nm for conventional devices, respectively (**Figure 4.11**). Because Ag is known to island on glass without a wetting layer, we employed PEIE as a semitransparent adhesion layer for the bottom electrode. This application of PEIE is uniquely suited for ATR spectroscopy techniques as it has a refractive index matched to glass and is completely non-absorbing in the visible spectrum, unlike metallic adhesion layers such as Ti. This allows the growth of pure, ultra-smooth Ag films without changing the local dielectric environment or plasmonic response of the metal. Indeed there is no presence of LSPR in the transmission/reflection spectra (**Figure 4.9**a,c)

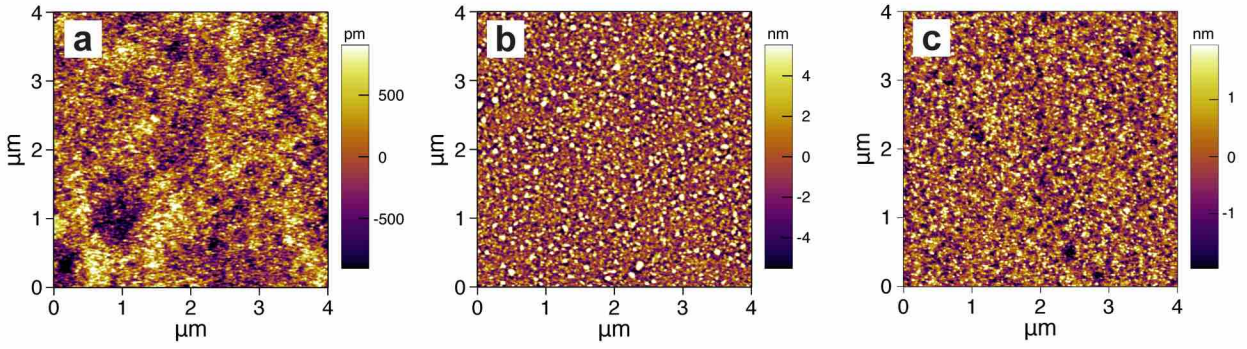

Figure 4.11 Tapping mode AFM micrographs of the surfaces of (a) the bottom Ag electrode, (b) top Ag electrode (anode) for the inverted devices, and (c) top Ag electrode (cathode) for the conventional geometry. The corresponding device structures are shown in **Figure 4.9**a, c, and f, respectively. Up to an order of magnitude higher roughness is observed for the two top electrodes, which we attribute to the underlying organic active layers. [232]

indicative of Ag islanding, which we observed to be completely stable at room temperature.

Since the bottom electrode structure Glass/PEIE/Ag was unchanged between both inverted and conventional devices, **Figure 4.11**a is representative of both device structures. However, the top electrodes in both device structures exhibited up to an order of magnitude larger roughness due to the inherent roughness of the underlying organic layers. While the quality of the Ag/air interface is critical to the damping of the SPP propagation, our early experiments indicated the bottom electrode plays a pivotal role in the predictability of the angular EQE and reflectivity response. As it is the most easily adjusted, every effort should be made to eliminate the lower electrode's roughness. This allows for accurate device modeling to be performed using literature values of refractive indices, without the need for effective refractive index fitting of constituent layers.

4.2.5 Attenuated total reflection setup

A detailed schematic diagram of the custom-built Kretschmann ATR setup for testing the dispersion of both EQE and reflectivity of OPV devices is shown in **Figure 4.12**. Light from a

halogen lamp was coupled into a monochromator (Newport 130 1/8m), with its output calibrated to a spectral full width at half maximum (FWHM) of 5 nm. A series of lenses and an aperture were used to collimate the beam divergence to less than 1° and remove spherical aberrations. A calcite Glan-Thompson polarizer was then used to polarize the light to either TM- or TE-polarization. Light was directed to either a calibrated silicon reference cell or the sample, following an identical optical path length in each case. Samples were attached to a motorized rotation stage for angular control of the incident light, coupled into each device using a hemicylindrical BK-7 lens and index matching fluid. To maximize photocurrent signal, we employed the overfilling method of device illumination, whereby the beam size exceeds the device area. Since devices used in this study had a diameter of 1 mm, a 1 mm diameter circular

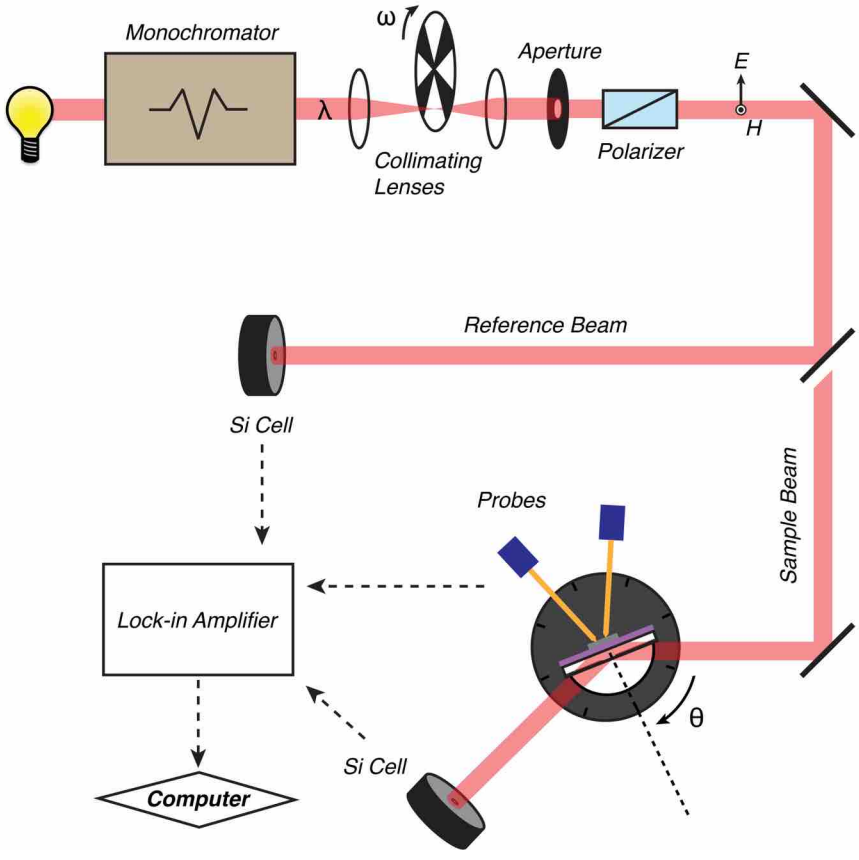

Figure 4.12 Schematic diagram of the Kretschmann configuration based ATR spectroscopy setup used in this study for probing the spectral and angular response of the device EQE and reflectivity. [232]

aperture was used on the reference cell and positioned to capture the same portion of the incident beam. Photocurrent signals from the device or reference cell were detected using a Stanford Research Systems SR530 lock-in amplifier at a modulation frequency of 185 Hz.

The use of the overfilling method during ATR-based EQE testing requires we correct for focusing effects from the hemicylindrical prism, as the average beam intensity over the projected device area varies with angle. We are able to extract the focusing factor as a function of angle by comparing the normalized angular response of the EQE under TE-polarized illumination to that predicted by our model (**Figure 4.13**). The focusing factor at normal incidence was calculated experimentally by scanning the EQE of the device with and without the prism, and accounts for the additional incoupling compared to the bare aperture of the reference cell. As can be seen here, after accounting for the angular intensity variation, we show an excellent agreement between the TM-polarized response, reproducing the SPR peak to within 1° offset. This small shift is likely due to the effect of surface roughness at the Ag/air interface, as the location of the dip in EQE at the onset of total internal reflection from the glass/Ag interface matches exactly. This normalization was performed for each individual device tested to ensure minor device-to-device variations in electrode size from shadow masking did not impact the focusing factor, and is accounted for in all of the ATR-based EQE data shown in this study.

In the case of angular reflectivity measurements using ATR (**Figure 4.15**a,b), unmasked films deposited simultaneously with the inverted and conventional devices (**Figure 4.9**c,f) were used so the entirety of the reflected light could be collected. To ensure the same portion of the beam was being probed as the devices, an additional 1 mm diameter aperture was inserted directly before the prism. Finally a calibrated silicon reference cell was attached to the motorized stage to capture the reflected light. This data was compared to a 150 nm thick Ag mirror as a

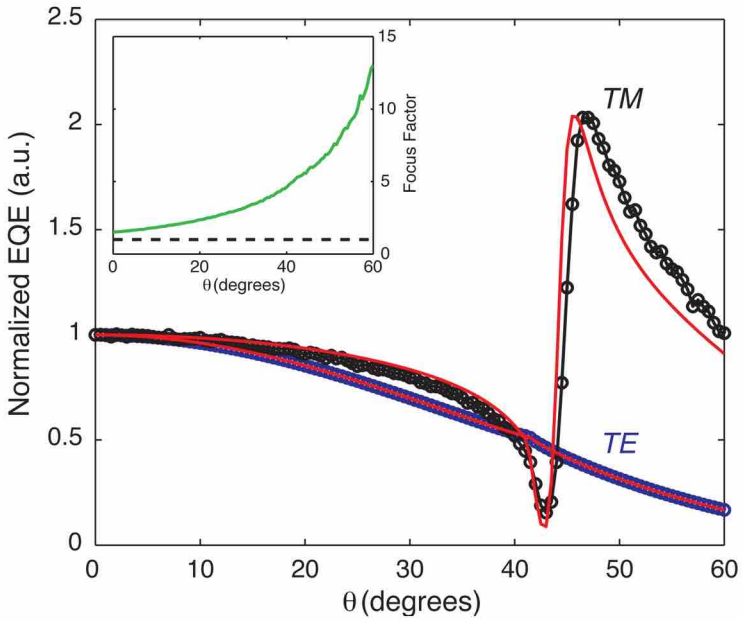

Figure 4.13 Example fitting of normalized EQE versus incident angle of an inverted device for TE and TM-polarized light (modeled data is shown in red). After accounting for the focusing factor (*Inset*) we observe excellent agreement between experiment and prediction for the SPR response. [232]

100 %*R* reference over the same angle-wavelength range. Because the projected area of the device stacks and silver mirrors remained unchanged during measurement (samples were effectively underfilled), there was no need to use a normalization to account for focusing from the prism.

4.2.6 SPR in "inverted" OPV nanocavities

Having experimentally validated our optical model at normal incidence (**Figure 4.9**), we now consider the spectroscopic performance of inverted devices at SPR. **Figure 4.8**c shows an ATR scan of reflectivity and EQE at a wavelength of 550 nm at angles past the critical angle for total internal reflection from the glass/Ag interface. For the SPR condition, we expect a near-zero reflectivity, as the light is strongly guided in the planar device structure and back-reflection is attenuated. The drop in reflectivity is accompanied by a concomitant increase in photocurrent

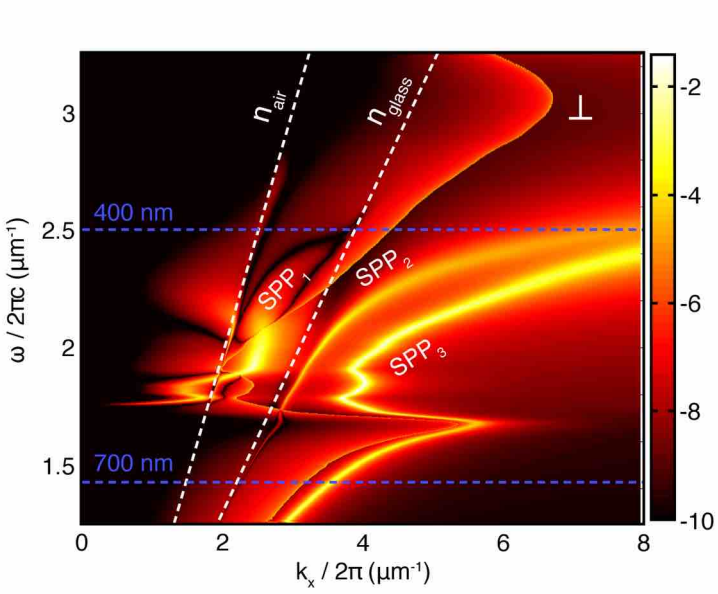

Figure 4.14 Calculated decay rate dispersion for a perpendicularly oriented exciton dipole located at the heterojunction in the inverted MDM structure. Dotted white lines indicate the light lines in air and in glass, while horizontal blue dotted lines delineate the measurement range used in this study. The dissipated power is shared among three principal decay channels: an SPP at the air/anode interface (SPP_1), an SPP at the glass/cathode interface (SPP_2), and an SPP shared between both silver contacts (SPP_3). [232]

(EQE) upon reaching SPR. As **Figure 4.8**d shows, our simulations indicate this to be an antisymmetric SPP mode located at the air-silver interface, further confirmed by the full device dispersion curve (**Figure 4.14**) solved using the dyadic Green's functions.[223] The generated SPP mode in this work is denoted SPP_1. Additionally, there are two other SPP modes that are supported within this structure: SPP mode between the silver-substrate interface (SPP_2) and the gap plasmon mode shared between both contacts and the internal medium (SPP_3).[207] Since wavevector matching in the Kretschmann configuration is limited to below the substrate (glass) light line, it is only possible to probe SPP_1 with this method. However, in applications such as integrated optical circuits, excitation of all three modes is possible, significantly improving optical field confinement to the active layers and providing additional control over the spectroscopic dispersion.

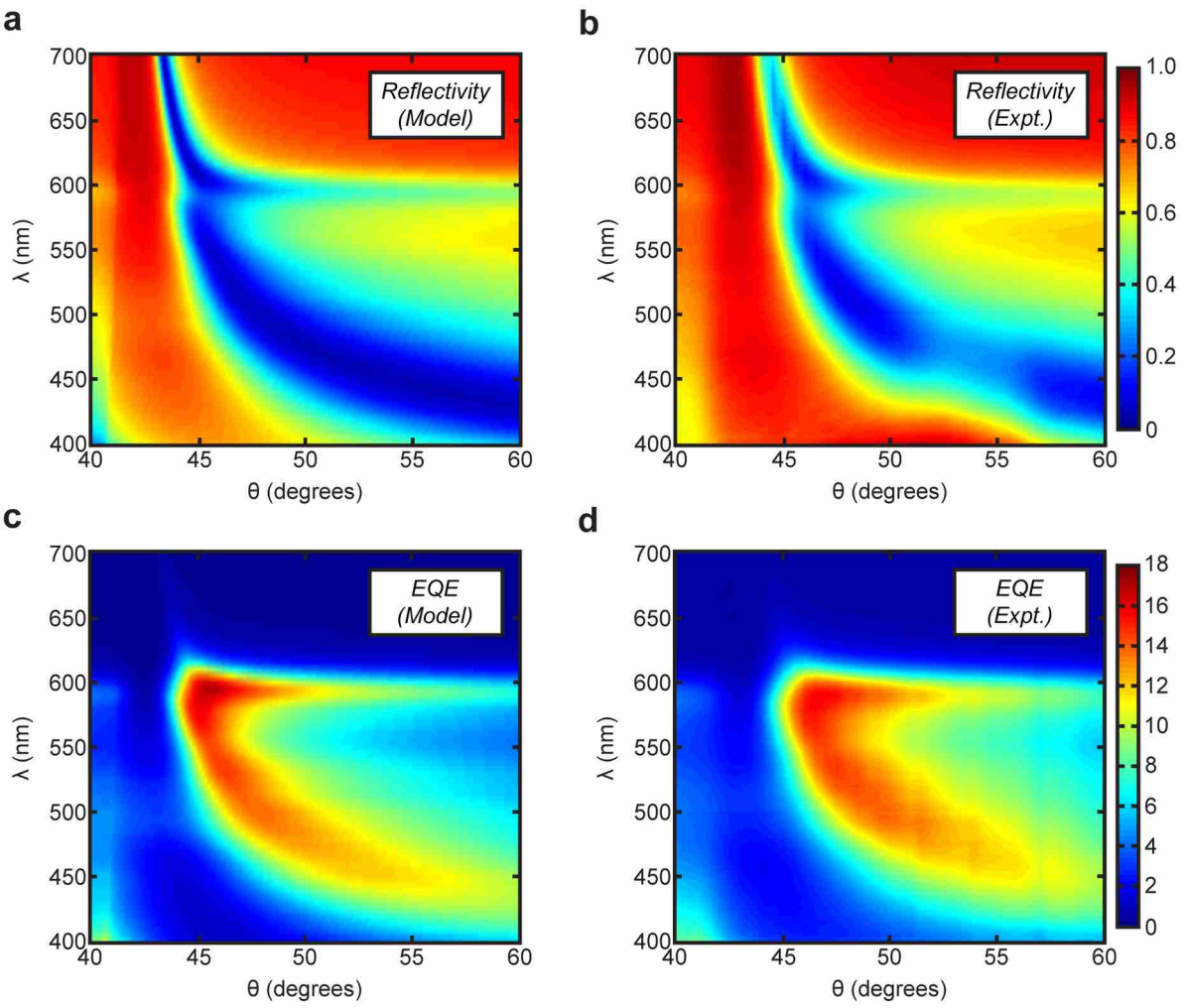

Figure 4.15 (a) Modeled and (b) measured reflectivity (a.u.) as a function of the incidence angle and free-space wavelength for the inverted MDM device structure. The experiment accurately reproduces the shape, magnitude, and location of the guided SPP_1 mode, except for a slight increase in reflectivity at the CT-exciton absorption peak in C_{60} (λ = 460 nm). The corresponding device EQE (%) as a function of angle and wavelength is also shown for both (c) modeled and (d) measured values. While the reflectivity data shows a slight discrepancy in the region of C_{60} absorption, the EQE of these devices closely matches predicted values at all wavelengths. Note the same scale bars are used for both model and experiment. [232]

Figure 4.15a,b shows the modeled and experimentally measured reflectivity dispersion for an inverted device on- and off-resonance with the SPP_1 mode. We observe an excellent, quantitative match between the measured and predicted reflectivities across the visible spectrum, with the exception of an increased reflectivity at SPR ($\Delta R \sim 0.2$) near the charge transfer (CT) state absorption of C_{60} at 460 nm.[86] This is likely due to a preferential orientation of the CT

exciton's transition dipole out-of-plane, which would produce an increase in the extraordinary extinction coefficient and modify the effective index of the structure at plasmon resonance. We expect this effect to be most pronounced at SPR since the electric field aligns perpendicular to the plane, exciting only perpendicularly oriented dipoles. A similar reflectivity response is observed at the sharp SubPc absorption peak (585 nm), indicating that both electronic transitions exhibit high oscillator strengths. At decreasing angles below the SPR condition, a growing proportion of the excited dipoles have an in-plane orientation, significantly reducing the effect of the anisotropic C_{60} absorption. As a result, the refractive index difference due to the observed anisotropy becomes entirely absent at normal incidence (**Figure 4.9**). That being said, it does not appear that this increase in reflectivity at the 460 nm SPR peak significantly affects absorbed power in the C_{60} layer, as the higher extinction coefficient directly offsets the reduced incoupling of light into the device.[199]

Figure 4.15c,d show that the measured EQE response is closely matched to the model prediction across the visible spectrum. The experimentally measured angular response is slightly broadened relative to the modeled (ideal) values, which we attribute to the anode's surface roughness at the Ag/air interface. To obtain these EQE fits, η_{CC} = 56% was assumed in the inverted device at SPR. The lower η_{CC} is attributed to a lower built-in field in devices using symmetric contacts, compared to that in conventional indium tin oxide (ITO) based cells. Furthermore, the use of PEIE causes electron doping of adjacent fullerene thin films, which can increase nongeminate charge recombination and decrease η_{CC}.[234] Importantly, accurate modeling of the EQE spectra at SPR and at normal incidence for the inverted geometry can only be obtained under the assumption that the MoO_x buffer is exciton-reflecting. This assumption differs from the behavior shown in Section 3.1.2 (and what we show below) of conventional

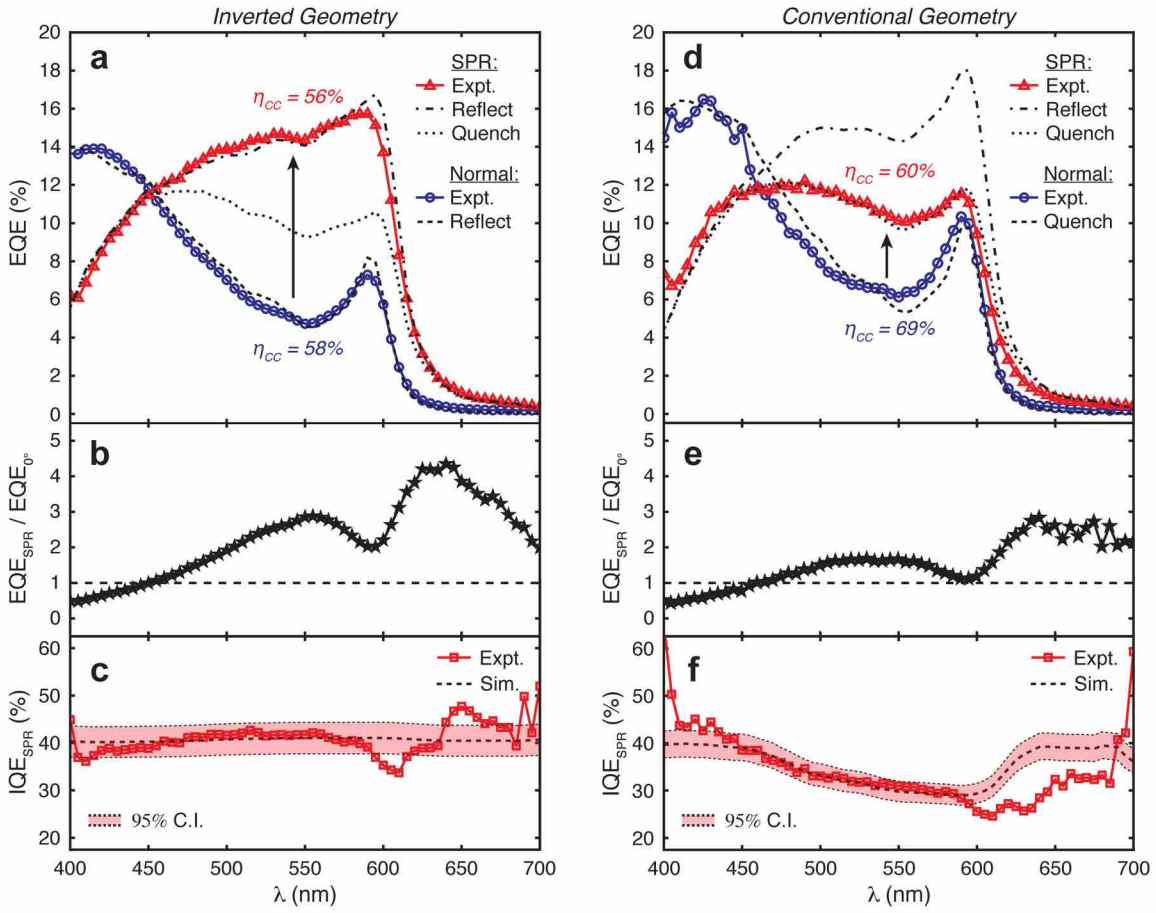

Figure 4.16 Spectral characteristics of an inverted device (a-c) and conventional device (d-f). (a,d) Measured EQE spectra at normal incidence (blue circles) and measured along the SPR condition (red triangles) as compared to the corresponding models. The dashed lines indicate the simulated response at normal incidence for exciton reflection and quenching boundary conditions in the inverted and conventional device, respectively. The dotted and dash-dotted lines indicate the simulated response at SPR for SubPc exciton quenching and reflection boundary conditions, respectively. While collection efficiency appears to drop slightly on-resonance in (d), a significant shift in the spectral shape due to the elimination of exciton quenching in SubPc by MoO_x is observed in (a). (b,e) The corresponding measured enhance-ment of photocurrent and EQE at SPR over that at normal incidence. IQE at SPR in the (c) inverted device and (f) conventional device assuming exciton reflection and quenching at the SubPc/MoO_x interface, respectively. Red squares indicate calculated IQE values from the measured devices and dashed lines indicate the corresponding models, with shaded regions representing the 95% confidence intervals. [232]

SubPc/C_{60} devices employing a MoO_x buffer layer. In conventional structures, accurate modeling of EQE spectra is achieved only if exciton quenching is assumed to occur at the SubPc/MoO_x interface. To illustrate this point, **Figure 4.16**a compares the EQE trace at SPR to simulations assuming a reflecting or quenching boundary condition.

To understand the difference in boundary conditions at the SubPc/MoO_x interface, we draw attention to the SubPc layer thickness used in this work, 9 nm, which closely matches L_D of SubPc.[46] We conclude that the majority of exciton recombination in the inverted devices studied here are due to interface recombination and not relaxation in the bulk. Increasing the L_D cannot drastically alter the shape of the modeled EQE spectrum (**Figure 4.16**a) – this can only be achieved by varying the boundary condition. We also note that if charge collection efficiency were changing between SPR and normal incidence conditions, we would see a shift in EQE across all wavelengths, not solely in the SubPc spectrum. Based on this analysis, the most appropriate conclusion is that the boundary condition at the MoO_x/SubPc interface is indeed changing from exciton quenching in conventional devices to exciton reflecting in inverted devices, based on deposition order.

It is well known that many organics in contact with MoO_x exhibit Fermi level pinning and band bending due to electron transfer to the oxide and subsequent hole buildup in the neighboring organic monolayers.[235, 236] Thus it follows that exciton-polaron annihilation with this space charge is likely responsible for the observed quenching behavior by MoO_x. We hypothesize that a change in molecular orientation at the donor/MoO_x interface upon reversed deposition order could shut off this quenching pathway.

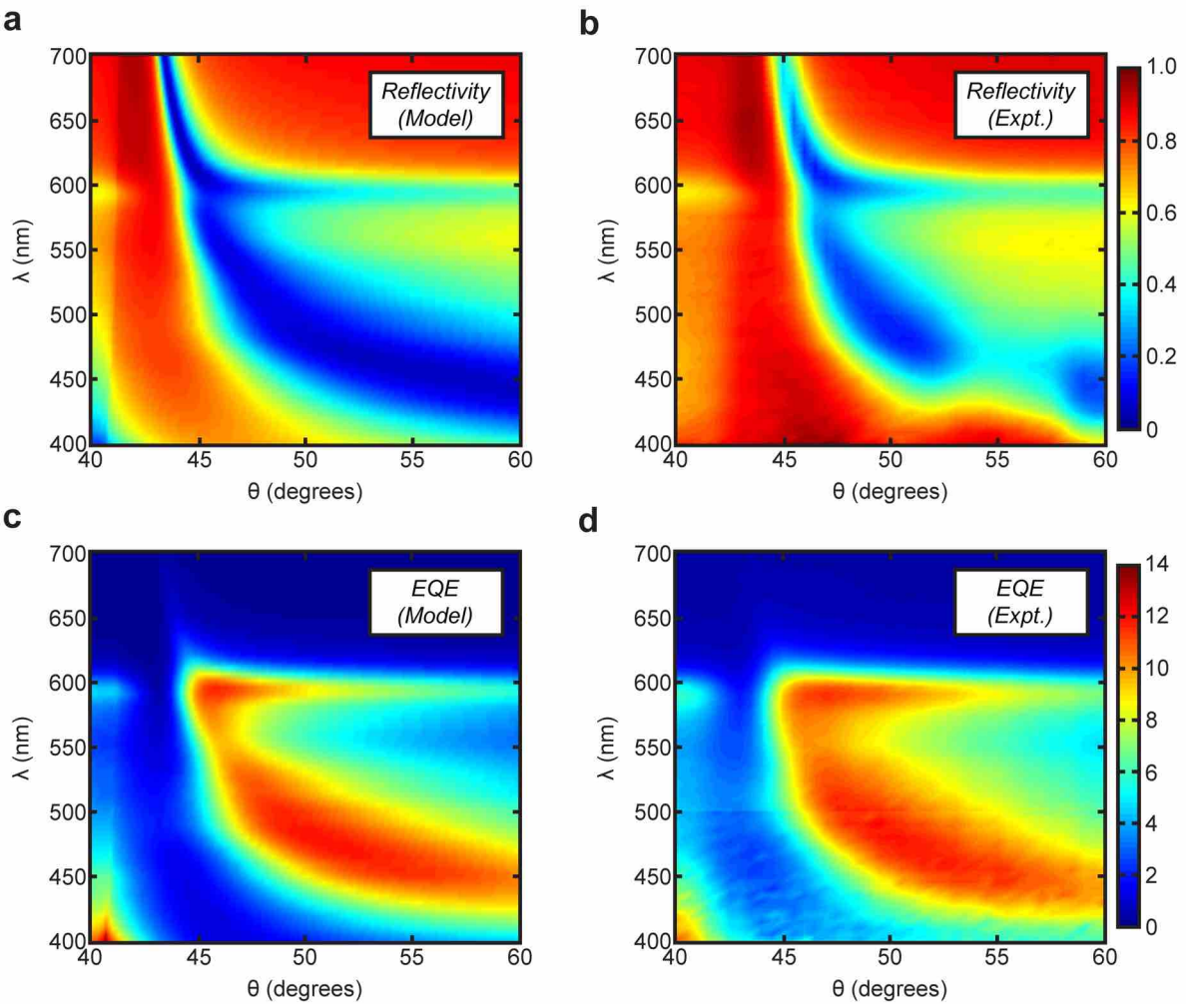

Figure 4.17 (a) Modeled and (b) measured reflectivity (a.u.) as a function of the incidence angle (in glass) and free-space wavelength for the conventional MDM device structure. The corresponding device EQE (%) as a function of angle and wavelength is also shown for both (c) modeled and (d) measured values. Note the same scale bars are used for both model and experiment. [232]

4.2.7 SPR in conventional OPV nanocavities

As can be seen in **Figure 4.17**, both the reflectivity and EQE are accurately matched between model and experiment for the conventional device. Again, we observe a slight discrepancy between measured and modeled reflectivity at the C_{60} aborption peak (λ = 460 nm), consistent with the inverted geometry. This asymmetry in the CT-exciton absorption does not appear to affect the observed performance, as the increased reflectivity is directly offset by an increase in

absorption within the C_{60} active layer. Finally, we note the presence of some horizontal and vertical linear artifacts in **Figure 4.15**d and **Figure 4.17**d, which are due to the interpolation of the colormap used in the figures and should not be considered physically relevant. The horizontal artifact at λ = 500 nm is due to a switch in the lock-in amplifier sensitivity, as the measurement scans were broken up into two separate wavelength ranges to maximize the signal-to-noise ratio.

We observed a similar increase in reflectivity (ΔR ~ 0.3) at 460 nm as seen with the inverted devices, albeit with a slightly larger deviation from the model due to an increased absorption in the C_{60} layer at SPR. Again this feature did not appear at angles close to normal incidence (**Figure 4.9**), further confirming that it is due to a slight orientation anisotropy in the extraordinary extinction coefficient. In contrast to the inverted devices, however, we observed a very good match to the measured EQE dispersion with the assumption that MoO_x quenches the excitons in SubPc (**Figure 4.16**d). Furthermore, we observed a ~9% drop in η_{CC} at SPR relative to normal incidence. This reduction is a broadband effect, impacting both donor and acceptor photocurrent production, and must originate from a higher nongeminate recombination rate under SPR conditions. Due to the low quantum yield of photon emission from CT states in SubPc/C_{60}, it is unlikely that the observed increase in recombination rate at SPR is caused by optical coupling of the CT emission to SPP modes. We speculate that the effect may result from hot electron injection into C_{60} from the SPP-supporting contact at resonance,[94] since the η_{CC} approaches that of the inverted geometry with electron doping from PEIE.

4.2.8 Broadband absorption and photocurrent enhancement at SPR

Both devices exhibited a broadband enhancement in photocurrent production at SPR over what is obtained at normal incidence, surpassing enhancement factors of 4.3x and 2.8x for the inverted

and conventional geometries, respectively (**Figure 4.16**b,e). The measured enhancement in EQE is directly attributed to a non-parasitic increase in active layer absorption efficiency, reaching a factor of 9x in both geometries under SPR conditions (**Figure 4.18**). EQE enhancement factors were found to be slightly lower than predicted from our calculated absorption enhancements, attributed to a low signal-to-noise ratio for both devices at normal incidence for wavelengths longer than ~625 nm (**Figure 4.19**). As shown in **Figure 4.18**a,b, at SPR the optical power is dissipated in the active layers at wavelengths corresponding to molecular electronic transitions. At photon energies below the SubPc bandgap, most power dissipation is confined to SPP thermalization near the Ag/air interface, further confirming the nature of the SPP_1 mode probed in this study. At wavelengths shorter than ~450nm (approaching ω_{sp}), SPP propagation is lossy, yielding a reduction in absorption efficiency and EQE below that at normal incidence (**Figure 4.18**c). Furthermore, as a result of exciton reflection at the MoO_x/SubPc interface in the inverted device, a 42% higher IQE in the SubPc spectrum was observed compared to the conventional device.

Interestingly, both devices exhibited nearly identical absorption spectra at SPR across the visible spectrum (**Figure 4.18**d). This is in direct contrast to performance at normal incidence, where absorption in the inverted structure is less efficient than in the conventional structure, due to a suboptimal optical field profile. Hence, the absorption and EQE enhancements at SPR are larger the inverted device architecture. Notably, the EQE spectra at SPR exhibited a nearly 50 nm redshift in the onset of absorption (**Figure 4.16**a,d) and a nearly flat absorption profile for wavelengths ranging from 450 to 600 nm (**Figure 4.18**d). This confirms that near-field SPP coupling is suited for broadening the sharp absorption peaks in organics and improving the spectral coverage of OPVs.

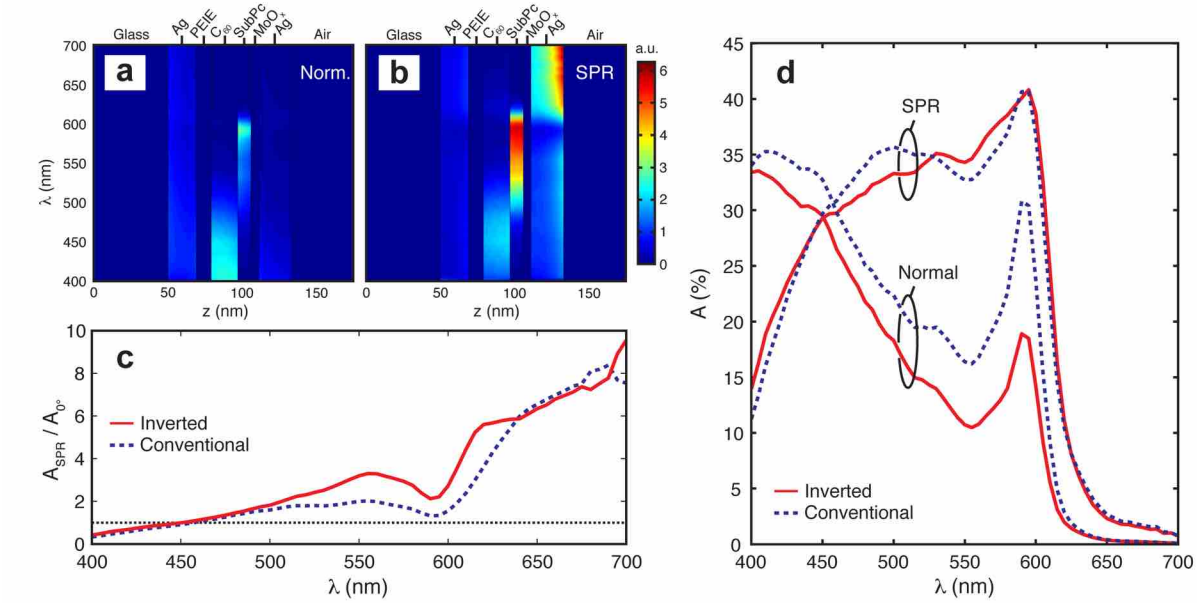

Figure 4.18 Spatial distribution of absorbed power vs. incident wavelength within the inverted geometry at (a) normal incidence and (b) SPR. (c) Modeled enhancement of active layer absorptivity for both structures at SPR over that at normal incidence. (d) Absorption efficiency of conventional and inverted devices simulated at normal incidence and SPR, illustrating the nearly identical absorption in both structures at SPR regardless of active layer orientation, which strongly affects absorption at normal incidence. [232]

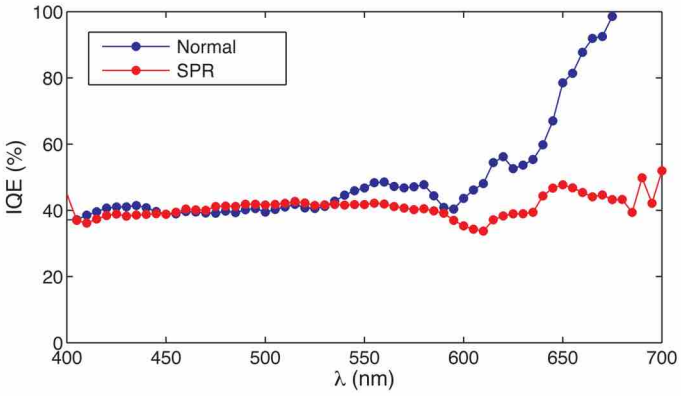

Figure 4.19 Measured IQE values for the inverted device at normal incidence (blue circles) and SPR (red circles). The higher absorption at long wavelengths at SPR yields a high signal-to-noise ratio, producing a flat IQE across the visible spectrum. At normal incidence, minimal photocurrent generation past 625 nm gives a low signal-to-noise ratio and an unphysically large IQE. For this reason, the measured EQE enhancement is reduced below predicted values. [232]

4.3 Conclusions

We have investigated the broadband enhancement of photocurrent generation from SPP coupling in planar OPV devices with inverted and conventional MDM geometries. We observed a significantly broadened absorption with a nearly 50 nm increase in spectral coverage towards longer wavelengths and EQE enhancements at SPR reaching 4.3x and 2.8x over that at normal incidence for inverted and conventional structures, respectively. These results were quantitatively supported by device modeling, which indicated that the remarkably high EQE at SPR in the SubPc spectrum of our inverted devices arose from both a 9x enhancement in absorption efficiency and a modification of the boundary condition of the SubPc/MoO_x interface. This typically quenching interface becomes exciton-reflecting for inverted cells, indicating exciton recombination at the MoO_x boundary is sensitive to deposition order. Furthermore, the results demonstrated how SPP coupling may be used to maximize absorption efficiency and increase spectral coverage, independent of η_D.

4.4 Future work

Direct means of excitation enable a number of applications, including OPDs for biosensing[227] and refractive index monitoring through passive[204] or active electrical stimulation.[215] The excitation of SPP modes can be accomplished in other ways as well, including linear and non-linear dispersion elements and luminescent coatings.[237, 238] These might enable future applications in photovoltaic window coatings[220-222] or in lateral tandem OPV configurations.[239] The angle and polarization-specific requirements for enhancement of photocurrent generation are thereby relaxed.

While our study has focused on the SPP_1 mode located at the Ag/air interface, coupling to other modes such as the gap plasmon (SPP_3) should minimize power dissipation in the metal contacts and further confine absorption to the active layers. Moreover, the devices in this study exhibited efficient photocurrent generation with active layer thickness on the order of ~λ/8 at the free space wavelength of 600 nm. By further reducing active layer thicknesses or using low-bandgap organic dyes, such confinement can be dramatically improved. Indeed simulations

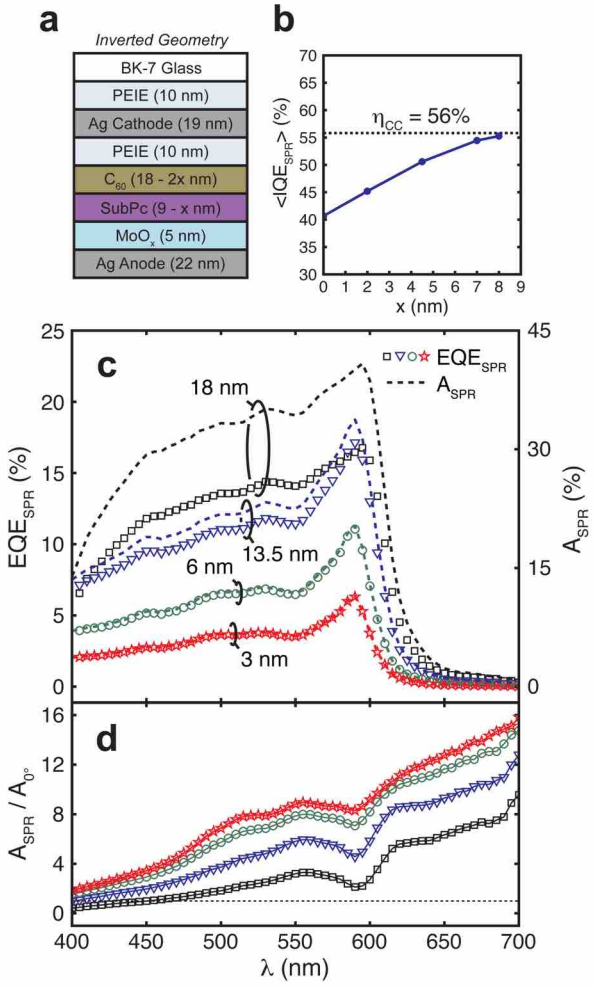

Figure 4.20 (a) Inverted device structure with a variable reduction in active layer thickness (x), with x = 0 nm corresponding to the inverted devices experimentally measured in this study. (b) Average IQE for the devices in (a), which asymptotically approaches η_{CC}. (c) EQE (symbols) and absorption efficiency (dashed lines) at SPR for the displayed active layer thickness. (d) Absorption efficiency enhancements at SPR over that at normal incidence for the corresponding devices in (c). All data displayed here corresponds to modeled values. [232]

indicate the potential for monolayer-scale detectors (**Figure 4.20**). OPDs with such a low modal volume may find applications as transducers for integrated on-chip plasmonic interconnects.[184, 222, 240-243]

Chapter 5

Summary and Outlook

In this thesis, we have presented multiple approaches to circumventing the competition between light absorption and exciton diffusion in OPVs. In Chapter 2 we investigated the impact of active layer mixing on exciton diffusion and CT dissociation in PMHJ solar cells. This approach is widely used to decouple the directions of light and exciton propagation within OPVs, such that active layer thicknesses can be increased significantly beyond L_D. However, in BHJ and PMHJ devices, the mixed layer morphology becomes the limiting factor in photocurrent generation and performance. By varying composition within the mixed layer of a SubPc/BCP:C_{60}/C_{60} PMHJ, we were able to systematically control the domain size of the fullerene domains at the heterojunction. Using cAFM, we determined an exponential dependence of domain size on fullerene volume fraction in small molecule binary blends. By correlating domain size in the mixed layer to PL quenching, we demonstrated that domains surpassing $4 \cdot L_D$ in diameter can be tolerated in BHJs with minimal reduction in η_D. In a 1-dimensional system such as a PHJ, layer dimensions are constrained well below this value, however the 3-dimensional distribution of the heterojunction in mixed layers increases the probability of reaching the interface due to geometric factors. By factoring out η_D from the IQE of the PMHJ devices, we also find η_{CT} drops exponentially below a critical fullerene domain size of ~43 nm. Below this value, the

recombination of the CT state progressively outcompetes the CT dissociation process. We attribute this trend to a shift in the CT population to more localized, Coulombically-bound states.

In Chapter 3 we demonstrated an alternative approach to the BHJ architecture for improving η_D in the active layers. As most η_D losses arise from either bulk recombination or quenching at the electrode interfaces, we introduced the EDL concept – a transparent active layer used to form a CHJ and improve the adjacent interlayer's IQE. Through both experiment and modeling, we validated this concept in an archetypal SubPc/C_{60} SHJ using a transparent, 5 nm thick α-NPD layer as an EDL for SubPc. We demonstrated a 66% enhancement in the η_D of the SubPc interlayer, yielding an increase in J_{sc} from 3.94 mA/cm^2 to 4.90 mA/cm^2, all without affecting the active layer absorption. However we also observed a significant decrease in FF from 61.5% to 49.2% upon EDL incorporation, resulting in the PCE remaining unchanged. Using impedance spectroscopy, we then demonstrated the FF reduction arises from space charge accumulation at the two heterojunctions due to the injection barrier introduced at the EDL/interlayer interface. We varied the V_{bi} of a CHJ and showed the interlayer/C_{60} subjunction is shut down prematurely by field inversion, while the EDL/interlayer subjunction is relatively insensitive to its effects. Through a combinatorial EDL study, we then determined the design criteria for creating a high-FF CHJ: the ΔE_{HOMO} should be kept below 0.2 eV to mitigate space charge accumulation, and materials should be selected such that the V_{MPPs} of the two subjunctions are closely matched and neither becomes voltage-limiting. Using these principles, we demonstrated champion TAPC/SubNc/C_{60} CHJ devices with a 46% PCE improvement over their SHJ reference cells (4.1% vs. 2.8%). Additionally, optimized CHJs exhibited nearly 100% η_D in the interlayer, confirming the effectiveness of the EDL in mitigating exciton recombination losses.

Finally in Chapter 4 we focused on enhancing absorption in OPVs using SPP coupling. As an alternative to LSP enhancements from metal nanoparticles and nanostructured electrodes, we investigated the use of plasmonic metal nanocavities serving as both the electrode and SPP-generating layers. Using a custom-built ATR setup in the Kretschmann geometry, we were able to directly stimulate SPPs at the Ag/air interface in SubPc/C_{60} PHJ-embedded MDM structures. At SPR conditions, we observed a nearly 50 nm broadening of the active layer absorption and EQE to longer wavelengths, increasing the spectral coverage. Furthermore, we demonstrated a 4.3x and 2.8x peak enhancement in EQE over normal incidence for inverted and conventional device structures, respectively. Using transfer matrix simulations, we attributed this to a 9-fold improvement in absorption efficiency at SPR. The large increases in absorption efficiency and EQE were achieved without affecting η_D in the active layers.

The methods presented in this thesis should not be considered mutually exclusive; all three are fully compatible with one another. Depending on the application, one must leverage the need for high IQE (diffusion efficiency) against EQE (absorption + diffusion efficiency), and all three offer unique advantages in this respect. Buffer layers are ubiquitous to all OPVs and are necessary for eliminating quenching and functioning as optical spacers. As such, EDLs can be applied to virtually any device structure to create a CHJ and are not limited to PHJ architectures. For example, ternary BHJs behave similarly to planar CHJs, exhibiting multiple heterojunctions operating electrically in parallel (but distributed throughout the bulk). Between these two architectures, similar design principles should apply, while the addition of a third absorber can significantly extend spectral coverage. In the case of solar concentrators, devices operate at high current densities and are much more susceptible to bimolecular recombination than in AM 1.5G conditions. Such applications are better suited for high-IQE planar CHJs than BHJs, as the planar

structure of the CHJ minimizes non-geminate recombination of charge carriers and the reduced loss of excitons to heat should assist in thermal management. Furthermore, CHJs may find applications as subcells in series tandems structures, as they can produce a high amount of photocurrent from a narrow absorption spectrum (when using an EDL) and can be more easily tuned for current-matching than BHJ subcells.

Simple plasmonic OPVs employing an MDM structure are well suited for ITO-free applications such as flexible PV systems for rapid, low-cost deployment, building-integrated PV, and semitransparent, power generating windows, while also being compatible with high throughput roll-to-roll fabrication. Semitransparent PVs are of particular interest, as their integration into windows requires no additional support structures or land use over what is already in place. Since noble gases are already applied between multi-pane windows to improve thermal insulation, encapsulation – which is a critical design consideration for moisture and oxygen-sensitive OPVs – is already provided. Depending on the incoupling strategy used, light absorption in MDM structures can be strongly enhanced off-normal while maintaining a high transparency for normal-incidence viewing. Since solar illumination is usually at oblique angles to a building's surface, this aspect appears highly beneficial. Especially in the case of semi-transparent PVs where absorption is limited, it is imperative to maximize device IQE. While the SPP devices shown here were only planar SHJs, we expect much better performance with plasmonic CHJs and BHJs.

Although the future remains uncertain for OPVs, it is likely they will play a role in the future development of a clean energy infrastructure. As has been outlined by Jacobson *et al.*, no single PV (or clean energy) technology can sustain the expanding needs of our global society. Instead, a diversified approach must be taken to stem global warming. By expanding new PV

applications and technologies, the path to a clean energy economy is made easier. We foresee OPVs playing an integral part in this process, and the work demonstrated here should help towards that goal.

Appendix A

List of publications and presentations

A.1 Publications

1. M. E. Sykes, A. Barito, and M. Shtein, "Resolving individual junction capacitances in cascade heterojunction organic photovoltaics," (*In preparation*)

2. A. Barito, M. E. Sykes, D. Bilby, S. J. Raney, K. L. Agrawal, B. Dong, P. F. Green, J. Kim, and M. Shtein, "Fundamental role of Förster resonant energy transfer in single- and multi-junction organic photovoltaics," (*In preparation*)

3. M. E. Sykes, J. Amonoo, K. Bergemann, P. F. Green, S. R. Forrest, and M. Shtein, "Critical domain sizes for efficient exciton transport and dissociation in small-molecular organic photovoltaics," (*In preparation*)

4. J. A. Amonoo, A. Li, G. E. Purdum, M. E. Sykes, B. Huang, E. F. Palermo, A. J. McNeil, M. Shtein, Y.-L. Loo, and P. F. Green, "Controlling morphology and enhancing thermal stability of polymer solar cells using all-conjugated gradient copolymers," (*Submitted*)

5. D. E. Wilcox, M. H. Lee, M. E. Sykes, A. Niedringhaus, E. Geva, B. D. Dunietz, M. Shtein, and J. P. Ogilvie, "Ultrafast charge-transfer dynamics at the boron subphthalocyanine chloride / C_{60} heterojunction: Comparison between experiment and theory," *Journal of Physical Chemistry Letters* **6**, 569 (2015).

6. S. E. Morris, D. Bilby, M. E. Sykes, H. Hashemi, M. J. Waters, J. Kieffer, J. Kim, and M. Shtein, "Effect of axial halogen substitution on the performance of subphthalocyanine based organic photovoltaic cells," *Organic Electronics* **15**, 3660 (2014).

7. D. E. Wilcox, M. E. Sykes, A. Niedringhaus, M. Shtein, J. P. Ogilvie, "Heterodyne-detected and ultrafast time-resolved second-harmonic generation for sensitive measurements of charge transfer," *Optics Letters* **39**, 4274 (2014).

8. A. Barito, M. E. Sykes, B. Huang, D. Bilby, B. Frieberg, J. Kim, P. F. Green, and M. Shtein, "Universal design principles for small molecular cascade heterojunction solar cells with high fill factor and internal quantum efficiency approaching 100%," *Advanced Energy Materials* **4**, 1400216 (2014).

9. M. E. Sykes, A. Barito, J. Amonoo, P. F. Green, and M. Shtein, "Broadband plasmonic photocurrent enhancement in planar organic photovoltaics embedded in a metallic nanocavity," *Advanced Energy Materials* **4**, 1301937 (2014).

10. D. Bilby, J. Amonoo, M. E. Sykes, B. Frieberg, B. Huang, J. Hungerford, M. Shtein, P. F. Green, and J. Kim, "Reduction of open circuit voltage loss in a polymer photovoltaic cell via interfacial molecular design: Insertion of a molecular spacer," *Applied Physics Letters* **103**, 203902 (2013).

11. A. Barito, M. E. Sykes, D. Bilby, J. Amonoo, Y. Jin, S. E. Morris, P. F. Green, J. Kim, and M. Shtein, "Recovering lost excitons in organic photovoltaics with a transparent dissociation layer," *Journal of Applied Physics* **113**, 203110 (2013).

12. K. Agrawal, M. E. Sykes, K. H. An, B. Freiberg, P. F. Green, and M. Shtein, "Influence of exciton lifetime on charge carrier dynamics in an organic heterostructure," *Applied Physics Letters* **102**, 113304 (2013).

A.2 Presentations

1. "Universal design principles for cascade heterojunction organic photovoltaics with broad spectral coverage and power conversion efficiency greater than 8%," A. Barito, M. E. Sykes, D. Bilby, B. Huang, K. L. Agrawal, B. X. Dong, B. Frieberg, P. F. Green, J. Kim, and M. Shtein, MRS Fall Meeting, Boston, MA (2014).

2. "Effect of copolymer chain architecture on active layer morphology and device performance," J. Amonoo, A. Li, M. Sykes, B. Huang, E. Palermo, A. McNeil, M. Shtein, P. F. Green, APS Meeting, Denver, CO (2014).

3. "Reduction of open circuit voltage loss in a polymer photovoltaic cell via interfacial molecular design," D. Bilby, J. Amonoo, M. Sykes, S. Morris, B. Frieberg, B. Huang, J. Hungerford, M. Shtein, P. Green, J. Kim, ACS National Meeting and Exposition, Indianapolis, IN (2013).

4. "Exciton dissociation layers for maximizing current generation in organic photovoltaics," A. Barito, M. E. Sykes, S. E. Morris, J. Amonoo, D. Bilby, J. Kim, P. F. Green, and M. Shtein, MRS Spring Meeting, San Francisco, CA (2013).

5. "Optically enhanced exciton diffusion in OPVs," M. Sykes, A. Barito, D. Bilby, J. Kim, and M. Shtein, MRS Spring Meeting, San Francisco, CA (2013).

6. “Plexciton-enabled photon recycling in Metal-Dielectric-Metal OPVs,” M. Sykes, A. Barito, K.H. An, and M. Shtein, MRS Fall Meeting, Boston, MA (2012).

7. “Optical field modulation of current in organic light emitting diodes,” K. Agrawal, M. Sykes, K.H. An, and M. Shtein, MRS Spring Meeting, San Francisco, CA (2012).

8. “Tailoring plasmonic and dielectric nanostructures for angle-selective photon management in organic photovoltaics,” M. Sykes, B. Roberts, N. Dissanayake, K.H. An, M. Shtein and P.C. Ku, EFRC External Review, Baltimore, MD (2012).

9. “Plasmon-enhanced exciton generation in organic photovoltaics,“ M. Sykes, B. Roberts, K. H. An, P.C. Ku, M. Shtein, Science for our Nation’s Energy Future: EFRC Summit and Forum, Washington D.C. (2011).

10. “High-efficiency surface plasmon energy harvesting using optimized organic photovoltaics,” M. Sykes, B. Roberts, K.H. Ah, P.C. Ku, M. Shtein, MRS Spring Meeting, San Francisco, CA (2011).

Bibliography

1. O. Edenhofer, *IPCC Special Report on Renewable Energy Sources and Climate Change Mitigation*, Cambridge University Press, 2011.

2. G. Ceballos, P. R. Ehrlich, A. D. Barnosky, A. García, R. M. Pringle and T. M. Palmer, *Scientific Reports* **1**, e1400253 (2015).

3. *International Energy Outlook 2014*, U.S. Energy Information Administration, 2014.

4. M. Z. Jacobson, M. A. Delucchi, G. Bazouin, Z. A. F. Bauer, C. C. Heavey, E. Fisher, S. B. Morris, D. J. Y. Piekutowski, T. A. Vencill and T. W. Yeskoo, *Energy & Environmental Science*, DOI: 10.1039/c5ee01283j (2015).

5. S. B. Darling and F. You, *RSC Advances* **3**, 17633 (2013).

6. J. Jean, P. R. Brown, R. L. Jaffe, T. Buonassisi and V. Bulović, *Energy & Environmental Science* **8**, 1200 (2015).

7. O. Awartani, B. I. Lemanski, H. W. Ro, L. J. Richter, D. M. DeLongchamp and B. T. O'Connor, *Advanced Energy Materials* **3**, 399 (2013).

8. S. Biswas, O. Shalev and M. Shtein, *Annual Review of Chemical and Biomolecular Engineering* **4**, 289 (2013).

9. M. Kaltenbrunner, M. S. White, E. D. Glowacki, T. Sekitani, T. Someya, N. S. Sariciftci and S. Bauer, *Nature Communications* **3**, 770 (2012).

10. *ASTM G173-03(2012), Standard Tables for Reference Solar Spectral Irradiances: Direct Normal and Hemispherical on 37° Tilted Surface*, ASTM International, West Conshohocken, PA, 2012.

11. N. C. Giebink, G. P. Wiederrecht, M. R. Wasielewski and S. R. Forrest, *Physical Review B* **83**, 195326 (2011).

12. A. W. Hains, Z. Liang, M. A. Woodhouse and B. A. Gregg, *Chemical Reviews* **110**, 6689 (2010).

13. C. C. Mattheus, W. Michaelis, C. Kelting, W. S. Durfee, D. Wöhrle and D. Schlettwein, *Synthetic Metals* **146**, 335 (2004).

14. L. Zhang, S. M. Fakhouri, F. Liu, J. C. Timmons, N. A. Ran and A. L. Briseno, *Journal of Materials Chemistry* **21**, 1329 (2011).

15. M. Pope and C. E. Swenberg, *Electronic Processes in Organic Crystals*, Clarendon Press, Oxford University Press, 1999.

16. J. A. Carr and S. Chaudhary, *Energy & Environmental Science* **6**, 3414 (2013).

17. H. Bässler, *Physica Status Solidi (b)* **175**, 15 (1993).

18. S. M. Menke and R. J. Holmes, *Energy & Environmental Science* **7**, 499 (2014).

19. S. M. Menke, W. A. Luhman and R. J. Holmes, *Nature Materials* **12**, 152 (2013).

20. O. Shalev and M. Shtein, *Organic Electronics* **14**, 94 (2013).

21. F. C. Krebs, *Solar Energy Materials and Solar Cells* **93**, 394 (2009).

22. J. J. van Franeker, M. Turbiez, W. Li, M. M. Wienk and R. A. Janssen, *Nature Communications* **6**, 6229 (2015).

23. Y. Zhou, C. Fuentes-Hernandez, J. Shim, J. Meyer, A. J. Giordano, H. Li, P. Winget, T. Papadopoulos, H. Cheun, J. Kim, M. Fenoll, A. Dindar, W. Haske, E. Najafabadi, T. M. Khan, H. Sojoudi, S. Barlow, S. Graham, J. L. Bredas, S. R. Marder, A. Kahn and B. Kippelen, *Science* **336**, 327 (2012).

24. M. Shtein, H. F. Gossenberger, J. B. Benziger and S. R. Forrest, *Journal of Applied Physics* **89**, 1470 (2001).

25. C. W. Tang, *Applied Physics Letters* **48**, 183 (1986).

26. P. Peumans, A. Yakimov and S. R. Forrest, *Journal of Applied Physics* **93**, 3693 (2003).

27. P. Peumans and S. R. Forrest, *Chemical Physics Letters* **398**, 27 (2004).

28. A. J. Barker, K. Chen and J. M. Hodgkiss, *Journal of the American Chemical Society* **136**, 12018 (2014).

29. C. L. Braun, *The Journal of Chemical Physics* **80**, 4157 (1984).

30. S. Gélinas, A. Rao, A. Kumar, S. L. Smith, A. W. Chin, J. Clark, T. S. v. d. Poll, G. C. Bazan and R. H. Friend, *Science* **343**, 512 (2014).

31. M. Hilczer and M. Tachiya, *Journal of Physical Chemistry C* **114**, 6808 (2010).

32. X.-Y. Zhu, Q. Yang and M. Muntwiler, *Accounts of Chemical Research* **42**, 1779 (2009).

33. K. Vandewal, S. Albrecht, E. T. Hoke, K. R. Graham, J. Widmer, J. D. Douglas, M. Schubert, W. R. Mateker, J. T. Bloking, G. F. Burkhard, A. Sellinger, J. M. Frechet, A.

Amassian, M. K. Riede, M. D. McGehee, D. Neher and A. Salleo, *Nature Materials* **13**, 63 (2014).

34. N. C. Giebink, G. P. Wiederrecht, M. R. Wasielewski and S. R. Forrest, *Physical Review B* **82**, 155305 (2010).

35. N. R. Monahan, K. W. Williams, B. Kumar, C. Nuckolls and X. Y. Zhu, *Physical Review Letters* **114**, 247003 (2015).

36. S. Albrecht, K. Vandewal, J. R. Tumbleston, F. S. Fischer, J. D. Douglas, J. M. Frechet, S. Ludwigs, H. Ade, A. Salleo and D. Neher, *Advanced Materials* **26**, 2533 (2014).

37. B. Verreet, K. Cnops, D. Cheyns, P. Heremans, A. Stesmans, G. Zango, C. G. Claessens, T. Torres and B. P. Rand, *Advanced Energy Materials* **4**, 1301413 (2014).

38. M. A. Baldo and S. R. Forrest, *Physical Review B* **64**, 085201 (2001).

39. L. Yan, M. G. Mason, C. W. Tang and Y. Gao, *Applied Surface Science* **175**, 412 (2001).

40. L. Yan, N. J. Watkins, S. Zorba, Y. Gao and C. W. Tang, *Applied Physics Letters* **79**, 4148 (2001).

41. G. F. Burkhard, E. T. Hoke, Z. M. Beiley and M. D. McGehee, *The Journal of Physical Chemistry C* **116**, 26674 (2012).

42. W.-I. Jeong, Y. E. Lee, H.-S. Shim, T.-M. Kim, S.-Y. Kim and J.-J. Kim, *Advanced Functional Materials* **22**, 3089 (2012).

43. C. K. Renshaw, J. D. Zimmerman, B. E. Lassiter and S. R. Forrest, *Physical Review B* **86**, 085324 (2012).

44. B. Verreet, A. Bhoolokam, A. Brigeman, R. Dhanker, D. Cheyns, P. Heremans, A. Stesmans, N. C. Giebink and B. P. Rand, *Physical Review B* **90**, 115304 (2014).

45. S. Chen, S. W. Tsang, T. H. Lai, J. R. Reynolds and F. So, *Advanced Materials* **26**, 6125 (2014).

46. A. Barito, M. E. Sykes, D. Bilby, J. Amonoo, Y. Jin, S. E. Morris, P. F. Green, J. Kim and M. Shtein, *Journal of Applied Physics* **113**, 203110 (2013).

47. J. D. A. Lin, O. V. Mikhnenko, J. Chen, Z. Masri, A. Ruseckas, A. Mikhailovsky, R. P. Raab, J. Liu, P. W. M. Blom, M. A. Loi, C. J. García-Cervera, I. D. W. Samuel and T.-Q. Nguyen, *Materials Horizons* **1**, 280 (2014).

48. W. A. Luhman and R. J. Holmes, *Advanced Functional Materials* **21**, 764 (2011).

49. R. R. Lunt, N. C. Giebink, A. A. Belak, J. B. Benziger and S. R. Forrest, *Journal of Applied Physics* **105**, 053711 (2009).

50. D. M. DeLongchamp, R. J. Kline, D. A. Fischer, L. J. Richter and M. F. Toney, *Advanced Materials* **23**, 319 (2011).

51. L. A. A. Pettersson, L. S. Roman and O. Inganäs, *Journal of Applied Physics* **86**, 487 (1999).

52. I. Filiński, *Physica Status Solidi (b)* **49**, 577 (1972).

53. C. C. Katsidis and D. I. Siapkas, *Applied Optics* **41**, 3978 (2002).

54. K. H. An, B. O'Connor, K. P. Pipe and M. Shtein, *Organic Electronics* **10**, 1152 (2009).

55. K. S. Chen, H. L. Yip, J. F. Salinas, Y. X. Xu, C. C. Chueh and A. K. Jen, *Advanced Materials* **26**, 3349 (2014).

56. X. Tong, B. E. Lassiter and S. R. Forrest, *Organic Electronics* **11**, 705 (2010).

57. K. Yao, X.-K. Xin, C.-C. Chueh, K.-S. Chen, Y.-X. Xu and A. K. Y. Jen, *Advanced Functional Materials* **25**, 567 (2015).

58. E. Centurioni, *Applied Optics* **44**, 7532 (2005).

59. A. K. Ghosh and T. Feng, *Journal of Applied Physics* **49**, 5982 (1978).

60. J. J. M. Halls, C. A. Walsh, N. C. Greenham, E. A. Marseglia, R. H. Friend, S. C. Moratti and A. B. Holmes, *Nature* **376**, 498 (1995).

61. G. Yu, J. Gao, J. C. Hummelen, F. Wudl and A. J. Heeger, *Science* **270**, 1789 (1995).

62. C. Liu, C. Yi, K. Wang, Y. Yang, R. S. Bhatta, M. Tsige, S. Xiao and X. Gong, *ACS Applied Materials and Interfaces* **7**, 4928 (2015).

63. S. Liu, P. You, J. Li, J. Li, C.-S. Lee, B. S. Ong, C. Surya and F. Yan, *Energy & Environmental Science* **8**, 1463 (2015).

64. Y. Liu, J. Zhao, Z. Li, C. Mu, W. Ma, H. Hu, K. Jiang, H. Lin, H. Ade and H. Yan, *Nature Communications* **5**, 5293 (2014).

65. M. C. Scharber and N. S. Sariciftci, *Progress in Polymer Science* **38**, 1929 (2013).

66. R. Pandey and R. J. Holmes, *Applied Physics Letters* **100**, 083303 (2012).

67. J. Bisquert and G. Garcia-Belmonte, *The Journal of Physical Chemistry Letters* **2**, 1950 (2011).

68. D. M. N. M. Dissanayake, A. Ashraf, Y. Pang and M. D. Eisaman, *Advanced Energy Materials* **4**, 1300525 (2014).

69. B. P. Lyons, N. Clarke and C. Groves, *Energy & Environmental Science* **5**, 7657 (2012).

70. U. Wurfel, D. Neher, A. Spies and S. Albrecht, *Nature Communications* **6**, 6951 (2015).

71. W. Chen, M. P. Nikiforov and S. B. Darling, *Energy & Environmental Science* **5**, 8045 (2012).

72. N. E. Jackson, B. M. Savoie, T. J. Marks, L. X. Chen and M. A. Ratner, *The Journal of Physical Chemistry Letters* **6**, 77 (2015).

73. R. Pandey, A. A. Gunawan, K. A. Mkhoyan and R. J. Holmes, *Advanced Functional Materials* **22**, 617 (2012).

74. J. D. Roehling, K. J. Batenburg, F. B. Swain, A. J. Moulé and I. Arslan, *Advanced Functional Materials* **23**, 2115 (2013).

75. G. J. Hedley, A. J. Ward, A. Alekseev, C. T. Howells, E. R. Martins, L. A. Serrano, G. Cooke, A. Ruseckas and I. D. Samuel, *Nature Communications* **4**, 2867 (2013).

76. S. Kouijzer, J. J. Michels, M. van den Berg, V. S. Gevaerts, M. Turbiez, M. M. Wienk and R. A. Janssen, *Journal of the American Chemical Society* **135**, 12057 (2013).

77. F. Yang, M. Shtein and S. R. Forrest, *Nature Materials* **4**, 37 (2004).

78. S. Sweetnam, K. R. Graham, G. O. Ngongang Ndjawa, T. Heumuller, J. A. Bartelt, T. M. Burke, W. Li, W. You, A. Amassian and M. D. McGehee, *Journal of the American Chemical Society* **136**, 14078 (2014).

79. J. Xue, B. P. Rand, S. Uchida and S. R. Forrest, *Advanced Materials* **17**, 66 (2005).

80. W. Cao and J. Xue, *Energy & Environmental Science* **7**, 2123 (2014).

81. C. W. Chen, Z. Y. Huang, Y. M. Lin, W. C. Huang, Y. H. Chen, J. Strzalka, A. Y. Chang, R. D. Schaller, C. K. Lee, C. W. Pao and H. W. Lin, *Physical Chemistry Chemical Physics* **16**, 8852 (2014).

82. Y. H. Chen, L. Y. Lin, C. W. Lu, F. Lin, Z. Y. Huang, H. W. Lin, P. H. Wang, Y. H. Liu, K. T. Wong, J. Wen, D. J. Miller and S. B. Darling, *Journal of the American Chemical Society* **134**, 13616 (2012).

83. X. Xiao, K. J. Bergemann, J. D. Zimmerman, K. Lee and S. R. Forrest, *Advanced Energy Materials* **4**, 1301557 (2014).

84. X. Xiao, J. D. Zimmerman, B. E. Lassiter, K. J. Bergemann and S. R. Forrest, *Applied Physics Letters* **102**, 073302 (2013).

85. A. N. Bartynski, C. Trinh, A. Panda, K. Bergemann, B. E. Lassiter, J. D. Zimmerman, S. R. Forrest and M. E. Thompson, *Nano Letters* **13**, 3315 (2013).

86. S. Kazaoui, N. Minami, Y. Tanabe, H. J. Byrne, A. Eilmes and P. Petelenz, *Physical Review B* **58**, 7689 (1998).

87. Z. T. Liu, C. Y. Kwong, C. H. Cheung, A. B. Djurišić, Y. Chan and P. C. Chui, *Synthetic Metals* **150**, 159 (2005).

88. K. J. Bergemann, J. A. Amonoo, B. Song, P. F. Green and S. R. Forrest, *Nano Letters* **15**, 3994 (2015).

89. A. Barito, M. E. Sykes, B. Huang, D. Bilby, B. Frieberg, J. Kim, P. F. Green and M. Shtein, *Advanced Energy Materials* **4**, 1400216 (2014).

90. J. A. Amonoo, E. Glynos, X. C. Chen and P. F. Green, *The Journal of Physical Chemistry C* **116**, 20708 (2012).

91. L. S. C. Pingree, O. G. Reid and D. S. Ginger, *Nano Letters* **9**, 2946 (2009).

92. C. J. Takacs, S. D. Collins, J. A. Love, A. A. Mikhailovsky, D. Wynands, G. C. Bazan, T.-Q. Nguyen and A. J. Heeger, *ACS Nano* **8**, 8141 (2014).

93. H. Yan, D. Li, C. He, Z. Wei, Y. Yang and Y. Li, *Nanoscale* **5**, 11649 (2013).

94. R. Dhanker, N. Chopra and N. C. Giebink, *Advanced Functional Materials* **24**, 4775 (2014).

95. W. Chen, T. Xu, F. He, W. Wang, C. Wang, J. Strzalka, Y. Liu, J. Wen, D. J. Miller, J. Chen, K. Hong, L. Yu and S. B. Darling, *Nano Letters* **11**, 3707 (2011).

96. *ASTM E112-13, Standard Test Methods for Determining Average Grain Size*, ASTM International, West Conshohocken, PA, 2013.

97. P. A. Vesilind, *Resource Recovery and Conservation* **5**, 275 (1980).

98. S. R. Forrest, *Chemical Reviews* **97**, 1793 (1997).

99. K. Asadi, H. J. Wondergem, R. S. Moghaddam, C. R. McNeill, N. Stingelin, B. Noheda, P. W. M. Blom and D. M. de Leeuw, *Advanced Functional Materials* **21**, 1887 (2011).

100. S. Bommel, N. Kleppmann, C. Weber, H. Spranger, P. Schafer, J. Novak, S. V. Roth, F. Schreiber, S. H. Klapp and S. Kowarik, *Nature Communications* **5**, 5388 (2014).

101. A. A. Bakulin, A. Rao, V. G. Pavelyev, P. H. van Loosdrecht, M. S. Pshenichnikov, D. Niedzialek, J. Cornil, D. Beljonne and R. H. Friend, *Science* **335**, 1340 (2012).

102. A. E. Jailaubekov, A. P. Willard, J. R. Tritsch, W. L. Chan, N. Sai, R. Gearba, L. G. Kaake, K. J. Williams, K. Leung, P. J. Rossky and X. Y. Zhu, *Nature Materials* **12**, 66 (2013).

103. B. M. Savoie, A. Rao, A. A. Bakulin, S. Gelinas, B. Movaghar, R. H. Friend, T. J. Marks and M. A. Ratner, *Journal of the American Chemical Society* **136**, 2876 (2014).

104. K. Vandewal, J. Widmer, T. Heumueller, C. J. Brabec, M. D. McGehee, K. Leo, M. Riede and A. Salleo, *Adv Mater* **26**, 3839 (2014).

105. G. H. Jung and J.-L. Lee, *Journal of Materials Chemistry A* **1**, 3034 (2013).

106. B. E. Lassiter, G. Wei, S. Wang, J. D. Zimmerman, V. V. Diev, M. E. Thompson and S. R. Forrest, *Applied Physics Letters* **98**, 243307 (2011).

107. P. Peumans and S. R. Forrest, *Applied Physics Letters* **79**, 126 (2001).

108. M. Vogel, S. Doka, C. Breyer, M. C. Lux-Steiner and K. Fostiropoulos, *Applied Physics Letters* **89**, 163501 (2006).

109. Y. Hirose, A. Kahn, V. Aristov, P. Soukiassian, V. Bulovic and S. R. Forrest, *Physical Review B* **54**, 13748 (1996).

110. A. C. Arias, M. Granström, D. S. Thomas, K. Petritsch and R. H. Friend, *Physical Review B* **60**, 1854 (1999).

111. I. Hancox, P. Sullivan, K. V. Chauhan, N. Beaumont, L. A. Rochford, R. A. Hatton and T. S. Jones, *Organic Electronics* **11**, 2019 (2010).

112. L. S. Roman, W. Mammo, L. A. A. Pettersson, M. R. Andersson and O. Inganäs, *Advanced Materials* **10**, 774 (1998).

113. V. Shrotriya, G. Li, Y. Yao, C.-W. Chu and Y. Yang, *Applied Physics Letters* **88**, 073508 (2006).

114. Y. Yi, P. E. Jeon, H. Lee, K. Han, H. S. Kim, K. Jeong and S. W. Cho, *Journal of Chemical Physics* **130**, 094704 (2009).

115. F. L. Zhang, A. Gadisa, O. Inganäs, M. Svensson and M. R. Andersson, *Applied Physics Letters* **84**, 3906 (2004).

116. B. P. Rand, P. Peumans and S. R. Forrest, *Journal of Applied Physics* **96**, 7519 (2004).

117. P. Peumans, V. Bulović and S. R. Forrest, *Applied Physics Letters* **76**, 2650 (2000).

118. H. Kageyama, H. Kajii, Y. Ohmori and Y. Shirota, *Applied Physics Express* **4**, 032301 (2011).

119. M. Hirade and C. Adachi, *Applied Physics Letters* **99**, 153302 (2011).

120. S. Grob, M. Gruber, A. N. Bartynski, U. Hörmann, T. Linderl, M. E. Thompson and W. Brütting, *Applied Physics Letters* **104**, 213304 (2014).

121. C.-F. Lin, S.-W. Liu, C.-C. Lee, T. Sakurai, M. Kubota, W.-C. Su, J.-C. Huang, T.-L. Chiu, H.-C. Han, L.-C. Chen, C.-T. Chen and J.-H. Lee, *Solar Energy Materials and Solar Cells* **137**, 138 (2015).

122. J. C. Wang, S. Q. Shi, C. W. Leung, S. P. Lau, K. Y. Wong and P. K. L. Chan, *Applied Physics Letters* **100**, 053301 (2012).

123. J. D. Zimmerman, B. Song, O. Griffith and S. R. Forrest, *Applied Physics Letters* **103**, 243905 (2013).

124. T. Fleetham, B. O'Brien, J. P. Mudrick, J. Xue and J. Li, *Applied Physics Letters* **103**, 083303 (2013).

125. T. B. Fleetham, J. P. Mudrick, W. Cao, K. Klimes, J. Xue and J. Li, *ACS Applied Materials and Interfaces* **6**, 7254 (2014).

126. A. Hinderhofer, A. Gerlach, K. Broch, T. Hosokai, K. Yonezawa, K. Kato, S. Kera, N. Ueno and F. Schreiber, *The Journal of Physical Chemistry C* **117**, 1053 (2013).

127. D. Hong, Y. R. Do, H. T. Kwak and S. Yim, *Journal of Applied Physics* **109**, 063507 (2011).

128. S. Kawata, Y.-J. Pu, C. Ohashi, K.-i. Nakayama, Z. Hong and J. Kido, *Journal of Materials Chemistry C* **2**, 501 (2014).

129. B. E. Lassiter, R. R. Lunt, C. K. Renshaw and S. R. Forrest, *Optics Express* **18**, A444 (2010).

130. C. Schünemann, D. Wynands, K.-J. Eichhorn, M. Stamm, K. Leo and M. Riede, *The Journal of Physical Chemistry C* **117**, 11600 (2013).

131. K. Soo Yook, B. Doo Chin, J. Yeob Lee, B. E. Lassiter and S. R. Forrest, *Applied Physics Letters* **99**, 043308 (2011).

132. P. Sullivan, T. S. Jones, A. J. Ferguson and S. Heutz, *Applied Physics Letters* **91**, 233114 (2007).

133. W. Zhao, J. P. Mudrick, Y. Zheng, W. T. Hammond, Y. Yang and J. Xue, *Organic Electronics* **13**, 129 (2012).

134. Y. Zhou, T. Taima, T. Kuwabara and K. Takahashi, *Advanced Materials* **25**, 6069 (2013).

135. R. R. Lunt, J. B. Benziger and S. R. Forrest, *Advanced Materials* **22**, 1233 (2010).

136. K. Cnops, B. P. Rand, D. Cheyns and P. Heremans, *Applied Physics Letters* **101**, 143301 (2012).

137. T. D. Heidel, D. Hochbaum, J. M. Sussman, V. Singh, M. E. Bahlke, I. Hiromi, J. Lee and M. A. Baldo, *Journal of Applied Physics* **109**, 104502 (2011).

138. Z. R. Hong, R. Lessmann, B. Maennig, Q. Huang, K. Harada, M. Riede and K. Leo, *Journal of Applied Physics* **106**, 064511 (2009).

139. G. Zhang, W. Li, B. Chu, L. Chen, F. Yan, J. Zhu, Y. Chen and C. S. Lee, *Applied Physics Letters* **94**, 143302 (2009).

140. O. L. Griffith and S. R. Forrest, *Nano Letters* **14**, 2353 (2014).

141. M. Ichikawa, D. Takekawa, H.-G. Jeon and G. D. R. Banoukepa, *Organic Electronics* **14**, 814 (2013).

142. S. M. Menke and R. J. Holmes, *ACS Applied Materials and Interfaces* **7**, 2912 (2015).

143. C. W. Schlenker, V. S. Barlier, S. W. Chin, M. T. Whited, R. E. McAnally, S. R. Forrest and M. E. Thompson, *Chemistry of Materials* **23**, 4132 (2011).

144. N. C. Giebink, B. E. Lassiter, G. P. Wiederrecht, M. R. Wasielewski and S. R. Forrest, *Physical Review B* **82**, 155306 (2010).

145. H. H. P. Gommans, D. Cheyns, T. Aernouts, C. Girotto, J. Poortmans and P. Heremans, *Advanced Functional Materials* **17**, 2653 (2007).

146. M. S. Dresselhaus, G. Dresselhaus and P. C. Eklund, *Science of Fullerenes and Carbon Nanotubes*, Academic Press, 1996.

147. M. T. Greiner, M. G. Helander, W. M. Tang, Z. B. Wang, J. Qiu and Z. H. Lu, *Nature Materials* **11**, 76 (2012).

148. A. Kahn, N. Koch and W. Gao, *Journal of Polymer Science, Part B: Polymer Physics* **41**, 2529 (2003).

149. K. L. Mutolo, E. I. Mayo, B. P. Rand, S. R. Forrest and M. E. Thompson, *Journal of the American Chemical Society* **128**, 8108 (2006).

150. H. J. Byrne, W. Maser, W. W. Rühle, A. Mittelbach, W. Hönle, H. G. v. Schnering, B. Movaghar and S. Roth, *Chemical Physics Letters* **204**, 461 (1993).

151. H. Gommans, B. Verreet, B. P. Rand, R. Muller, J. Poortmans, P. Heremans and J. Genoe, *Advanced Functional Materials* **18**, 3686 (2008).

152. Y. Kawamura, H. Sasabe and C. Adachi, *Japanese Journal of Applied Physics* **43**, 7729 (2004).

153. N. F. Mott and R. W. Gurney, *Electronic Processes in Ionic Crystals*, Oxford University Press, London, 1940.

154. S. L. M. van Mensfoort, V. Shabro, R. J. de Vries, R. A. J. Janssen and R. Coehoorn, *Journal of Applied Physics* **107**, 113710 (2010).

155. N. Beaumont, S. W. Cho, P. Sullivan, D. Newby, K. E. Smith and T. S. Jones, *Advanced Functional Materials* **22**, 561 (2012).

156. A. Foertig, A. Wagenpfahl, T. Gerbich, D. Cheyns, V. Dyakonov and C. Deibel, *Advanced Energy Materials* **2**, 1483 (2012).

157. C. H. Seaman, *Solar Energy* **29**, 291 (1982).

158. W. Tress, S. Corvers, K. Leo and M. Riede, *Advanced Energy Materials* **3**, 873 (2013).

159. W. Tress and O. Inganäs, *Solar Energy Materials and Solar Cells* **117**, 599 (2013).

160. W. Tress, K. Leo and M. Riede, *Advanced Functional Materials* **21**, 2140 (2011).

161. G. Garcia-Belmonte, A. Guerrero and J. Bisquert, *The Journal of Physical Chemistry Letters* **4**, 877 (2013).

162. G. Garcia-Belmonte, P. P. Boix, J. Bisquert, M. Sessolo and H. J. Bolink, *Solar Energy Materials and Solar Cells* **94**, 366 (2010).

163. S. Y. Kim, *Journal of Applied Physics* **95**, 2560 (2004).

164. W. Song, S. K. So, D. Wang, Y. Qiu and L. Cao, *Applied Surface Science* **177**, 158 (2001).

165. K. Sugiyama, H. Ishii, Y. Ouchi and K. Seki, *Journal of Applied Physics* **87**, 295 (2000).

166. P. M. Borsenberger, L. Pautmeier, R. Richert and H. Bässler, *The Journal of Chemical Physics* **94**, 8276 (1991).

167. A. Fleissner, H. Schmid, C. Melzer and H. von Seggern, *Applied Physics Letters* **91**, 242103 (2007).

168. H. Kageyama, H. Ohishi, M. Tanaka, Y. Ohmori and Y. Shirota, *Advanced Functional Materials* **19**, 3948 (2009).

169. S. Noh, C. K. Suman, Y. Hong and C. Lee, *Journal of Applied Physics* **105**, 033709 (2009).

170. Y.-C. Tseng, A. U. Mane, J. W. Elam and S. B. Darling, *Solar Energy Materials and Solar Cells* **99**, 235 (2012).

171. B. E. Lassiter, C. Kyle Renshaw and S. R. Forrest, *Journal of Applied Physics* **113**, 214505 (2013).

172. B. P. Rand, D. P. Burk and S. R. Forrest, *Physical Review B* **75** (2007).

173. F. Gao, W. Tress, J. Wang and O. Inganäs, *Physical Review Letters* **114** (2015).

174. Z. Tang, B. Liu, A. Melianas, J. Bergqvist, W. Tress, Q. Bao, D. Qian, O. Inganas and F. Zhang, *Advanced Materials* **27**, 1900 (2015).

175. M. Zhang, H. Wang and C. W. Tang, *Applied Physics Letters* **97**, 143503 (2010).

176. F. Liu, P. Paul Ruden, I. H. Campbell and D. L. Smith, *Applied Physics Letters* **99**, 123301 (2011).

177. N. Matsumoto and C. Adachi, *Journal of Physical Chemistry C* **114**, 4652 (2010).

178. J. Yang and J. Shen, *Journal of Applied Physics D: Applied Physics* **33**, 1768 (2000).

179. K. Cnops, B. P. Rand, D. Cheyns, B. Verreet, M. A. Empl and P. Heremans, *Nature Communications* **5**, 3406 (2014).

180. H. A. Atwater and A. Polman, *Nature Materials* **9**, 205 (2010).

181. K. R. Catchpole and A. Polman, *Optics Express* **16**, 21793 (2008).

182. D. M. Callahan, J. N. Munday and H. A. Atwater, *Nano Letters* **12**, 214 (2012).

183. P. Berini, *Laser & Photonics Reviews* **8**, 197 (2014).

184. D. K. Gramotnev and S. I. Bozhevolnyi, *Nature Photonics* **4**, 83 (2010).

185. P. Neutens, P. Van Dorpe, I. De Vlaminck, L. Lagae and G. Borghs, *Nature Photonics* **3**, 283 (2009).

186. S.-W. Baek, J. Noh, C.-H. Lee, B. Kim, M.-K. Seo and J.-Y. Lee, *Scientific Reports* **3**, 1726 (2013).

187. F.-C. Chen, J.-L. Wu, C.-L. Lee, Y. Hong, C.-H. Kuo and M. H. Huang, *Applied Physics Letters* **95**, 013305 (2009).

188. J.-Y. Lee and P. Peumans, *Optics Express* **18**, 10078 (2010).

189. D. H. Wang, K. H. Park, J. H. Seo, J. Seifter, J. H. Jeon, J. K. Kim, J. H. Park, O. O. Park and A. J. Heeger, *Advanced Energy Materials* **1**, 766 (2011).

190. X. Yang, C.-C. Chueh, C.-Z. Li, H.-L. Yip, P. Yin, H. Chen, W.-C. Chen and A. K. Y. Jen, *Advanced Energy Materials* **3**, 666 (2013).

191. K. Yao, M. Salvador, C.-C. Chueh, X.-K. Xin, Y.-X. Xu, D. W. deQuilettes, T. Hu, Y. Chen, D. S. Ginger and A. K. Y. Jen, *Advanced Energy Materials* **4**, 1400206 (2014).

192. S. Basu Mallick, N. P. Sergeant, M. Agrawal, J.-Y. Lee and P. Peumans, *MRS Bulletin* **36**, 453 (2011).

193. J. W. Leem, S. Kim, C. Park, E. Kim and J. S. Yu, *ACS Applied Materials and Interfaces* **7**, 6706 (2015).

194. C. Min, J. Li, G. Veronis, J.-Y. Lee, S. Fan and P. Peumans, *Applied Physics Letters* **96**, 133302 (2010).

195. B. Niesen, B. P. Rand, P. Van Dorpe, D. Cheyns, L. Tong, A. Dmitriev and P. Heremans, *Advanced Energy Materials* **3**, 145 (2013).

196. A. J. Smith, C. Wang, D. Guo, C. Sun and J. Huang, *Nature Communications* **5**, 5517 (2014).

197. J. You, X. Li, F.-x. Xie, W. E. I. Sha, J. H. W. Kwong, G. Li, W. C. H. Choy and Y. Yang, *Advanced Energy Materials* **2**, 1203 (2012).

198. H. Choi, J. P. Lee, S. J. Ko, J. W. Jung, H. Park, S. Yoo, O. Park, J. R. Jeong, S. Park and J. Y. Kim, *Nano Letters* **13**, 2204 (2013).

199. R. R. Grote, S. J. Brown, J. B. Driscoll, R. M. Osgood, Jr. and J. A. Schuller, *Optics Express* **21**, A847 (2013).

200. J. Khan, S. E. Harton, P. Akcora, B. C. Benicewicz and S. K. Kumar, *Macromolecules* **42**, 5741 (2009).

201. S. K. Kumar, N. Jouault, B. Benicewicz and T. Neely, *Macromolecules* **46**, 3199 (2013).

202. P. Drude, *Annalen der Physik* **308**, 369 (1900).

203. D. Palik and G. Ghosh, *Handbook of Optical Constants of Solids*, Academic Press, New York, 1985.

204. E. Kretschmann and H. Raether, *Zeitschrift für Naturforschung A* **23**, 2135 (1968).

205. G. Mie, *Annalen der Physik* **330**, 377 (1908).

206. S. Wedge, I. R. Hooper, I. Sage and W. L. Barnes, *Physical Review B* **69** (2004).

207. M. Furno, M. C. Gather, B. r. Lüssem and K. Leo, *Applied Physics Letters* **100**, 253301 (2012).

208. J. B. D. Soole, H. P. Hughes and N. Apsley, *Journal of Applied Physics* **61**, 2022 (1987).

209. D. Woolf, M. Loncar and F. Capasso, *Optics Express* **17**, 19996 (2009).

210. B. O'Connor, C. Haughn, K.-H. An, K. P. Pipe and M. Shtein, *Applied Physics Letters* **93**, 223304 (2008).

211. K. L. Agrawal, M. E. Sykes, K. Hyup An, B. Frieberg, P. F. Green and M. Shtein, *Applied Physics Letters* **102**, 113304 (2013).

212. V. Bulović, V. B. Khalfin, G. Gu, P. E. Burrows, D. Z. Garbuzov and S. R. Forrest, *Physical Review B* **58**, 3730 (1998).

213. Q. Huang, K. Walzer, M. Pfeiffer, V. Lyssenko, G. He and K. Leo, *Applied Physics Letters* **88**, 113515 (2006).

214. H. Riel, S. Karg, T. Beierlein, W. Rieß and K. Neyts, *Journal of Applied Physics* **94**, 5290 (2003).

215. K. H. An, M. Shtein and K. P. Pipe, *Optics Express* **18**, 4041 (2010).

216. J. Lee, S.-Y. Kim, C. Kim and J.-J. Kim, *Applied Physics Letters* **97**, 083306 (2010).

217. H.-W. Lin, S.-W. Chiu, L.-Y. Lin, Z.-Y. Hung, Y.-H. Chen, F. Lin and K.-T. Wong, *Advanced Materials* **24**, 2269 (2012).

218. B. O'Connor, K. H. An, K. P. Pipe, Y. Zhao and M. Shtein, *Applied Physics Letters* **89**, 233502 (2006).

219. C. Zhang, D. Zhao, D. Gu, H. Kim, T. Ling, Y. K. Wu and L. J. Guo, *Advanced Materials* **26**, 5696 (2014).

220. R. F. Bailey-Salzman, B. P. Rand and S. R. Forrest, *Applied Physics Letters* **88**, 233502 (2006).

221. R. Betancur, P. Romero-Gomez, A. Martinez-Otero, X. Elias, M. Maymó and J. Martorell, *Nature Photonics* **7**, 995 (2013).

222. C.-Y. Chang, L. Zuo, H.-L. Yip, C.-Z. Li, Y. Li, C.-S. Hsu, Y.-J. Cheng, H. Chen and A. K. Y. Jen, *Advanced Energy Materials* **4**, 1301645 (2014).

223. K. Celebi, T. D. Heidel and M. A. Baldo, *Optics Express* **15**, 1762 (2007).

224. L. T. Vuong, G. Kozyreff, R. Betancur and J. Martorell, *Applied Physics Letters* **95**, 233106 (2009).

225. E. A. Schiff, *Journal of Applied Physics* **110**, 104501 (2011).

226. X. Sheng, J. Hu, J. Michel and L. C. Kimerling, *Optics Express* **20**, A496 (2012).

227. M. Bora, K. Çelebi, J. Zuniga, C. Watson, K. M. Milaninia and M. A. Baldo, *Optics Express* **17**, 329 (2009).

228. T. Kume, S. Hayashi, H. Ohkuma and K. Yamamoto, *Japanese Journal of Applied Physics* **34**, 6448 (1995).

229. T. Kume, S. Hayashi and K. Yamamoto, *Japanese Journal of Applied Physics* **32**, 3486 (1993).

230. J. K. Mapel, M. Singh, M. A. Baldo and K. Celebi, *Applied Physics Letters* **90**, 121102 (2007).

231. T. Wakamatsu, K. Saito, Y. Sakakibara and H. Yokoyama, *Japanese Journal of Applied Physics* **34**, L1467 (1995).

232. M. E. Sykes, A. Barito, J. A. Amonoo, P. F. Green and M. Shtein, *Advanced Energy Materials* **4**, 1301937 (2014).

233. S. Zhang, L. Berguiga, J. Elezgaray, T. Roland, C. Faivre-Moskalenko and F. Argoul, *Surface Science* **601**, 5445 (2007).

234. C. Z. Li, C. C. Chueh, F. Ding, H. L. Yip, P. W. Liang, X. Li and A. K. Jen, *Advanced Materials* **25**, 4425 (2013).

235. I. Irfan and Y. Gao, *Journal of Photonics for Energy* **2**, 021213 (2012).

236. I. Irfan, A. James Turinske, Z. Bao and Y. Gao, *Applied Physics Letters* **101**, 093305 (2012).

237. N. C. Giebink, G. P. Wiederrecht and M. R. Wasielewski, *Nature Photonics* **5**, 694 (2011).

238. Z. H. Kafafi, T. D. Heidel, J. K. Mapel, K. Celebi, M. Singh, M. A. Baldo and P. A. Lane, *Proceedings of SPIE* **6656**, 66560I (2007).

239. C. Kim and J. Kim, *Optics Express* **16**, 19988 (2008).

240. H. Ditlbacher, F. R. Aussenegg, J. R. Krenn, B. Lamprecht, G. Jakopic and G. Leising, *Applied Physics Letters* **89**, 161101 (2006).

241. N. Engheta, *Science* **317**, 1698 (2007).

242. A. Kriesch, S. P. Burgos, D. Ploss, H. Pfeifer, H. A. Atwater and U. Peschel, *Nano Letters* **13**, 4539 (2013).

243. H. W. Lee, G. Papadakis, S. P. Burgos, K. Chander, A. Kriesch, R. Pala, U. Peschel and H. A. Atwater, *Nano Letters* **14**, 6463 (2014).